

# A Levelized Comparison of Pulsed and Steady-State Tokamaks

by

Daniel Joseph Segal

B.S. Engineering Physics, University of Wisconsin (2014)

Submitted to the Department of Nuclear Science and Engineering  
in partial fulfillment of the requirements for the degree of

Master of Science in Nuclear Science and Engineering

at the

MASSACHUSETTS INSTITUTE OF TECHNOLOGY

February 2019

© Massachusetts Institute of Technology 2019. All rights reserved.

Author .....

Department of Nuclear Science and Engineering  
January 9, 2019

Certified by .....

Jeffrey P. Freidberg  
KEPCO Professor Emeritus  
Thesis Supervisor

Certified by .....

Anne E. White  
Cecil and Ida Green Associate Professor  
Thesis Reader

Accepted by .....

Ju Li  
Battelle Energy Alliance Professor  
Chair, Department Committee on Graduate Students



# A Levelized Comparison of Pulsed and Steady-State Tokamaks

by

Daniel Joseph Segal

Submitted to the Department of Nuclear Science and Engineering  
on January 9, 2019, in partial fulfillment of the  
requirements for the degree of  
Master of Science in Nuclear Science and Engineering

## Abstract

The goal of fusion energy research is to build an economically competitive reactor. This is difficult due to the complicated system composing a reactor and the nonlinearities it entails. Practically, to even get to the neighborhood of an economic reactor requires hundreds of simulations – which in turn necessitate quick running fusion systems codes. Moving towards these economic reactors then involves finding what design parameters provide the most leverage in lowering reactor costs.

As highlighted by the difference between European and American designs, however, the most important decision for tokamaks is whether to run them as *pulsed* or *steady-state*. This paper aims to fairly compare the two modes of operation using a single, comprehensive model. Benchmarked against other codes, this model actually shows that no fusion reactor is achievable without some technological advancements. This can be seen through every referenced design using nonstandard values of  $H$  and  $N_G$ .

The interesting result this paper shows is that developing high-temperature superconducting (HTS) tape could actually make both steady-state and pulsed tokamaks economically competitive against solar and coal. Further, this HTS tape actually has different best uses for the two modes of operation, appearing in the magnet structures of: TF coils for steady state and the central solenoid for pulsed. Developments in this technology should produce economic reactors within the coming decade.

Thesis Supervisor: Jeffrey P. Freidberg

Title: Professor of Nuclear Science and Engineering (Emeritus)



# Contents

<b>1</b>	<b>Introducing Fusion Reactor Design</b>	<b>17</b>
1.1	Distinguishing Pulsed from Steady-State . . . . .	18
1.2	Pricing a Fusion Reactor . . . . .	19
1.3	Modeling Fusion Systems . . . . .	21
1.4	Discussing HTS Magnet Technology . . . . .	22
<b>2</b>	<b>Designing a Steady-State Tokamak</b>	<b>25</b>
2.1	Defining Plasma Parameters . . . . .	26
2.1.1	Understanding Tokamak Geometry . . . . .	26
2.1.2	Prescribing Plasma Profiles . . . . .	28
2.2	Solving the Steady Current . . . . .	31
2.2.1	Enforcing the Greenwald Density Limit . . . . .	31
2.2.2	Declaring the Bootstrap Current . . . . .	34
2.2.3	Deriving the Fusion Power . . . . .	35
2.2.4	Using Current Drive . . . . .	37
2.2.5	Completing the Steady Current . . . . .	38
2.3	Handling Current Drive Self-Consistently . . . . .	39
<b>3</b>	<b>Formalizing the Systems Model</b>	<b>41</b>
3.1	Explaining Static Variables . . . . .	42
3.2	Connecting Dynamic Variables . . . . .	42
3.3	Enforcing Power Balance . . . . .	46
3.3.1	Collecting Power Sources . . . . .	46
3.3.2	Approximating Radiation Losses . . . . .	48

3.3.3	Estimating Heat Conduction Losses . . . . .	49
3.3.4	Writing the Lawson Parameter . . . . .	51
3.3.5	Finalizing the Primary Constraint . . . . .	53
3.4	Collecting Limiting Constraints . . . . .	56
3.4.1	Introducing the Beta Limit . . . . .	56
3.4.2	Giving the Kink Safety Factor . . . . .	58
3.4.3	Working under the Wall Loading Limit . . . . .	58
3.4.4	Setting a Maximum Power Cap . . . . .	60
3.4.5	Listing the Heat Loading Limit . . . . .	61
3.5	Summarizing the Fusion Systems Model . . . . .	62
<b>4</b>	<b>Designing a Pulsed Tokamak</b>	<b>65</b>
4.1	Modeling Plasmas as Circuits . . . . .	66
4.1.1	Drawing the Circuit Diagram . . . . .	66
4.1.2	Plotting Pulse Profiles . . . . .	68
4.1.3	Specifying Circuit Variables . . . . .	72
4.1.4	Constructing the Pulse Length . . . . .	76
4.2	Producing Flux Balance . . . . .	77
4.2.1	Rearranging the Circuit Equation . . . . .	78
4.2.2	Adding Poloidal Field Coils . . . . .	79
4.3	Improving Tokamak Geometry . . . . .	81
4.3.1	Defining Central Solenoid Dimensions . . . . .	81
4.3.2	Calculating Component Thicknesses . . . . .	82
4.3.3	Revisiting Central Solenoid Dimensions . . . . .	85
4.4	Piecing Together the Generalized Current . . . . .	87
4.5	Simplifying the Generalized Current . . . . .	88
4.5.1	Recovering the Steady Current . . . . .	88
4.5.2	Extracting the Pulsed Current . . . . .	89
4.5.3	Rationalizing the Generalized Current . . . . .	90

<b>5</b>	<b>Completing the Systems Model</b>	<b>91</b>
5.1	Describing a Simple Algebra . . . . .	91
5.2	Generalizing Previous Equations . . . . .	93
5.2.1	Including Limiting Constraints . . . . .	93
5.2.2	Minimizing Intermediate Quantities . . . . .	95
5.2.3	Assigning Dynamic Variables . . . . .	96
5.2.4	Detailing the Equation Solver . . . . .	96
5.3	Wrapping up the Logic . . . . .	99
<b>6</b>	<b>Presenting the Code Results</b>	<b>101</b>
6.1	Testing the Code against other Models . . . . .	102
6.1.1	Comparing with the PSFC ARC Reactor . . . . .	103
6.1.2	Contrasting with the ARIES ACT Studies . . . . .	104
6.1.3	Benchmarking with the Process DEMO Designs . . . . .	106
6.2	Developing Prototype Reactors . . . . .	113
6.2.1	Navigating around Charybdis . . . . .	117
6.2.2	Pinning down Proteus . . . . .	117
6.2.3	Highlighting Operation Differences . . . . .	118
6.3	Learning from the Data . . . . .	118
6.3.1	Picking a Design Point . . . . .	118
6.3.2	Utilizing High Field Magnets . . . . .	123
6.3.3	Looking at Design Alternatives . . . . .	126
<b>7</b>	<b>Planning Future Work for the Model</b>	<b>133</b>
7.1	Incorporating Stellarator Technology – Ladon . . . . .	133
7.2	Making a Composite Reactor – Janus . . . . .	134
7.3	Bridging Confinement Scalings – Daedalus . . . . .	135
7.4	Addressing Model Shortcomings . . . . .	136
7.4.1	Integrating Pedestal Temperature Profiles . . . . .	137
7.4.2	Expanding the Radiation Loss Term . . . . .	137
7.4.3	Taking Flux Sources Seriously . . . . .	137

<b>8</b>	<b>Concluding Reactor Discussion</b>	<b>139</b>
<b>A</b>	<b>Cataloging Model Variables</b>	<b>141</b>
A.1	Static Variables . . . . .	141
A.2	Dynamic Variables . . . . .	142
A.3	Intermediate Variables . . . . .	142
<b>B</b>	<b>Simulating with Fussy.jl</b>	<b>143</b>
B.1	Getting the Code to Work . . . . .	143
B.2	Sorting out the Codebase . . . . .	144
B.2.1	Typing out Structures . . . . .	145
B.2.2	Referencing Input Decks and Solutions . . . . .	147
B.2.3	Acknowledging Utility Functions . . . . .	147
B.2.4	Mentioning Base Level Files . . . . .	147
B.3	Delving into Reactor Methods . . . . .	148
B.4	Demonstrating Code Usage . . . . .	149
B.4.1	Initializing the Workspace . . . . .	150
B.4.2	Running a Study . . . . .	150
B.4.3	Extracting Results . . . . .	151
B.4.4	Plotting Curves . . . . .	152
<b>C</b>	<b>Discussing Fusion Power</b>	<b>157</b>
C.1	Theoretical Background . . . . .	157
C.2	Bosch-Hale Reactivity . . . . .	159
<b>D</b>	<b>Selecting Plasma Profiles</b>	<b>163</b>
D.1	Density – $n$ . . . . .	163
D.2	Temperature – $T$ . . . . .	165
D.3	Pressure – $p$ . . . . .	167
D.4	Bootstrap Current – $f_{BS}$ . . . . .	167
D.5	Volume Averaged Powers . . . . .	169



<b>E</b>	<b>Determining Plasma Flux Surfaces</b>	<b>171</b>
E.1	Flux Surface Coordinates . . . . .	172
E.2	Cross-sectional Area and Volume . . . . .	173
E.3	Surface and Volume Integrals . . . . .	174
<b>F</b>	<b>Expanding on the Bootstrap Current</b>	<b>177</b>
F.1	Summarized Results . . . . .	177
F.2	Detailed Analysis . . . . .	179
<b>G</b>	<b>Elaborating on the Current Drive</b>	<b>185</b>
G.1	Summarized Results . . . . .	185
G.2	Detailed Analysis . . . . .	186
<b>H</b>	<b>Compending Code Plots</b>	<b>195</b>
H.1	Magnet Strength Scans . . . . .	196
H.2	Cost Sensitivity Studies . . . . .	217
	<b>References</b>	<b>234</b>

# List of Figures

1-1	Cut-Away of Tokamak Reactor . . . . .	18
1-2	Comparison of Pulsed and Steady-State Current . . . . .	19
1-3	Steady State Magnet Components . . . . .	23
1-4	Pulsed Magnet Components . . . . .	23
2-1	Geometry of a Tokamak . . . . .	27
2-2	Geometric Parameters . . . . .	28
2-3	Radial Plasma Profiles . . . . .	29
2-4	Greenwald Density Limit . . . . .	33
3-1	Current Balance in a Tokamak . . . . .	45
3-2	Power Balance in a Reactor . . . . .	52
3-3	H-Mode Confinement Time Scaling . . . . .	54
4-1	A Simple Plasma Transformer Description . . . . .	67
4-2	Time Evolution of Circuit Profiles . . . . .	69
4-3	Dimensions of Tokamak Cross-Section . . . . .	82
5-1	Equation Selection for Fusion System . . . . .	92
5-2	Reactor Cost Minimization . . . . .	97
6-1	ARC and ACT Studies Cost Dependence on the H Factor . . . . .	105
6-2	ARC Model Comparison . . . . .	108
6-3	ARIES ACT I Model Comparison . . . . .	109
6-4	ARIES ACT II Model Comparison . . . . .	110
6-5	DEMO Steady Model Comparison . . . . .	111

6-6	DEMO Pulsed Model Comparison . . . . .	112
6-7	Designing Reactor Prototypes . . . . .	114
6-8	Steady State Prototype Comparison . . . . .	115
6-9	Pulsed Prototype Comparison . . . . .	116
6-10	Limiting Constraint Regimes . . . . .	119
6-11	Steady State Cost Curves . . . . .	121
6-12	Pulsed Cost Curves . . . . .	122
6-13	Pulsed $B_{CS}$ Sensitivities . . . . .	124
6-14	Pulsed Monte Carlo Sampling . . . . .	125
6-15	Bootstrap Current Monte Carlo Sampling . . . . .	127
6-16	Internal Inductance Sensitivities . . . . .	128
6-17	Pulsed H Sensitivities . . . . .	130
6-18	Steady State Current Drive Efficiency . . . . .	131
6-19	Current Drive Efficiency vs. Launch Angle . . . . .	132
7-1	Cut-Away of Stellarator Reactor . . . . .	134
7-2	Current Balance in a Tokamak . . . . .	135
B-1	A Blank Plot . . . . .	153
B-2	An Empty Plot . . . . .	154
B-3	An Unscaled Plot . . . . .	154
B-4	A Scaled Plot . . . . .	155
C-1	Comparing Nuclear Fusion and Fission . . . . .	158
C-2	The D-T Fusion Reaction . . . . .	159
D-1	Radial Plasma Profiles . . . . .	163
E-1	Cut-Away of Tokamak Reactor . . . . .	171
E-2	Dimensions of Tokamak Cross-Section . . . . .	174

# List of Tables

3.1	Dynamic Variables . . . . .	42
4.1	Piecewise Linear Scheme for Pulsed Operation . . . . .	69
4.2	Example TF Coils and Central Solenoid Critical Values . . . . .	84
5.1	Main Equation Bank . . . . .	94
6.1	ARC Variables . . . . .	108
6.2	ACT I Variables . . . . .	109
6.3	ACT II Variables . . . . .	110
6.4	DEMO Steady Variables . . . . .	111
6.5	DEMO Pulsed Variables . . . . .	112
6.6	Charybdis Variables . . . . .	115
6.7	Proteus Variables . . . . .	116
6.8	Proteus and Charybdis Comparison . . . . .	117
A.1	List of Static Variables . . . . .	141
A.2	List of Dynamic Variables . . . . .	142
A.3	List of Intermediate Variables (Noncomprehensive) . . . . .	142
C.1	Bosch-Hale Parametrization Coefficients . . . . .	161
C.2	Tabulated Bosch-Hale Reactivities . . . . .	161

# List of Equations

1.1	Magnetic Energy – $W_M$ . . . . .	20
1.3	Cost-per-Watt – $C_W$ . . . . .	21
2.1	Minor Radius – $a$ . . . . .	27
2.2	Density Profile – $n$ . . . . .	29
2.4	Temperature Profile – $T$ . . . . .	30
2.5	Current Density Profile – $J$ . . . . .	30
2.6	Normalized Poloidal Magnetic Field – $b_p$ . . . . .	31
2.7	Current Balance – $I$ . . . . .	31
2.10	Greenwald Density – $\bar{n}$ . . . . .	32
2.14	Bootstrap Current – $I_{BS}$ . . . . .	35
2.19	Dilution Factor – $f_D$ . . . . .	36
2.21	Fusion Power – $P_F$ . . . . .	36
2.25	Heating Power – $P_H$ . . . . .	38
2.26	Current Drive – $I_{CD}$ . . . . .	38
2.28	Steady Current – $I_P$ . . . . .	39
2.29	Current Drive Efficiency – $\eta_{CD}$ . . . . .	40
3.1	Scanned Temperature – $\bar{T}$ . . . . .	43
3.3	Current Fractions – $f$ . . . . .	44
3.6	Power Balance – $P$ . . . . .	46
3.8	Plasma Resistance – $R_P$ . . . . .	47
3.10	Ohmic Power – $P_\Omega$ . . . . .	47
3.15	Bremsstrahlung Power – $P_{BR}$ . . . . .	49
3.20	Heat Conduction Losses – $P_\kappa$ . . . . .	50
3.23	Triple Product – $\bar{n} \cdot \bar{T} \cdot \tau_E$ . . . . .	52

3.25	Generalized Confinement Time Scaling Law – $\tau_E$	53
3.26	Loss Power – $P_{src}$	54
3.27	ELMy H-Mode Confinement Time Scaling Law – $\tau_E^H$	55
3.28	Primary Constraint – $B_0$	55
3.35	Plasma Pressure – $\bar{p}$	57
3.38	Troyon Beta Limit – $\beta_N$	57
3.41	Kink Safety Factor – $q_*$	58
3.43	Surface Area – $S_P$	59
3.45	Wall Loading Limit – $P_W$	59
3.47	Electric Power – $P_E$	60
3.51	Maximum Power Limit – $P_{max}$	61
3.55	Heat Loading Limit – $q_{DV}$	62
4.12	Ramp-Up Time – $\tau_{RU}$	70
4.16	Flat-top Time – $\tau_{FT}$	71
4.17	Ramp-Down Time – $\tau_{RD}$	71
4.19	Dwell Time – $\tau_{DW}$	72
4.20	Duty Factor – $f_{duty}$	73
4.23	Inductive Current – $I_{ID}$	74
4.26	Central Solenoid Inductance – $L_1$	75
4.29	Plasma Inductance – $L_2$	75
4.34	Mutual Inductance – $M$	76
4.40	Central Solenoid Flux – $\Phi_{CS}$	78
4.42	Ramp-Up Flux – $\Phi_{RU}$	79
4.43	Flat-top Flux – $\Phi_{FT}$	79
4.44	PF Coil Flux – $\Phi_{PF}$	79
4.48	Plasma Perimeter – $l_p$	80
4.50	Vertical Field Strength – $B_V$	80
4.53	Flux Balance – $\Phi$	81
4.56	Blanket Thickness – $b$	83
4.57	TF Coil Thickness – $c$	83

4.61	Central Solenoid Thickness – $d$ . . . . .	84
4.64	Central Solenoid Height – $h_{CS}$ . . . . .	85
4.65	Central Solenoid Inner Radius – $R_{CS}$ . . . . .	85
4.75	Generalized Current – $I_P$ . . . . .	88
5.3	General Model Equation – $G(\overline{T})$ . . . . .	93
5.6	General Model Solution – $\gamma_{RB\{I,T\}}$ . . . . .	98
6.1	DEMO Loss Power – $P_L^{DEMO}$ . . . . .	106
7.1	L-Mode Confinement Time Scaling Law – $\tau_E^L$ . . . . .	136
7.2	I-Mode Confinement Time Scaling Law – $\tau_E^I$ . . . . .	136
C.2	Fusion Energy – $E_F$ . . . . .	158
C.3	Neutron Power – $P_n$ . . . . .	158
C.4	Alpha Power – $P_\alpha$ . . . . .	158
C.9	Bosch-Hale Reactivity – $\langle\sigma v\rangle$ . . . . .	160
E.14	Shaping Parameter – $g$ . . . . .	173
E.24	Volume Integral – $Q_V$ . . . . .	175
E.25	Surface Integral – $Q_S$ . . . . .	175
F.7	Internal Inductance – $l_i$ . . . . .	178





# Chapter 1

## Introducing Fusion Reactor Design

The central goal of fusion energy research is to build an economically competitive nuclear reactor. It has long been joked, though, that fusion power will always be twenty years away. This is mainly due to the nonlinearities inherent to a reactor system and the high upfront cost of building new machines. The model developed for this paper uses standard theory and empirical fits to find cost trends from this nonlinear system. An important conclusion is that building an economic reactor using existing technology would be impossible. One solution may be improving magnet technology – as MIT is exploring with high-temperature superconducting (HTS) tape.

As can be seen by comparing the European and American/Asian fusion reactor design efforts, though, one of the most important decisions is whether to run the reactor as pulsed (EU<sup>1,2</sup>) or steady-state (US<sup>3</sup> and Korea<sup>4</sup>). The distinction between the two mainly manifests itself in the choice of auxiliary current drive: inductive for pulsed and lower hybrid for steady-state.<sup>5</sup> With the model built for this thesis, it is possible to perform a direct comparison of these two modes of operation.

Due to the speed and simplicity of the model, hundreds of reactors can be simulated in minutes. Further, the model has been benchmarked against other ones from the literature,<sup>3,6–8</sup> allowing it to answer several critical questions regarding the comparison of the two modes of operation. A major finding of this is that HTS tape should

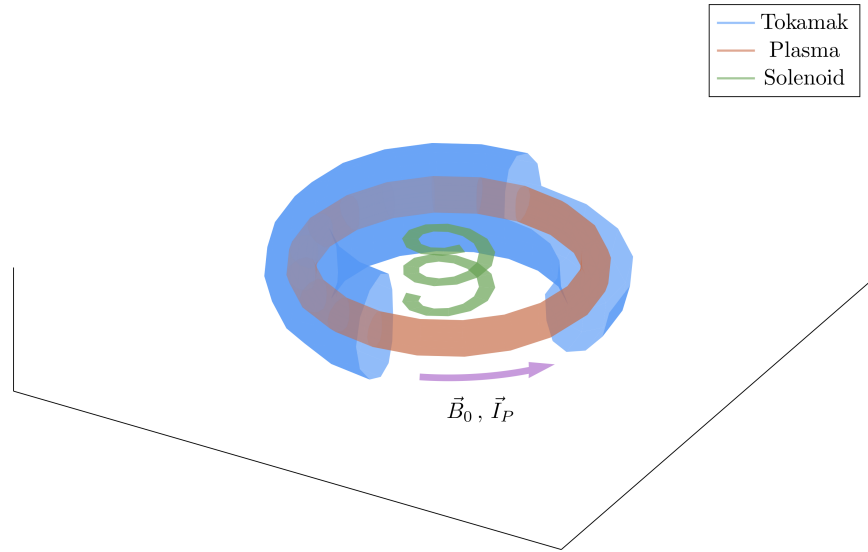


Figure 1-1: Cut-Away of Tokamak Reactor

The three main components of a magnetic fusion reactor are: the tokamak structure, the plasma fuel, and the coiled solenoid at the center. Here, the directions of the magnetic field ( $B_0$ ) and plasma current ( $I_P$ ) variables are shown to be in the toroidal direction.

appear in different places for the two modes of operation: within the central solenoid for pulsed machines and inside the TF coils for steady-state ones. A more apparent finding is that pulsed can be competitive and the US should investigate it further.

## 1.1 Distinguishing Pulsed from Steady-State

The leading candidate for the first economically competitive fusion reactor is a tokamak. As shown in Fig. 1-1, tokamaks are doughnut-shaped metal structures that use magnets to confine their fusion-grade plasmas. The challenge in building such a device comes from the various physics and engineering constraints it must satisfy – i.e. not surpassing acceptable levels of neutron damage, plasma pressure, etc.

One of the most contentious points of reactor design, however, is whether to run it as: pulsed (the European effort<sup>1,2</sup>) or steady-state (the American/Asian approach<sup>3,4</sup>). Here, pulsed operation refers to how a reactor is ramped up and down several times

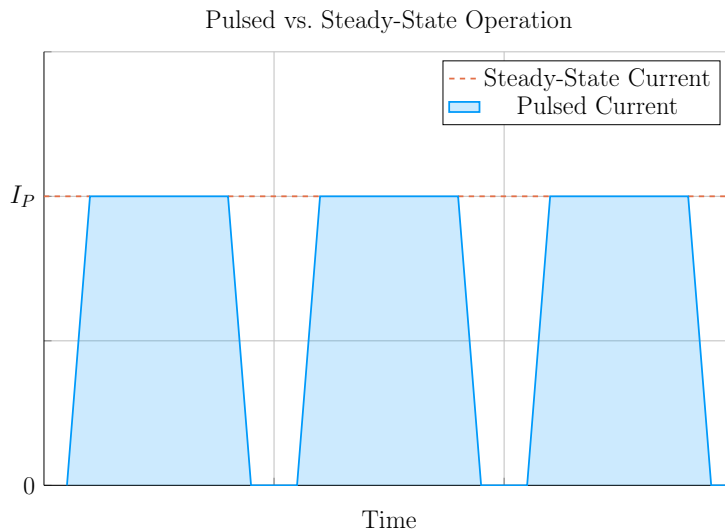


Figure 1-2: Comparison of Pulsed and Steady-State Current

Inside a pulsed reactor, current is ramped up and down several times a day – with downtime in-between. Steady state reactors are meant to remain on for weeks or months.

a day. Whereas steady-state implies a machine is functionally kept ramped up the entirety of its fifty-year campaign. These behaviors are shown in Fig. 1-2. The difficulties involved with the two modes of operation are then: cyclical stresses for pulsed devices and expensive current drive for steady state ones.<sup>5</sup>

The main way these two modes of operation, *pulsed* and *steady-state*, influence reactor design, however, is through the current balance equation (derived later). What this means practically is a tokamak plasma requires some current to stay in equilibrium and this current has to be partially generated by auxiliary systems: inductively for pulsed and non-inductively for steady-state.<sup>5</sup> To fairly compare the two modes of operation thus requires a generalized handling of current balance that can incorporate both sets of auxiliary systems.

## 1.2 Pricing a Fusion Reactor

To truly compare tokamaks used as fusion reactors, though, the obvious metrics are costs. ITER – the most expensive experiment in the world<sup>9,10</sup> – has a history full of

countries backing out for high construction costs and rejoining only after they finally get lowered.<sup>5</sup> The problem is \$20B is a lot of money and 20 years is a long time. Moreover, approximating true costs of the experiment is made difficult due to the need to project (or neglect) economies-of-scale for expensive components, such as the superconducting magnets and irradiated materials.

Therefore, this paper adopts stand-ins for the conventional capital cost and cost-per-watt metrics. This is done for simplicity, both in: formulating the relations and conveying the two metrics to physicists. The approximation for the capital cost – how much a tokamak costs to build – is then the magnetic energy.<sup>11</sup>

$$W_M \propto R^3 B^2 \tag{1.1}$$

In this magnetic energy proportion relation, the tokamak’s major radius –  $R$  – is involved in a volumetric term ( $R^3$ ) and  $B$  is the strength (in Teslas) of the toroidal magnetic field. This quantity simply states that the two surefire ways to make a machine more expensive are to build it bigger and to use stronger magnets. As these terms also improve confinement, this cost introduces a trade-off between size and magnet technology. This is why the proposed ARC reactor – designed with HTS tape – could be half the size of ITER, which uses conventional LTS technology.<sup>5,6</sup>

The next metric, the cost-per-watt, is defined by dividing the capital cost (i.e. the magnetic energy) by the main source of power output. For tokamaks, this source of power is fusion – discussed in more detail in Appendix C. The cost-per-watt thus measures how economically competitive a reactor will be once it is build. This is how to compare the rate of return for different base-load power sources (e.g. fission, coal, and solar).

$$\tilde{C}_W = \frac{W_M}{P_F} \tag{1.2}$$

A final correction can be made on the cost-per-watt to account for reactor downtime, which is fundamental to pulsed operation. This is handled through the duty factor ( $f_{duty}$ ) that is defined as the ratio of a reactor’s quasi-steady-state flattop duration

to the entire pulse length of a tokamak – as shown in Fig. 1-2. In the context of the cost-per-watt, it scales down the fusion power:

$$C_W = \frac{W_M}{f_{duty} \cdot P_F} \quad (1.3)$$

For a steady-state reactor, this duty factor is assumed to be held at one. Pulsed machines, on the other hand, can see up to thirty minutes of downtime,<sup>8</sup> which leads to duty factors around 80%. Analysis in Section 4.1.4, however, shows that pulsed reactors may also have duty factors near unity.

Combined, these two cost metrics allow designers to pinpoint economically competitive tokamaks within reactor space. Although not rigorous in an engineering context, these capital cost and cost-per-watt approximations do provide true physics meaning when comparing different machines – whether they run as pulsed or steady-state.

## 1.3 Modeling Fusion Systems

Before reactors can be priced, though, they have to be modeled. Therefore the first half of this thesis is devoted to the theory behind tokamak design. Emphasis is placed more on a physicist’s intuition than an engineer’s costing rigor. This is justified by the nonlinearities inherent to fusion systems and rationalized by this paper’s results matching more sophisticated models with high fidelity.

Stepping back, however, a fusion systems model is an approach to designing reactors based on satisfying various physics and engineering constraints. There are already many of these models in the field.<sup>6,7,12–18</sup> Zero-dimensional (0-D) systems models then form a particular subclass of these that reduce the inherently 3-D problem of design to a collection of scalar, averaged values. This reduction in complexity allows models to be orders of magnitude faster. The natural corollary of which is that hundreds of reactors can be simulated in minutes.

Within the context of reactor design, these 0-D systems models serve an important role due to their speed and simplicity. Although not truly self-consistent,\* these models are capable of exploring large areas of reactor space. This is especially important in the early stages of tokamak planning when researchers are selecting a design point. These models also have use when searching for general costing trends – as shown in this document.

What makes this paper’s systems model different from others in the field, though, is its generalized handling of both modes of tokamak operation: pulsed and steady-state. This was necessitated by a desire to fairly compare the two. The most fundamental result of this analysis is that both modes are actually capable of leading to economically competitive reactors – assuming some technological advancements.

## 1.4 Discussing HTS Magnet Technology

As mentioned, no economically competitive fusion reactor can be built using existing technology – regardless of whether it runs as pulsed or steady-state. This is why MIT has been exploring HTS magnet technology for their SPARC reactor in an effort to nearly double the maximum achievable field strength. What this paper shows is that this logic is indeed correct and HTS may be the final magnet advancement needed for the conventional fusion paradigm (i.e. D-T fuel, H-Mode, etc.)

More concretely, this paper shows that new HTS technology is capable of lowering reactor costs – both for pulsed and steady-state operation. Further, this HTS tape has different uses within the two modes of operation – as set by cost concerns (see Figs. 1-3 and 1-4). This analysis shows that HTS should be employed in the TF coils for steady-state reactors *and* in the central solenoid for pulsed ones. This is because pulsed machines require lower toroidal field strengths, which are achievable with less expensive LTS (low-temperature superconducting) magnets.

---

\*For speed concerns, 0-D fusion systems models often ignore self consistency in quantities like pressure profiles and use empirical fits to estimate values such as the confinement time.

Now that the problem has been thoroughly introduced, we will go over the theory behind steady-state and, then, pulsed tokamaks. A couple detours will be taken along the way to show how the model can be incorporated into a fusion systems code. This code – `Fussy.jl` – is the topic of Appendix B and is freely available at:

[git.io/tokamak](https://git.io/tokamak)

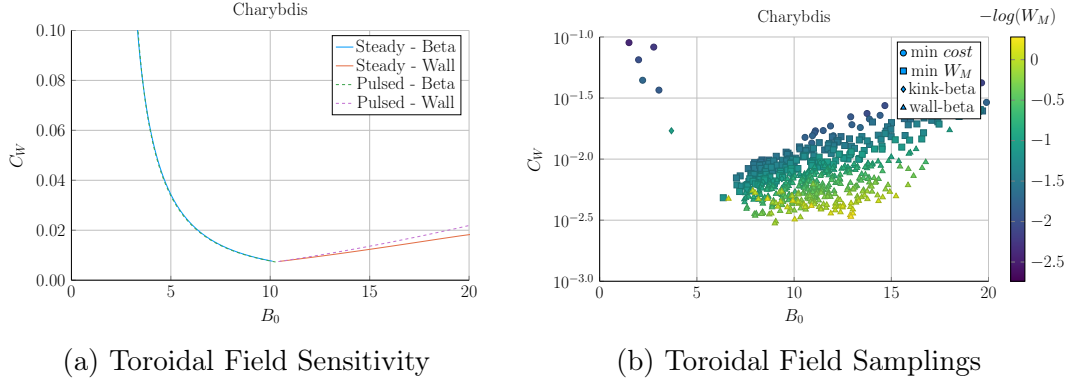


Figure 1-3: Steady State Magnet Components

Steady-state reactors benefit from increased toroidal field strength until neutron wall loading starts to dominate design (at around 10-15 T for Charybdis). This is well within the range accessible to HTS magnets.

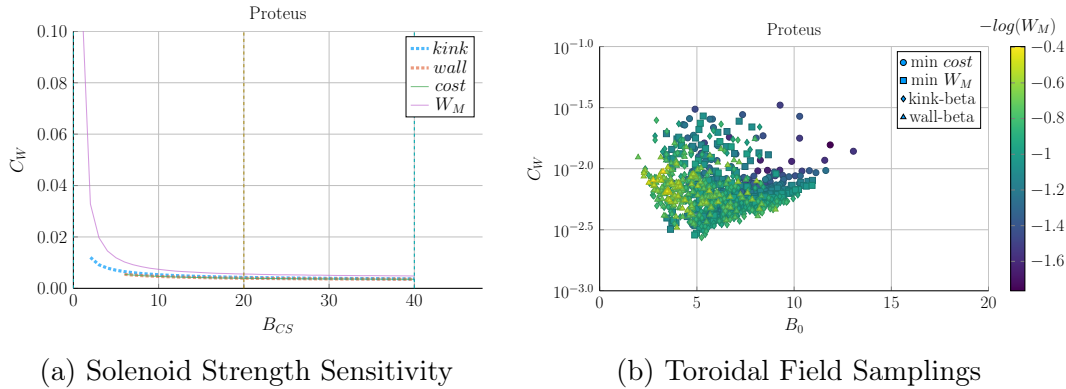


Figure 1-4: Pulsed Magnet Components

Pulsed reactors are shown to receive strong decreases in reactor cost as the central solenoid field strength is increased, until around 20 T. However, the TF coils do not receive the same cost reduction with field strength – as shown by the minimum cost appearing at 5 T.





## Chapter 2

# Designing a Steady-State Tokamak

This chapter explores a simple model for designing steady-state tokamaks. In the next couple chapters, the model is first formalized for use in a systems code and then generalized to handle pulsed operation. These derivations highlight that the only difference between the two modes of operation is how they generate their auxiliary plasma current: lower-hybrid current drive (LHCD) for steady-state operation and inductive sources for when a reactor is purely pulsed.<sup>5</sup>

Along the way, equations will be derived that get rather complicated. To remedy the situation, a distinction between dynamic and static variables is now given, which will allow splitting most equations into dynamic and static parts. Dynamic values – i.e. the tokamak’s major radius ( $R_0$ ) and magnet strength ( $B_0$ ), as well as the plasma’s current ( $I_P$ ), temperature ( $\bar{T}$ ), and density ( $\bar{n}$ ) – are first-class variables in the model (see Table 3.1). Everything is derived to relate them. Static values, on the other hand, can be treated as code inputs, which remain constant throughout a reactor solve. These most obviously include the various geometric and profile parameters introduced next section.

The overall structure of this chapter, then, is built around developing an equation for plasma current in a steady-state tokamak. It is shown that this value arises from balancing current in a reactor using both a plasma’s own bootstrap current ( $I_{BS}$ ),

as well the tokamak’s auxiliary driven current ( $I_{CD}$ ). These relations necessitate geometric parameters and plasma profiles, which will be given shortly. Along the way, definitions will also be needed for the Greenwald density ( $N_G$ ) and the fusion power ( $P_F$ ). What is shown by this is that the current does not actually depend directly on the major radius ( $R_0$ ) or magnet strength ( $B_0$ ) of a tokamak – allowing these variables to be put off until next chapter.

## 2.1 Defining Plasma Parameters

As mentioned previously, the zero-dimensional model derived here can closely approximate solutions from higher-dimensional codes that might take many hours to run. The essence of reducing three-dimensional behaviors to one dimensional profiles – and zero-dimensional averaged values – begins with defining the most important plasma parameters. These are the: current density (J), temperature (T), and density (n) of a plasma.

Solving this problem most generally usually involves decoupling the geometry of the plasma from the shaping of its nearly parabolic radial-profiles – both of which will be explained shortly.

### 2.1.1 Understanding Tokamak Geometry

The first thing people see when they look at a tokamak is its geometry – see Fig. 2-1. How big is it? Is it stretched out like a bicycle tire or compressed to the point of being nearly spherical? Would a slice across the major radius result in two cross-sections that were: circular, elliptic, or triangular?

These questions lend themselves to the three important geometric variables – the inverse aspect ratio ( $\varepsilon$ ), the elongation ( $\kappa$ ), and the triangularity ( $\delta$ ). The inverse

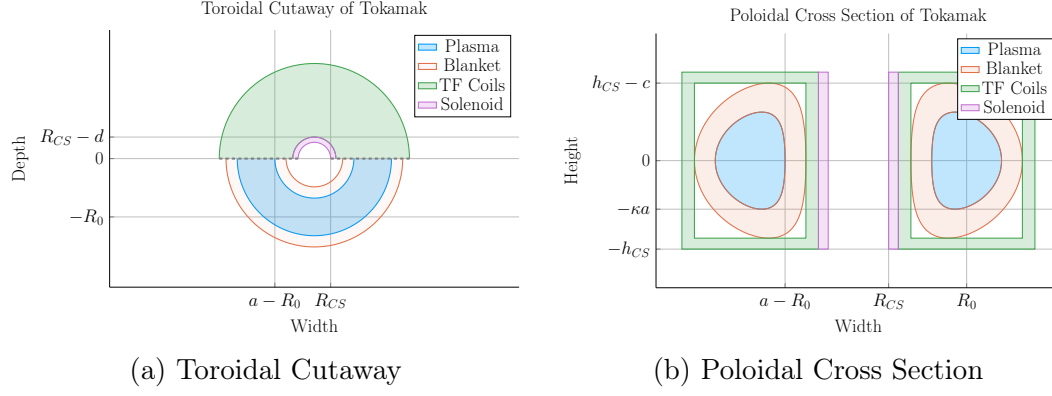


Figure 2-1: Geometry of a Tokamak

This diagram is of a tokamak's toroidal (top) view and the poloidal cross section of a slice across its major axis. Included are the four components of a reactor: the plasma, its metallic blanket, the toroidal field magnets surrounding them, and the central solenoid. These have thicknesses of  $a$ ,  $b$ ,  $c$  and  $d$ , respectively.  $R_{CS}$  is where the solenoid begins.

aspect ratio is a measure of how stretched out the device is, or formulaically:

$$a = \varepsilon \cdot R_0 \quad (2.1)$$

This says that the minor radius ( $a$ ), measured in meters, is related to the major radius of the machine ( $R_0$ ) through  $\varepsilon$ . Or more tangibly, the minor radius is related to the two small cross-sections that result from a slice across a machine's major radius.

The two remaining geometric parameters –  $\kappa$  and  $\delta$  – are then related to the shape of the poloidal cross-sections. As the name hints, elongation ( $\kappa$ ) is a measure of how stretched out the tokamak is vertically – is the cross-section a circle or an oval? The triangularity ( $\delta$ ) is then how much the cross-sections point outward from the center of the device. All three's effects can be seen in Fig. 2-2. Their exact usage within describing flux surfaces is then explained in Appendix E.

These geometric factors also allow the volumetric and surface integrals governing fusion power and bootstrap current to be condensed to simple radial ones – see Eqs. (E.24) and (E.25). The only remaining step is to define the radial profiles for: the density ( $n$ ), temperature ( $T$ ), and current density ( $J$ ) of a plasma.

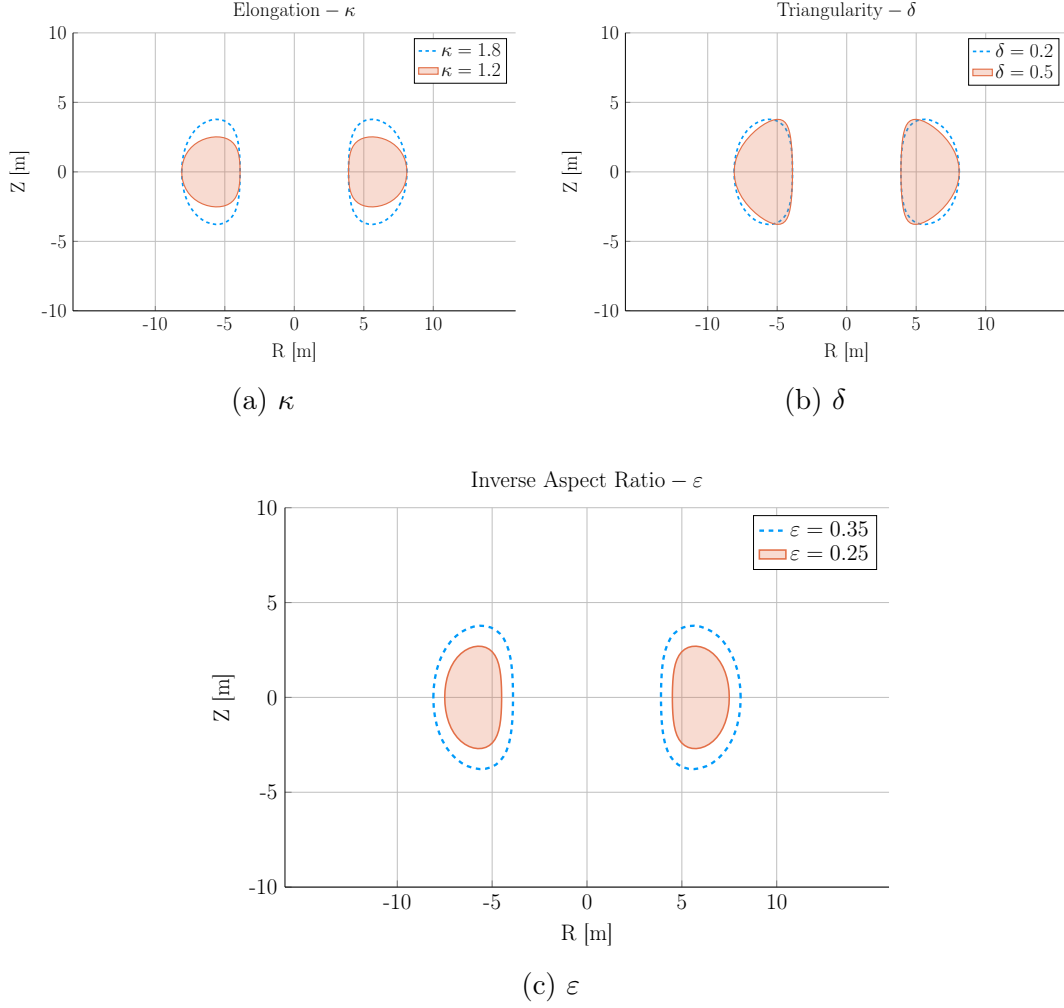


Figure 2-2: Geometric Parameters

These three geometric parameters allow the toroidal cross-sections to scale radially ( $\varepsilon$ ), stretch vertically ( $\kappa$ ), and become more triangular ( $\delta$ ).

### 2.1.2 Prescribing Plasma Profiles

The first step in defining radial profiles is realizing that all three quantities are essentially parabolic – i.e. the temperature, density and current density, shown in Fig. 2-3, are peaked at some radius (usually the center) and then decay to zero somewhere before the walls of the tokamak enclosure.

Although not self-consistent, these profiles do capture enough of the physics to approximate relevant phenomenon, such as transport and fusion power.<sup>19</sup>

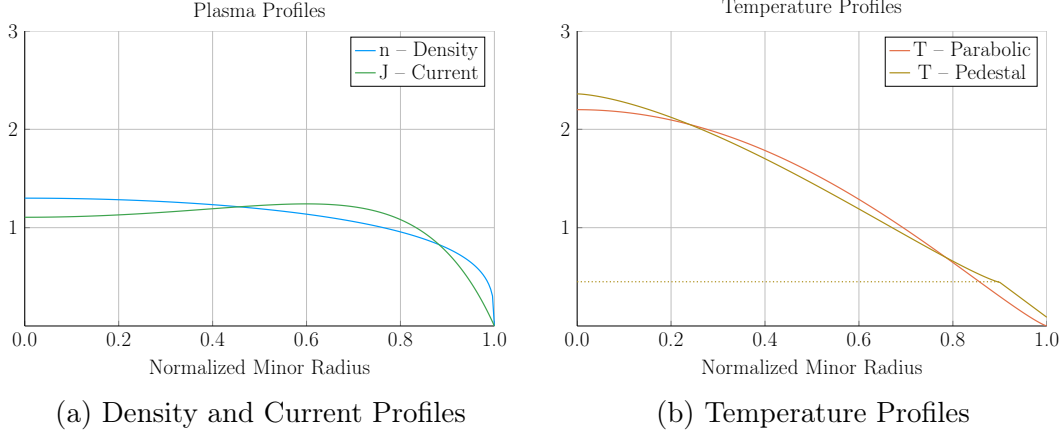


Figure 2-3: Radial Plasma Profiles

The three most fundamental profiles of a fusion plasma are its temperature, density, and current. These allow the model to reduce from three dimensions to just half of one.

## The Density Profile

To begin, density has the simplest profile. This is because it is relatively flat, remaining near the average value –  $\bar{n}$  – throughout the body of the plasma until quickly decaying to zero near the edge of the plasma.\* For this reason, a parabolic profile with a very low peaking factor –  $\nu_n$  – is well suited.

$$n(\rho) = \bar{n} \cdot (1 + \nu_n) \cdot (1 - \rho^2)^{\nu_n} \quad (2.2)$$

Here,  $\rho$  is a normalized radial-like flux label, with  $\rho = 0$  occurring at the magnetic axis and  $\rho = 1$  being at the outer plasma surface (i.e. the 95% surface). The variable  $\bar{n}$  is then referred to as the volume-averaged density because using the volume integral – given by Eq. (E.24) – over the density profile results in that value, after dividing through by the volume ( $V$ ):

$$\bar{n} = \frac{\int n(\mathbf{r}) d\mathbf{r}}{V} \quad (2.3)$$

---

\*Even in H-Mode plasmas where density profiles have a pedestal,<sup>20</sup> they usually have much less of a peak than temperatures<sup>21</sup> – especially in a reactor setting.<sup>22</sup>

A final point to make is this parabolic profile allows for a short closed-form relation for the Greenwald density limit – substantially simplifying this fusion systems model.

### The Temperature Profile

The use of a parabolic profile for the plasma temperature is slightly more dubious. This is because H-Mode plasmas are actually highly peaked at the center, decaying to a non-zero pedestal temperature near the edge before finally dropping sharply to zero. This model chooses to forego this pedestal representation for a simple parabolic one – although the pedestal approach is discussed in Appendix D. Analogous to the density, the profile treats  $\bar{T}$  as the average value and  $\nu_T$  as the peaking parameter.

$$T(\rho) = \bar{T} \cdot (1 + \nu_T) \cdot (1 - \rho^2)^{\nu_T} \quad (2.4)$$

### The Current Density Profile

The plasma current density is the third profile and cannot safely be represented by a simple parabola. This is because having an adequate bootstrap current relies heavily on a profile being peaked off-axis – i.e. at some radius not at the center. This hollow profile can then be modeled with the commonly given plasma internal inductance ( $l_i$ ). Concretely, the current's hollow profile is described by:

$$J(\rho) = \bar{J} \cdot \frac{\gamma^2 \cdot (1 - \rho^2) \cdot e^{\gamma \rho^2}}{e^\gamma - 1 - \gamma} \quad (2.5)$$

The intermediate  $\gamma$  quantity can then be numerically solved for from the plasma internal inductance using the following relations – with  $b_p$  representing the normalized poloidal magnetic field. These are derived in Appendix F.

$$l_i = \frac{4\kappa}{1 + \kappa^2} \int_0^1 b_p^2 \rho d\rho \quad (F.7)$$

$$b_p(\rho) = \frac{-e^{\gamma\rho^2}(\gamma\rho^2 - 1 - \gamma) - 1 - \gamma}{\rho(e^\gamma - 1 - \gamma)} \quad (2.6)$$

Combined, these three geometric parameters and profiles lay the foundation for this zero-dimensional fusion systems model.

## 2.2 Solving the Steady Current

As suggested, one of the most important equations in a fusion reactor is current balance. In steady-state operation, all of a plasma's current ( $I_P$ ) must come from a combination of its own bootstrap current ( $I_{BS}$ ), as well as auxiliary current drive ( $I_{CD}$ ). This can be represented mathematically as:

$$I_P = I_{BS} + I_{CD} \quad (2.7)$$

The goal is then to write equations for bootstrap current and driven current. This will make heavy use of the Greenwald density limit. The steady current will then be shown to be only a function of temperature! In other words, this current is independent of a tokamak's geometry and magnet strength. As will be pointed out then, though, a subtlety arises that will bring the two back into the picture – self-consistency in the current drive efficiency ( $\eta_{CD}$ ).

### 2.2.1 Enforcing the Greenwald Density Limit

The Greenwald density limit is a density limit that applies to all tokamaks. It sets a hard limit on the density and how it scales with current and reactor size. Although currently lacking a true first-principles theoretical explanation, it does have a real meaning within the design context. Operate at too low a density and run the risk of never entering H-Mode. Run the density too high, and cause the tokamak's plasma

to disrupt. To this, Fig. 2-4 shows that most shots exist in the regime between the two extremes.

As no theoretical backing exists, the Greenwald density limit can simply be written (with citation) as:<sup>23</sup>

$$\hat{n} = N_G \cdot \left( \frac{I_P}{\pi a^2} \right) \quad (2.8)$$

Here,  $\hat{n}$  has units of  $10^{20} \frac{\text{particles}}{\text{m}^3}$ ,  $N_G$  is the Greenwald density fraction, and  $I_P$  is again the plasma current (measured in mega-amps). The final variable is then the minor radius –  $a$  – which was previously defined through:

$$a = \varepsilon \cdot R_0 \quad (2.1)$$

The next step is transforming the *line-averaged* density ( $\hat{n}$ ) into the *volume-averaged* version ( $\bar{n}$ ) used in this model. Harnessing the simplicity of the density's parabolic profile allows this relation to be written in a closed form as:

$$\hat{n} = \frac{\sqrt{\pi}}{2} \cdot \left( \frac{\Gamma(\nu_n + 2)}{\Gamma(\nu_n + \frac{3}{2})} \right) \cdot \bar{n} \quad (2.9)$$

Here,  $\Gamma(\dots)$  represents the gamma function: the non-integer analogue of the factorial function.

Combining these pieces allows the volume-averaged density to be written in standardized units as:

$$\bar{n} = K_n \cdot \left( \frac{I_P}{R_0^2} \right) \quad (2.10)$$

$$K_n = \frac{2N_G}{\varepsilon^2 \pi^{3/2}} \cdot \left( \frac{\Gamma(\nu_n + \frac{3}{2})}{\Gamma(\nu_n + 2)} \right) \quad (2.11)$$

The format of the previous equation pair will be used throughout the remainder of the paper. The top equation relates dynamic variables (i.e.  $\bar{n}$ ,  $I_P$ , and  $R_0$ ), while the static-value coefficient ( $K_n$ ) lumps together static quantities, such as:  $N_G$ ,  $\varepsilon$ ,  $2$ ,  $\pi$ , and  $\nu_n$ .



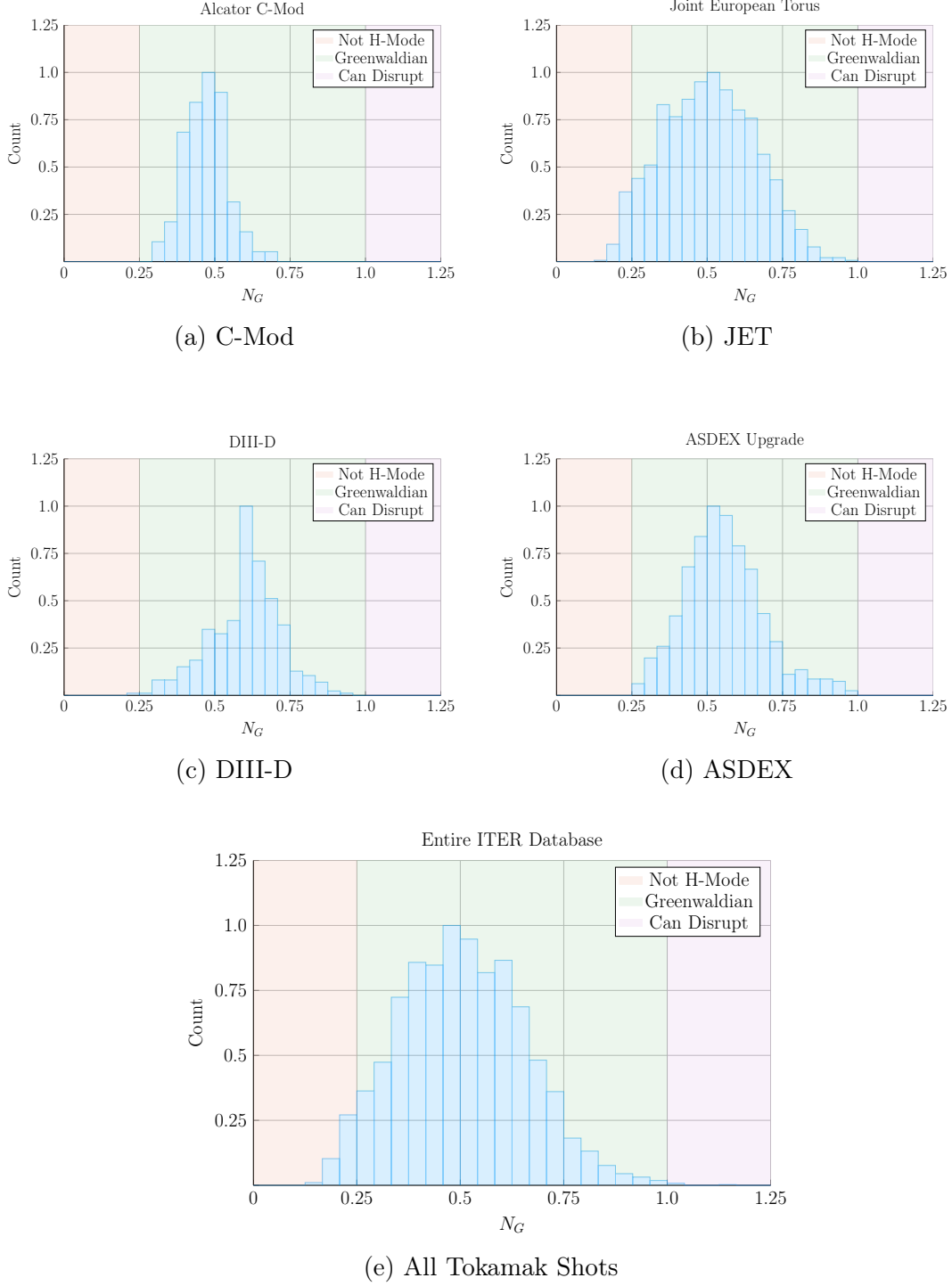


Figure 2-4: Greenwald Density Limit

The Greenwald Limit is a robust metric of what densities an H-Mode plasma can attain – here referred to as a *Greenwaldian* region. Although empirical in nature, it accurately predicts when a tokamak will undergo degraded plasma transport.<sup>23,24</sup>

### 2.2.2 Declaring the Bootstrap Current

The first term to define in current balance, Eq. (2.7), is the bootstrap current. This bootstrap current is a mechanism of tokamak plasmas that helps supply some of the current needed to keep a plasma in equilibrium. Its underlying behavior stems from particles stuck in banana-shaped orbits on the outer edges of the device propelling the majority species along their helical trajectories around the tokamak.

Utilizing the surface integral from Eq. (E.25), the bootstrap current ( $I_{BS}$ ) can be written in terms of the temperature and density profiles:

$$I_{BS} = 2\pi a^2 \kappa g \int_0^1 J_{BS} \rho d\rho \quad (2.12)$$

$$\begin{aligned} J_{BS} &= f \left( n, T, \frac{dn}{d\rho}, \frac{dT}{d\rho} \right) \\ &\equiv -4.85 \cdot n \cdot T \cdot \frac{R_0 \sqrt{\varepsilon} \rho}{d\psi/d\rho} \cdot \left( \frac{1}{n} \frac{dn}{d\rho} + 0.54 \frac{1}{T} \frac{dT}{d\rho} \right) \end{aligned} \quad (2.13)$$

Here,  $g$  is a geometric factor (of order 1) given by Eq. (E.14). While the second definition for the bootstrap current density –  $J_{BS}$  – comes from using well known theoretical results plus several simplifying assumptions, including the large aspect limit. The value of  $d\psi/d\rho$  is given in Appendix F.

As shown later in the results, bootstrap fractions are often under-predicted by this model. This is due to parabolic profiles (i.e. for the temperature) having much less steep declines near the edge (i.e. in their derivatives) than characteristic H-Mode profiles with pedestals. This implies that the area most positively impacted by a pedestal profile for temperature would be the bootstrap current derivation. The instructions to do so are given in Appendix D.4.

Finally, summarizing the results of Appendix F, the bootstrap current is found to be only a function of temperature and static variables! In standardized units, it can be

written as:

$$I_{BS} = K_{BS} \cdot \bar{T} \quad (2.14)$$

$$K_{BS} = 4.879 \cdot K_n \cdot \left( \frac{1 + \kappa^2}{2} \right) \cdot \varepsilon^{5/2} \cdot H_{BS} \quad (2.15)$$

$$H_{BS} = (1 + \nu_n)(1 + \nu_T)(\nu_n + 0.054\nu_T) \int_0^1 \frac{\rho^{5/2} (1 - \rho^2)^{\nu_n + \nu_T - 1}}{b_p} d\rho \quad (2.16)$$

Quickly noting, this  $H_{BS}$  term serves as the analogue of static-value coefficients (e.g.  $K_{BS}$  and  $K_n$ ) when they contain an integral. And  $b_p$  represents the poloidal magnet strength given by Eq. 2.6.

### 2.2.3 Deriving the Fusion Power

The next segue on our journey to solving for the steady current is deriving the fusion power ( $P_F$ ), which appears in current drive. A comprehensive introduction to this is given in Appendix C. Summarized, however, a formula for fusion power from a D-T reaction – in megawatts – is given by the following volume integral:<sup>25</sup>

$$P_F = \int E_F n_D n_T \langle \sigma v \rangle d\mathbf{r} \quad (2.17)$$

$$E_F = 17.6 \text{ MeV} \quad (2.18)$$

This  $E_F$  quantity is the energy created from a deuterium-tritium fusion reaction. The  $n_D$  and  $n_T$  variables then represent the density of the deuterium and tritium ions, respectively. Assuming a 50-50 mixture of the two, they can be related to the electron density – i.e. the one used in this model – through the dilution factor ( $f_D$ ). This dilution factor represents the decrease in available fuel from part of the plasma actually being composed of non-hydrogen gasses:

$$n_D = n_T = f_D \cdot \left( \frac{n}{2} \right) \quad (2.19)$$

Lastly, the fusion reactivity,  $\langle\sigma v\rangle$ , is a nonlinear function of the temperature,  $T$ , which the model approximates using the Bosch-Hale tabulation (described in Appendix C). As this tabulated value appears inside an integral, it seems important to point out that the temperature is now the most difficult dynamic variable to handle – over  $R_0$ ,  $B_0$ ,  $\bar{n}$ , and  $I_P$ . This will come into play when the model is formalized next chapter.

The next step in the derivation of fusion power is transforming the three-dimensional volume integral (see Eq. 2.17) into a zero-dimension averaged value. First, the volume integral for this model's geometry is given by:

$$Q_V = 4\pi^2 R_0 a^2 \kappa g \int_0^1 Q(\rho) \rho d\rho \quad (\text{E.24})$$

Where  $Q$  is an arbitrary function of  $\rho$  and  $g$  is a geometric factor approximately equal to one – both described in Appendix E. The fusion power can now be rewritten as:

$$P_F = g \kappa E_F R_0 (\pi a f_D)^2 \int_0^1 n^2 \langle\sigma v\rangle \rho d\rho \quad (2.20)$$

In standardized units, this becomes:

$$P_F = K_F \cdot \bar{n}^2 \cdot R_0^3 \cdot (\sigma v) \quad (2.21)$$

$$K_F = 278.3 \cdot f_D^2 \cdot (\varepsilon^2 \kappa g) \quad (2.22)$$

Where the standardized fusion reactivity is now,

$$(\sigma v) = 10^{21} (1 + \nu_n)^2 \int_0^1 (1 - \rho^2)^{2\nu_n} \langle\sigma v\rangle \rho d\rho \quad (2.23)$$

At this point, the current drive needed for steady-state can now be defined.

## 2.2.4 Using Current Drive

As may have been lost along the way, this chapter's mission is to define a formula for steady current – from the current balance equation for steady-state tokamaks:

$$I_P = I_{BS} + I_{CD} \quad (2.7)$$

In standardized units, current drive is often formulated in the literature as:<sup>26</sup>

$$I_{CD} = \eta_{CD} \cdot \left( \frac{P_H}{\bar{n}R_0} \right) \quad (2.24)$$

Here,  $\eta_{CD}$  is the current drive efficiency with units  $\left( \frac{\text{MA}}{\text{MW}\cdot\text{m}^2} \right)$  and  $P_H$  is the heating power – in megawatts – driven by LHCD (and absorbed by the plasma).\*

Let it be known, though, that driving current in a plasma is hard! In fact, pulsed reactor designers (i.e. European fusion researchers) think it is so difficult, they may choose to forego it completely – focusing only on inductive sources that necessitate reactor fatigue and downtime.

For LHCD, a common current drive efficiency ( $\eta_{CD}$ ) seen in many designs is  $0.3 \pm 0.1$  in the standard units.<sup>3,6,26</sup> It is however inherently a function of all the plasma parameters – with subtlety put off until the discussion of self-consistency. For now it assumed to have some constant/static value.

The remaining step in deriving an equation for driven current ( $I_{CD}$ ), then, is finding a formula for the heating power ( $P_H$ ). The way fusion systems models – like this one – handle the heating power is through the physics gain factor,  $Q$ . Sometimes referred to as big  $Q$ , this value represents how many times over the heating power ( $P_H$ ) is amplified as it is transformed into fusion power ( $P_F$ ):

$$P_H = \frac{P_F}{Q} \quad (2.25)$$

---

\*A more formal introduction to LHCD, as well as the reasoning behind selecting it over neutral beam (NBCD) and electron cyclotron current drive (ECCD), are given in Appendix G.

Now, utilizing the previously defined Greenwald density and fusion power:

$$\bar{n} = K_n \cdot \left( \frac{I_P}{R_0^2} \right) \quad (2.10)$$

$$P_F = K_F \cdot \bar{n}^2 \cdot R_0^3 \cdot (\sigma v) \quad (2.21)$$

The current from LHCD can be written as:

$$I_{CD} = K_{CD} \cdot I_P \cdot (\sigma v) \quad (2.26)$$

$$K_{CD} = (K_F K_n) \cdot \frac{\eta_{CD}}{Q} \quad (2.27)$$

As  $\eta_{CD}$  and  $Q$  appear within a static coefficient, it is implied that both remain constant throughout a solve. This subtlety is lifted when handling  $\eta_{CD}$  self-consistently, which will be discussed shortly. However, even in this context, it proves beneficial to think of  $\eta_{CD}$  as a sequence of static variables – set by the model rather than the user.

## 2.2.5 Completing the Steady Current

The goal of this chapter has been to derive a simple formula for steady current ( $I_P$ ). The problem started with current balance in a steady-state reactor:

$$I_P = I_{BS} + I_{CD} \quad (2.7)$$

Two equations were then found for the bootstrap ( $I_{BS}$ ) and driven ( $I_{CD}$ ) current:

$$I_{BS} = K_{BS} \cdot \bar{T} \quad (2.14)$$

$$I_{CD} = K_{CD} \cdot I_P \cdot (\sigma v) \quad (2.26)$$

Combining these three equations and solving for the total plasma current ( $I_P$ ) – in mega-amps – yields:

$$I_P = \frac{K_{BS} \bar{T}}{1 - K_{CD}(\sigma v)} \quad (2.28)$$

This is the answer we have been seeking!

As mentioned before, this simple formula appears to only depend on temperature!\* Apparently, the plasma should have the same current at some temperature (i.e.  $\bar{T} = 15$  keV), regardless of the size of the machine or the strength of its magnets. This has the important corollary that each temperature maps to only one current value. Further, each temperature would then map to a single magnet strength, capital cost, etc. (as shown next chapter).

As has become a mantra, though, the subtlety of this behavior lies in the self-consistency of the current-drive efficiency –  $\eta_{CD}$ .

## 2.3 Handling Current Drive Self-Consistently

Although a thorough description of the wave theory behind lower-hybrid current drive (LHCD) is well outside the scope of this text, it does motivate the solving of a tokamak's major radius ( $R_0$ ) and magnet strength ( $B_0$ ). It also shows how what was once a simple problem has now transformed into a rather complex one – a common occurrence with plasmas.

The logic behind finding a self-consistent current-drive efficiency is starting at some plausible value (i.e.  $\eta_{CD} = 0.3$ ), solving for the steady current – i.e.  $I_P = f(\bar{T})$  – and then somehow iteratively creeping towards a value deemed self-consistent. What this means is that in addition to the solver described in the last section, there needs to be a black-box function that solutions are sent through to get better guesses at  $\eta_{CD}$ .

---

\*This dependence only on temperature refers to dynamic variables. The plasma current can still be highly volatile to many of the static variables, such as:  $\varepsilon$ ,  $\kappa$ ,  $N_G$ ,  $f_D$ ,  $\nu_n$ ,  $l_i$ , etc.

The black-box function we use is a variation of the Ehst-Karney model.<sup>27</sup> A thorough description of this algorithm is given in Appendix G.

As mentioned previously, a self-consistent  $\eta_{CD}$  is found once a trip through the Ehst-Karney black-box results in the same  $\eta_{CD}$  as was sent in – to some tolerable level of error. This consistency incorporates an explicit dependence on the tokamak configuration. Mathematically,

$$\tilde{\eta}_{CD} = f(R_0, B_0, \bar{n}, \bar{T}, I_P) \quad (2.29)$$

As such, to recalculate it after every solution of the steady current requires a value for both  $B_0$  and  $R_0$  – the targets of this model’s primary and limiting constraints. These will be the highlight of the next chapter.



# Chapter 3

## Formalizing the Systems Model

The goal of this chapter is to take a step back from the steady current derivation and see the larger picture behind reactor design. As such, a more in-depth description of static and dynamic variables is given. This discussion of dynamic variables will then lend itself to a description of the framework underpinning the fusion systems model. As such, we will now need formulas for the radius and magnet strength of the tokamak. Moving forward, the current will remain a connecting piece as we redirect focus to pulsed tokamaks and compare the underlying solvers of the two schemes.

The end result of this analysis will then be equations that allow the density ( $\bar{n}$ ), current ( $I_P$ ), major radius ( $R_0$ ), and magnet strength ( $B_0$ ) to be written as functions of the temperature ( $\bar{T}$ ) and static variables (e.g.  $\nu_n$ ,  $N_G$ ,  $f_D$ ). These formulas are the product of applying constraints required for all tokamak reactors with several other limiting constraints. The constraints relevant to all tokamak reactors are: the Greenwald limit, current balance, and power balance. Limiting constraints then include: the Troyon beta limit, the kink safety factor, the wall loading limit, the maximum power constraint, and the heat loading limit.

Actual methodologies for solving for the five dynamic variables simultaneously – i.e. for  $\bar{T}$ ,  $\bar{n}$ ,  $I_P$ ,  $R_0$ ,  $B_0$  – are put off until Chapter 5 when current balance is in a generalized form.

### 3.1 Explaining Static Variables

In this model, static variables are ones that remain constant while solving for a reactor. These include geometric scalings (i.e.  $\varepsilon$ ,  $\delta$ ,  $\kappa$ ), profile parameters (i.e.  $\nu_n$ ,  $\nu_T$ ,  $l_i$ ), and a couple dozen physics constants related to pulsed and steady-state design (e.g.  $Q$ ,  $N_G$ ,  $f_D$ ). For a complete list of static variables, consult Appendix A.1. The point to make now is that this model treats static variables as immutable objects. As such they often reside in static coefficients –  $K_\square$  – which are treated as constants.

### 3.2 Connecting Dynamic Variables

Dynamic variables – i.e.  $\bar{T}$ ,  $\bar{n}$ ,  $I_P$ ,  $R_0$ ,  $B_0$  – are the first-class variables of this fusion systems model. They represent the fundamental properties of a plasma and tokamak (which constitute a fusion reactor). As such, they will be reintroduced one at a time, explaining how they fit into the model – with the equations capable of representing them.

Table 3.1: Dynamic Variables

Symbol	Name	Units
$I_P$	Plasma Current	MA
$\bar{T}$	Plasma Temperature	keV
$\bar{n}$	Electron Density	$10^{20} \text{ m}^{-3}$
$R_0$	Major Radius	m
$B_0$	Magnet Strength	T

At its core, this fusion systems model is a simple algebra problem: solve five equations with five unknowns (i.e.  $\bar{T}$ ,  $\bar{n}$ ,  $I_P$ ,  $R_0$ ,  $B_0$ ). Although this naive approach would work, we can do a little better by reducing these five equations down to just one. This was already done while deriving the steady current. It just happened that the current was not directly dependent on the tokamak size ( $R_0$ ) or magnet strength ( $B_0$ ).\*

---

\*Note that the magnet strength ( $B_0$ ) used throughout this text refers particularly to the strength of the toroidal magnetic field on axis – i.e. at  $\rho = 0$ .

This will prove more challenging for the generalized current needed for pulsed operation. Even so, this equation will still be reduced to one equation with a single unknown –  $I_P$ . A solution to which can be solved much faster than the naive 5 equation approach. This is one reason the model is so fast.

### **The Plasma Temperature – $\bar{T}$**

The plasma temperature, measured in keV (kilo-electron-volts), is one of the most nonlinear variables in the fusion systems framework. It first proved troublesome when it was shown that a pedestal profile – not the parabolic one used here – would be needed for an accurate calculation of bootstrap current. The black-box tabulation for reactivity –  $(\sigma v)$  – which appeared inside the fusion power only further exposed this nonlinearity.

Acknowledging that temperature is the most difficult to handle parameter prompts its use as the scanned variable. What this means practically is scanning temperatures is the most straightforward method to produce curves of reactors. By example, a scan may be run over the average temperatures ( $\bar{T}$ ): 10, 15, 20, 25, and 30 keV – where each corresponds to its own reactor with its own toroidal field strength ( $B_0$ ), plasma current ( $I_P$ ), etc. In equation form, this becomes:

$$\boxed{\bar{T} = \text{const.}} \tag{3.1}$$

The constant value, here, happens to be 10 keV in one run, 15 keV for the next, and 30 keV in the fifth.

### **The Plasma Density – $\bar{n}$**

The Greenwald density limit is a constraint with a simple form that applies to all tokamak reactors.<sup>23</sup> It is for this reason – as well as being a good approximation – that a parabolic profile was rationalized over a pedestal (H-Mode) one for the density.

Repeated, the Greenwald limit is:

$$\bar{n} = K_n \cdot \frac{I_P}{R_0^2} \quad (2.10)$$

Where  $K_n$  is given by Eq. (2.11). This is an exceptionally simple relationship and why it guided the model. Unlike the next three variables, it is actually used in their derivations.

### The Plasma Current – $I_P$

The plasma current is what separates steady-state from pulsed operation. From before, the steady current was found to be:

$$I_P = \frac{K_{BS}\bar{T}}{1 - K_{CD}(\sigma v)} \quad (2.28)$$

This was derived by setting the total current equal to the two sources of current: bootstrap and current drive. In fractional form, this can be written as,

$$I_P = I_{BS} + I_{CD} \rightarrow 1 = f_{BS} + f_{CD} \quad (3.2)$$

This says that the current fractions of bootstrap and current drive must sum to one. As shown next chapter, inductive sources can be included into this current balance:

$$1 = f_{BS} + f_{CD} + f_{ID} \quad (3.3)$$

This equation shows how steady-state and pulsed operation can coexist (see Fig. 3-1). The final point to make is reducing the model to being purely pulsed – i.e. neglecting the current drive:

$$1 = f_{BS} + f_{ID} \quad (3.4)$$

Therefore, the next chapter will generalize the steady current to allow pulsed operation, and then simplify it to the purely pulsed case. Just as steady current faced

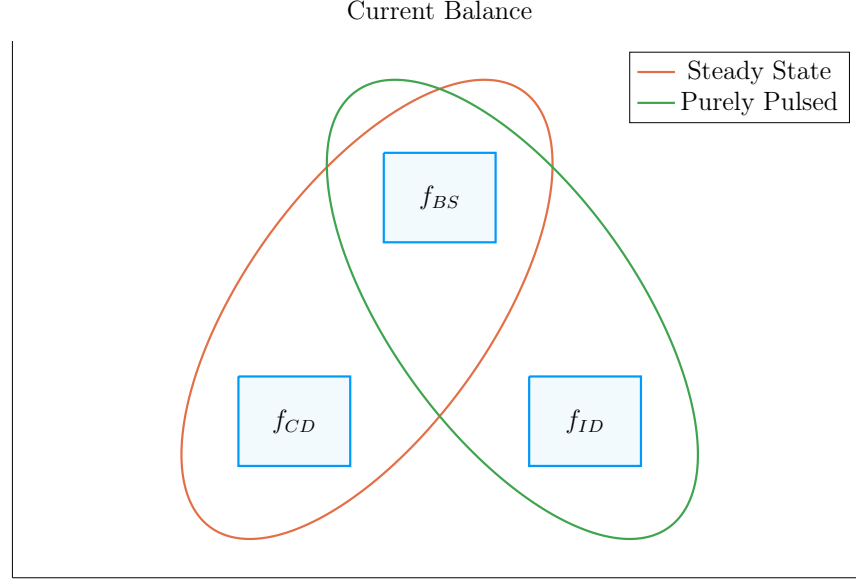


Figure 3-1: Current Balance in a Tokamak

In a tokamak, there needs to be a certain amount of current – and that current has to come from somewhere. All efficient reactors have an adequate bootstrap current. What provides the remaining current is what distinguishes steady state from pulsed operation.

self-consistency issues with  $\eta_{CD}$ , this current will also involve its own root solving conundrum – the description of which will be given in the following two chapters.

### The Tokamak Magnet Strength – $B_0$

The tokamak magnet strength has no unique equation to eliminate it. With foresight, the one this model uses is the power balance equation essential to every reactor. Similar to current balance, power balance is what separates a reactor from a device incapable of producing net electricity. As such, it is referred throughout this document as: the primary constraint. It will be derived later this chapter.

### The Tokamak Major Radius – $R_0$

Much like the magnet strength, the major radius has no unique relation to express it. This model therefore uses the radius equation to handle a reactor's various physics and engineering constraints. This list of requirements further restricts reactor space

to the curves shown in the results section. Collectively, these are referred to as the limiting constraints – discussed later this chapter. These constraints just all happen to depend on the size of the reactor – the reason they are chosen to represent the radius.

### 3.3 Enforcing Power Balance

What separates a reactor from a device incapable of producing net electricity is power balance. Within a tokamak, it accounts for how the power going into a plasma’s core exactly matches the power coming out of it. To approximate this conservation equation, two sets of power will be introduced: the sources and the sinks.

The sources have mainly been introduced at this point – they include the alpha power ( $P_\alpha$ ) from fusion reactions and the heating power ( $P_H$ ), as well as a new ohmic power term ( $P_\Omega$ ). The remaining two powers – the sinks – then appear through the radiation and heat conduction losses, which will be given shortly. In equation form, power balance becomes:

$$\sum_{sources} P = \sum_{sinks} P \quad (3.5)$$

or expanded to fit this model:

$$P_\alpha + P_H + P_\Omega = P_{BR} + P_\kappa \quad (3.6)$$

For clarity, the left-hand side of this equality are the sources. Whereas the remaining two are sinks, i.e. Bremsstrahlung radiation ( $P_{BR}$ ) and heat conduction losses ( $P_\kappa$ ).

#### 3.3.1 Collecting Power Sources

As suggested, the two dominant sources of power in a tokamak are: alpha power ( $P_\alpha$ ) and auxiliary heating ( $P_H$ ). From Appendix C, it was determined that alpha particles (i.e. helium nuclei) carry around 20% of the total fusion power; or as we put

it mathematically:

$$P_\alpha = \frac{P_F}{5} \quad (\text{C.4})$$

Additionally, it was determined that the heating power is what was eventually amplified into fusion power – or through equation:

$$P_H = \frac{P_F}{Q} \quad (2.25)$$

The final source term is then the ohmic power ( $P_\Omega$ ). This contribution term is the same as what occurs when current is run through a copper wire. From a simple circuits picture, the power across the plasma is related to its current and resistance – in our standardized units – through:<sup>7</sup>

$$P_\Omega = 10^6 \cdot I_P^2 \cdot R_P \quad (3.7)$$

This fusion systems model, then, handles the plasma resistance ( $R_P$ ) with the neo-classical Spitzer resistivity. Through equation,<sup>5</sup>

$$R_P = \frac{K_{RP}}{R_0 \bar{T}^{3/2}} \quad (3.8)$$

$$K_{RP} = 5.6e-8 \cdot \left( \frac{Z_{eff}}{\varepsilon^2 \kappa} \right) \cdot \left( \frac{1}{1 - 1.31\sqrt{\varepsilon} + 0.46\varepsilon} \right) \quad (3.9)$$

Combined with the Greenwald limit, ohmic power can be written more compactly as,

$$P_\Omega = K_\Omega \cdot \left( \frac{\bar{n}^2 R_0^3}{\bar{T}^{3/2}} \right) \quad (3.10)$$

$$K_\Omega = 10^6 \cdot \frac{K_{RP}}{K_n^2} \quad (3.11)$$

With the sources defined, we are now in a position to discuss the two sink terms used in this model's power balance.

### 3.3.2 Approximating Radiation Losses

All nuclear reactors emit radiation. From a power balance perspective, this means some power has to always be reserved to recoup from its losses – measured in megawatts. In a fusion reactor, the three most important types of radiation are: Bremsstrahlung radiation, line radiation, and synchrotron radiation.

This model chooses to only model Bremsstrahlung radiation – as it usually dominates within the plasma’s core.\* However, adding the effects of line-radiation and synchrotron radiation would drive results closer to real-world experiments. For example, line-radiation would better account for the effects of heavy impurities that are emitted from the divertor plate and first wall.

For clarity, Bremsstrahlung – or braking – radiation is what occurs when a charged particle (e.g. an electron) is accelerated by some means. In a tokamak, this happens all the time as electrons collide with the ion species.<sup>28</sup> This term can then be described by the following volume integral:<sup>5</sup>

$$P_{BR} = \int S_{BR} d\mathbf{r} \quad (3.12)$$

Where the radiation power density ( $S_{BR}$ ) is given by:

$$S_{BR} = \left( \frac{\sqrt{2}}{3\sqrt{\pi^5}} \cdot \frac{e^6}{\varepsilon_0^2 c^3 h m_e^{3/2}} \right) \cdot (Z_{eff} n^2 T^{1/2}) \quad (3.13)$$

The constants in the left set of parentheses all have their usual physics meanings (i.e.  $c$  is the speed of light and  $m_e$  is the mass of an electron). What is new is the effective charge:  $Z_{eff}$ . This effective charge is defined through:<sup>5</sup>

$$Z_{eff} = \frac{1}{n_e} \sum_j n_j Z_j^2 \quad (3.14)$$

The effective charge is, therefore, a scheme for reducing the charge each ion has to

---

\*Within most designs, Bremsstrahlung radiation outweighs the other two’s contribution, to core power balance, two-to-one.<sup>3,8</sup>



a single representative value. Fundamental charge, here, is what: neutrons lack, electrons and hydrogen have one of, and helium has two. As such, a plasma with a purely deuterium and tritium fuel would have an effective charge of one. This value would then quickly rise if a Tungsten tile – with 74 units of charge – were to fall into the plasma core from the walls of the tokamak.\*

Using the volume integral – seen in the derivation of fusion power – then allows the Bremsstrahlung power to be written in standardized units as:

$$P_{BR} = K_{BR} \bar{n}^2 \bar{T}^{1/2} R_0^3 \quad (3.15)$$

$$K_{BR} = 0.1056 \frac{(1 + \nu_n)^2 (1 + \nu_T)^{1/2}}{1 + 2\nu_n + 0.5\nu_T} Z_{eff} \varepsilon^2 \kappa g \quad (3.16)$$

This power term represents the radiation power losses involved in power balance. All that is needed now is a formula for heat conduction losses – one of the most difficult plasma behaviors to model to date.

### 3.3.3 Estimating Heat Conduction Losses

Heat is energy that moves about randomly on a microscopic level. Macroscopically, it generally moves from hotter areas to colder ones. As hinted by the plasma profile for temperature, heat emanates from the center of a plasma and migrates towards the walls of its tokamak enclosure. It therefore is a critical quantity to calculate when balancing power that is entering and leaving the plasma core.

The difficulty of estimating heat conduction, though, lies in the nonlinear behaviors of plasmas – i.e. no quick-running computation today can properly model it. As such, reactor designers have turned towards experimentalists for empirical scaling laws based on the dozen or so strongest tokamaks in the world. These are collectively referred to as confinement time scalings, e.g. the ELMy H-Mode Scaling Law.

---

\*Typical effective charges ( $Z_{eff}$ ) for a reactor are expected to be between 1 and 3.<sup>3,6,8</sup>

The derivation of this heat conduction loss term ( $P_\kappa$ ), therefore, starts in a manner similar to the previous powers. To begin, an equation for  $P_\kappa$  can be found using the following volume integral:<sup>5</sup>

$$P_\kappa = \frac{1}{\tau_E} \int U d\mathbf{r} \quad (3.17)$$

This volume integral includes two new terms: the confinement time ( $\tau_E$ ) and the internal energy (U). Before explaining these terms, a qualitative description is in order. As mentioned previously, the heat – or microscopically random – energy is captured by the internal energy (U). The confinement time ( $\tau_E$ ) is, then, how long it would take for the heat to undergo an e-folding if the device was shut down.

An actual formula for confinement time will be delayed until the end of this section, when it is needed for solving the magnet strength ( $B_0$ ). The internal energy (U), however, can be given now as it has its typical physics meaning. This assumes that all three plasma species are held at nearly the same temperature (T) as the electrons:

$$U = \frac{3}{2} (n + n_D + n_T) T \quad (3.18)$$

The density of deuterium and tritium –  $n_D$  and  $n_T$ , respectively – are again related to the electron density (used in this model) through the dilution factor, assuming a 50-50 mix of D-T fuel:

$$n_D = n_T = f_D \cdot \left( \frac{n}{2} \right) \quad (3.19)$$

After several substitutions, the equations here can be combined to form an equation for  $P_\kappa$  – the heat conduction losses – in standardized units:

$$P_\kappa = K_\kappa \frac{R_0^3 \bar{n} \bar{T}}{\tau_E} \quad (3.20)$$

$$K_\kappa = 0.4744 (1 + f_D) \frac{(1 + \nu_n)(1 + \nu_T)}{1 + \nu_n + \nu_T} (\varepsilon^2 \kappa g) \quad (3.21)$$

Now that all five terms have been defined in power balance, the next step is expanding it and solving for the tokamak's toroidal magnetic field strength:  $B_0$ .

### 3.3.4 Writing the Lawson Parameter

Before arriving at a formula for the magnet strength ( $B_0$ ) using power balance, it seems appropriate to take a detour and explain an intermediate solution: the Lawson Parameter.<sup>25</sup> Within the fusion community, the Lawson Parameter is the cornerstone in any argument on the possibility of a tokamak ever being used as a reactor.

An equation for the Lawson Parameter – sometimes referred to as the *triple product* – is easily found in the literature as:<sup>5</sup>

$$n \cdot T \cdot \tau_E = \frac{60}{E_F} \cdot \frac{T^2}{\langle \sigma v \rangle} \quad (3.22)$$

Similar to the steady current derived earlier, the right-hand side is only dependent on temperature. Further, as the left-hand side is a measure of difficult to achieve parameters, the goal is to minimize both sides. As shown in Fig. 3-2, this occurs when the plasma temperature is around 15 keV – a fact well known by many fusion engineers. As will be seen, this is a simplified result of our model. This is why  $\bar{T} = 15$  keV is not always the optimum temperature – but is usually in the right neighborhood of a reasonable reactor design.

As all the terms in power balance have already been defined, the starting point will be simply repeating the standardized equations for all five included powers.

$$P_\alpha = \frac{P_F}{5} \quad (C.4)$$

$$P_H = \frac{P_F}{Q} \quad (2.25)$$

$$P_\Omega = K_\Omega \cdot \left( \frac{\bar{n}^2 R_0^3}{\bar{T}^{3/2}} \right) \quad (3.10)$$

$$P_{BR} = K_{BR} \bar{n}^2 \bar{T}^{1/2} R_0^3 \quad (3.15)$$

$$P_\kappa = K_\kappa \frac{R_0^3 \bar{n} \bar{T}}{\tau_E} \quad (3.20)$$

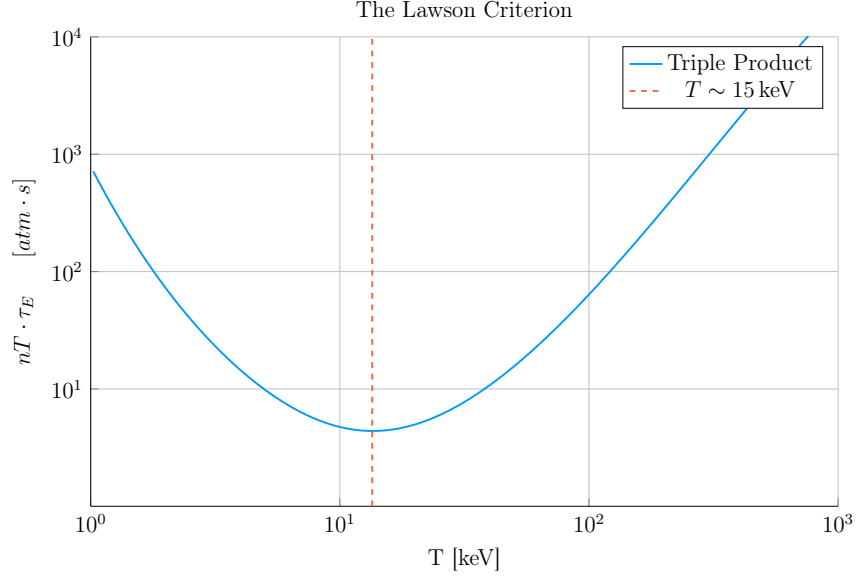


Figure 3-2: Power Balance in a Reactor

Power balance is what differentiates a reactor from a net power loss experiment. When cast as the Lawson Parameter for fusion, it explains why D-T fusion plasmas often have a temperature around 15 keV.

With the fusion power again being,

$$P_F = K_F \cdot \bar{n}^2 \cdot R_0^3 \cdot (\sigma v) \quad (2.21)$$

These can then be substituted into power balance:

$$P_\alpha + P_H + P_\Omega = P_{BR} + P_\kappa \quad (3.6)$$

After a couple lines of algebra, power balance can be rewritten in a form analogous to the triple product:

$$\bar{n} \cdot \bar{T} \cdot \tau_E = \frac{K_\kappa \bar{T}^2}{\left( K_P (\sigma v) + K_{OH} \bar{T}^{-3/2} \right) - K_{BR} \bar{T}^{1/2}} \quad (3.23)$$

$$K_P = K_F \cdot \left( \frac{5 + Q}{5 \times Q} \right) \quad (3.24)$$

As expected, this shares a form similar to the simple Lawson Parameter:

$$n \cdot T \cdot \tau_E = \frac{60}{E_F} \cdot \frac{T^2}{\langle \sigma v \rangle} \quad (3.22)$$

The main difference is that this model does not ignore ohmic power and radiation losses completely. The inclusion of radiation for example sometimes bars a range of temperatures from being physically realizable.\* With this intermediate relation in place, the goal is now to give a formula for the confinement time and solve it for the magnetic field strength ( $B_0$ ) – thus giving the Primary Constraint.

### 3.3.5 Finalizing the Primary Constraint

The goal now is to transform the Lawson Parameter into an equation for magnet strength ( $B_0$ ). This choice to solve the equation for  $B_0$  was motivated by the goals of analysis and how it will fit into the fusion systems model. To solve the primary constraint, the confinement time scaling law will now need to be introduced. At the end, a complicated – albeit highly useful – relation will be the reward.

The energy confinement time,  $\tau_E$ , is one of the most difficult to obtain terms in all of fusion energy. It is an attempt to reduce all the nonlinear behaviors of a plasma to a simple measure of how fast its internal energy would be ejected from the tokamak if the device was instantaneously shut down. As such, reactor designers have turned toward experimentalists for empirical scaling laws based on a database of the world's tokamaks (see Fig. 3-3). These all share a form similar to:

$$\tau_E = K_\tau H \frac{I_P^{\alpha_I} R_0^{\alpha_R} a^{\alpha_a} \kappa^{\alpha_\kappa} \bar{n}^{\alpha_n} B_0^{\alpha_B} A^{\alpha_A}}{P_{src}^{\alpha_P}} \quad (3.25)$$

This regressional fit is how the field actually designs machines (i.e. ITER).<sup>30</sup> Let it be

---

\*The denominator of Eq 3.23 has discontinuities when the  $K_{BR} \bar{T}^{1/2}$  term exactly equals the parenthesised one. Therefore, valid reactors only exist outside the discontinuities, when the entire triple product is finite and positive.

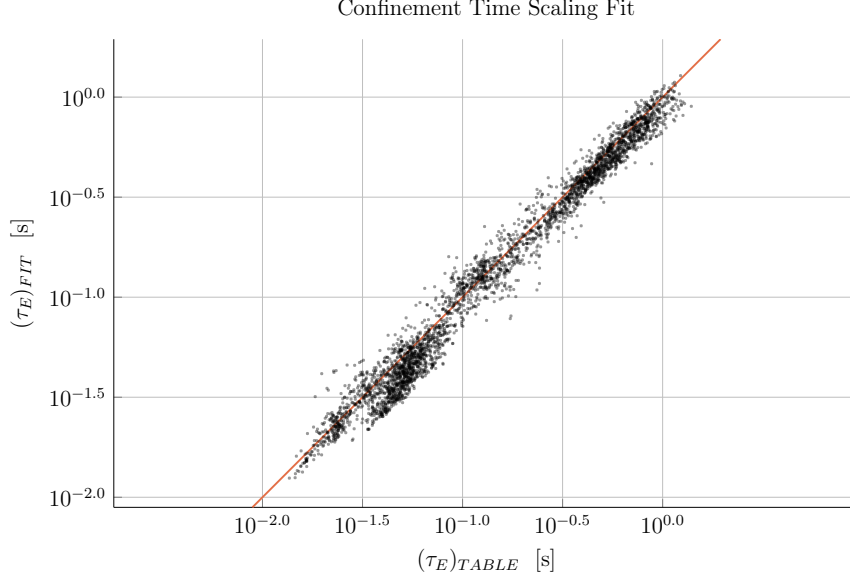


Figure 3-3: H-Mode Confinement Time Scaling

This plot shows how well the ELMy H-Mode Scaling Law does for fitting  $\tau_E$  to the ITER98 database of global tokamaks. For most values, the fit is at least 80% accurate with the measured value.<sup>29</sup>

known, though, that fits of this kind often do remarkably well, having relative errors less than 20% on interpolated data.<sup>29</sup> The new terms in this equation are:  $P_{src}$ ,  $K_\tau$ , H, A, and the  $\alpha_\square$  factors.

First, the loss power is a metric used in the engineering community to quantify the power being transported out of the “core” of the plasma by charged particles (i.e. not the neutrons).<sup>7</sup> To optimize fits, experimentalists have defined this as a combination of the source power terms:

$$P_{src} = P_\alpha + P_H + P_\Omega \quad (3.26)$$

Moving on,  $K_\tau$  is simply a constant fit-makers use in their scalings. Whereas H is the enhancement factor over this empirical fit. Next, A is the average mass number of the fuel source, in atomic mass units. Where for a 50-50 D-T fuel, this is 2.5, as deuterium weighs two amus and tritium weighs three. Lastly, the alpha factors (e.g.

$\alpha_n, \alpha_a, \alpha_P$ ) are fitting parameters that represent each variable's relative importance in the scaling.

For ELMy H-Mode, this confinement scaling law can be written as:

$$\tau_E^H = 0.145 H \frac{I_P^{0.93} R_0^{1.39} a^{0.58} \kappa^{0.78} \bar{n}^{0.41} B_0^{0.15} A^{0.19}}{P_{src}^{0.69}} \quad (3.27)$$

However, similar scaling laws can be written for L-Mode, I-Mode, etc. One final remark to make before moving on is that even these fits have subtleties. The value of  $\kappa$ , for example, may have a slightly different geometric meaning from tokamak to tokamak. And the exact definition of loss power –  $P_{src}$  – introduces an even larger area of discrepancy.

Returning to the problem at hand, though, this model's Lawson Parameter (eq. 3.23) can be simplified after expanding the left-hand side using the Greenwald density and substituting in a confinement time scaling law. After a few lines of algebra, this can be transformed into a formula for  $B_0$ !

$$B_0 = \left( \frac{G_{PB}}{K_{PB}} \cdot \left( I_P^{\alpha_I^*} R_0^{\alpha_R^*} \right)^{-1} \right)^{\frac{1}{\alpha_B}} \quad (3.28)$$

$$G_{PB} = \frac{\bar{T} \cdot \left( K_P(\sigma v) + K_\Omega \bar{T}^{-3/2} \right)^{\alpha_P}}{\left( K_P(\sigma v) + K_\Omega \bar{T}^{-3/2} - K_{BR} \bar{T}^{1/2} \right)} \quad (3.29)$$

$$K_{PB} = H \cdot \left( \frac{K_\tau K_n^{\alpha_n^*}}{K_\kappa} \right) \cdot (\varepsilon^{\alpha_a} \kappa^{\alpha_\kappa} A^{\alpha_A}) \quad (3.30)$$

Here, we have added new starred alpha values for the density, current, and radius:

$$\alpha_n^* = 1 + \alpha_n - 2\alpha_P \quad (3.31)$$

$$\alpha_I^* = \alpha_I + \alpha_n^* \quad (3.32)$$

$$\alpha_R^* = \alpha_R + \alpha_a - 2\alpha_n^* - 3\alpha_P \quad (3.33)$$

This equation for  $B_0$  – derived from power balance – is thus the primary constraint for reactor design. It is the first step in connecting the plasma (i.e.  $\bar{n}$ ,  $\bar{T}$ , and  $I_P$ ) to its tokamak enclosure (i.e.  $B_0$  and  $R_0$ ). The remaining step is finding an equation – or in this case, equations – for the major radius of the device. These radius equations will collectively be referred to as: the limiting constraints.

## 3.4 Collecting Limiting Constraints

As of now, the only missing equation within our list of dynamic variables – i.e.  $R_0$ ,  $B_0$ ,  $\bar{T}$ ,  $\bar{n}$ , and  $I_P$  – is for the major radius of the tokamak. This equation will come from around five potential limits, each either physical or engineering-based. These limits will then correspond to different curves through reactor space. As will be shown, many of the reactors on these curves will be invalid (as they violate at least one of the other limits). To this, our analysis is always based on selecting the most stringent criterion.

Before tackling the subject of finding reactors that exist on the fine line of satisfying every limiting constraints, however, it is essential to collect them one-by-one. These are: the Troyon Beta Limit, the Kink Safety Factor, the Wall Loading Limit, the Power Cap Constraint, and the Heat Loading Limit.

The goal of this section is to solve for each of these constraints on the major radius. As with the primary constraint, this choice of solving for  $R_0$  was not completely unique, just motivated by physics and engineering concerns. It just so happens that each limit described here depends on the size of a reactor – which is not true for the magnetic field strength.

### 3.4.1 Introducing the Beta Limit

The Beta Limit is the most important limiting constraint – especially for steady-state reactors. It sets a maximum on the amount of pressure a plasma is willing



to tolerate. As with future limiting constraints, literature-based equations will be transformed into formulas for  $R_0$ . Each will then contain some limiting quantity that can be handled by a static variable – as  $\beta_N$  will be used shortly.

The starting point for this limit is to define the important plasma physics quantity: the plasma beta ( $\beta$ ). This value is a ratio between a plasma's internal pressure and the pressure exerted on it by the tokamak's magnetic configuration. Mathematically,<sup>5</sup>

$$\beta = \frac{\text{plasma pressure}}{\text{magnetic pressure}} = \frac{\bar{p}}{\left(\frac{B_0^2}{2\mu_0}\right)} \quad (3.34)$$

Using this model's temperature and density profiles, the volume-averaged pressure ( $\bar{p}$ ) can be written in units of atmospheres (i.e. atm) as:

$$\bar{p} = 0.1581 (1 + f_D) \frac{(1 + \nu_n)(1 + \nu_T)}{1 + \nu_n + \nu_T} \bar{n} \bar{T} \quad (3.35)$$

Moving forward, the final step is plugging this definition for the plasma beta into the Troyon Beta Limit derived using standard MHD stability analysis. This equation can be written in the following form, where  $\beta_N$  is the normalized plasma beta – i.e. a static variable usually set between 2% and 4%.<sup>12</sup>

$$\beta = \beta_N \frac{I_P}{aB_0} \quad (3.36)$$

Substituting the plasma  $\beta$  from eq. 3.34, into this relation results in the model's first equation for the tokamak radius:

$$R_0 = \frac{K_{TB} \bar{T}}{B_0} \quad (3.37)$$

$$K_{TB} = 4.027 \times 10^{-2} \cdot \left(\frac{K_n \varepsilon}{\beta_N}\right) \cdot (1 + f_D) \cdot \frac{(1 + \nu_n)(1 + \nu_T)}{1 + \nu_n + \nu_T} \quad (3.38)$$

As mentioned, this is often the dominating constraint in a steady-state reactor. The

one that usually dominates pulsed designs – the kink safety factor – will be the focus of the next subsection.

### 3.4.2 Giving the Kink Safety Factor

Just like how the Troyon Beta Limit set a fluids-based maximum on plasma pressure, the Kink Safety Factor sets one on the plasma’s current. This constraint usually only appears in pulsed designs, as it is assumed that getting to this high a current in steady-state (with only LHCD) would prove extremely unpractical.

The starting point, again, is an equation from the literature for the kink condition:<sup>7,31</sup>

$$q_* = 5\varepsilon^2 \cdot \frac{R_0 B_0}{I_P} \cdot \left( \frac{1 + \kappa^2 \cdot (1 + 2\delta^2 - 1.2\delta^3)}{2} \right) \quad (3.39)$$

Here the safety factor –  $q_*$  – typically has values around 3.

Rearranged, the kink safety factor can now be written in standardized units as:

$$R_0 = \frac{K_{SF} I_P}{B_0} \quad (3.40)$$

$$K_{SF} = \frac{q_*}{5\varepsilon^2} \cdot \left( \frac{2}{1 + \kappa^2 \cdot (1 + 2\delta^2 - 1.2\delta^3)} \right) \quad (3.41)$$

This relation is the limiting constraint important for most pulsed reactor designs. As with the Beta Limit, these two are derived through plasma physics alone. The remaining limiting constraints, however, are engineering-based in origin – they include: the Wall Loading Limit, the Power Cap Constraint, and the Heat Loading Limit. Each will be defined shortly.

### 3.4.3 Working under the Wall Loading Limit

The first engineering-based limiting constraint – the wall loading limit – will prove to be an important quantity when determining the magnet strength at which reactor

costs begin to increase. As hinted, its definition originates from nuclear engineering concerns: it is a measure of the maximum neutron damage a tokamak's walls can take over the lifetime of the machine.\*

The first step in deriving a limiting constraint for wall loading is a description of the problem it models. In a reactor, fusion reactions typically make high-energy neutrons – with around 14.1 MeV of kinetic energy – that collide with the tokamak enclosure. Therefore a simple metric would be limiting the amount of neutron power that can be unloaded on the surface area of a tokamak. This can be written as:<sup>13</sup>

$$P_W = \frac{P_n}{S_P} \quad (3.42)$$

$$S_P = 4\pi^2 a R_0 \cdot \frac{(1 + \frac{2}{\pi} (\kappa^2 - 1))}{\kappa} \quad (3.43)$$

Here,  $S_P$  is the surface area of the tokamak's inner wall and  $P_n$  is the neutron power derived in Appendix C. The quantity,  $P_W$ , then serves a role analogous to:  $\beta_N$  for the beta limit and  $q_*$  for the kink safety factor – it is a static variable representing the maximum allowed wall loading. For fusion reactors,  $P_W$  is assumed to be around 2-4  $\frac{\text{MW}}{\text{m}^2}$ . It will be shown that the wall loading limit is important in any tokamak, however – regardless of operating mode (i.e. steady-state or pulsed).

Finishing this limiting constraint, the Wall Loading limit can be written in standardized units as:

$$R_0 = K_{WL} \cdot I_P^{\frac{2}{3}} \cdot (\sigma v)^{\frac{1}{3}} \quad (3.44)$$

$$K_{WL} = \left( \frac{K_F K_n^2}{5\pi^2 P_W} \cdot \frac{\kappa}{\varepsilon} \cdot \frac{1}{1 + \frac{2}{\pi} \cdot (\kappa^2 - 1)} \right)^{\frac{1}{3}} \quad (3.45)$$

---

\*For clarity, the wall loading limit should actually be an energy fluence limit. It is converted to an instantaneous power limit for ease of design purposes.

### 3.4.4 Setting a Maximum Power Cap

As opposed to the previous three limiting constraints, the maximum power cap is more of a constraint set by economic competitiveness. Because no conventional reactor – coal, solar, or otherwise – has a 4000 MW reactor, neither should fusion.\* It makes sense from a practical position after realizing the long history of tokamaks being delayed, underfunded, or completely canceled. Mathematically, this has the simple form:

$$P_E \leq P_{CAP} \quad (3.46)$$

Here,  $P_{CAP}$  is the maximum allowed power output of a reactor. Similar to the other limiting quantities,  $P_{CAP}$  is treated as a static variable (i.e. set to 4000 MW). The electrical power output of the reactor ( $P_E$ ) is then related to the fusion power by:<sup>5</sup>

$$P_E = 1.273 \eta_T \cdot P_F \quad (3.47)$$

The variable  $\eta_T$  in this equation is the thermal efficiency of the reactor – which is usually found to be around 40%. And the constant in front (i.e. 1.273) represents some extra power the reactor makes as fuel is bred by the fusion neutrons passing through a tokamak’s lithium-filled blanket. Explicitly this results from including the energy released by lithium-6 as it undergoes neutron capture ( $E_{Li}$ ).<sup>5</sup>

$$1.273 = \frac{E_F + E_{Li}}{E_F} \quad (3.48)$$

$$E_{Li} = 4.8 \text{ MeV} \quad (3.49)$$

Substituting in fusion power and solving for the major radius results in:

$$R_0 = K_{PC} \cdot I_P^2 \cdot (\sigma v) \quad (3.50)$$

---

\*Note that this 4000 MW (electric) is a maximum. A 1000 MW reactor would obviously not violate this constraint. Instead it would likely be pressing on either the kink or beta limit.

$$K_{PC} = K_F K_n^2 \cdot \left( \frac{1.273 \eta_T}{P_{max}} \right) \quad (3.51)$$

This limiting constraint can be used to create curves of reactors, although it is mainly used as a stopping point for designs – i.e. if you get to the power-cap regime, you have gone too far. This is different than the next constraint, which is fundamentally an unsolved problem within the modern tokamak design paradigm.<sup>32</sup>

### 3.4.5 Listing the Heat Loading Limit

Fusion plasmas are hot. The commonly given relation is one electron volt is around 20,000 °F – which would make 15 keV equate to around a quarter-billion Fahrenheit. Although this connotation of temperature is slightly deceptive, heat damage to a tokamak is an all too real concern. The problem is there is currently no solution to the problem. Although researchers have explored various types of heat divertors, none have been shown to withstand the gigawatts-per-square-meter of heat emitted from a reactor-size tokamak.<sup>32</sup>

As such, this model takes an approach similar to the research community, calculating it at the end as a manual check on the difficulty of building such a device – but not using it to explicitly guide design. For completeness though, a limiting constraint will still be derived. The first step is giving the heat loading limit commonly found in the literature:<sup>13</sup>

$$q_{DV} = \frac{K_{DV}}{K_F} \cdot \frac{P_F I_P^{1.2}}{R_0^{2.2}} \quad (3.52)$$

$$K_{DV} = \frac{18.31 \times 10^{-3}}{\varepsilon^{1.2}} \cdot K_P \cdot \left( \frac{2}{1 + \kappa^2} \right)^{0.6} \quad (3.53)$$

This is the heat load that impinges on an extended leg, double null divertor – primarily from the outer midplane of the plasma core. After a simple rearrangement and

substitution for fusion power, this becomes:

$$R_0 = K_{DH} \cdot I_P \cdot (\sigma v)^{\frac{1}{3.2}} \quad (3.54)$$

$$K_{DH} = \left( \frac{K_{DV} K_n^2}{q_{DV}} \right)^{\frac{1}{3.2}} \quad (3.55)$$

At this point all the limiting constraints have been defined. The next step is taking a step back and motivating the derivation of a generalized current equation suitable for pulsed tokamaks.

### 3.5 Summarizing the Fusion Systems Model

Stepping back, this chapter focused on the bigger picture behind designing a zero-dimension fusion systems model. It started with a description of various design parameters and then moved onto explaining the five relations needed to close the model – i.e. for  $\bar{T}$ ,  $\bar{n}$ ,  $I_P$ ,  $B_0$ , and  $R_0$ .

Before generalizing the steady current to allow modeling pulsed reactors, however, a quick recap of the equations will prove beneficial. The first variable described was temperature – i.e. scan five evenly-spaced  $\bar{T}$  values between 10 and 30 keV. This was then quickly followed by the Greenwald density limit – a simple relation that applies to all fusion reactors. These two equations can be written as:

$$\bar{T} = \text{const.} \quad (3.1)$$

$$\bar{n} = K_n \cdot \frac{I_P}{R_0^2} \quad (2.10)$$

The next variable handled was the steady current:

$$I_P = \frac{K_{BS} \bar{T}}{1 - K_{CD}(\sigma v)} \quad (2.28)$$

As was mentioned then, this equation only depends directly on the temperature, but is strongly affected by a tokamak's configuration –  $R_0$  and  $B_0$  – through the current drive efficiency ( $\eta_{CD}$ ). For pulsed reactors, this equation proves too simple as it ignores inductive current. To remedy the situation, current balance will be revisited next chapter. The main point to make now, though, is that the  $R_0$  and  $B_0$  dependence will be made explicit.

Moving on, the remaining equations were, then, the primary and limiting constraints for  $B_0$  and  $R_0$ , respectively. It was through these relations that a tokamak's configuration was brought back into the fold. The choice of solving the two constraints for their respective variables was not completely unique – as it was motivated by the foresight of how they fit into the model. Repeated below, they served as the proper vehicles for closing the system of equations.

$$B_0 = \left( \frac{G_{PB}}{K_{PB}} \cdot \left( I_P^{\alpha_I^*} R_0^{\alpha_R^*} \right)^{-1} \right)^{\frac{1}{\alpha_B}} \quad (3.28)$$

$$R_0 = \frac{K_{TB} \bar{T}}{B_0} \quad (3.37)$$

$$R_0 = \frac{K_{SF} I_P}{B_0} \quad (3.40)$$

$$R_0 = K_{WL} \cdot I_P^{\frac{2}{3}} \cdot (\sigma v)^{\frac{1}{3}} \quad (3.44)$$

$$R_0 = K_{PC} \cdot I_P^2 \cdot (\sigma v) \quad (3.50)$$

$$R_0 = K_{DH} \cdot I_P \cdot (\sigma v)^{\frac{1}{3.2}} \quad (3.54)$$

The next step now is to learn how to generalize the current formula and design a pulsed tokamak reactor (see Chapter 4). After this is done, Chapter 5 will pick up where this chapter leaves off – transforming this fusion systems model into a simple reactor solver.





# Chapter 4

## Designing a Pulsed Tokamak

Pulsed tokamaks are the flagship of the European fusion reactor-design effort. As such, this paper's model will now be generalized to accommodate this mode of operation. Fundamentally, this involves transforming current balance into flux balance – by adding inductive (pulsed) sources to stand alongside the LHCD (steady-state) ones.

The first step in generalizing current balance will be understanding the problem from a basic electrical engineering perspective – i.e. with circuit analysis. The resulting equation will then be transformed into the flux balance seen in other models from the literature.<sup>7</sup> All that will need to be done then is solving the problem for plasma current ( $I_P$ ) and simplifying it for various situations – e.g. steady-state operation.

This generalized plasma current will then be found to be a function of the other dynamic variables (i.e.  $R_0$ ,  $B_0$ , and  $\bar{T}$ ). This, of course, is more difficult to handle computationally than the steady current, which only depended directly on the temperature ( $\bar{T}$ ). A discussion about solving this new root solving problem will be the topic of the next chapter.

## 4.1 Modeling Plasmas as Circuits

Although it may have been lost along the way, what makes plasmas so interesting and versatile – in comparison to gases – is their ability to respond to electric and magnetic fields. It seems natural then to model plasma current from a circuits perspective (i.e. with resistors, voltage sources, and inductors). By name, this circuit is referred to as a transformer where: the plasma is the secondary and the yet-to-be discussed central solenoid (of the tokamak) is the primary.

The first step in deriving a current equation is to determine the circuit equations that govern pulsed operation in a tokamak. This will be done in two steps. First, we will draw a circuit diagram and write equations that describe it. Next, we will use a simple schematic for how current evolves in a transformer to reduce the resulting differential equations to simple algebraic ones – as is the hallmark of our model.

### 4.1.1 Drawing the Circuit Diagram

Understanding a circuit always starts with drawing a simple diagram, see Fig. 4-1. This figure depicts the transformer governing a pulsed reactor. The left sub-circuit is, therefore, the transformer's primary: the central solenoid which provides most of the inductive current.\* Whereas, the right sub-circuit is the plasma acting as the transformer's secondary.

This is handled with standard circuit equations for voltages, resistors, and inductors:<sup>11</sup>

$$V_i = \sum_j^n \frac{d}{dt} (M_{ij} I_j) + I_i R_i , \quad \forall i = 1, 2, \dots, n \quad (4.1)$$

Without going into the inductances (M) and resistances (R), the variable  $n$  is the number of sub-circuits, here being 2. Whereas, the variables  $i$  and  $j$  are the indices of sub-circuits (i.e. 1 for the primary, 2 for the secondary). For illustrative purposes,

---

\*The central solenoid is a coiled metal structure that fits within the inner ring of the tokamak enclosure. For now, every other flux source (besides this central solenoid) is neglected.

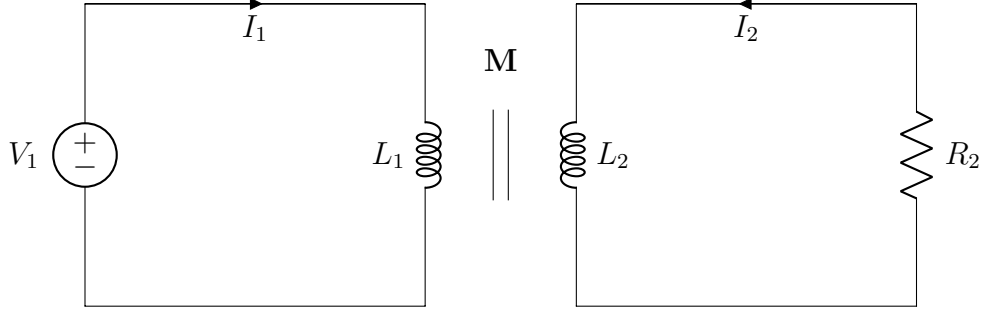


Figure 4-1: A Simple Plasma Transformer Description

A plasma transformer consists of a solenoid primary (left) and a plasma secondary (right). They are connected by their mutual inductance,  $M$ . Note, here, that the two currents –  $I_1$  and  $I_2$  – travel in opposite directions.

this would reduce to the following relation for a battery attached to a lightbulb:

$$V = IR \quad (4.2)$$

Back to the transformer diagram, the equations for the two subcircuits can be expanded and greatly simplified. Besides ignoring every inductive source other than the central solenoid, the next powerful assumption is treating the solenoid as a superconductor (i.e. with negligible resistance). Lastly, the inductances between components and themselves are held constant – independent of time. This allows the coupled transformer equations to be written as:

$$V_1 = L_1 \dot{I}_1 - M \dot{I}_2 \quad (4.3)$$

$$-I_2 R_P = L_2 \dot{I}_2 - M \dot{I}_1 \quad (4.4)$$

With  $I_1$  and  $I_2$  going in opposite directions. Note, here, that the subscript on  $M$  has been dropped, as there are only two components. This was done in conjunction to adding internal (self-)inductance terms. Mathematically, the mapping between variables is:

$$M = M_{12} = M_{21} \quad (4.5)$$

$$L_1 = M_{11} \tag{4.6}$$

$$L_2 = M_{22} \tag{4.7}$$

Repeated, the one subscript represents the primary – the central solenoid – and the two stands for the plasma as the transformer’s secondary. Exact definitions for the inductances will be put off until the end of the next subsection.

### 4.1.2 Plotting Pulse Profiles

Up until now, little has been discussed that has a time dependence. For steady-state tokamaks, this did not occur because it is an extreme case where pulses could last weeks or months. By definition, though, a pulsed machine has pulses – with around ten scheduled per day.<sup>33</sup> For this reason, a fusion pulse is now investigated in detail.

Transformer pulses between the central solenoid and the plasma occur on the timescale of hours. During this time, a plasma is brought up to some quasi-steady-state current ( $I_P^*$ ) for several hour and then ramped back down using the available flux in the solenoid (measured in volt-seconds). For clarity, each pulse is subdivided into four phases: ramp-up, flat-top, ramp-down, and dwell. Pictorially represented in Fig. 4-2, these divisions allow a simple scheme for transforming the coupled circuit differential equations – from Eqs. (4.3) and (4.4) – into simple algebraic formulas.

Along the way, we will approximate derivatives with linear piecewise functions. Using  $t_i$  to represent the initial time and  $t_f$  as the final one, these can be written as:

$$\dot{I} = \frac{I(t_f) - I(t_i)}{t_f - t_i} \tag{4.8}$$

Table 4.1 shows how the data from Fig. 4-2 can be written in this piecewise fashion.

The exact definitions for the plasma’s inductive current ( $I_P^*$ ) and the maximum voltage in the central solenoid ( $V_{max}$ ) will be put off until the end of the section.

## Tokamak Circuit Profiles

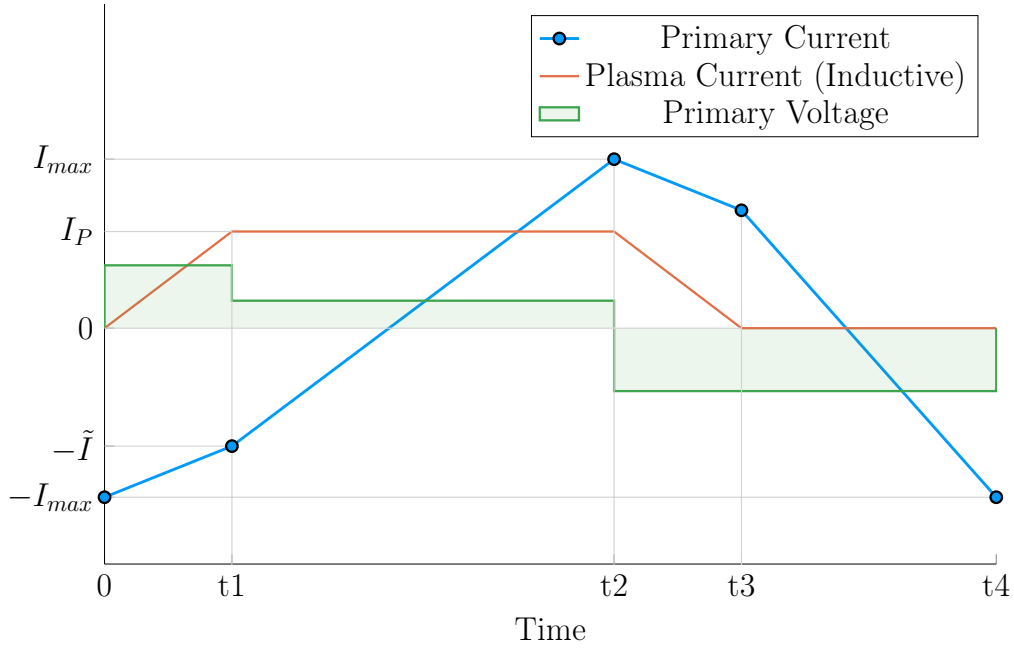


Figure 4-2: Time Evolution of Circuit Profiles

A circuit pulse involves four phases: (1) Ramp-Up, (2) Flattop, (3) Ramp-Down, and (4) Dwell. In reality, flattop can last more than 90% of the pulse.<sup>8</sup> This makes the slope of the primary current during this phase much shallower than depicted.

### The Ramp-Up Phase – RU

The first phase in every plasma pulse is the ramp-up. During ramp-up, the central solenoid starts discharging from its fully charged values, as the plasma is brought to its quasi-steady-state current. As this occurs on the timescale of minutes – not hours

Table 4.1: Piecewise Linear Scheme for Pulsed Operation

(a) Currents			(b) Voltage			
Time	$I_1$	$I_2$	Phase	$t_i$	$t_f$	$V_1$
0	$-I_{max}$	0	Ramp-Up	0	$t_1$	$+V_{max}$
t1	$-\tilde{I}$	$I_P^*$	Flattop	$t_1$	$t_2$	$+\tilde{V}$
t2	$+I_{max}$	$I_P^*$	Ramp-Down	$t_2$	$t_3$	$-V_{max}$
t3	$+\tilde{I}$	0	Dwell	$t_3$	$t_4$	$-V_{max}$
t4	$-I_{max}$	0				

– resistive effects of the plasma can safely be ignored. This results in the ramp-up equations becoming:

$$V_{max} = \frac{1}{\tau_{RU}} \cdot \left( L_1 \cdot (I_{max} - \tilde{I}) - M \cdot I_{ID} \right) \quad (4.9)$$

$$0 = \frac{1}{\tau_{RU}} \cdot \left( M \cdot (I_{max} - \tilde{I}) - L_2 \cdot I_{ID} \right) \quad (4.10)$$

Simplifying these equations will be done shortly, for now the new terms are what is important. The maximum voltage of the solenoid is  $V_{max}$  – usually measured in kilovolts. Next,  $I_{max}$  is the solenoid’s current at the beginning of ramp-up. Whereas  $\tilde{I}$  is the magnitude of the current once the plasma is at its flattop inductive-drive current –  $I_{ID}$ . The  $\tau_{RU}$  quantity, then, is the duration of time it takes to ramp-up (i.e. RU). Again,  $L_1$  and  $L_2$  are the microhenry-scale internal inductances of the solenoid and plasma, respectively, and  $M$  is the mutual inductance between them.

The last step in discussing ramp-up is giving the two important formulas that come from it:

$$\tilde{I} = I_{max} - I_{ID} \cdot \left( \frac{L_2}{M} \right) \quad (4.11)$$

$$\tau_{RU} = \frac{I_{ID}}{V_{max}} \cdot \left( \frac{L_1 L_2 - M^2}{M} \right) \quad (4.12)$$

## The Flattop Phase – FT

The most important phase in any reactor’s pulse is flattop: the quasi-steady-state time when the tokamak is making electricity. Flattops are assumed to last a few hours for a profitable machine, during which the central solenoid almost completely discharges to overcome a plasma’s resistive losses – thus, keeping it in a quasi-steady-state mode of operation. For a steady-state reactor, this phases constitutes the entirety of the pulse.

Although the resistance cannot safely be neglected for the flattop – as it was for ramp-up – the plasma’s inductive current ( $I_{ID}$ ) is assumed constant. This leads to its derivative in equations cancelling out! Mathematically,

$$\tilde{V} = \frac{L_1}{\tau_{FT}} \cdot (I_{max} + \tilde{I}) \quad (4.13)$$

$$I_{ID}R_P = \frac{M}{\tau_{FT}} \cdot (I_{max} + \tilde{I}) \quad (4.14)$$

As with ramp-up, the simplifications will be given shortly. The new terms here, however, are an intermediate voltage for the central solenoid ( $\tilde{V}$ ), and the duration of the flattop ( $\tau_{FT}$ ). The resistance term was given in Eq. (3.8). Solutions can now be found by substituting  $\tilde{I}$  – from Eq. (4.11) – into the flattop equations:

$$\tilde{V} = I_{ID}R_P \cdot \left( \frac{L_1}{M} \right) \quad (4.15)$$

$$\tau_{FT} = \frac{I_{max} \cdot 2M - I_{ID} \cdot L_2}{I_{ID}R_P} \quad (4.16)$$

## The Ramp-Down Phase – RD

Due to the simplicity – and symmetry – of this model’s reactor pulse, ramp-down is the exact mirror of ramp-up. It takes the same amount of time and results in the same algebraic equations. For brevity, this will just be represented as:

$$\tau_{RD} = \tau_{RU} \quad (4.17)$$

For clarity, this is the time when a plasma’s current is brought down from its flattop value to zero.

## The Dwell Phase – DW

Where the first three phases had little ambiguity, the dwell phase changes definition from model to model. For now, it is assumed to be the time it takes the central solenoid to reset after a plasma has been completely ramped-down to an off setting. To get a more realistic duty factor for cost estimates, it could include an evacuation time, set to last up to thirty minutes.<sup>12</sup> During this evacuation, a plasma is vacuumed out of a device as it undergoes some inter-pulse maintenance.

Ignoring evacuation for now, the dwell phase involves resetting the central solenoid when the plasma's current is negligible. This corresponds to the secondary of the transformer being an open circuit – fundamentally the central solenoid is the only component. In equation form,

$$V_{max} = \frac{L_1}{\tau_{DW}} \cdot (I_{max} + \tilde{I}) \quad (4.18)$$

Or substituting in  $\tilde{I}$  and solving for  $\tau_{DW}$ ,

$$\tau_{DW} = \frac{L_1}{M} \cdot \frac{(I_{max} \cdot 2M - I_{ID} \cdot L_2)}{V_{max}} \quad (4.19)$$

### 4.1.3 Specifying Circuit Variables

The goal now is to collect the results from the four phases and introduce the inductance, resistance, voltage, and current terms relevant to our model. This will motivate recasting the problem as flux balance in a reactor – the form commonly used in the literature (and discussed next section).<sup>7</sup>



First, collecting the phase durations in one place:

$$\tau_{RU} = \frac{I_{ID}}{V_{max}} \cdot \left( \frac{L_1 L_2 - M^2}{M} \right) \quad (4.12)$$

$$\tau_{FT} = \frac{I_{max} \cdot 2M - I_{ID} \cdot L_2}{I_{ID} R_P} \quad (4.16)$$

$$\tau_{RD} = \tau_{RU} \quad (4.17)$$

$$\tau_{DW} = \frac{L_1}{M} \cdot \frac{(I_{max} \cdot 2M - I_{ID} \cdot L_2)}{V_{max}} \quad (4.19)$$

These can be used in the definition of the duty-factor: the fraction of time a reactor is putting electricity on the grid. Formulaically,

$$f_{duty} = \frac{\tau_{FT}}{\tau_{pulse}} \quad (4.20)$$

$$\tau_{pulse} = \tau_{RU} + \tau_{FT} + \tau_{RD} + \tau_{DW} \quad (4.21)$$

As will turn out, the solving of pulsed current actually only involves Eq. (4.16). What is interesting about this, is that there is no explicit dependence on ramp-down or dwell! Whereas ramp-up passes  $\tilde{I}$  to the flattop phase, the other two are just involved in calculating the duty factor.

The remainder of this subsection will then be defining the following circuit variables:  $I_{ID}$ ,  $I_{max}$ ,  $V_{max}$ ,  $L_1$ ,  $L_2$ , and  $M$ . Again, the resistance was defined last chapter as:

$$R_P = \frac{K_{RP}}{R_0 \bar{T}^{3/2}} \quad (3.8)$$

### The Inductive Current – $I_{ID}$

The inductive current is what separates pulsed from steady-state operation. It comes from rewriting the current balance given by Eq. (3.3) as:

$$I_{ID} = I_P - (I_{BS} + I_{CD}) \quad (4.22)$$

From before,  $I_P$  is the total plasma current in mega-amps,  $I_{BS}$  is the bootstrap current, and  $I_{CD}$  is the current from LHCD (i.e. lower hybrid current drive). For this model, the relation can be rewritten as:

$$I_{ID} = I_P \cdot \left(1 - K_{CD}(\sigma v)\right) - K_{BS} \bar{T} \quad (4.23)$$

### The Central Solenoid Maximums – $V_{max}$ and $I_{max}$

For this simple model, the central solenoid has two maximum values: the voltage and current. The voltage is the easier to give value. Literature values have this around:<sup>6</sup>

$$V_{max} \approx 5 \text{ kV} \quad (4.24)$$

The maximum current, on the other hand, can be defined through Ampere's Law on a coiled central solenoid:<sup>11</sup>

$$I_{max} = \frac{B_{CS} h_{CS}}{N \mu_0} \quad (4.25)$$

Here,  $B_{CS}$  is a magnetic field strength the central solenoid is assumed to operate at (i.e. 12 T),  $h_{CS}$  is the height of the solenoid,  $N$  is the number of coils, and  $\mu_0$  has its usual physics meaning (i.e.  $40 \pi \frac{\mu\text{H}}{\text{m}}$ ). As will be seen, the value of  $N$  does not directly affect the model, as it cancels out in the final flux balance. The height of the central solenoid will, then, be the focus of an upcoming section on improving tokamak geometry.

## The Central Solenoid Inductance – $L_1$

For a central solenoid with circular cross-sections of finite thickness ( $d$ ), the inductance can be written as:<sup>12</sup>

$$L_1 = G_{LT} \cdot \left( \frac{\mu_0 \pi N^2}{h_{CS}} \right) \quad (4.26)$$

$$G_{LT} = \frac{R_{CS}^2 + R_{CS} \cdot (R_{CS} + d) + (R_{CS} + d)^2}{3} \quad (4.27)$$

Note that  $R_{CS}$  is the inner radius of the central solenoid and  $(R_{CS} + d)$  is the outer one. In the limit where  $d$  is negligible, this says that the inductance is quadratically dependent on the radius of the central solenoid:

$$\lim_{d \rightarrow 0} G_{LT} = G_{LT}^\dagger = R_{CS}^2 \quad (4.28)$$

The formulas for both  $R_{CS}$  and  $d$  will be defined in a few sections.

## The Plasma Inductance – $L_2$

The plasma inductance is a composite of several different terms, but overall scales with radius. Through equation,

$$L_2 = K_{LP} R_0 \quad (4.29)$$

This static coefficient –  $K_{LP}$  – then combines three inductive behaviors of the plasma. The first is its own self inductance (through  $l_i$ ).<sup>5</sup> The next is a resistive component through the Ejima coefficient ( $C_{ejima}$ ), which is usually set to  $\sim 1/3$ .<sup>7</sup> And lastly, a geometric component – involving  $\varepsilon$  and  $\kappa$  – is given by the Hirshman-Neilson model.<sup>34</sup> Mathematically,

$$K_{LP} = \mu_0 \cdot \left( \frac{l_i}{2} + C_{ejima} + \frac{(b_{HN} - a_{HN})(1 - \varepsilon)}{(1 - \varepsilon) + \kappa d_{HN}} \right) \quad (4.30)$$

Here the HN values come from the 1985 Hirshman-Neilson paper:

$$a_{HN}(\varepsilon) = 2.0 + 9.25\sqrt{\varepsilon} - 1.21 \varepsilon \quad (4.31)$$

$$b_{HN}(\varepsilon) = \ln(8/\varepsilon) \cdot (1 + 1.81\sqrt{\varepsilon} + 2.05 \varepsilon) \quad (4.32)$$

$$d_{HN}(\varepsilon) = 0.73\sqrt{\varepsilon} \cdot (1 + 2\varepsilon^4 - 6\varepsilon^5 + 3.7\varepsilon^6) \quad (4.33)$$

## The Mutual Inductance – M

The mutual inductance – M – represents the coupling between the solenoid primary and the plasma secondary. A common method for treating this mutual inductance is through a coupling coefficient,  $k$ , that links the two self-inductances. Formulaically,

$$M = k\sqrt{L_1 L_2} \quad (4.34)$$

The value of the coupling coefficient,  $k$ , is always less than (or equal to) 1, but usually has a value around a third. With all the equations defined, we are now at a position to explain one of the larger nuances of this fusion systems framework: determining the pulse length of a tokamak.

### 4.1.4 Constructing the Pulse Length

This subsection focuses on a quantitative estimate for how to select a pulse length. As no fusion reactor exists in the world today, the writers believe this is an acceptable calculation. Further, the resulting length of two hours matches the durations of other studies in the literature.<sup>7,35</sup>

Starting at the end, our goal is to find the pulse length of a tokamak reactor in seconds – as dictated by cyclical stress concerns. The first piece of information is the expected lifetime of the central solenoid,  $N \approx 10$  years. The next is the desired

number of pulses the central solenoid will have to last:  $M \approx 50,000$  pulses.\* This gives a rough estimate of around 10 pulses a day – or a flattop lasting two hours.

With the pulse length defined, we are now in a position to justify neglecting the duty factor for pulsed reactors in this model. Using expected reactor values – while assuming a central solenoid with around 4000 turns – leads to the following scalings:

$$\tau_{FT} \sim \tau_{pulse} \sim O(\text{hours}) \quad (4.35)$$

$$\tau_{RU} \sim \tau_{RD} \sim \tau_{DW} \sim O(\text{mins}) \quad (4.36)$$

As such, even pulsed tokamak reactors should have a duty factor of around unity:

$$f_{duty} \approx 1 \quad (4.37)$$

This analysis of course would change if the central solenoid became an inexpensive component to replace. For example, if a tokamak had a new one installed annually, the pulse length could shorten to be on the order of minutes.

Now that all the terms in a pulsed circuit have been explored, we will move on to rearranging the flattop equation to reproduce flux balance. This will then naturally lead to a generalized current equation – which is the main result of the chapter.

## 4.2 Producing Flux Balance

The goal of this section is to arrive at a conservation equation for flux balance that mirrors the ones in the literature. The fusion systems model this one attempts to follow most is the PROCESS code.<sup>7</sup> In a manner similar to power balance, flux balance can be written as:

$$\sum_{sources} \Phi = \sum_{sinks} \Phi \quad (4.38)$$

---

\*This 50,000 pulses is based on the values from the ITER design specifications.<sup>35</sup>

### 4.2.1 Rearranging the Circuit Equation

The way to arrive at flux balance from our circuit equations is to rearrange the flattop phase's duration equation:

$$\tau_{FT} = \frac{I_{max} \cdot 2M - I_{ID} \cdot L_2}{I_{ID} R_P} \quad (4.16)$$

Multiplying through by the right-hand side's denominator and moving the negative term over to the left yields:

$$2MI_{max} = I_{ID} \cdot (L_2 + R_P \tau_{FT}) \quad (4.39)$$

This equation is flux balance, where the left-hand side are the sources (e.g. the central solenoid), and the other terms are the sinks (i.e. ramp-up and flattop). The source term can currently be encapsulated within the central solenoid flux:

$$\Phi_{CS} = 2MI_{max} \quad (4.40)$$

The sinks, namely the ramp-up inductive losses ( $\Phi_{RU}$ ) and the flattop resistive losses ( $\Phi_{FT}$ ), are what drain this flux. Here, again, ramp-down and dwell are not included as sinks because flux balance only tracks until the end of flattop. They come into play when measuring the cost of electricity – through the duty factor from Eq. (4.20).

Relabeling terms, flux balance can now be rewritten as:

$$\Phi_{CS} = \Phi_{RU} + \Phi_{FT} \quad (4.41)$$

With the ramp-up and flattop flux given, respectively, by:

$$\Phi_{RU} = L_2 \cdot I_{ID} \quad (4.42)$$

$$\Phi_{FT} = (R_P \tau_{FT}) \cdot I_{ID} \quad (4.43)$$

On comparing these quantities to the ones from the PROCESS paper,<sup>7</sup>  $\Phi_{RU}$  and  $\Phi_{FT}$  are exactly the same. The source terms, on the other hand, are off for two reasons – both related to the central solenoid being the only source term in flux balance. This can partially be remedied by adding the second most dominant source of flux a posteriori – i.e. the PF coils. The second, and inherently limiting factor, is the simplicity of the current model. All that can be shown to this regard is that the  $\Phi_{CS}$  terms does reasonably predict the values from the PROCESS code.<sup>8</sup>

#### 4.2.2 Adding Poloidal Field Coils

Adding the effect of PF coils – belts of current driving plates on the outer edges of the tokamak – leads to as much as a 50% improvement<sup>7,8</sup> over relying solely on the central solenoid for flux generation. From the literature, this can be modeled as:<sup>12</sup>

$$\Phi_{PF} = \pi B_V \cdot (R_0^2 - (R_{CS} + d)^2) \quad (4.44)$$

Where again  $R_{CS}$  and  $d$  are the inner radius and thickness of the central solenoid, respectively. These will be the topic of the next section.

Moving forward, the vertical field –  $B_V$  – is a magnetic field oriented up-and-down with the ground. It is needed to prevent a tokamak plasma from drifting radially out of the machine. From the literature, the magnitude of this vertical field (valid for a circular plasma) is given by:<sup>7</sup>

$$|B_V| = \frac{\mu_0 I_P}{4\pi R_0} \cdot \left( \ln \left( \frac{8}{\varepsilon} \right) + \beta_p + \frac{l_i}{2} - \frac{3}{2} \right) \quad (4.45)$$

Analogous to the previously covered plasma beta, the poloidal beta can be represented

by:<sup>36</sup>

$$\beta_p = \frac{\bar{p}}{\left(\frac{\bar{B}_p}{2\mu_0}\right)} \quad (4.46)$$

Where the average poloidal magnetic field comes from a simple application of Ampere's law:

$$\bar{B}_p = \frac{\mu_0 I_P}{l_p} \quad (4.47)$$

The variable  $l_p$  is then the perimeter of the tokamak's cross-sectional halves:

$$l_p = 2\pi a \cdot \sqrt{g_p} \quad (4.48)$$

Here,  $g_p$  is another geometric scaling factor,

$$g_p = \frac{1 + \kappa^2(1 + 2\delta^2 - 1.2\delta^3)}{2} \quad (4.49)$$

After a few lines of algebra, this relation for the magnitude of the vertical magnetic field can be written in standardized units as:

$$|B_V| = \left(\frac{1}{10 \cdot R_0}\right) \cdot (K_{VI} I_P + K_{VT} \bar{T}) \quad (4.50)$$

$$K_{VT} = K_n \cdot (\varepsilon^2 g_P) \cdot (1 + f_D) \frac{(1 + \nu_n)(1 + \nu_T)}{1 + \nu_n + \nu_T} \quad (4.51)$$

$$K_{VI} = \ln\left(\frac{8}{\varepsilon}\right) + \frac{l_i}{2} - \frac{3}{2} \quad (4.52)$$

For clarity, this will be plugged into the new PF coil flux contribution ( $\Phi_{PF}$ ):

$$\Phi_{PF} = \pi B_V \cdot (R_0^2 - (R_{CS} + d)^2) \quad (4.44)$$

Which then gets plugged into a more complete flux balance equation:

$$\Phi_{CS} + \Phi_{PF} = \Phi_{RU} + \Phi_{FT} \quad (4.53)$$



The  $R_{CS}$  and  $d$  terms found in  $\Phi_{PF}$  will now be discussed as they are needed for this more sophisticated tokamak geometry.

## 4.3 Improving Tokamak Geometry

From before, this fusion systems model has been said to depend on the major and minor radius:  $R_0$  and  $a$ , respectively. Along the way, various geometric parameters have been defined (e.g.  $\varepsilon$ ,  $\kappa$ ,  $\delta$ ) to describe the geometry further. Now three more thicknesses will be added – i.e.  $b$ ,  $c$ , and  $d$  – as well as two fundamental dimension related to the solenoid: its inner radius ( $R_{CS}$ ) and height ( $h_{CS}$ ). These are the topics of this section.

### 4.3.1 Defining Central Solenoid Dimensions

The best way to conceptualize tokamak geometry is through cartoon – see Fig. 4-3. What this shows is that there is a gap at the very center of a tokamak. This gap extends radially outwards to  $R_{CS}$  meters where the coiled central solenoid – of thickness  $d$  – begins. Between the outer edge of the solenoid and the wall of the torus (i.e. the doughnut) are the blanket and toroidal field (TF) coils.

The blanket and TF coils have thicknesses of  $b$  and  $c$ , respectively. Before defining them, however, it proves useful to relate them inside equations for the inner radius ( $R_{CS}$ ) and height ( $h_{CS}$ ) of the central solenoid.

$$R_{CS} = R_0 - (a + b + c + d) \tag{4.54}$$

$$h_{CS} = 2 \cdot (\kappa a + b + c) \tag{4.55}$$

Again, this relation is pictorially represented in Fig. 4-3. The next step is defining:  $b$ ,  $c$ , and  $d$  – to close the variable loop.

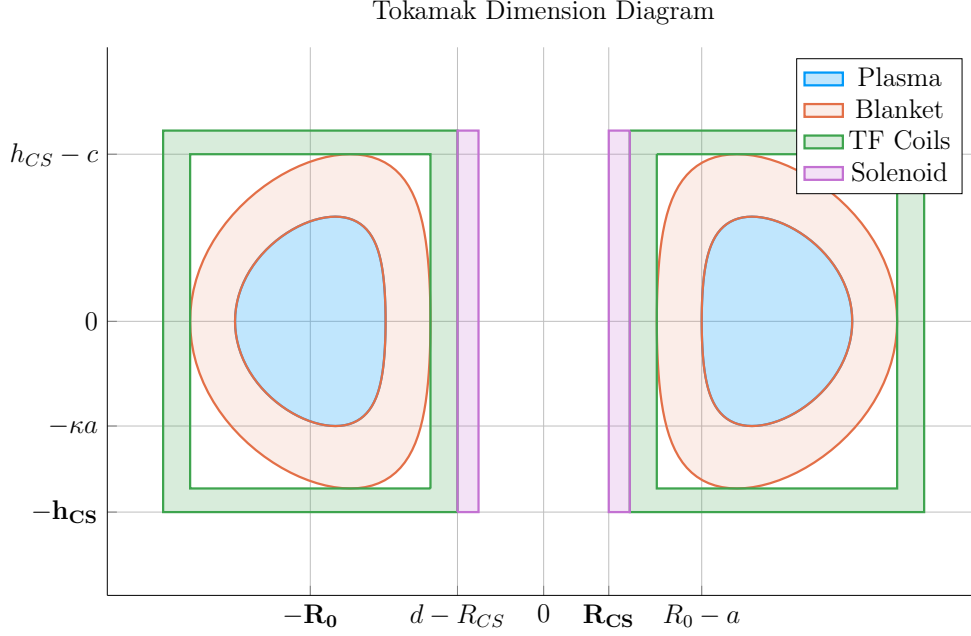


Figure 4-3: Dimensions of Tokamak Cross-Section

Geometrically, a tokamak consists mainly of four components: the plasma, its metallic blanket, the toroidal field magnets surrounding them, and the central solenoid. These have thicknesses of  $a$ ,  $b$ ,  $c$  and  $d$ , respectively.  $R_{CS}$  is where the solenoid begins.

### 4.3.2 Calculating Component Thicknesses

In between the inner surface of the central solenoid and the major radius of the tokamak are four thicknesses:  $a$ ,  $b$ ,  $c$ , and  $d$ . This subsection will go over them one at a time.

#### The Minor Radius – $a$

The minor radius was the first of these thicknesses we encountered. To calculate it, we introduced the inverse aspect ratio ( $\varepsilon$ ) to relate it to the major radius ( $R_0$ ):

$$a = \varepsilon \cdot R_0 \quad (2.1)$$

### The Blanket Thickness – $b$

The blanket is an area between the TF coils and the torus that is composed mainly of lithium and steel. It serves to both: protect the superconducting magnet structures from neutron damage, as well as breed more tritium fuel from stray fusion neutrons.<sup>37</sup> In equation form, the blanket thickness is given by:<sup>13</sup>

$$b = 1.23 + 0.074 \ln P_W \quad (4.56)$$

Here,  $P_W$  is part of a small correction to account for extra wall loading (as discussed in Section 3.4.3). Most blankets are, therefore, usually around a meter.<sup>6,13</sup>

Moving forward, the remaining two thicknesses –  $c$  and  $d$  – are handled differently: estimating structural steel portions as well as magnetic current-carrying ones.

### The Toroidal Field Coil Thickness – $c$

The thickness of the TF coils –  $c$  – is a little beyond the scope of this paper. It does, however, have a form that combines a structural steel component with a magnetic portion. From a previous model, this can be given as:<sup>13</sup>

$$c = G_{CI} R_0 + G_{CO} \quad (4.57)$$

$$G_{CI} = \frac{B_0^2}{4\mu_0\sigma_{TF}} \cdot \frac{1}{(1 - \varepsilon_b)} \cdot \left( \frac{4\varepsilon_b}{1 + \varepsilon_b} + \ln \left( \frac{1 + \varepsilon_b}{1 - \varepsilon_b} \right) \right) \quad (4.58)$$

$$G_{CO} = \frac{B_0}{\mu_0 J_{TF}} \cdot \frac{1}{(1 - \varepsilon_b)} \quad (4.59)$$

The critical stress –  $\sigma_{TF}$  – in  $G_{CI}$  implies it depends on the structural component, whereas the maximum current density –  $J_{TF}$  – implies a magnetic predisposition in  $G_{CO}$ . The use of  $G_{\square}$  in these quantities, instead of  $K_{\square}$  is because they include

the toroidal magnetic field strength:  $B_0$ . For this reason, they are referred to as dynamic coefficients. Lastly, the term  $\varepsilon_b$  represents the blanket inverse aspect ratio that combines the minor radius with the blanket thickness:

$$\varepsilon_b = \frac{a + b}{R_0} \quad (4.60)$$

### The Central Solenoid Thickness – $d$

Finishing this discussion where we started, the central solenoid's thickness –  $d$  – has a form similar to the TF coils (i.e.  $c$ ). It can be represented as:<sup>13</sup>

$$d = K_{DR}R_{CS} + K_{DO} \quad (4.61)$$

$$K_{DR} = \frac{3B_{CS}^2}{6\mu_0\sigma_{CS} - B_{CS}^2} \quad (4.62)$$

$$K_{DO} = \frac{6B_{CS}\sigma_{CS}}{6\mu_0\sigma_{CS} - B_{CS}^2} \cdot \left( \frac{1}{J_{OH}} \right) \quad (4.63)$$

Here, the use of  $K_{\square}$  for the coefficients signifies their use as static coefficients. Therefore,  $B_{CS}$  must be treated as a static variable representing the magnetic field strength in the central solenoid. For prospective solenoids using high temperature superconducting (HTS) tape,  $B_{CS}$  may be around 20 T. The values of  $\sigma_{CS}$  and  $J_{CS}$  have similar meanings to the ones for TF coils. These are collected in Table 4.2 with example values representative of our model.

Before moving on, it seems important to say that although  $K_{DI}$  and  $K_{DO}$  do not

Table 4.2: Example TF Coils and Central Solenoid Critical Values

(a) Stresses [MPa]			(b) Current Densities [MA/m <sup>2</sup> ]		
Item	Symbol	Limit	Item	Symbol	Limit
Solenoid	$\sigma_{CS}$	600	Solenoid	$J_{CS}$	100
TF Coils	$\sigma_{TF}$	600	TF Coils	$J_{TF}$	200

depend on dynamic variables,  $R_{CS}$  most definitely does. This is what makes the central solenoid's thickness difficult.

### 4.3.3 Revisiting Central Solenoid Dimensions

Now that the various thicknesses have been defined (i.e.  $a$ ,  $b$ ,  $c$ , and  $d$ ), the equations for the solenoid's dimensions –  $R_{CS}$  and  $h_{CS}$  – can be revisited and simplified. From before,

$$R_{CS} = R_0 - (a + b + c + d) \quad (4.54)$$

$$h_{CS} = 2 \cdot (\kappa a + b + c) \quad (4.55)$$

Repeated, the four thicknesses in these equations are:

$$a = \varepsilon \cdot R_0 \quad (2.1)$$

$$b = 1.23 + 0.074 \ln P_W \quad (4.56)$$

$$c = G_{CI}R_0 + G_{CO} \quad (4.57)$$

$$d = K_{DR}R_{CS} + K_{DO} \quad (4.61)$$

Substituting these thicknesses into the central solenoid's dimensions results in:

$$h_{CS} = 2 \cdot (R_0 \cdot (\varepsilon \kappa + G_{CI}) + (b + G_{CO})) \quad (4.64)$$

$$R_{CS} = \frac{1}{1 + K_{DR}} \cdot (R_0 \cdot (1 - \varepsilon - G_{CI}) - (K_{DO} + b + G_{CO})) \quad (4.65)$$

These are the complete central solenoid dimension formulas. To make them more

tractable to the reader, they will now be simplified one step at a time.\*

The first simplification to make while estimating central solenoid dimensions is to neglect the magnetic current-carrying portions of the central solenoid and TF coils. This results in:

$$\lim_{\substack{G_{CO} \rightarrow 0 \\ K_{DO} \rightarrow 0}} h_{CS} = h_{CS}^{\dagger} = 2R_0 \cdot (K_{EK} + \varepsilon_b + G_{CI}) \quad (4.66)$$

$$\lim_{\substack{G_{CO} \rightarrow 0 \\ K_{DO} \rightarrow 0}} R_{CS} = R_{CS}^{\dagger} = \frac{R_0}{1 + K_{DR}} \cdot (1 - \varepsilon_b - G_{CI}) \quad (4.67)$$

The new static coefficient, here, is:

$$K_{EK} = \varepsilon \cdot (\kappa - 1) \quad (4.68)$$

The next simplification is ignoring the TF coil thickness – and thus magnetic field dependence – altogether:

$$\lim_{G_{CI} \rightarrow 0} h_{CS}^{\dagger} = h_{CS}^{\ddagger} = 2R_0 \cdot (K_{EK} + \varepsilon_b) \quad (4.69)$$

$$\lim_{G_{CI} \rightarrow 0} R_{CS}^{\dagger} = R_{CS}^{\ddagger} = \frac{R_0}{1 + K_{DR}} \cdot (1 - \varepsilon_b) \quad (4.70)$$

These oversimplifications will be used later this chapter while simplifying the generalized current equation to something more tractable. For now, they highlight how the dimensions change as different components are neglected. The next step is bringing plasma physics back into flux balance and solving for the generalized current.

---

\*The same simplification exercise will be done again after the generalized current is derived later this chapter.

## 4.4 Piecing Together the Generalized Current

The goal of this section is to quickly expand flux balance using all the defined quantities and then rearrange it into an equation for plasma current – which is suitable for root solving. This starts with a restatement of flux balance in a reactor:

$$\Phi_{CS} + \Phi_{PF} = \Phi_{RU} + \Phi_{FT} \quad (4.53)$$

$$\Phi_{CS} = 2MI_{max} \quad (4.40)$$

$$\Phi_{PF} = \pi B_V \cdot (R_0^2 - (R_{CS} + d)^2) \quad (4.44)$$

$$\Phi_{RU} = L_2 \cdot I_{ID} \quad (4.42)$$

$$\Phi_{FT} = (R_P \tau_{FT}) \cdot I_{ID} \quad (4.43)$$

The first step is realizing that the central solenoid flux can now be rewritten using the new geometry in a standardized form:

$$\Phi_{CS} = K_{CS} \cdot \sqrt{R_0 G_{LT} h_{CS}} \quad (4.71)$$

$$K_{CS} = 2k B_{CS} \cdot \sqrt{\frac{\pi K_{LP}}{\mu_0}} \quad (4.72)$$

Next, we will slightly simplify the PF coil flux using a dynamic variable coefficient:

$$\Phi_{PF} = G_V \cdot \frac{K_{VI} I_P + K_{VT} \bar{T}}{R_0} \quad (4.73)$$

$$G_V = \frac{\pi}{10} \cdot (R_0^2 - (R_{CS} + d)^2) \quad (4.74)$$

This allows us to rewrite the generalized current as:

$$I_P = \frac{(K_{BS} + G_{IV}/G_{IP}) \cdot \bar{T}}{1 - K_{CD}(\sigma v) - G_{ID}/G_{IP}} \quad (4.75)$$

$$G_{IU} = K_{VT} G_V + K_{CS} R_0^{3/2} \cdot \frac{\sqrt{h_{CS} G_{LT}}}{\bar{T}} \quad (4.76)$$

$$G_{ID} = K_{VI} G_V \quad (4.77)$$

$$G_{IP} = K_{LP} R_0^2 + \frac{K_{RP} \tau_{FT}}{\bar{T}^{3/2}} \quad (4.78)$$

As we will show in the next section, this form not only has a form remarkably similar to the steady current – it reduces to it in the limit of infinitely long pulses!

## 4.5 Simplifying the Generalized Current

This section focuses on making various simplifications to the generalized current:

$$I_P = \frac{(K_{BS} + G_{IU}/G_{IP}) \cdot \bar{T}}{1 - K_{CD}(\sigma v) - G_{ID}/G_{IP}} \quad (4.75)$$

As promised, this will start with the trivial simplification of the generalized current into the steady state one. Next it will move on to a basic simplification for the purely pulsed case. These two activities should shed some light on how to interpret the equation in the more complicated hybrid case (that is actually used by the model).

### 4.5.1 Recovering the Steady Current

The place to start with the steady current simplification is in the dynamic coefficient,  $G_{IP}$ :

$$G_{IP} = K_{LP} R_0^2 + \frac{K_{RP} \tau_{FT}}{\bar{T}^{3/2}} \quad (4.78)$$

As can be seen, as  $\tau_{FT} \rightarrow \infty$ , so does the coefficient,

$$\lim_{\tau_{FT} \rightarrow \infty} G_{IP} = \infty \quad (4.79)$$



Because  $G_{IU}$  and  $G_{ID}$  remain constant, their contribution to plasma current becomes insignificant in this limit. Concretely,

$$\lim_{\tau_{FT} \rightarrow \infty} I_P = \frac{K_{BS} \bar{T}}{1 - K_{CD}(\sigma v)} \quad (4.80)$$

This is precisely the steady current given by Eq. (2.28)! The generalized current automatically works when modeling steady-state tokamaks.\*

### 4.5.2 Extracting the Pulsed Current

For pulsed reactors, we have to resolve a similar problem – except now  $\tau_{FT}$  is expected to be a reasonably sized number (i.e. 2 hours).

With an aim at intuition, the reactor is first treated as purely pulsed – having no current drive assistance:

$$\lim_{\eta_{CD} \rightarrow 0} I_P = \frac{(K_{BS} + G_{IU}/G_{IP}) \cdot \bar{T}}{1 - (G_{ID}/G_{IP})} \quad (4.81)$$

Next, for simplicity-sake, the PF coil contribution to flux balance is assumed negligible, as it was always meant to be a correction term:

$$\lim_{\Phi_{PF} \ll \Phi_{CS}} G_{IU} = K_{CS} R_0^{3/2} \cdot \frac{\sqrt{h_{CS} G_{LT}}}{\bar{T}} \quad (4.82)$$

$$\lim_{\Phi_{PF} \ll \Phi_{CS}} G_{ID} = 0 \quad (4.83)$$

Piecing this altogether, we can write a new current for this highly simplified case,

$$I_P^\dagger = K_{BS} \bar{T} + \frac{K_{CS} R_0^{3/2} \cdot \sqrt{h_{CS} G_{LT}}}{K_{LP} R_0^2 + K_{RP} \tau_{FT} \bar{T}^{-3/2}} \quad (4.84)$$

---

\*It should be noted that this is much harder when setting  $\tau_{FT}$  to a large, but finite number – as  $\eta_{CD}$  still needs to be solved self-consistently.

As this is not quite simple enough, these previous simplifications will be incorporated:

$$G_{LT}^{\dagger} = R_{CS}^2 \quad (4.28)$$

$$h_{CS}^{\dagger} = 2R_0 \cdot (K_{EK} + \varepsilon_b) \quad (4.69)$$

$$R_{CS}^{\dagger} = \frac{R_0}{1 + K_{DR}} \cdot (1 - \varepsilon_b) \quad (4.70)$$

Taking these into consideration results in the following current formula:

$$I_P^{\dagger} = K_{BS} \bar{T} + \left( \frac{K_{CS} R_0^3}{K_{LP} R_0^2 + K_{RP} \tau_{FT} \bar{T}^{-3/2}} \cdot \frac{(1 - \varepsilon_b) \cdot \sqrt{2(K_{EK} + \varepsilon_b)}}{1 + K_{DR}} \right) \quad (4.85)$$

In the limit that the pulse length drops to zero (and bootstrap current is negligible),

$$\lim_{\tau_{FT} \rightarrow 0} I_P^{\dagger} = R_0 \cdot \left( \frac{K_{CS}}{K_{LP}} \cdot \frac{(1 - \varepsilon_b) \cdot \sqrt{2(K_{EK} + \varepsilon_b)}}{1 + K_{DR}} \right) \quad (4.86)$$

This implies that a purely pulsed current scales with major radius to leading order.

### 4.5.3 Rationalizing the Generalized Current

From the previous two subsections, we arrived at equations for infinitely large and infinitely small pulse lengths:

$$\lim_{\tau_{FT} \rightarrow \infty} I_P = \frac{K_{BS} \bar{T}}{1 - K_{CD}(\sigma v)} \quad (4.80)$$

$$\lim_{\tau_{FT} \rightarrow 0} I_P^{\dagger} = R_0 \cdot \left( \frac{K_{CS}}{K_{LP}} \cdot \frac{(1 - \varepsilon_b) \cdot \sqrt{2(K_{EK} + \varepsilon_b)}}{1 + K_{DR}} \right) \quad (4.86)$$

What these imply at an intuitive level is that at small pulses, current scales with the major radius. While for long pulses, current scales with plasma temperature. In the general case, of course, the problem becomes much harder to predict – as shown by the code's results using Eq. (4.75).

# Chapter 5

## Completing the Systems Model

As opposed to previous chapters, this one will focus on the numerics behind the fusion systems model. A simple algebra will lead to a generalized solver for exploring reactor space for low cost and interesting machines. This will then naturally segue into a discussion of how plots are made and should be interpreted. The remaining chapters will then decouple the presentation of results from their analytic conclusions.

### 5.1 Describing a Simple Algebra

In essence, the systems model used here is a simple algebra problem – given five equations, solve for five unknowns. The goal is then to pick the five equations that best represent modern fusion reactor design (as shown in Fig. 5-1). Moreover, this selection should be done in such a way that actually reduces the system of equations to a simple univariate root solving problem (i.e. one equation with one unknown). As will be shown in the results, this model does reasonably well: matching other modeling campaigns in seconds.

The logical place to start in a discussion of this algebra problem is with the three equations fundamental to all reactor-grade tokamaks – both in steady-state and pulsed operation. These are: the Greenwald density limit, power balance, and current

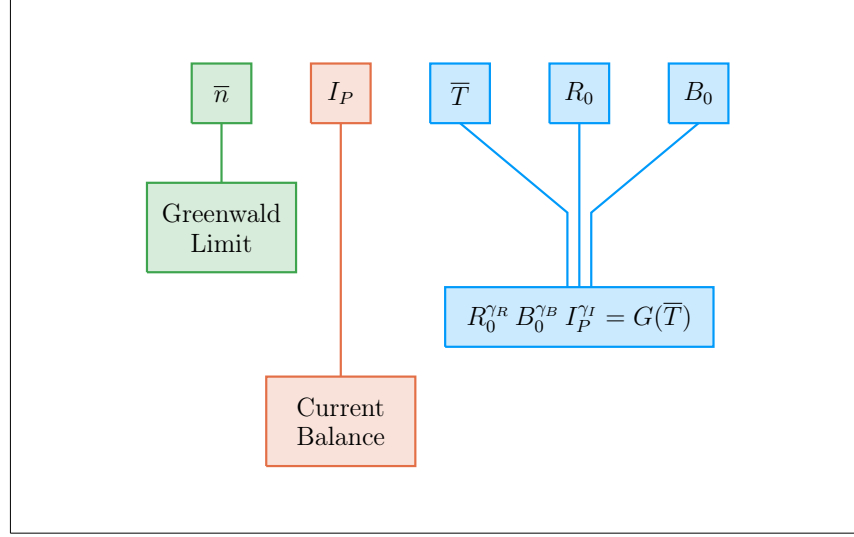


Figure 5-1: Equation Selection for Fusion System

This systems model selects five variables to solve for all the dynamic variables. These are the Greenwald limit for density, current balance for the plasma current, and three generalized formulas for the temperature, major radius, and toroidal field strength.

balance. The Greenwald density's importance was hinted early on when it was used to simplify every equation derived thereafter.

$$\bar{n} = K_n \cdot \frac{I_P}{R_0^2} \quad (2.10)$$

The two balance equations proved to be slightly more complicated. As was shown, current balance was the more difficult of the two – bringing forth the notion of self-consistency for steady-state machines and a highly-coupled multi-root equation for pulsed ones. As such, current balance stands as the equation everything is substituted into to do a final univariate root solve.

$$I_P = \frac{(K_{BS} + G_{IV}/G_{IP}) \cdot \bar{T}}{1 - K_{CD}(\sigma v) - G_{ID}/G_{IP}} \quad (4.75)$$

Although slightly buried in Eq. (4.75), the right-hand side actually depends on all the dynamic variables (including  $I_P$  through the wall loading term in blanket thickness). Through equation,

$$I_P = f(I_P, \bar{T}, R_0, B_0) \quad (5.1)$$

The remaining equation common to all reactor-grade tokamaks is, then, power balance – the relation that quantifies net electricity production capabilities. Due to the use of the ELMy H-Mode scaling law for modeling the diffusion coefficient, this had the complicated form of:

$$R_0^{\alpha_R^*} \cdot B_0^{\alpha_B} \cdot I_P^{\alpha_I^*} = \frac{G_{PB}}{K_{PB}} \quad (5.2)$$

Although rather cumbersome, this equation actually remains relatively simple in that all three quantities on the left-hand side are separable. To close the system, two more equations of this form are needed. These have the following form and will be described next.

$$R_0^{\gamma_R} \cdot B_0^{\gamma_B} \cdot I_P^{\gamma_I} = G(\bar{T}) \quad (5.3)$$

## 5.2 Generalizing Previous Equations

Where the equations defined up to this point in the chapter are shared among all fusion reactors, the remaining two equations – needed to close the system – must be partially chosen by the user. These equations come in three varieties: limits, intermediate quantities, and dynamic variables. By convention, we enforce that at least one limit must be used. The other constraint can then come from any of the three defined collections, which we will refer to as the closure equation.

### 5.2.1 Including Limiting Constraints

The limits category is composed of the limiting constraints given in Chapter 3. These include the physics derived limits from MHD theory – i.e. the beta limit ( $\beta_N$ ) and the kink safety factor ( $q_*$ ). Where for clarity, these set maximums on the allowed plasma pressure and current, respectively. There were, also, several engineering limits that described: wall loading, heat loading, and maximum power capacity. For this paper, wall loading from neutrons ( $P_W$ ) is assumed to be important, whereas the other two

engineering limits are assumed to not explicitly guide design.

Combined all these limits, as well as the yet to be defined dynamic and intermediate equations, are given in Table 5.1. These share a remarkably similar form to power balance when put into a generalized, separable state. This hints at why the major radius ( $R_0$ ), the toroidal field strength ( $B_0$ ), and the plasma current ( $I_P$ ) can easily be separated and substituted out of the current balance equation.

Before moving on, it proves useful to explain the two limits not used to explicitly guide reactor design – divertor heat loading and the maximum power capacity. The simpler

Table 5.1: Main Equation Bank

To close the system of equations for potential reactors, different equations can be used to lock down tokamak designs. These include physics and engineering limits (L), as well as ways to set dynamic (D) or intermediate (I) variables to constant values.

Variable	Category	$G(\bar{T})$	$\gamma_R$	$\gamma_B$	$\gamma_I$
Power Balance	-	$G_{PB}/K_{PB}$	$\alpha_R^*$	$\alpha_B$	$\alpha_I^*$
Beta ( $\beta_N$ )	L	$K_{TB}\bar{T}$	1	1	0
Kink ( $q_*$ )	L	$K_{KF}$	1	1	-1
Wall Loading ( $P_W$ )	L	$K_{WL}(\sigma v)^{1/3}$	1	0	-2/3
Power Cap ( $P_E$ )	L	$K_{PC}(\sigma v)$	1	0	-2
Heat Loading ( $q_{DV}$ )	L	$K_{DV}(\sigma v)^{1/3.2}$	1	0	-1
Major Radius ( $R_0$ )	D	$(R_0)_{const}$	1	0	0
Magnet Strength ( $B_0$ )	D	$(B_0)_{const}$	0	1	0
Plasma Current ( $I_P$ )	D	$(I_P)_{const}$	0	0	1
Plasma Temperature ( $\bar{T}$ )	D	$(\bar{T})_{const}/\bar{T}$	0	0	0
Electron Density ( $\bar{n}$ )	D	$(\bar{n})_{const}/K_n$	-2	0	1
Plasma Pressure ( $\bar{p}$ )	I	$(\bar{p})_{const}/K_n K_{nT} \bar{T}$	-2	0	1
Bootstrap Current ( $f_{BS}$ )	I	$(f_{BS})_{const}/K_{BS} \bar{T}$	0	0	-1
Fusion Power ( $P_F$ )	I	$(P_F)_{const}/K_F K_n^2(\sigma v)$	-1	0	2
Magnetic Energy ( $W_M$ )	I	$(W_M)_{const}/K_{WM}$	3	2	0
Cost-per-Watt ( $C_W$ )	I	$(C_W)_{const} \cdot (K_F K_n^2(\sigma v)/K_{WM})$	4	2	-2

of the two to reason is the heat loading limit. Although removing the gigawatts-per-square-meter of heat is extremely difficult, it remains an unsolved problem worthy of its own research machine.<sup>32</sup> As such, it is only kept to provide a human-interpreted measure of difficulty. The power cap, on the other hand, is just handled informally. If a reactor surpasses it (i.e.  $P_E > 4000MW$ ), it is considered invalid.

While the maximum power cap informally sets a maximum major radius for a machine, there also exists an implicit minimum major radius. This minimum radius occurs due to the hole-size constraint – i.e. at some point there is no longer enough room on the inside of the machine to store the central solenoid, blanket, and TF coils.

At this point, we can now explain how various quantities in the systems model can be set to user-given constant values. This basically allows users to treat one dynamic – or intermediate – variable as a static one (e.g. the temperature or bootstrap fraction).

### 5.2.2 Minimizing Intermediate Quantities

Whereas the limits from the previous section represented constraints with real physics and engineering repercussions, the intermediate quantities here are just used to find when reactors reach certain user-supplied values. Most notable are the capital cost (through the magnetic energy –  $W_M$ ) and the cost-per-watt ( $C_W$ ). However, the model also allows users to set values for the bootstrap fraction, plasma pressure, and fusion power. As mentioned previously, these are given in Table 5.1 through a generalized representation of the form:

$$R_0^{\gamma_R} \cdot B_0^{\gamma_B} \cdot I_P^{\gamma_I} = G(\bar{T}) \quad (5.3)$$

What this collection of variables is really useful for, though, is finding minimum cost reactors – both in a capital context as well as a cost-per-watt one. This is done in a three stage process. The first of which is to find a valid reactor – i.e. one that satisfies every limiting constraint. Practically, this is done by searching over a range of scanned temperatures.

After a valid reactor is found, its cost is recorded – leading to a drill-down stage. In this step, the cost is continuously halved until a valid reactor cannot be found. Once this invalid reactor is reached, it sets a bound on the minimum cost reactor. As such, the final stage is a simple bisection step where the minimum cost is honed down to some acceptable margin of error. This process is illustrated in Fig. 5-2.

### 5.2.3 Assigning Dynamic Variables

The remaining collection of closure equations is for the five dynamic variables in the systems model:  $R_0$ ,  $B_0$ ,  $\bar{n}$ ,  $\bar{T}$ , and  $I_P$ . As we are making equations of the following form, the formulas for  $R_0$ ,  $B_0$ , and  $I_P$  are trivial.

$$R_0^{\gamma_R} \cdot B_0^{\gamma_B} \cdot I_P^{\gamma_I} = G(\bar{T}) \quad (5.3)$$

Next, the equation for  $\bar{n}$  – shown in Table 5.1 – is a simple reversal of the Greenwald limit. The remaining equation is then from the original temperature equation:

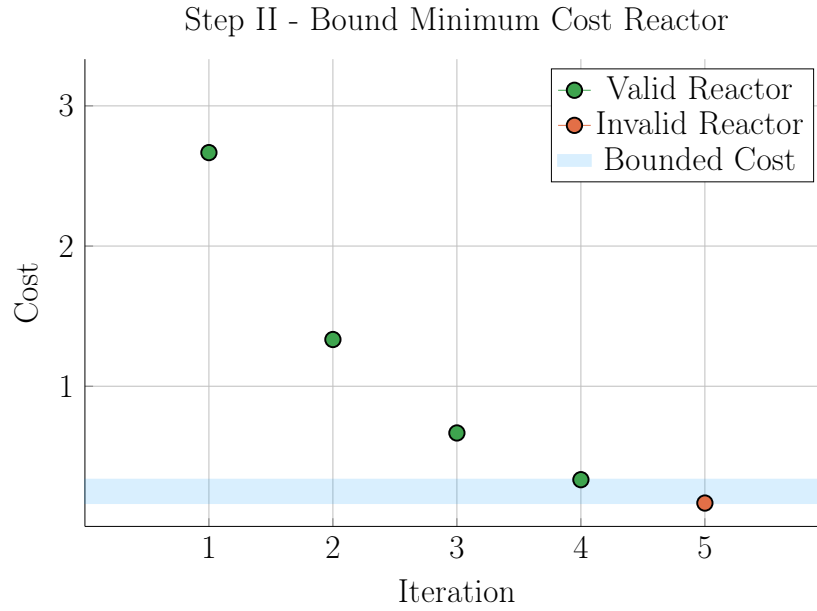
$$\bar{T} = \text{const.} \quad (3.1)$$

As was assumed earlier, Eq. (3.1) is sort of a default equation for the systems model. By this, we mean reactor curves can be created by scanning over temperatures, i.e. set  $\bar{T} = 5$  keV in one run, 10 in the next, etc. This temperature equation also brings up a difficulty for the algebraic solver, as it does not depend on: current, radius, or magnet strength. Overcoming this difficulty is discussed next subsection.

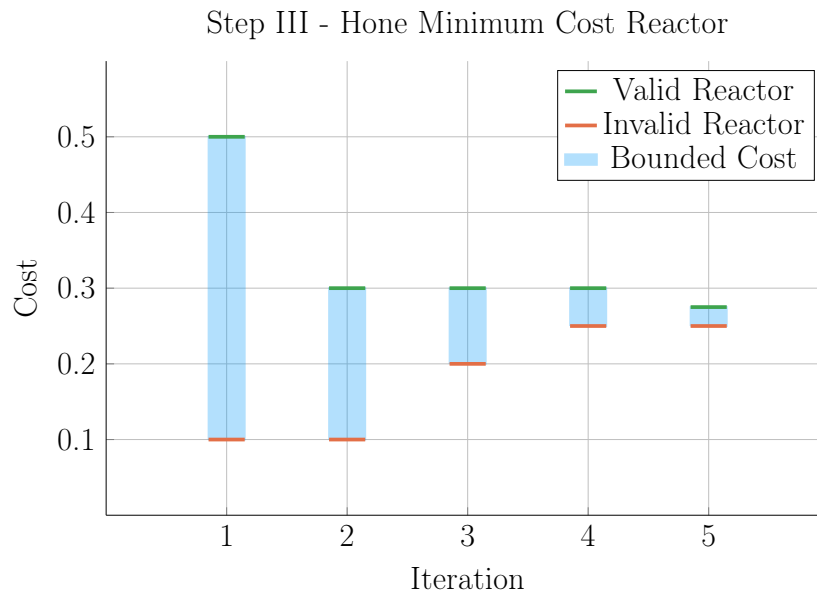
### 5.2.4 Detailing the Equation Solver

The algorithm that motivated this generalized equation approach most notably bifurcates in the situation where the closure equation does not depend on  $R_0$ ,  $B_0$ , or  $I_P$  (i.e. for the temperature equation). The two scenarios are given in Eqs. (5.4) to (5.10) – where at least  $R_0$  and  $B_0$  are substituted out of the system. In the temperature





(a) Minimize Step II



(b) Minimize Step III

Figure 5-2: Reactor Cost Minimization

After a valid reactor has been found, it is a simple process to find the minimum cost reactor. This involves first continually searching for reactors that are half the cost until a valid one can no longer be found (a). After the costing interval has been bounded by a valid and invalid reactor, the interval is bisected until there is negligible error (b).

case,  $I_P$  is not needed to be explicitly removed.

Concretely, the root solve for the temperature scenario is for the current, whereas it is for the temperature in all other cases. The nomenclature in the code is a *solve* for Scenario I (i.e. root solving for plasma current), and a *match* for Scenario II (i.e. root solving for plasma temperature).

### Scenario I – Solve for $I_P$

$$R_0(\bar{T}) = \left( G_1^{\gamma_{B,2}} \cdot G_2^{-\gamma_{B,1}} \cdot I_P^{(\gamma_{B,1} \gamma_{I,2} - \gamma_{B,2} \gamma_{I,1})} \right)^{\frac{1}{\gamma_{RBT}}} \quad (5.4)$$

$$B_0(\bar{T}) = \left( G_1^{-\gamma_{R,2}} \cdot G_2^{\gamma_{R,1}} \cdot I_P^{(\gamma_{I,1} \gamma_{R,2} - \gamma_{I,2} \gamma_{R,1})} \right)^{\frac{1}{\gamma_{RBT}}} \quad (5.5)$$

$$\gamma_{RBT} = \gamma_{R,1} \gamma_{B,2} - \gamma_{R,2} \gamma_{B,1} \quad (5.6)$$

### Scenario II – Match for $\bar{T}$

$$R_0(\bar{T}) = \left( G_1^{(\gamma_{B,2} \gamma_{I,3} - \gamma_{B,3} \gamma_{I,2})} \cdot G_2^{(\gamma_{B,3} \gamma_{I,1} - \gamma_{B,1} \gamma_{I,3})} \cdot G_3^{(\gamma_{B,1} \gamma_{I,2} - \gamma_{B,2} \gamma_{I,1})} \right)^{\frac{1}{\gamma_{RBI}}} \quad (5.7)$$

$$B_0(\bar{T}) = \left( G_1^{(\gamma_{I,2} \gamma_{R,3} - \gamma_{I,3} \gamma_{R,2})} \cdot G_2^{(\gamma_{I,3} \gamma_{R,1} - \gamma_{I,1} \gamma_{R,3})} \cdot G_3^{(\gamma_{I,1} \gamma_{R,2} - \gamma_{I,2} \gamma_{R,1})} \right)^{\frac{1}{\gamma_{RBI}}} \quad (5.8)$$

$$I_P(\bar{T}) = \left( G_1^{(\gamma_{R,2} \gamma_{B,3} - \gamma_{R,3} \gamma_{B,2})} \cdot G_2^{(\gamma_{R,3} \gamma_{B,1} - \gamma_{R,1} \gamma_{B,3})} \cdot G_3^{(\gamma_{R,1} \gamma_{B,2} - \gamma_{R,2} \gamma_{B,1})} \right)^{\frac{1}{\gamma_{RBI}}} \quad (5.9)$$

$$\gamma_{RBI} = (\gamma_{R,1} \gamma_{B,2} \gamma_{I,3} + \gamma_{R,2} \gamma_{B,3} \gamma_{I,1} + \gamma_{R,3} \gamma_{B,1} \gamma_{I,2}) - \quad (5.10)$$

$$(\gamma_{R,1} \gamma_{B,3} \gamma_{I,2} + \gamma_{R,2} \gamma_{B,1} \gamma_{I,3} + \gamma_{R,3} \gamma_{B,2} \gamma_{I,1})$$

### 5.3 Wrapping up the Logic

As stated at the beginning of the chapter, this systems model basically reduces to a simple 5 equation/5 unknown algebra problem. The Greenwald density was implicitly used in the initial derive to simplify the logic. The current balance was then delegated to be the root solve equation. Lastly, three equations were needed to remove the major radius and magnet strength, as well as either the current or temperature. These 16 equations were given in Table 5.1 with the generalized solution given in Eqs. (5.4) to (5.10).

This now sets the stage for the most interesting part of the document – the results. These will come in several forms. The first result type will be temperature scans that allow us to validate the model against other designs from the literature. These are created using the Scenario I solver.

The Scenario II matcher will then be used to create sensitivity studies and Monte Carlo samplings. These simple one variable sensitivities will reveal local trends from sweeping various static (i.e. input) variables – namely  $H$ ,  $\kappa$ ,  $B_{CS}$ , etc. – one at a time. Whereas the samplings will, then, highlight global trends as many static/input variables are allowed to vary simultaneously.

These Scenario II matchers are further subdivided in regards to the nature of their closure equation. The first type comes from finding so called two limit solutions, which live at the point where the beta and kink (or wall) limits are just marginally satisfied. The second main type is then minimum cost reactors – measured in either a capital cost or cost-per-watt context. These will be used in depth next chapter.



# Chapter 6

## Presenting the Code Results

Now that our fusion systems model has been formulated and completed, the next logical step is to build a codebase and explore reactor space. To this, the code encompassing this document’s model – `Fussy.jl` – is available at [git.io/tokamak](https://git.io/tokamak) (with a short guide given in Appendix B). The results from this chapter will be divided into three sections. The first is an attempt to test how accurate the model is by comparing it with other codes in the field.<sup>1,6,7</sup> The next will be two prototypes developed to fairly compare pulsed and steady state reactors, the initial motivation for this project.

This chapter will then conclude with a discussion on how best to lower reactor costs. In line with the MIT mission, this will highlight how using stronger magnets leads to more compact, economically competitive machines. The new piece of insight, then, is how to optimally incorporate high-temperature superconducting (HTS) tape technology – the assumed technological advancement found in the ARC design family.

Succinctly, we will show that HTS tape should be used in the TF coils for steady-state tokamaks (i.e.  $B_0$ ), whereas it should only appear in the central solenoid (i.e.  $B_{CS}$ ) for pulsed ones. This is a fundamentally new result!

## 6.1 Testing the Code against other Models

After developing a new model, the first next step is to make sure its results are sensical. The goal, however, is not to go too far, i.e. by: comparing it with too many models or requiring perfect matches with their results. To this, we will compare Fussy.jl with five designs from the literature – hopefully casting a wide enough net through reactor-space to prove sufficient. It should be noted that for how simple this model is, it does a remarkable job matching the other group’s more sophisticated frameworks. It also highlights how discrepancies arise in this highly non-linear computational problem.

The first reactor design that will provide a basis for comparison is the ARC reactor.<sup>6</sup> As it was also designed by MIT researchers, the fit is shown to be almost exact. This of course probably involves a fair amount of inherent biases stemming from shared scientific philosophies and knowledge base.

The next set of reactor designs come from the ARIES four-act study.<sup>3</sup> This ARIES team is a United States effort to reevaluate the problem of designing a fusion reactor around once a decade. The most recent study focused on how tokamaks would look as you assume optimistic and conservative values for physics and engineering parameters. Although our model recovers their results, it does highlight one peculiarity of their algorithm – reliance on the minimum achievable value of  $H$ .

The final series of reactors comes from the major codebase used among European fusion systems experts: PROCESS.<sup>7</sup> As such, this group actually gives an example for pulsed vs. steady-state tokamaks. Although these designs have the most discrepancies with our model, discussion will be given that remedy some of the shortcomings. These basically amount to: alternative definitions for heat loss appearing in the ELMy H-Mode Scaling Law, as well as the simplified nature of our flux balance equation – which only accounts for central solenoid and PF coil source terms.

The most important detail to take from the comparisons done in Tables 6.1 to 6.4, however, is that each steady state design from the literature has  $H$  factors and Greenwald densities ( $N_G$ ) that violate standard values (i.e. 1.0). What this means

practically is steady-state reactors are not possible in the current tokamak paradigm – some technological advancement is needed.

### 6.1.1 Comparing with the PSFC ARC Reactor

As mentioned, this model matches the results from the ARC design almost perfectly – see Table 6.1 and Fig. 6-2. This probably stems from how both models were developed within the MIT community. Two notable discrepancies between the models, however, are in the fusion power ( $P_F$ ) and bootstrap current fraction ( $f_{BS}$ ). These discrepancies likely arise from the use of simple parabolic profiles for temperature and, thus, can be seen in the subsequent model comparisons.

Before moving on, though, it is important to explain how the plots and table used for this comparison are made. First, a list of temperatures between 1 and 40 keV is scanned to produce a set of reactors – each with their own size ( $R_0$ ), magnet strength ( $B_0$ ), etc. These reactors are then turned into the curves shown in Fig. 6-2 by mapping to their respective values. Note that  $R_0$  vs.  $B_0$  is then a measure of the accuracy in the tokamak’s engineering, while  $I_P$  vs.  $\bar{T}$  is a measure on its plasma’s physics.

Once these curves are created, a design point is chosen on them that has the least distance to the marked point (from the original papers). These points – or reactors – are then compared in detail in Table 6.1. Note that the output between the two is what is different. Also for clarity,  $V$  is the volume of a tokamak in cubic meters, and the dash on the inductive current fraction  $f_{ID}$  implies it makes up 0% of the current.

The use of a dash for  $\beta_N$  brings up the final piece of information needed to understand the plots and table creation process – limiting constraints. Note that in Fig. 6-2, the solid curve has two portions: **beta** and **wall**. These are the portions where the beta limit and the wall loading limit are the driving constraints, respectively. For example at  $B_0 = 5$  T, the wall loading ( $P_W$ ) will be much less than the maximum allowed  $2.5 \text{ MW/m}^2$ . This is why the dash is next to  $\beta_N$  in Table 6.1, as it is held at the maximum allowed value (i.e.  $\beta_N = 0.026$ .)

Finally, the reason there is a dashed **pulsed** curve and a solid **steady** one is because this reactor was run in both modes of operation. The pulsed label is actually a slight misnomer as it implies the generalized current balance formula is used – over the simple steady current given by Eq. (2.28). Because pulses are set to 50 years, they are functionally steady-state regardless. The real reason the two curves diverge is because the steady current has a self-consistent current drive efficiency ( $\eta_{CD}$ ).

### 6.1.2 Contrasting with the ARIES ACT Studies

Moving on, the ARIES ACT study focuses on how steady-state reactors would look under both a conservative and optimistic perspective. This is highlighted in Fig. 6-1, which shows how costs decrease as the H factor is allowed to increase. Notice that for every value of H, the ACT I study (i.e. the optimistic act) has a lower cost than the design from ACT II (i.e. the conservative one).

This figure also highlights another peculiarity of the ARIES study – a reliance on the minimum possible value of H. Note that just left of the reactor point on both plots is a highly erratic portion of the curve. As such, if even a slightly smaller value of H were used in either case, a quite distinct reactor would occur. This is not a robust way to design machines. A better approach would be to build with some safety factor – i.e. at a slightly more optimistic value of H. This can be seen in ARC’s H-Sweep.

### ACT I – Advanced Physics and Engineering

ACT 1 is the ARIES study that assumes advanced physics and engineering design parameters. Although this paper’s model does a fair job recovering the results from their paper – see Table 6.2 and Fig. 6-3 – it does show what optimistic design really means. As can be seen, this design actually only surpasses the minimum possible toroidal field strength by less than a Tesla! Practically, this means their reactor is barely realizable. Trying to build a 5 T device would not be possible using their stated reactor input parameters.



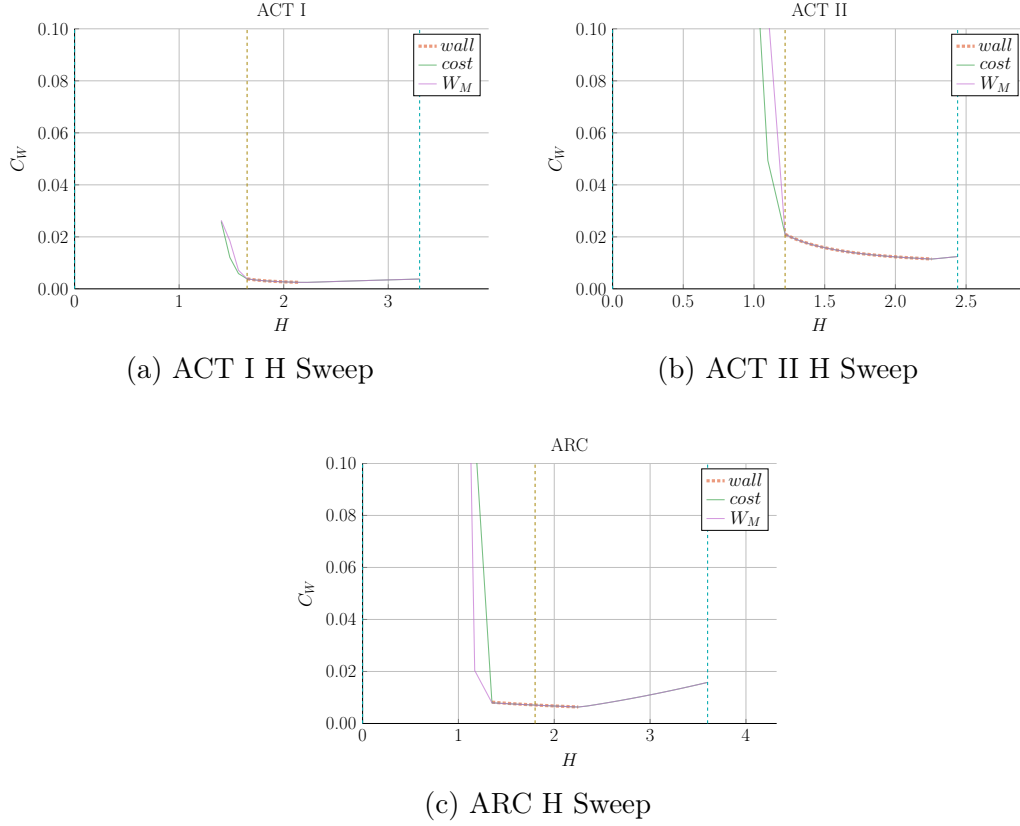


Figure 6-1: ARC and ACT Studies Cost Dependence on the H Factor

The cost of steady-state reactors can usually be reduced by increasing the enhancement factor. As shown, though, none of these reactors are possible at the standard  $H = 1$  value!

## ACT II – Conservative Physics and Engineering

ARIES more conservative design – ACT II – is much more like ARC in nature. From Fig. 6-4, it is obvious that this paper’s model is basically right on top of the reactor curve made with Fussy.jl. Much like ARC, too, it shows how the model overestimates fusion power and underestimates bootstrap fraction due to their selection of a pedestal profile for plasma temperature. This can be seen in Table 6.3.

### 6.1.3 Benchmarking with the Process DEMO Designs

The PROCESS team’s prospective designs for successors to ITER constitute the final set of model comparisons: the steady-state and pulsed DEMO reactors. As this paper is designed to compare these modes of operation, this study proves most informative. It also highlights how common model decisions can dramatically alter what reactors come out of the solvers.

The first discrepancy is how the PROCESS team defines the loss term in the ELMy H-Mode scaling law. As shown in their paper, they actually subtract out a Bremsstrahlung component, while leaving the fitting coefficients the same.<sup>7</sup> After modifying Fussy.jl to incorporate this definition, the steady-state reactor is easily reproducible in the  $R_0 - B_0$  slice of reactor space.

$$P_L^{DEMO} = P_{src} - P_{BR} \quad (6.1)$$

Unlike the steady-state case, however, the modified power loss term does not fix the pulsed one, as it actually draws the reactor curves further from the design in their paper. As such, it is flux balance that is now the main culprit for discrepancies between the two models. This makes sense, as this model uses highly simplified source terms – namely neglecting anything but the central solenoid and PF coils (as well as ignoring crucial physics for these two components). Even acknowledging the differences between the two models, Fussy.jl still does reasonably well at reproducing their much more sophisticated coding framework.

The final point to make is about selecting optimum points to build as the dynamic variables are allowed to make curves through reactor space. Up to this point, only steady-state tokamak designs have been explored. In every single one of these, though, the paper values have been very close to the point where the beta and wall loading curves intersect. This is because they all result in a minimum cost-per-watt.

For pulsed designs, on the other hand, kink curves start to appear for low magnetic field strengths. Just as beta-wall intersections were optimum places to design for low

cost-per-watt ( $C_W$ ) reactors, these beta-kink intersections will prove to be the place where minimum capital cost ( $W_M$ ) reactors usually occur. This is discussed in more detail in Section 6.3.1.

### DEMO Steady – A Steady-State ITER Successor

As shown in Fig. 6-5 and Table 6.4, the DEMO steady reactor is the design captured worst by the Fussy.jl model. Some discrepancy, however can be removed by using the PROCESS team’s modified version of heat loss, as given by Eq. (6.1).<sup>7</sup> Although not supported by the official ITER database fit,<sup>30</sup> the PROCESS team reduces the absorbed power by the Bremsstrahlung power<sup>38</sup> – which can lengthen  $\tau_E$  by more than 25%.<sup>8</sup>

With this correction, the  $R_0 - B_0$  curve is drawn to be right on top of their model’s design. The same cannot be said for the  $I_P - \bar{T}$  curve as steady current was shown to have little dependence on tokamak configuration ( $R_0$  and  $B_0$ ) and, correspondingly, the limiting constraint (e.g. `beta` and `wall`).

Note that the labels of `modified` and `pulsed` are slightly obscure in this context. Pulsed, for starters, is actually the generalized solver that does not rely on self-consistent current drive (i.e. in  $\eta_{CD}$ ). The modified label is then when the pulsed solver uses the  $P_L^{DEMO}$  value in approximating heat conductive losses.

### DEMO Pulsed – A Pulsed ITER Successor

This pulsed version of DEMO is the only reactor in our collection that is not run in steady-state. As such, it may be the most important one (i.e. it is the only pulsed reactor). The first observation from Fig. 6-6 is that this design actually has no valid wall loading portion – only a kink and beta curve exist! Even so, the results match relatively well (see Table 6.5). It should be noted, however, that its current drive is treated as an input and not handled self-consistently.

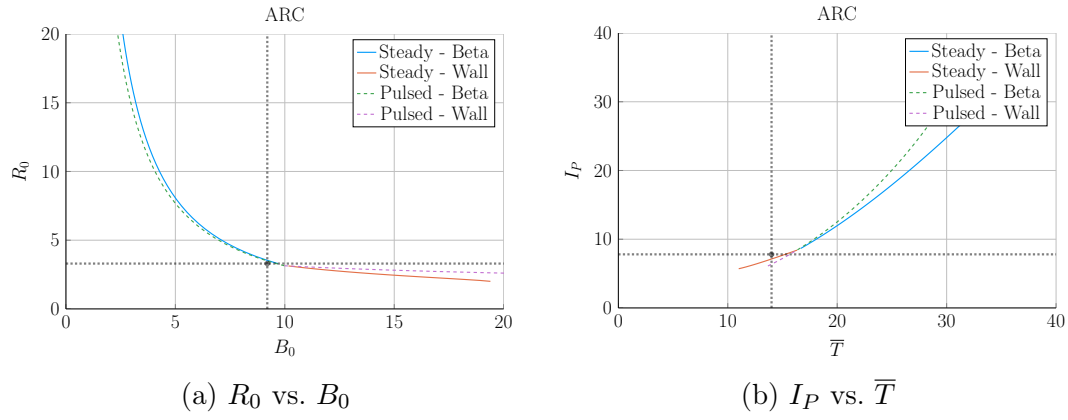


Figure 6-2: ARC Model Comparison

Table 6.1: ARC Variables

(a) Input Variables

Input	Value
$H$	1.8
$Q$	13.6
$N_G$	0.67
$\varepsilon$	0.333
$\kappa_{95}$	1.84
$\delta_{95}$	0.333
$\nu_n$	0.385
$\nu_T$	0.929
$l_i$	0.670
$A$	2.5
$Z_{eff}$	1.2
$f_D$	0.9
$\tau_{FT}$	1.6e9
$B_{CS}$	12.77

(b) Output Variables

Output	Original	Fussy.jl
$R_0$	3.3	3.4
$B_0$	9.2	9.5
$I_P$	7.8	8.8
$\bar{n}$	1.3	1.3
$\bar{T}$	14.0	16.8
$\beta_N$	0.026	-
$q_{95}$	7.2	6.1
$P_W$	2.5	2.2
$f_{BS}$	0.63	0.56
$f_{CD}$	0.37	0.44
$f_{ID}$	-	-
$V$	141	157
$P_F$	525	726
$\eta_{CD}$	0.321	0.316

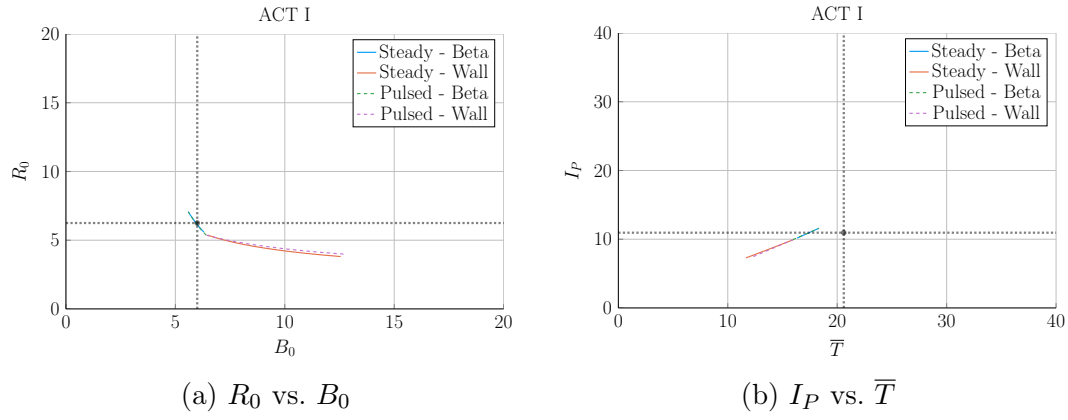


Figure 6-3: ARIES ACT I Model Comparison

Table 6.2: ACT I Variables

(a) Input Variables

Input	Value
$H$	1.65
$Q$	42.5
$N_G$	1.0
$\varepsilon$	0.25
$\kappa_{95}$	2.1
$\delta_{95}$	0.4
$\nu_n$	0.27
$\nu_T$	1.15
$l_i$	0.359
$A$	2.5
$Z_{eff}$	2.11
$f_D$	0.75
$\tau_{FT}$	1.6e9
$B_{CS}$	12.77

(b) Output Variables

Output	Original	Fussy.jl
$R_0$	6.25	6.23
$B_0$	6.0	6.0
$I_P$	10.95	10.78
$\bar{n}$	1.3	1.3
$\bar{T}$	20.6	17.2
$\beta_N$	0.0427	-
$q_{95}$	4.5	4.0
$P_W$	2.45	2.00
$f_{BS}$	0.91	0.91
$f_{CD}$	0.09	0.09
$f_{ID}$	-	-
$V$	582.0	621.4
$P_F$	1813	1865
$\eta_{CD}$	0.188	0.185

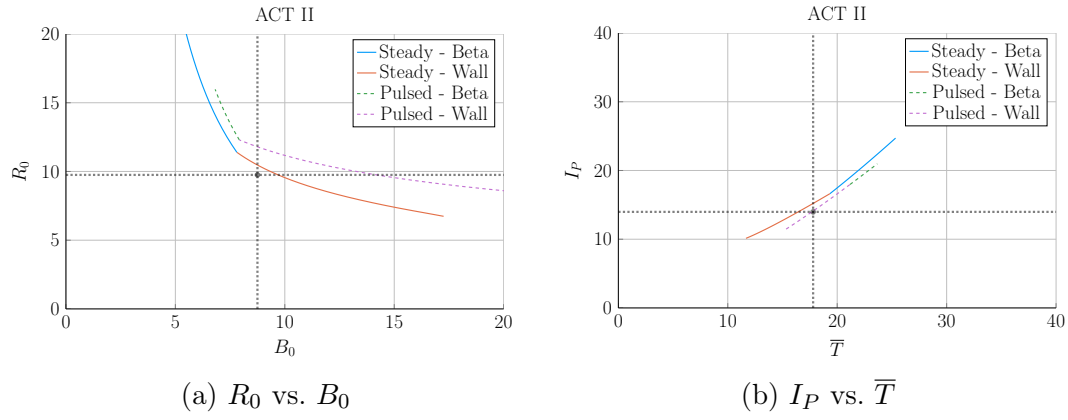


Figure 6-4: ARIES ACT II Model Comparison

Table 6.3: ACT II Variables

(a) Input Variables

Input	Value
$H$	1.22
$Q$	25.0
$N_G$	1.3
$\varepsilon$	0.25
$\kappa_{95}$	1.964
$\delta_{95}$	0.42
$\nu_n$	0.41
$\nu_T$	1.15
$l_i$	0.603
$A$	2.5
$Z_{eff}$	2.12
$f_D$	0.74
$\tau_{FT}$	1.6e9
$B_{CS}$	12.77

(b) Output Variables

Output	Original	Fussy.jl
$R_0$	9.75	10.22
$B_0$	8.75	9.05
$I_P$	13.98	14.84
$\bar{n}$	0.86	0.82
$\bar{T}$	17.8	17.4
$\beta_N$	0.026	0.023
$q_{95}$	8.0	6.6
$P_W$	1.46	-
$f_{BS}$	0.77	0.66
$f_{CD}$	0.23	0.34
$f_{ID}$	-	-
$V$	2209	2559
$P_F$	2637	3460
$\eta_{CD}$	0.256	0.307

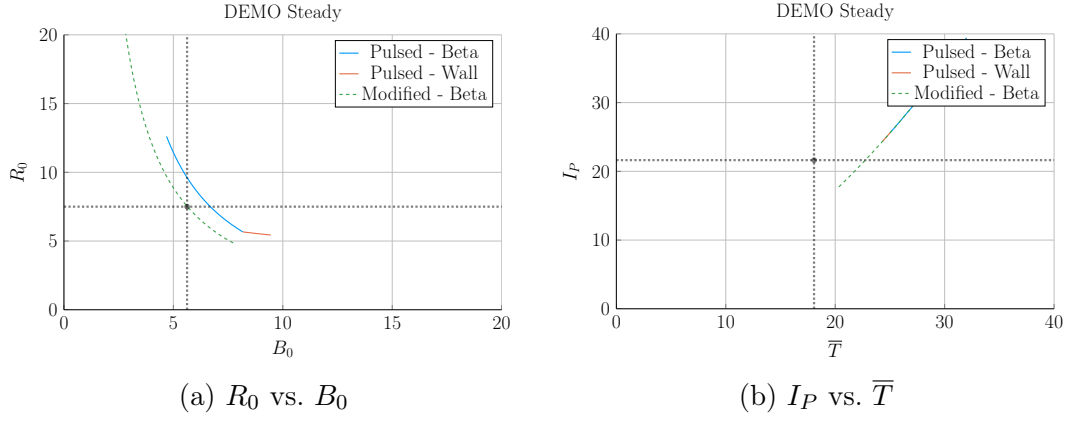


Figure 6-5: DEMO Steady Model Comparison

Table 6.4: DEMO Steady Variables

(a) Input Variables

Input	Value
$H$	1.4
$Q$	24.46
$N_G$	1.2
$\varepsilon$	0.385
$\kappa_{95}$	1.8
$\delta_{95}$	0.333
$\nu_n$	0.3972
$\nu_T$	0.9187
$l_i$	0.900
$A$	2.856
$Z_{eff}$	4.708
$f_D$	0.7366
$\tau_{FT}$	1.6e9
$B_{CS}$	12.85

(b) Output Variables

Output	Original	Fussy.jl	Modified
$R_0$	7.5	8.2	7.6
$B_0$	5.627	6.307	5.577
$I_P$	21.63	30.93	22.05
$\bar{n}$	0.875	1.048	0.855
$\bar{T}$	18.07	27.83	23.00
$\beta_N$	0.038	-	-
$q_{95}$	4.405	3.761	4.360
$P_W$	1.911	4.151	2.281
$f_{BS}$	0.611	0.424	0.492
$f_{CD}$	0.389	0.576	0.508
$f_{ID}$	-	-	-
$V$	2217	2879	2351
$P_F$	3255	8971	4306
$\eta_{CD}$	0.4152	-	-

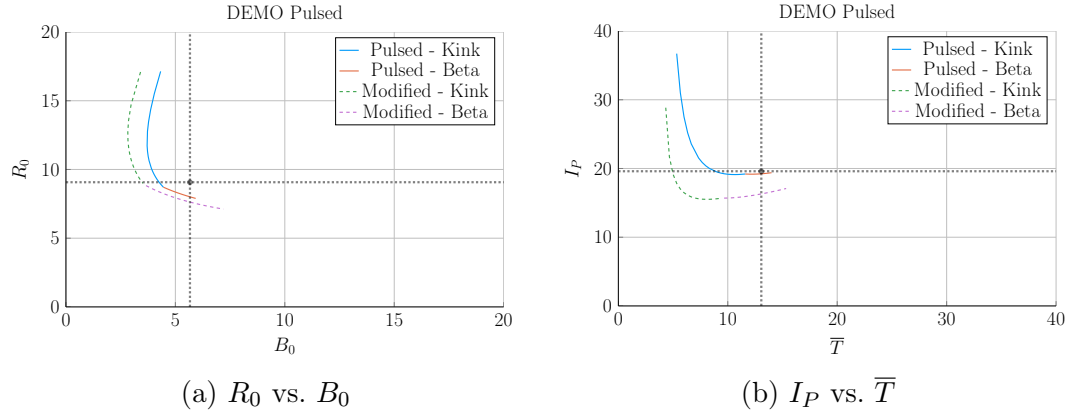


Figure 6-6: DEMO Pulsed Model Comparison

Table 6.5: DEMO Pulsed Variables

(a) Input Variables		(b) Output Variables			
Input	Value	Output	Original	Fussy.jl	Modified
$H$	1.1	$R_0$	9.07	8.10	7.61
$Q$	39.86	$B_0$	5.67	5.48	5.71
$N_G$	1.2	$I_P$	19.6	19.3	16.3
$\varepsilon$	0.3226	$\bar{n}$	0.7983	0.9795	0.9384
$\kappa_{95}$	1.59	$\bar{T}$	13.06	13.28	13.00
$\delta_{95}$	0.333	$\beta_N$	0.0259	-	-
$\nu_n$	0.27	$q_{95}$	3.247	2.853	3.303
$\nu_T$	1.094	$P_W$	1.05	1.47	1.23
$l_i$	1.155	$f_{BS}$	0.348	0.164	0.190
$A$	2.735	$f_{CD}$	0.096	0.106	0.103
$Z_{eff}$	2.584	$f_{ID}$	0.557	0.730	0.707
$f_D$	0.7753	$V$	2502	1751	1452
$\tau_{FT}$	7273	$P_F$	2037	2376	1756
$B_{CS}$	12.77	$\eta_{CD}$	0.2721	-	-



## 6.2 Developing Prototype Reactors

Now that the model used in Fussy.jl has been tested against other fusion systems codes in the field, we will develop our own prototype reactors. Because this paper is about making a levelized comparison of pulsed and steady-state tokamaks, we will develop middle-of-the-road reactors that only differ by operating mode. The parameters for these two designs are captured in Tables 6.6 and 6.7.

To compare the two modes of operation, the steady-state prototype, Charybdis, is the obvious choice to start with – as the model was tested against four of these typed reactors. It was also pointed out that the model did remarkably well when recreating ARC. As the authors share many of the ARC team’s philosophies, Charybdis uses static parameters very similar to theirs.<sup>6</sup>

Next, although led to believe Charybdis’ pulsed twin reactor – Proteus – would be created by a simple flip of the switch, it was a slight oversimplification. The first difference is that the pulsed twin, Proteus, is assumed to be purely pulsed:  $\eta_{CD} = 0$ . Further, the bootstrap current is much less important than it was for steady-state tokamaks. This corresponds to a current profile peaked at the origin – i.e. a parabola. Numerically, this is done by raising  $l_i$  from around 0.55 to 0.6.

The final difference creates the largest change in the twin reactors: the choice of necessary technological advancement. As mentioned several times before, the H factor is a common way designers artificially boost the confinement of their machines. This H value will thus be the technological advancement needed for Charybdis, the steady-state prototype. Next, as the main conclusion of this paper is to state the advantages of high magnetic fields, an inexpensive way to strengthen the central solenoid of Proteus – through  $B_{CS}$  – will be employed using HTS tape.

The goal now is to impose a constraint on both reactors’ economic competitiveness by setting their fusion power to a relatively low value – i.e. 1250 MW. As Fig. 6-7 shows, this results in Charybdis having an  $H$  factor of 1.7 and Proteus having a  $B_{CS}$  of around 20 T. As shown in the Proteus cost curve, this was at a point where the

ratio between the minimum capital cost and the minimum cost-per-watt leveled off.

Note that these technological advancements (in  $H$  and  $B_{CS}$ ) are necessary to get economic – or even physically realizable – reactors. This is the same reason why all the literature reactors used values for  $H$  and  $N_G$  that violate standard values.<sup>3,6</sup>

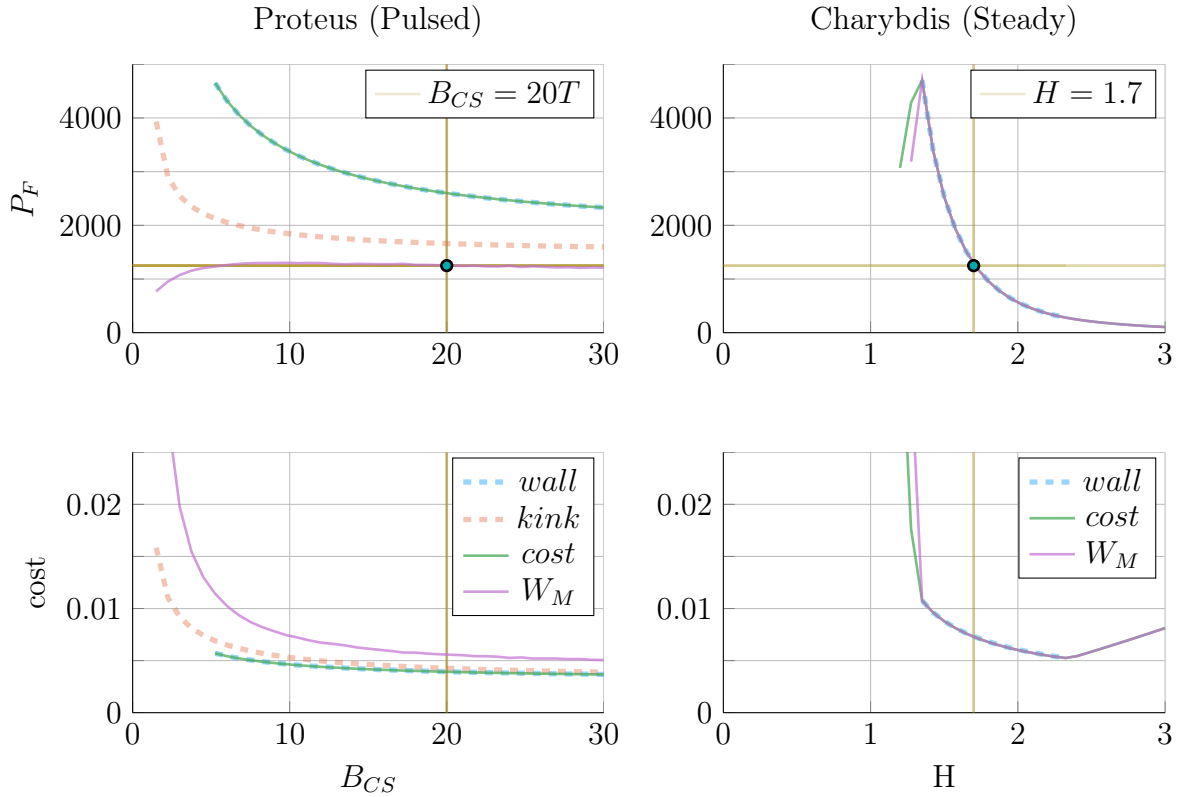


Figure 6-7: Designing Reactor Prototypes

As is convention in fusion engineering, designs are built using one assumed technological advancement. For steady-state reactors, we assume a method for improving confinement – by increasing  $H$ . While in the pulsed case, the advancement is inexpensive magnet technology for stronger fields in the central solenoid –  $B_{CS}$ .

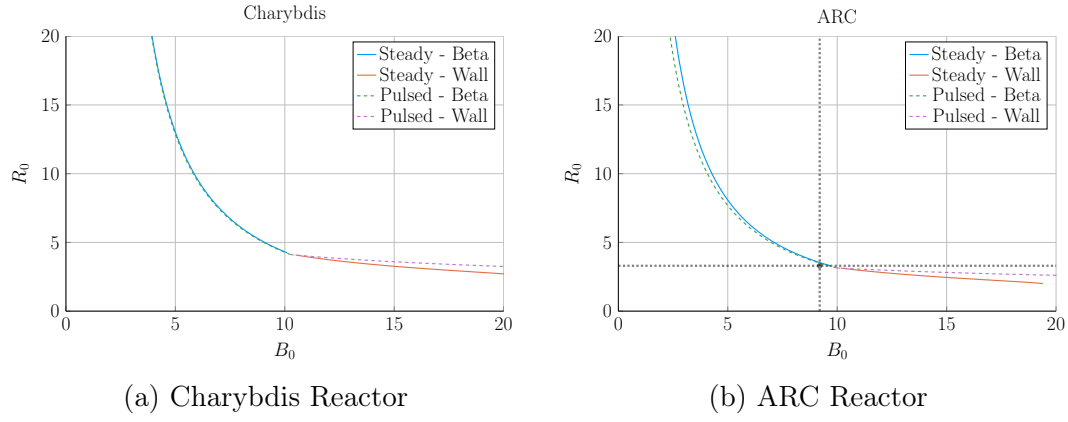


Figure 6-8: Steady State Prototype Comparison

Table 6.6: Charybdis Variables

(a) Input Variables

Input	Value
$H$	1.7
$Q$	25.0
$N_G$	0.9
$\varepsilon$	0.3
$\kappa_{95}$	1.8
$\delta_{95}$	0.35
$\nu_n$	0.4
$\nu_T$	1.1
$l_i$	0.558
$A$	2.5
$Z_{eff}$	1.75
$f_D$	0.9
$\tau_{FT}$	1.6e9
$B_{CS}$	12.0

(b) Output Variables

Output	Value
$R_0$	4.13
$B_0$	10.28
$I_P$	8.98
$\bar{n}$	1.47
$\bar{T}$	15.81
$\beta_N$	0.028
$q_{95}$	6.089
$P_W$	3.003
$f_{BS}$	0.723
$f_{CD}$	0.277
$f_{ID}$	0.0
$V$	225.5
$P_F$	1294
$\eta_{CD}$	0.291

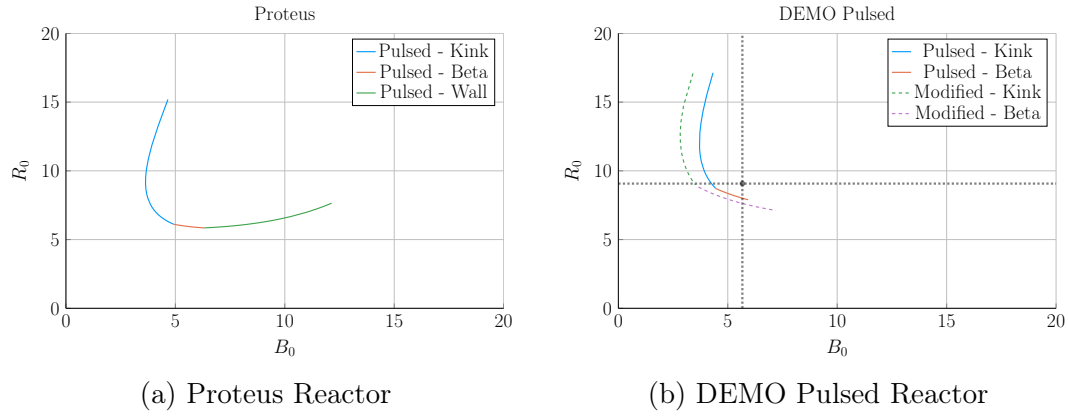


Figure 6-9: Pulsed Prototype Comparison

Table 6.7: Proteus Variables

(a) Input Variables

Input	Value
$H$	1.0
$Q$	25.0
$N_G$	0.9
$\varepsilon$	0.3
$\kappa_{95}$	1.8
$\delta_{95}$	0.35
$\nu_n$	0.4
$\nu_T$	1.1
$l_i$	0.633
$A$	2.5
$Z_{eff}$	1.75
$f_D$	0.9
$\tau_{FT}$	7200
$B_{CS}$	20.0

(b) Output Variables

Output	Value
$R_0$	6.11
$B_0$	4.93
$I_P$	15.54
$\bar{n}$	1.16
$\bar{T}$	11.25
$\beta_N$	0.028
$q_{95}$	2.5
$P_W$	1.763
$f_{BS}$	0.2675
$f_{CD}$	0.0
$f_{ID}$	0.7325
$V$	732.6
$P_F$	1667
$\eta_{CD}$	0.0

### 6.2.1 Navigating around Charybdis

The Charybdis reactor is the steady-state twin developed for this paper. As mentioned, its parameters are similar to the ARC design. This is shown in Fig. 6-8, where the two  $R_0 - B_0$  curves are almost interchangeable. Before moving on, it proves useful to note that the optimum place to build on these curves is where the two portions intersect – as it minimizes costs. These cost curves are shown in Fig. 6-11.

### 6.2.2 Pinning down Proteus

The pulsed twin reactor, Proteus, highlights the effects of a high field central solenoid. When compared to the Pulsed DEMO design, the  $R_0 - B_0$  curve looks far more favorable – i.e. each machine built at a certain magnet strength would be more compact (and cheaper). An interesting facet of Proteus is that it exhibits all three used limits: kink safety factor, Troyon beta, and wall loading. Cost curves are shown in Fig. 6-12.

Table 6.8: Proteus and Charybdis Comparison

The twin pulsed and steady-state prototypes show general trends in terms of what values the dynamic variables will have. As can be seen, the radius ( $R_0$ ) of the pulsed prototype (Proteus) is two meters larger than its steady-state twin (Charybdis).

(a) Charybdis		(b) Proteus	
Output	Value	Output	Value
$R_0$	4.13	$R_0$	6.11
$B_0$	10.28	$B_0$	4.93
$I_P$	8.98	$I_P$	15.54
$\bar{n}$	1.47	$\bar{n}$	1.16
$\bar{T}$	15.81	$\bar{T}$	11.25
$f_{BS}$	0.72	$f_{BS}$	0.27
$f_{CD}$	0.28	$f_{ID}$	0.73
$P_F$	1300	$P_F$	1650
$W_M$	9.48	$W_M$	7.09
$C_W$	0.007	$C_W$	0.004

### 6.2.3 Highlighting Operation Differences

Before moving onto general conclusions taken from the data, a quick investigation into the pulsed vs. steady-state twin results is in order. This comparison is best abridged in Table 6.8.

Most apparently, pulsed reactors are typically larger than steady-state ones and are meant to be run at higher plasma currents. The former behavior was seen with the DEMO designs,<sup>7,8</sup> – as the larger size was needed for long pulse lengths.<sup>39</sup> The latter was then already mentioned while discussing how steady-state reactors never saw a kink (current limiting) regime. Because higher currents improve confinement, pulsed machines can also be run at much lower temperatures.

These combined effects lead to the minimum cost reactors for steady-state operation having much higher toroidal field strengths than their pulsed counterparts. This is discussed in Section 6.3.2 when explaining optimum use of HTS tape.

## 6.3 Learning from the Data

Now that the model has been properly vetted and the prototypes have been designed, we can explore how pulsed and steady-state tokamaks scale. This will lead to three mostly independent results. The first result will explore how to minimize costs for a reactor by choosing optimum design points. The next will be an argument for how to properly utilize the HTS magnet technology in component design. Lastly, we will take a cursory look at the other parameters capable of lowering machine costs.

### 6.3.1 Picking a Design Point

With more than twenty design parameters, finding the most economic reactor is computationally intractable. Locating optimum reactors, however, becomes much more feasible when only focusing on dynamic variables – i.e. when keeping static

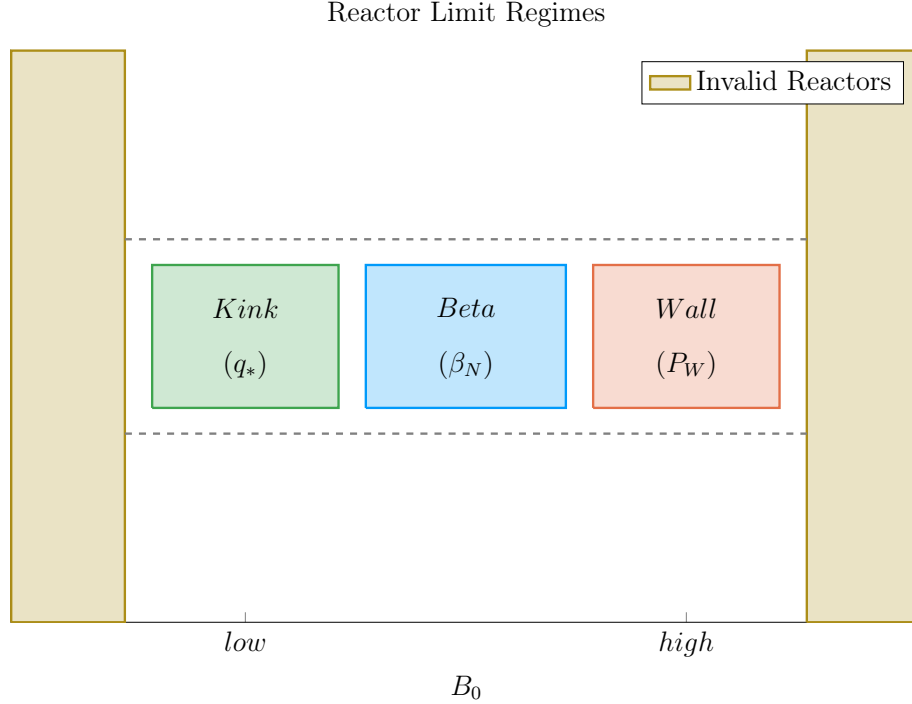


Figure 6-10: Limiting Constraint Regimes

At a simple level, a reactor has around three regimes of design limiting constraints. At low fields, the kink safety factor – through  $q_*$  and Eq. (3.40) – drives design. Then at high fields, wall loading – through  $P_W$  and Eq. (3.44) – guide reactors. And between the two, the beta limit – through  $\beta_N$  and Eq. (3.37) – is the limiting constraint.

variables constant. This method, for example, is how all the  $R_0 - B_0$  curves have been produced this chapter. Once these curves are produced, it is up to the user to choose which reactor on them to build. However, the guiding metric usually involves lowering some cost, either: capital cost or cost-per-watt.

Regardless of reactor type, most economic tokamaks operate near the beta limit – where plasma pressure is greatest. Besides being a regime highly sensitive to magnetic field strength, the beta limit is a constraint that occurs on every reactor (seen by the authors). This beta limit ( $\beta_N$ ) is usually nested between the kink limit ( $q_*$ ) to lower  $B_0$  values and wall loading ( $P_W$ ) to higher ones. Understanding these regimes is the first step towards building an intuition favoring economic machines – see Fig. 6-10.

Now that the beta limit curve has been designated as the most economic regime to operate in (usually), the goal is to select which reactor on it is the best one to build.

Starting with the easier of the two, the optimum design point for steady-state reactors is the point where wall loading first starts to dominate design. Due to the wall loading relation, given by Eq. (3.44), this causes the reactor to start increasing in size and cost – which is bad. This conclusion is justified by the cost curves for all five reactors in Fig. 6-11. As these show, it is also where the reactor designers pinned down their tokamaks.\*

The problem of selecting an optimum design for the pulsed case is more difficult. This is mainly due to there being a regime where the kink safety factor can actually be a guiding limiting constraint. Following the conclusion from steady-state reactors would be an oversimplification because there are actually two costs relevant to a reactor: capital cost and cost-per-watt. These beta-wall reactors are actually the points often best for minimizing cost-per-watt (i.e. your rate of return). The new beta-kink reactors, then, lead to cheaper to build machines – as they minimize capital cost. These conclusions are shown in Fig. 6-12.

Summarizing the conclusions of this subsection, the beta limit is usually the best constraint to operate at. For lowering the cost-per-watt, a reactor should always be run at the highest magnetic field strength ( $B_0$ ) that has the beta limit at its maximum allowed value. This most often occurs when wall loading takes over (for steady-state reactors) or reactors start being physically unrealizable (for pulsed ones). Building cheap to build reactors – i.e. minimizing capital cost – then actually proved to make pulsed design one of trade-offs. This is because the beta-kink curve intersection produces a low capital cost reactor, but at the price of operating at a subpar cost-per-watt. Designers should therefore balance the two cost metrics when pinning down a pulsed reactor.

---

\*Simply stated, the optimum reactor for steady-state tokamaks is one that just barely satisfies the beta and wall loading limit simultaneously – i.e. where the two curves intersect.



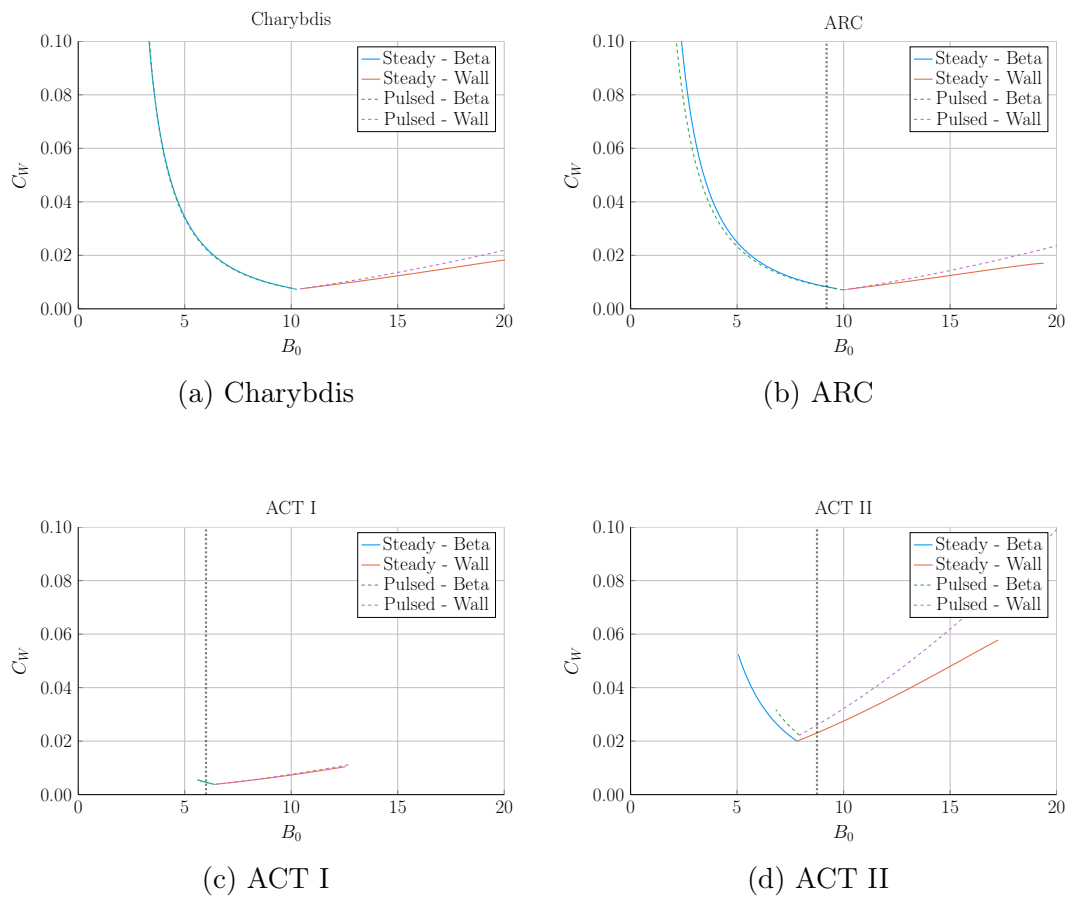
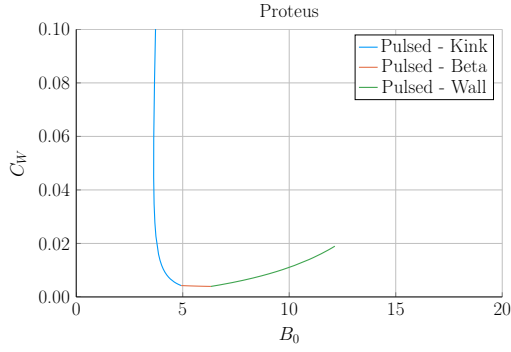
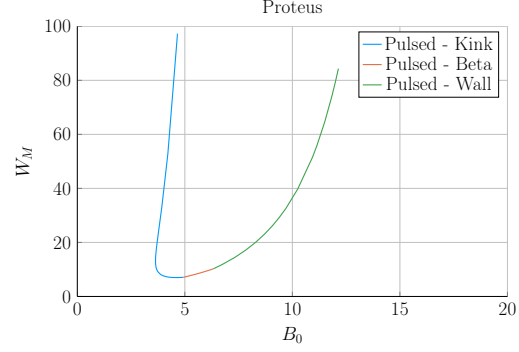


Figure 6-11: Steady State Cost Curves

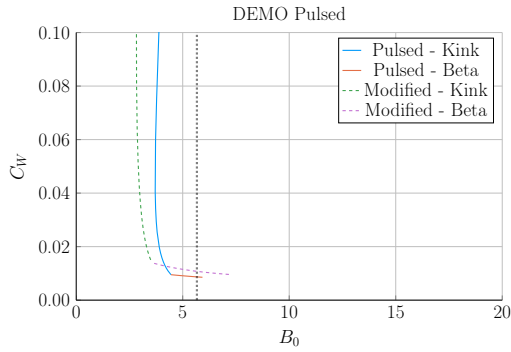
Steady state reactors typically have two regimes – a lower magnet strength **beta** limiting one and a high field **wall** loading one. As shown, each steady state scan produces a minimum cost reactor at the point where the two regimes meet.



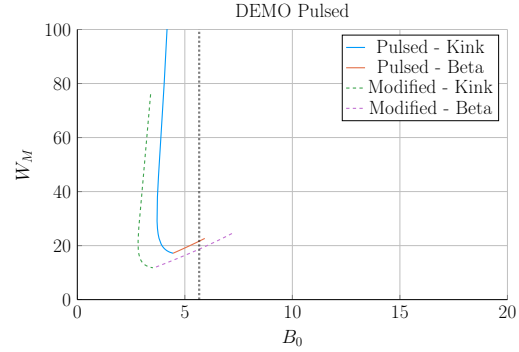
(a) Proteus Cost-per-Watt



(b) Proteus Capital Cost



(c) DEMO Pulsed Cost-per-Watt



(d) DEMO Pulsed Capital Cost

Figure 6-12: Pulsed Cost Curves

Pulsed reactor design is slightly more ambiguous than steady-state in terms of selecting an operating point. These plots show that the cost-per-watt is reduced at the highest field strength available to **beta** regime reactors. Whereas the minimum capital cost occurs when the **beta** and **kink** limit are both just marginally satisfied.

### 6.3.2 Utilizing High Field Magnets

The main conclusion for this paper is that high field magnets are the best route to building a compact, economically competitive fusion reactor. In line with the MIT ARC effort, these high fields will be built with high-temperature superconducting (HTS) tape. This innovation is set to nearly double the strength of conventional magnets. The real question is how to best use this technology.

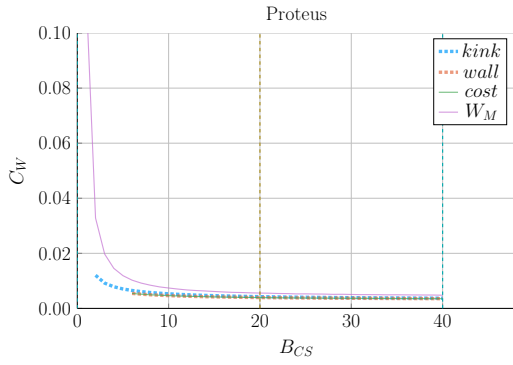
At a very simple level, there are two main places strong magnets can be employed: the toroidal fields ( $B_0$ ) and the central solenoid ( $B_{CS}$ ). The easier mode of operation to start with is steady-state. This is because steady-state tokamaks do not rely on a central solenoid to run their functionally infinite length pulses. Further, the cost curves in Fig. 6-11 show that all the designs would benefit from toroidal fields ( $B_0$ ) not achievable with conventional magnets – as they can only reach around 13 T.<sup>12</sup>

The more interesting result is that pulsed reactors gain no real benefit from using HTS toroidal field magnets – as mentioned previously in Section 6.2.3. Within the modern paradigm (i.e. D-T fuel, H-Mode, etc), pulsed reactors never have to exceed the limits of less expensive LTS magnets. The place HTS can really help is within the central solenoid, which governs how long a pulse can last. Further, these improvements to the central solenoid have diminishing returns past the range accessible to HTS tape. Therefore HTS would, again, be more than adequate for the modern paradigm. These conclusions are shown in Figs. 6-13 and 6-14.

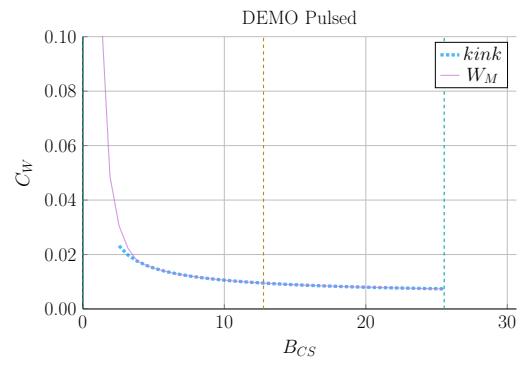
Summarizing this subsection, HTS tape is one of the best ways to lower the cost of fusion reactors at a commercial scale. For steady-state reactors, HTS works best in the toroidal field coils ( $B_0$ ), whereas the tape fares far better in the central solenoid ( $B_{CS}$ ) of pulsed reactors. As both effects saturate within the range of HTS tape, more sophisticated magnetic technology may not be necessary. HTS is thus one technological advancement that could help usher in an era of affordable fusion energy.\*

---

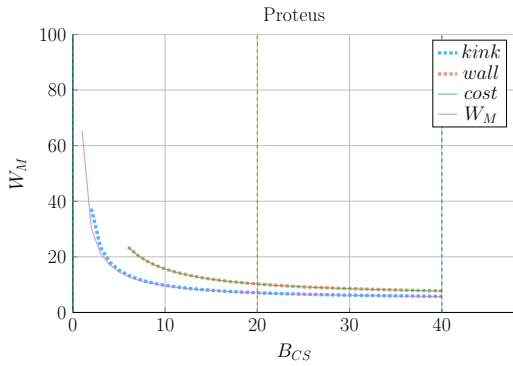
\*This notion of HTS technology leading the way to affordable fusion energy is in line with the 2018 FESAC TEC<sup>40</sup> and NAS Burning Plasma<sup>41</sup> reports.



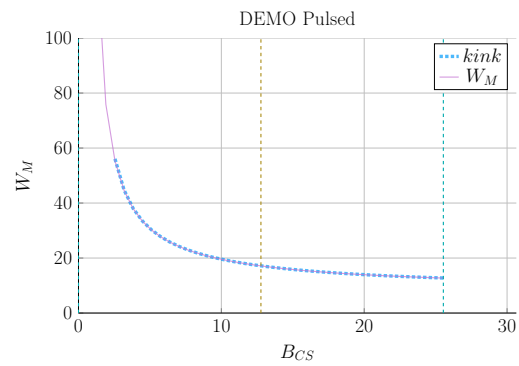
(a) Proteus Cost-per-Watt



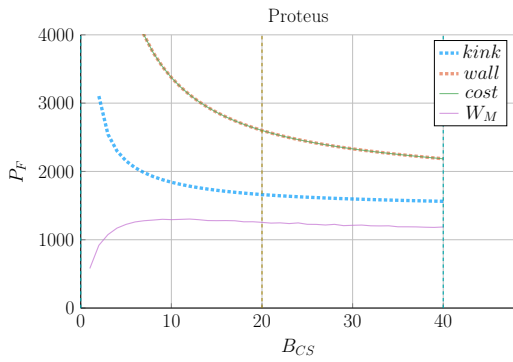
(b) DEMO Pulsed Cost-per-Watt



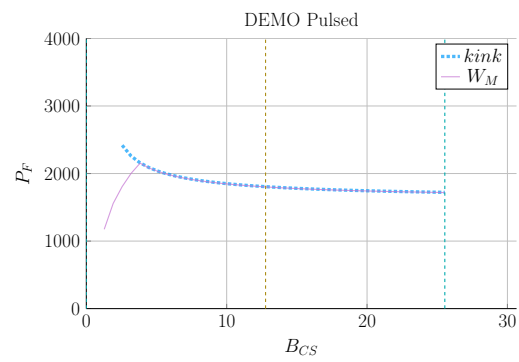
(c) Proteus Capital Cost



(d) DEMO Pulsed Capital Cost



(e) Proteus Fusion Power



(f) DEMO Pulsed Fusion Power

Figure 6-13: Pulsed  $B_{CS}$  Sensitivities

Pulsed machines become more economically attractive as their central solenoid is strengthened. However as these plots show, the positive benefits of this have rapidly diminishing returns. HTS tape's magnet range happens to be inside this regime.

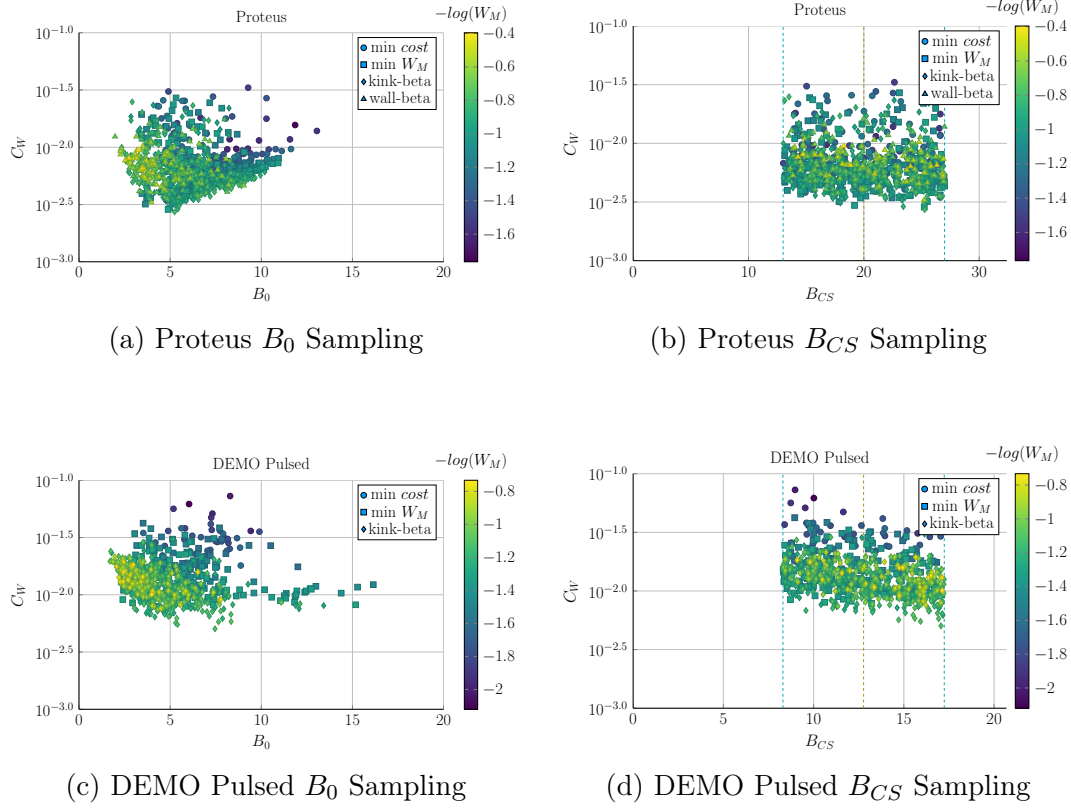


Figure 6-14: Pulsed Monte Carlo Sampling

As shown, pulsed machines have a preference towards small toroidal field strengths ( $B_0$ ) – as they minimize both capital costs and costs-per-watt. Further, increasing central solenoid strength ( $B_{CS}$ ) can lead to dramatically more competitive reactors. This effect saturates at higher field strengths, however, as is shown in subfigure (b).

### 6.3.3 Looking at Design Alternatives

Even in this relatively simple fusion model, there are more than twenty static/input variables a designer can tune to improve reactor feasibility. Many have practical limits, such as being physically realizable or fitting within the ELMY H-Mode database. The goal of this subsection is, therefore, to investigate some of the more interesting results. Although many more plots are available in Appendix H.

#### Capitalizing the Bootstrap Current

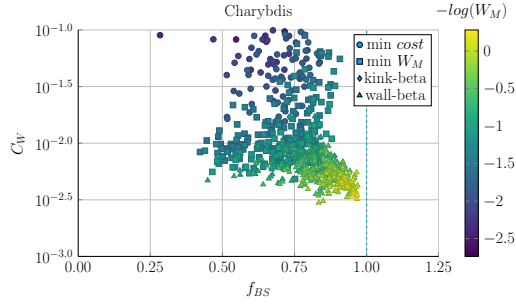
Besides artificially enhancing a plasmas confinement with the H-factor, steady-state reactor designers may also heavily rely on high bootstrap currents. This is because bootstrap current is the portion of current you do not have to pay for. The research groups most focused on this technological advancement are General Atomic's DIII-D<sup>24</sup> in San Diego and PPPL's NSTX-U in New Jersey.<sup>42</sup> Improving bootstrap fractions then relies on tailoring current profiles to be much more hollow.

Quickly reasoning this thought process are two sets of plots. The first plot (Fig. 6-15) highlights how the cheapest possible steady-state designs have bootstrap fractions approaching unity – they use almost no current drive. This makes sense as current drive is extremely cost prohibitive (i.e. why people consider pulsed tokamaks).

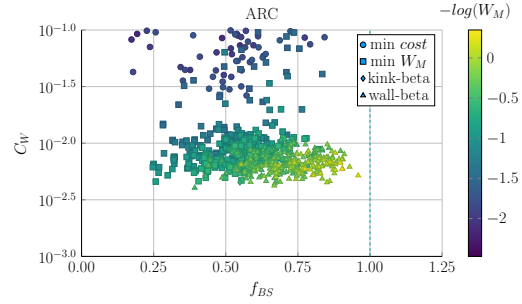
The next plot (Fig. 6-16) is the parameter that determines a current profile's peak radius:  $l_i$ . As can be seen, the current peak approaches the outer edge of the plasma as  $l_i$  decreases. This in turn boosts the bootstrap fraction closer to one – leading to inexpensive reactors.

#### Contextualizing the H-Factor

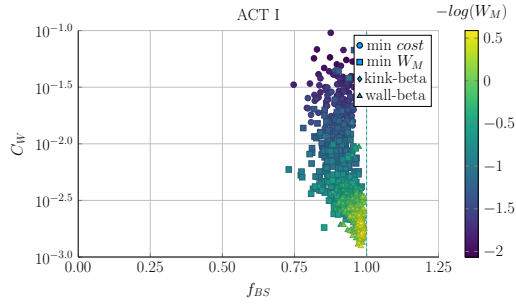
From before, increasing the H-factor always led to more cost effective steady-state reactors. This is because the enhanced confinement allows for smaller machines. This was already heavily explored in Fig. 6-1. These plots also show that steady



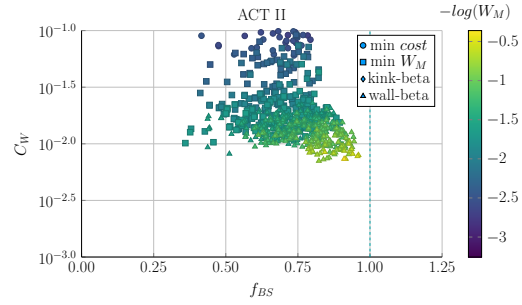
(a) Charybdis  $l_i$  Sampling



(b) ARC  $l_i$  Sampling



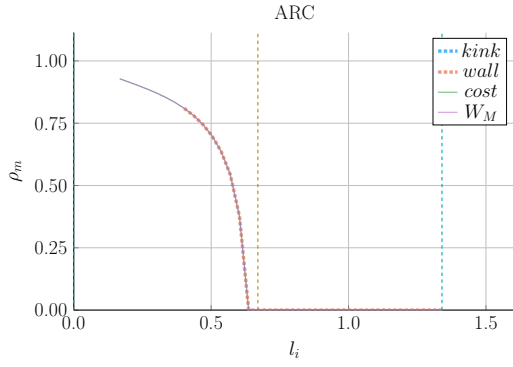
(c) ACT I  $l_i$  Sampling



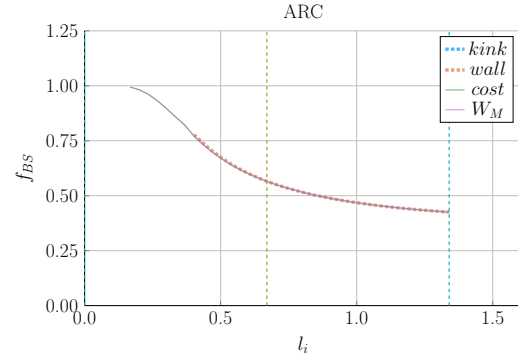
(d) ACT II  $l_i$  Sampling

Figure 6-15: Bootstrap Current Monte Carlo Sampling

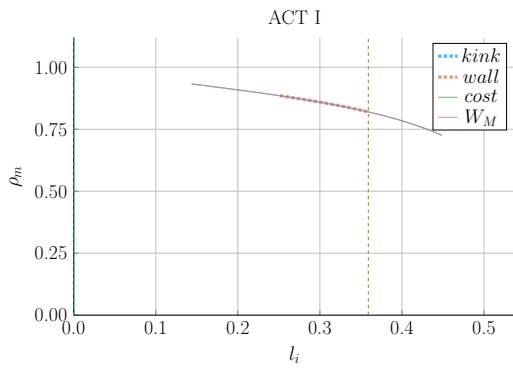
The purpose of these plots is to show that a high bootstrap current always reduces the cost of a steady state reactor – highly independent of actual input quantities (i.e.  $\varepsilon$ ,  $l_i$ , etc.)



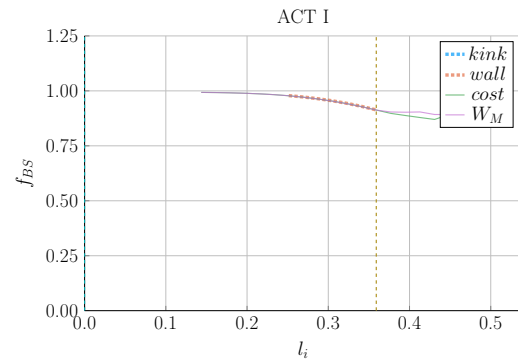
(a) ARC Peak Radius



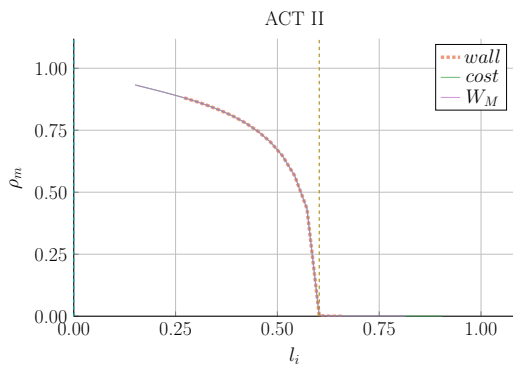
(b) ARC Bootstrap Fraction



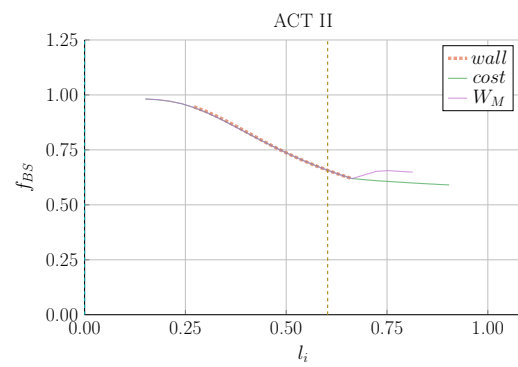
(c) ACT I Peak Radius



(d) ACT I Bootstrap Fraction



(e) ACT II Peak Radius



(f) ACT II Bootstrap Fraction

Figure 6-16: Internal Inductance Sensitivities

The internal inductance has a strong influence on the peaking radius ( $\rho_m$ ) of the hollow profile and the bootstrap current fraction ( $f_{BS}$ ). Lowering the internal inductance thus makes a profile more hollow, which in turn increases the bootstrap fraction.



state reactors would not be physically possible using a default H factor of one! In other words, steady-state tokamaks require some technical advancement before they can ever be used as fusion reactors.

For pulsed reactors, increasing H may always reduce capital costs, but it might actually increase the cost-per-watt. This is because the fusion power can decrease at a faster rate than the capital cost in a pulsed tokamak – both of which appear in Eq. (1.3) defining the cost-per-watt. This interesting result demonstrates the unusual behaviors of highly non-linear systems: intuition may not match model results.

### Showcasing the Current Drive Efficiency

The last exploration is less about building an economic machine and more about understanding the self-consistent current drive efficiency in steady-state tokamaks. Using the Ehst-Karney model<sup>27</sup> coupled with standard analysis<sup>5</sup> leads to a remarkably simple and accurate solver. As shown in Fig. 6-18, this model captures the physics almost exactly for the different designs.\*

In a similar fashion as the bootstrap fraction results, the variable that most captures how to directly maximize  $\eta_{CD}$  is the LHCD wave launch angle,  $\theta_{wave}$ . When below  $90^\circ$  it is considered outside launch, whereas up to  $135^\circ$  it is considered inside launch. Notably, these curves are not monotonic, there is an optimum launching angle – as shown in Fig. 6-19.

It should be noted that the launch angle was not found to have a major impact. This may be due to an oversimplification of the model, as sources suggest inside launch is preferable for multiple reasons.<sup>32</sup>

---

\*It did, however, not converge for the DEMO steady reactor. This is probably due to lack of self-consistency for  $\eta_{CD}$  in their systems framework.

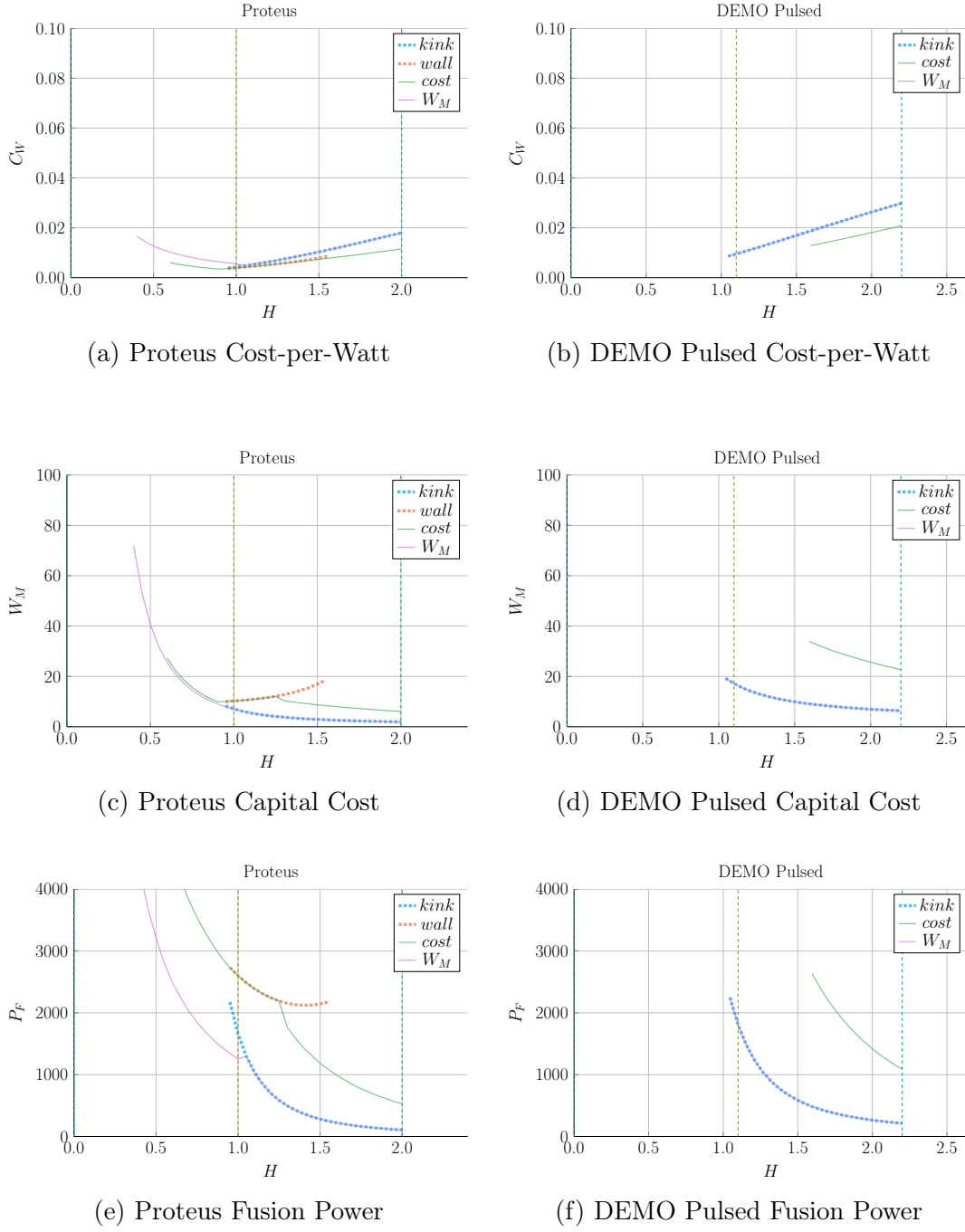


Figure 6-17: Pulsed H Sensitivities

One curious result from the model is that the enhancement factor ( $H$ ) can actually increase the cost-per-watt ( $C_W$ ) of a tokamak reactor. This is because  $C_W$  depends on both the capital cost ( $W_M$ ) and the fusion power ( $P_F$ ). Although the two do both generally decrease, the fusion power decreases at a faster rate for realistic values of  $H$ .

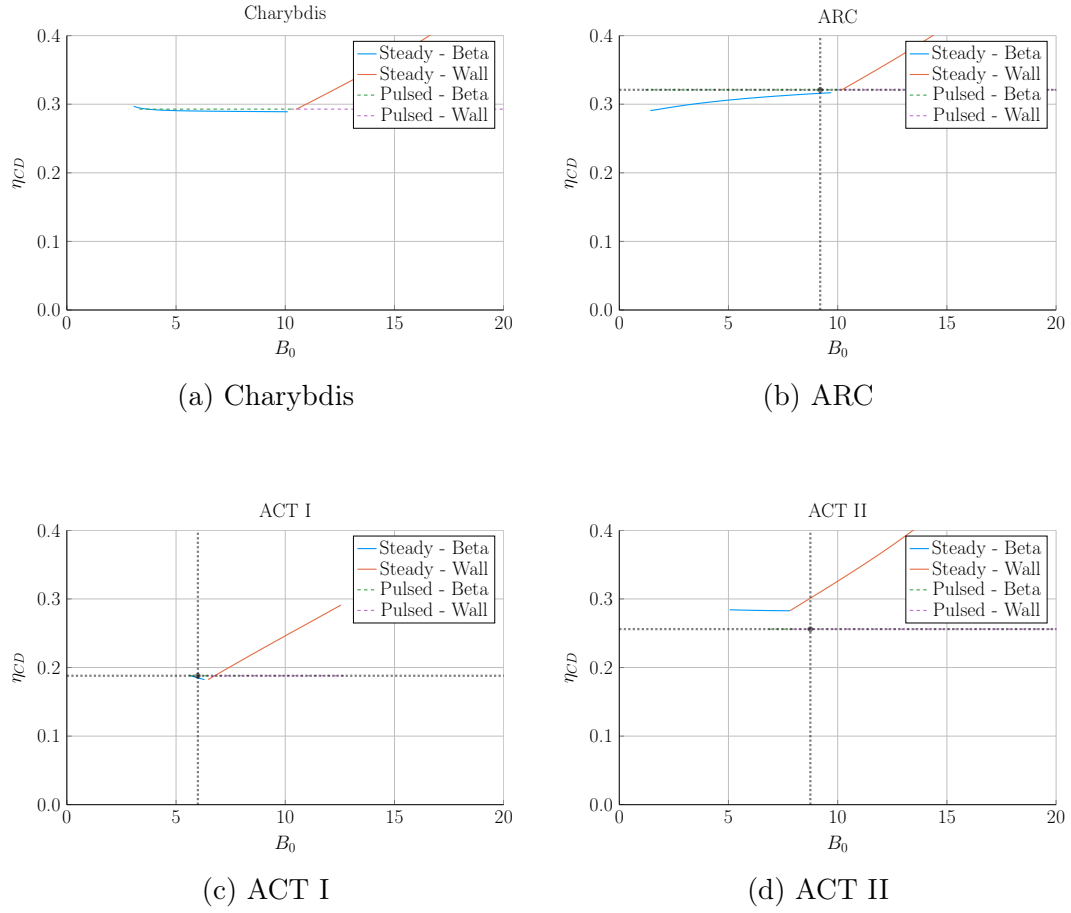
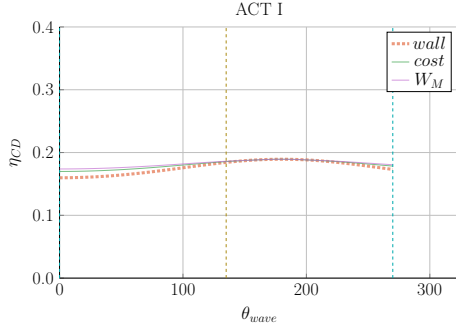
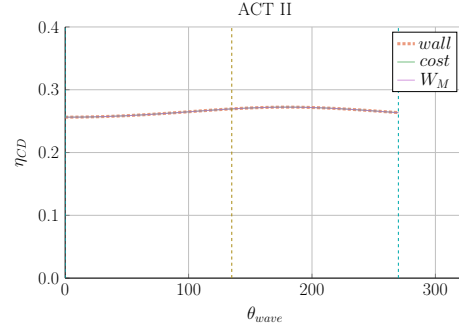


Figure 6-18: Steady State Current Drive Efficiency

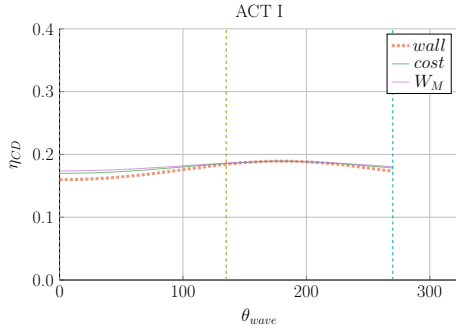
These plots shows that the Ehst-Karney current drive efficiency model<sup>27</sup> used by this document recovers values from other research studies with decent accuracy.



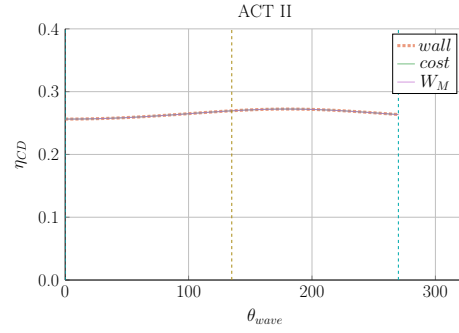
(a) Charybdis



(b) ARC



(c) ACT I



(d) ACT II

Figure 6-19: Current Drive Efficiency vs. Launch Angle

These plots show that the Ehst-Karney model does have an optimum angle, but most likely understates its importance – sources suggest inside launch is preferable for multiple reasons.<sup>32</sup>

# Chapter 7

## Planning Future Work for the Model

This model may run and produce interesting results, but there is always more to be done. This chapter explores three potential fusion reactors that could help guide real world designs. These are: a stellarator (Ladon), a steady-state/pulsed composite (Janus), and a tokamak capable of reaching H, L, and I modes (Daedalus). The chapter then concludes by describing several possible model improvements, including: adding radiation sources, using pedestal profiles, and improving flux balance.

### 7.1 Incorporating Stellarator Technology – Ladon

A stellarator is, at a basic level, a tokamak helically twisted along the length of its major circle (see Fig. 7-1). For a long time they were dismissed due to their poor transport properties.<sup>5</sup> Recent technological improvements, however, have eased this burden – as seen with the recent Wendelstein 7-X device in Germany. The problem now is the underdeveloped scaling laws that stem from a lack of machines and, more fundamentally, data points.<sup>43</sup>

To use this model to properly prototype our stellarator prototype, Ladon, one would need to replace at least: the Greenwald density limit and the confinement time scaling law. In place of the Greenwald limit will likely be some other density or current limit,

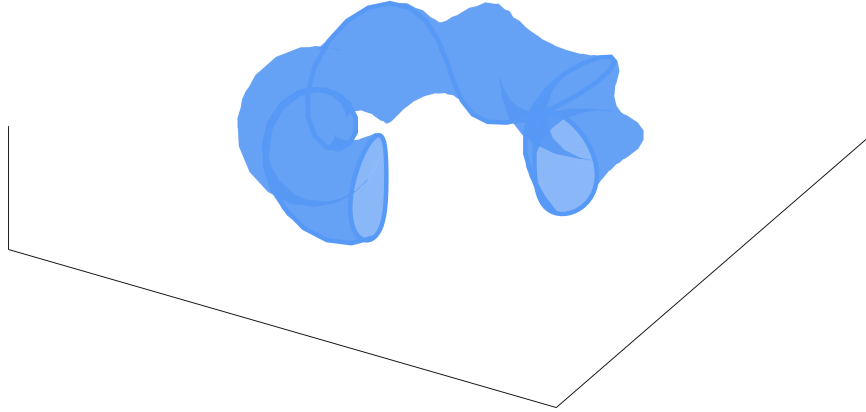


Figure 7-1: Cut-Away of Stellarator Reactor

A stellarator has a geometry similar to a tokamak, except it twists around its major axis. This eliminates the need for net current to keep the device in equilibrium.

possibly the Bremsstrahlung density limit.<sup>44</sup> This would likely require the density to be carried throughout analysis – and consequently appear as a column in Table 5.1.

## 7.2 Making a Composite Reactor – Janus

The next interesting reactor would be a composite tokamak incorporating pulsed and steady-state operation: Janus. Fundamentally, this would involve current coming from both LHCD (steady-state), as well as inductive (pulsed) sources. How the two can coexist is shown in Fig. 7-2. This scheme was actually already used in DEMO Pulsed, but the current drive was not handled self-consistently. Coupling the two current sources could reduce reliance on bootstrap current and lead to much more compact machines.

The arguments against this are mainly technical: why build two difficult auxiliary systems when one is needed – especially when they probably work against each other.

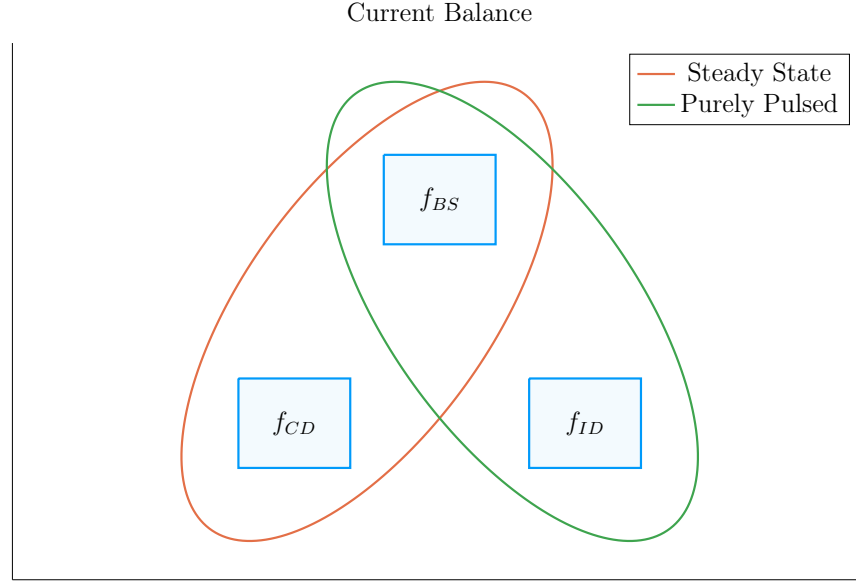


Figure 7-2: Current Balance in a Tokamak

In a tokamak, there needs to be a certain amount of current – and that current has to come from somewhere. All good reactors have an adequate bootstrap current. What provides the remaining current is what distinguishes steady state from pulsed operation.

Although rational, it may turn out that the larger current achievable with two sources may still lead to more economically competitive reactors.

## 7.3 Bridging Confinement Scalings – Daedalus

The final potential reactor – Daedalus – is designed so that it can be run in H-Mode, L-Mode, and I-Mode. Up until now, only H-Mode (high confinement) has been discussed due to its use in conventional reactor design. However, L-Mode (low) and I-Mode<sup>45</sup> (intermediate) may prove to produce more favorable scalings – in terms of cost – as more of reactor space is explored.

To design Daedalus, the first step is actually building under H-Mode. This is because L-Mode is available on every machine. The goal then is to find reactors that can also reach I-Mode – simultaneously improving that scaling law’s fit and possibly making the actual reactor more economic.

Presented below are the three confinement scaling laws, as well as the generalized formula. As should be noted, the I-Mode scaling currently lacks a true radial dependence – as it has only been found on two machines.<sup>45</sup> This is one reason Daedalus would be so valuable.\*

$$\tau_E = K_\tau H \frac{I_P^{\alpha_I} R_0^{\alpha_R} a^{\alpha_a} \kappa^{\alpha_\kappa} \bar{n}^{\alpha_n} B_0^{\alpha_B} A^{\alpha_A}}{P_{src}^{\alpha_P}} \quad (3.25)$$

$$\tau_E^H = 0.145 H \frac{I_P^{0.93} R_0^{1.39} a^{0.58} \kappa^{0.78} \bar{n}^{0.41} B_0^{0.15} A^{0.19}}{P_{src}^{0.69}} \quad (3.27)$$

$$\tau_E^L = 0.048 H \frac{I_P^{0.85} R_0^{1.2} a^{0.3} \kappa^{0.5} \bar{n}^{0.1} B_0^{0.2} A^{0.5}}{P_{src}^{0.5}} \quad (7.1)$$

$$\tau_E^I = \frac{0.014 H}{0.68^{\lambda_R} \cdot 0.22^{\lambda_a}} \cdot \frac{I_P^{0.69} R_0^{\lambda_R} a^{\lambda_a} \kappa^{0.0} \bar{n}^{0.17} B_0^{0.77} A^{0.0}}{P_{src}^{0.29}} \quad (7.2)$$

$$\lambda_R + \lambda_a = 2.2 \quad (7.3)$$

A final point to make is reemphasizing that the I-Mode scaling law – developed by the authors – is significantly underdeveloped. It is the target of ongoing research at the MIT PSFC.<sup>45</sup>

## 7.4 Addressing Model Shortcomings

Before moving on to the final conclusions, we will give a quick recap of several of the more overly simplified phenomena in this fusion systems framework. These include: approximating temperature profiles as simple parabolas, neglecting all radiation except Bremsstrahlung, and handling flux sources at too basic a level. This list is non-comprehensive, as more sophisticated analysis would also improve the physics behind: divertor heat loading, neutron wall loading, etc.

---

\*In H-Mode and L-Mode’s favor, they have been found on every machine that should see them.



### 7.4.1 Integrating Pedestal Temperature Profiles

One of the largest shortcomings of this model is not handling plasma profiles self-consistently. It instead treats them as simple parabolas. Although these parabolas work for densities and L-Mode plasma temperatures, the same cannot be said for H-Mode temperatures. This is because they have a distinct pedestal region on the outer edge of the plasma.

The usage of pedestal temperatures – discussed in Appendix D – therefore improves two aspects of the model: the fusion power and the bootstrap current. These were shown in the results to be over-calculated and underestimated, respectively. First, pedestals lower the total fusion power because they have a lower core temperature than parabolic profiles with the same average value. Conversely, the pedestal’s quick drop near the plasma’s edge would boost the bootstrap current, as it has a steep derivative there.

These improvements could easily be added to the code, because temperature was addressed to be a difficult-to-handle parameter from the beginning.

### 7.4.2 Expanding the Radiation Loss Term

The next area that would be improved by more sophisticated theory would be the radiation loss term. From before, it was pointed out that the Bremsstrahlung radiation was the dominant term within the plasma core and, therefore, provided a first-order approximation. Drawing the radiation losses closer to real world values would involve adding line radiation and synchrotron radiation. The former of which would be needed as high-Z impurities become more important.

### 7.4.3 Taking Flux Sources Seriously

The final oversimplification in the model deals with the flux sources involved in a pulsed reactor – which exist at multiple levels. First, the derivation of flux bal-

ance started with a simple transformer between a solenoid primary and a plasma secondary.

After we developed an equation for flux balance, we compared it to ones in the literature (i.e. PROCESS) to build confidence in the model. To draw this equation closer to theirs, we then added a PF coil contribution a posteriori. This implicitly ignored coupling between most of the components. Thus leading to another source of error for the model. Moreover, this formula for the PF coil contribution was much simpler than ones found in other fusion systems codes.

Even though this model may be extremely simple, it still matches more sophisticated frameworks at a much faster pace. These suggestions were just ways to account for more realistic physics.

# Chapter 8

## Concluding Reactor Discussion

The goal of this document was to fairly compare pulsed and steady-state tokamaks – using a single, comprehensive model. The main conclusion is that both modes of operation can produce economically competitive reactors, assuming some technological advancement. The advancement most supported by the results was in magnet technology, as MIT is currently exploring with high-temperature superconducting (HTS) tape. However a more fundamental result is that pulsed operation can be economically competitive and the United States should be putting a larger research effort behind it.

Although some skepticism should be allotted to these conclusions, it was shown that this simple algebraic solver was capable of matching more sophisticated frameworks with speed and ease. This model may not provide an engineer’s level of rigor for cost measurements, but does produce empirically-drawn costing trends applicable to the target physics audience. Ultimately, it serves to complement higher dimension codes when researchers want to investigate new areas of reactor space.

What the results truly show, though, is that no economic reactor can be built using existing technology – regardless of whether it runs as pulsed or steady-state. This is why every design from the literature exceeds standard values for  $H$  and  $N_G$ . Therefore, some technological advancement is needed. These may come from research

and development into:

- building stronger magnets using HTS tape
- discovering reliable regimes of enhanced confinement
- producing higher bootstrap fractions with tailored profiles
- optimizing aspect ratio and elongation geometric parameters

As mentioned, using HTS tape to nearly double achievable magnet strengths is one such advancement capable of making reactors economically viable. To best utilize this resource, though, HTS tape should appear only in the TF coils for steady-state machines and in the central solenoid for pulsed ones. This was because the optimum toroidal field strength for pulsed machines was found to be achievable with conventional low-temperature superconducting (LTS) magnets.

Further, it was shown that past the regime of magnet strengths relevant to HTS, cost curves undergo considerably diminished returns. As such, HTS technology might be the final major magnet advancement in the current H-Mode, D-T plasma paradigm.

# Appendix A

## Cataloging Model Variables

### A.1 Static Variables

Table A.1: List of Static Variables

Name	Value
is_pulsed	Is reactor pulsed or steady-state
$H$	Enhancement factor for ELMy H-mode scaling
$Q$	Physics Gain ( $P_F/P_H$ )
$\varepsilon$	Inverse aspect ratio
$\kappa_{95}$	Elongation at 95 flux surface
$\delta_{95}$	Triangularity at 95 flux surface
$\nu_n$	Density peaking factor
$\nu_T$	Temperature peaking factor
$Z_{eff}$	Effective charge
$f_D$	Dilution factor
$A$	Average mass number (in amus)
$l_i$	Internal inductance (interchangeable with $\rho_m$ )
$\rho_m$	Normalized radius of current peak (interchangeable with $l_i$ )
$N_G$	Greenwald density fraction
$\eta_T$	Thermal efficiency of the reactor
$\eta_{RF}$	Efficiency of the RF antenna
$\tau_{FT}$	Time of flattop for reactor pulse
$B_{CS}$	Strength of magnetic field in central solenoid
$(\beta_N)_{max}$	Maximum allowed normalized beta normal
$(q_*)_{max}$	Minimum allowed safety factor
$(P_W)_{max}$	Maximum allowed wall loading power per surface area

## A.2 Dynamic Variables

Table A.2: List of Dynamic Variables

Symbol	Name	Units
$I_P$	Plasma Current	MA
$\overline{T}$	Plasma Temperature	keV
$\bar{n}$	Electron Density	$10^{20} \text{ m}^{-3}$
$R_0$	Major Radius	m
$B_0$	Magnet Strength	T

## A.3 Intermediate Variables

Table A.3: List of Intermediate Variables (Noncomprehensive)

Name	Value
$C_W$	Cost-per-watt
$W_M$	Magnetic energy
$P_F$	Fusion power
$P_\Omega$	Resistive power
$P_{BR}$	Bremsstrahlung power
$P_\kappa$	Conductive heat losses
$P_W$	Wall loading
$\beta_N$	Plasma beta normal
$q_*$	Kink safety factor
$V$	Tokamak volume in cubic meters
$f_{BS}$	Bootstrap current fraction
$f_{CD}$	Current drive fraction
$f_{ID}$	Inductive current fraction
$\bar{p}$	Volume-averaged plasma pressure
$\langle \sigma v \rangle$	Bosch-Hale fusion reactivity
$R_P$	Plasma resistance
$\tau_E$	Confinement time
$a$	Tokamak minor radius
$b$	Blanket thickness
$c$	TF coil thickness
$d$	Central solenoid thickness
$R_{CS}$	Central solenoid inner radius

# Appendix B

## Simulating with Fussy.jl

Fussy.jl is a 0-D fusion systems code written using the Julia language. The reason for choosing Julia over say Matlab or Python was due to metaprogramming concerns and its tight-knit computational community, respectively. Incorporating the model used throughout this paper, the code is both quick to run and matches more sophisticated frameworks with high fidelity.

This chapter will be broken down into four steps. The first is getting a user up and running with the code. Once the user gets to this point, hopefully they will wonder how the code is structured – this is the second step. Next, we will explain the various functions callable on reactor objects – the atomic data structure for Fussy.jl. And lastly, there will be a quick tutorial.

### B.1 Getting the Code to Work

The hardest step of any codebase is getting it up and running. These instructions should get a user to a point where they are a few internet searches away from a working copy of Fussy.jl. As an aide, you can view an interactive collection of Fussy.jl Jupyter notebooks at the following website:

[www.fusion.codes](http://www.fusion.codes)

Although `fusion.codes` is a nice tool for viewing this document's results, it is a little slow for producing new data – and it also lacks a method for storing it. Therefore, an advanced user should first download a copy of Julia from:

[julialang.org/downloads](https://julialang.org/downloads)

Currently the `Fussy.jl` codebase is written using `v0.6`, but should be `v1.0` compatible by 2020. Using Julia nomenclature, `Fussy.jl` is a Julia package. It can be cloned using Julia conventions from the following Github repository:

<https://github.com/djseagal/Fussy.jl.git>

Once the `Fussy.jl` package has been cloned into your Julia package library, you should be able to access it through the Julia REPL or a Jupyter notebook. You can now reproduce every plot in this text. A quick test to see if your code works is:

```
using Fussy
cur_reactor = Reactor(15)
@assert cur_reactor.T_bar == 15
println("It works!")
```

If the code works, you should get a "It works!" message as output.

## B.2 Sorting out the Codebase

Assuming the user got to this section, the code works and now you want to know what you can do with it. The place to start is in the `src` folder, again viewable at:

[git.io/tokamak](https://git.io/tokamak)

Within the `src` folder are several subfolders as well as a few files (e.g. `Fussy.jl` and `defaults.jl`). In an attempt to not bore the reader, we will be painting with thick brushstrokes. Further, the `methods` subfolder will be the topic of the next section – as most involve calls on a reactor object.



### **B.2.1 Typing out Structures**

The place to start in any modeling framework is its data structures. These type definitions allow the building of nested hierarchies of constructed objects. The most atomic of these is the Reactor struct, but several other ones allow for solving broader scoped questions (i.e. Scans, Sensitivities, and Samplings.)

#### **The Reactor Structure**

Reactors are the most atomic data structure in this fusion systems model. They store all the fields needed to represent a reactor as it exists in reactor space. This obviously includes its temperature, current, and radius, but also includes derived quantities, such as the cost-per-watt and bootstrap fraction. They can be initialized, solved, updated, and honed. Most other data structures are just wrappers to hold these reactors – they are described next.

#### **The Scan Structure**

A Scan object is a collection of reactors made from scanning a list of temperatures. For example, a scan of five temperatures from 5 keV to 25 keV would result in several arrays of five reactors. Most often, one of these lists would correspond to beta reactors, one to kink reactors, and one to wall loading reactors. There may then be fewer than five reactors in a list if some of the reactors are invalid or fundamentally unsolvable. This is the data structure that produces the various comparison plots in the results.

#### **The Sensitivity Structure**

Sensitivity studies are how computationalists test the effect of changing a variable over multiple values – i.e. do a 20% sensitivity around the H factor. Like Scans, Sensitivities store various lists of reactors, each corresponding to an interesting data point. These include limit reactors where the beta limit and kink limit are just

satisfied or when the beta limit and wall loading are just satisfied. Additionally, they include the minimum capital cost reactors and the minimum cost-per-watt ones.

## The Sampling Structure

The Sampling struct was created to do simple Monte Carlo runs over a reactor's static values. While sensitivities only allow one variable to change at a time, samplings randomly assign a list of variables to some neighborhood of possible values. These are how the scatter plots are made. Succinctly, where sensitivity studies show local changes to variables, Monte Carlo samplings show global trends in reactor design.

## The Equation Structure

In order to store the various equations from Table 5.1 is the Equation Struct. It stores the  $\gamma$  exponents for:  $R_0$ ,  $B_0$ , and  $I_P$ . – as well as the function representing  $G(\bar{T})$ . Repeated these are the unknowns in:

$$R_0^{\gamma_R} \cdot B_0^{\gamma_B} \cdot I_P^{\gamma_I} = G(\bar{T}) \quad (5.3)$$

Concretely, there are 16 objects that use this struct – one for each equation (e.g. for fusion power, the beta limit, and temperature assignment).

## The Equation Set Structure

The step up from the Equation struct are the Equation Sets. These collections of three equations allow  $R_0$ ,  $B_0$ , and maybe  $I_P$  to be substituted out of the current balance root-solving equation. This is where Eqs. (5.4) to (5.10) come into play.

### B.2.2 Referencing Input Decks and Solutions

With more than twenty static variables in the model, the range of tokamak reactors is basically infinite. To help users build a net of designs to explore reactor space are seven input decks. These are the ones given in the results: ARC, ACT I/II, DEMO Steady/Pulsed, Proteus and Charybdis. Coupled with the non-prototype reactors are solution reactors that store various quantities from the original papers (e.g.  $P_F$ ,  $f_{BS}$ ,  $R_0$ ). These are how the comparison tables were constructed.

### B.2.3 Acknowledging Utility Functions

For the uninitiated, utility functions are grab bag functions that do not really belong in a codebase – but do anyway. This sentiment does not mean they are worthless, just not fusion related at all. In Fussy.jl, the most notable are a normalized integral calculator, a filter that includes numeric tolerances, and a robust root solver.

Although since incorporated into the official Roots.jl package, `find_roots` allows finding an arbitrary number of roots within a bounded range. This was needed because many roots can be found at various levels of the reactor solving problem – i.e. for  $I_P$ ,  $\bar{T}$ ,  $\eta_{CD}$ , etc.

### B.2.4 Mentioning Base Level Files

In addition to subdirectories within the `src` folder are three files: Fussy.jl, abstracts.jl, and defaults.jl. Fussy.jl is the package’s main file that actually stores the Fussy module. While, abstracts.jl stores various abstract structures that help clean up other files.

Finally, defaults.jl stores various default values that are important to the codebase. For example, this is where the various scaling law exponents are stored. It is also where the bounding values for the different root solving problems live. These include minimum and maximum values for:  $I_P$ ,  $\bar{T}$ ,  $\eta_{CD}$ .

Now that a majority of the files have been discussed, we can turn to the reactor methods. These constitute most of the interesting functionality within the codebase.

## B.3 Delving into Reactor Methods

The reactor is the most atomic data structure in this model. It therefore makes sense that it has many instance methods. These include all the coefficients, fluxes, powers, etc. It also includes methods that solve a reactor, perform a match on some field's value, or converge  $\eta_{CD}$  to self-consistency. The various subdirectories within the `src/methods/reactors` folder will now be discussed.

### Calculations

The calculation subdirectory of reactor methods are used to set various important values in the solver. For dynamic variables, these include:  $\bar{n}$ ,  $R_0$ ,  $B_0$ , and  $I_P$ . This folder also includes the calculation of the Bosch-Hale reactivity and the Ehst-Karney current drive efficiency.

### Coefficients and Composites

The coefficients and composites directories correspond to the model's static and dynamic coefficients, respectively. For clarity, static coefficients, including  $K_n$  and  $K_{CD}$ , were labeled with a K. Whereas, dynamic coefficients then started with G's – i.e.  $G_{PB}$  and  $G_V$ .

### Fluxes and Powers

Within flux balance and power balance were around a dozen terms or sub-terms. Although not directly used in the conservation equations, sub-terms are used to compare the model to ones from the literature. For clarity, fluxes include:  $\Phi_{CS}$ ,  $\Phi_{PF}$ ,  $\Phi_{RU}$ ,  $\Phi_{FT}$ ,  $\Phi_{res}$ , and  $\Phi_{ind}$ . The powers, then, include:  $P_F$ ,  $P_{BR}$ ,  $P_\kappa$ ,  $P_{src}$ ,  $P_W$ , etc.

## Profiles

The next collection of reactor methods are the various profiles. Most obviously, these include radial plasma profiles for density, temperature, and current density. However, this folder also includes the magnetic field strength as a function of radius – as was used within current drive efficiency calculations.

## Geometries

Additionally, there are many geometric relations. These include the various tokamak thicknesses: a, b, c, d – as well as the radius and height of the central solenoid. This group also includes the volume, perimeter, surface area, and cross-sectional area. It also includes the many subscripted fields. For example, the elongation (i.e.  $\kappa_{95}$ ) includes the following alternative definitions:  $\kappa_X$ ,  $\kappa_P$ , and  $\kappa_T$ .

## Formulas

The final set of reactor methods are formulas that do not really fit anywhere else. If a method is not related to geometry, power, calculations, etc, it ends up here. For example, this group includes:  $\beta_N$ ,  $f_{BS}$ ,  $C_W$ , and  $\tau_E$ . Total, there are around 25 formulas – as of the writing of this document.

## B.4 Demonstrating Code Usage

Now that the Fussy.jl package has been described in detail, the final step is showing a simple example that can recreate a figure from the results chapter. This will closely match the Jupyter notebook available at:

[www.git.io/fussy\\_sensitivity](http://www.git.io/fussy_sensitivity)

Our goal will be to make a cost curve for the ARC reactor as a function of H – a so called sensitivity study plot.

### B.4.1 Initializing the Workspace

The first step for any Fussy.jl Jupyter notebook is loading the required packages – i.e. the Fussy.jl and Plots.jl packages. This can be done using the following commands:

```
addprocs(6)

@everywhere using Fussy

using Plots
```

The Plots.jl package may take a minute to load – similar to Matlab’s initial boot time. If the kernel raises an error about Plots.jl not being installed, use the following lines:

```
import Pkg

Pkg.add("Plots")
```

### B.4.2 Running a Study

Now that the necessary packages have been loaded, we can move on to actually running the sensitivity study. We will split this command into two steps to make it more explicit.

The first step will be making several variables that store: boolean flags, numbers, and symbols – which are like strings, but prefaced with a colon (:) instead of surrounded by double quotes (").

```
cur_param = :H
cur_deck = :arc
is_pulsed = false
is_consistent = true
cur_sensitivity = 1.0
cur_num_points = 41
```

---

\*The `addprocs` and `@everywhere` commands are to parallelize the code. This is because `addprocs(6)` activates 6 worker processes and `@everywhere Fussy.jl` adds Fussy.jl to the main kernel and worker processes.

These six variables almost completely describe a sensitivity study. The first two say we are using the ARC reactor deck and running a sensitivity over the H-factor parameter. Next, the two boolean values refer to the reactor (1) being treated as pulsed or steady-state and (2) whether to handle  $\eta_{CD}$  self-consistently.\* Ergo, what these two flags do is make sure ARC is being handled as a steady-state reactor with a self-consistent  $\eta_{CD}$ . The last two variables are then ways to change the sensitivity of the study (with 1.0  $\rightarrow$  100%) and the number of reactors it will produce (i.e. 41).

Now all six of these variables can be piped into a call to the `Study` struct to start running the sensitivity study:

```
cur_study = Study(
    cur_param,
    deck = cur_deck,
    is_pulsed = is_pulsed,
    is_consistent = is_consistent,
    sensitivity = cur_sensitivity,
    num_points = cur_num_points
)
```

Note here that the equal signs inside the parentheses are called keyword arguments, which are common to most modern programming languages. After executing the command, the code will need to run for a few minutes.

### B.4.3 Extracting Results

At this point, a user should have a completed sensitivity study they wish to plot. To make the plot useful, the study data structure first has to be unpacked and its contents cleaned. This is the goal of this subsection.

First and foremost, a study has four families of reactors within it: beta-wall (i.e. "wall"), beta-kink (i.e. "kink"), minimum capital cost (i.e. "W\_M"), and minimum

---

\*Note that, currently, a pulsed reactor cannot be self-consistent in  $\eta_{CD}$  – it therefore causes an error.

cost-per-watt (i.e. "cost"). Therefore, we will extract these reactor lists into a new dictionary data structure:

```
cur_dict = Dict()

cur_dict["Beta-Wall"] = cur_study.wall_reactors
cur_dict["Beta-Kink"] = cur_study.kink_reactors

cur_dict["Min Cost-per-Watt"] = cur_study.cost_reactors
cur_dict["Min Capital Cost"] = cur_study.W_M_reactors
```

Next, we will want to filter out all the invalid reactors that constitute non-physically realizable ones. These would likely be reactors that could fit in your hand or take up a whole city block.

```
for (cur_key, cur_value) in cur_dict
    cur_dict[cur_key] = filter(
        cur_reactor -> cur_reactor.is_valid,
        deepcopy(cur_value)
    )
end
```

#### B.4.4 Plotting Curves

Our goal is now to turn our unpacked, clean reactor lists into plots – i.e. measuring costs-per-watt as a function of  $H$ . For simplicity, this will lack a lot of the features shown in the Jupyter notebook from the beginning of the section. Additionally, we will be doing it in an iterative process made possible by the Plots.jl framework.

The first step is simply making a plot object

```
cur_plot = plot()
```

After execution, this should produce the blank 2-D plot shown in Fig. B-1.



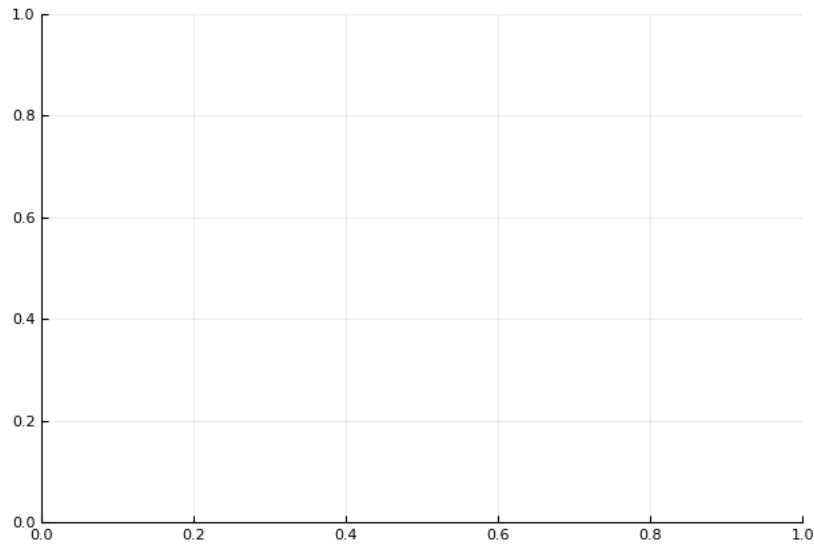


Figure B-1: A Blank Plot

A simple 2-D plot with no labels or data.

Next we will add a simple title and labels for the axes:

```
title!("ARC")

xlabel!("H")
ylabel!("Cost")
```

The exclamation marks ensure this title and the labels are added to the `cur_plot`. Upon execution, you should see a plot with this information (Fig. B-2).

Now we will loop over the dictionary of reactors and add them one at a time.

```
for (cur_key, cur_value) in cur_dict
    cur_x = map(cur_reactor -> cur_reactor.H, cur_value)
    cur_y = map(cur_reactor -> cur_reactor.cost, cur_value)
    plot!(cur_x, cur_y, label=cur_key)
end

plot!()
```

This results in the not very useful plot shown in Fig. B-3. Note that each label is exactly the key assigned to it in `cur_dict`.

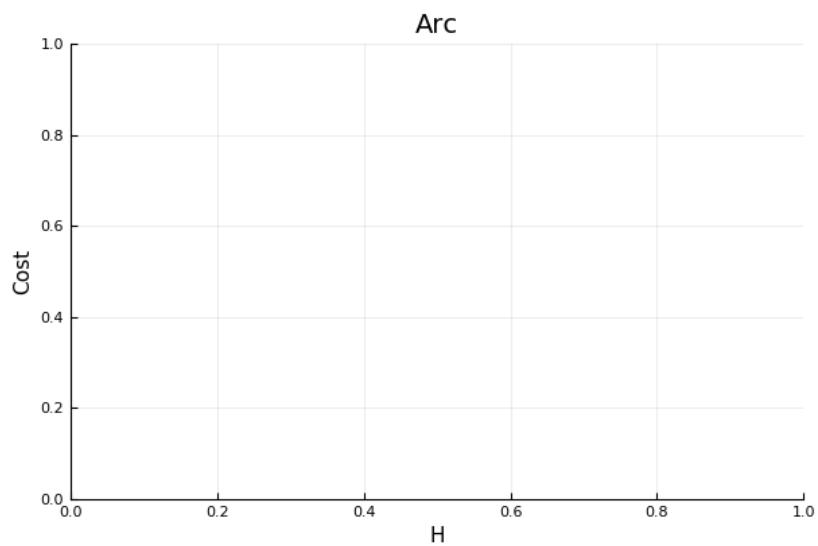


Figure B-2: An Empty Plot

A simple 2-D plot with labels, but no data.

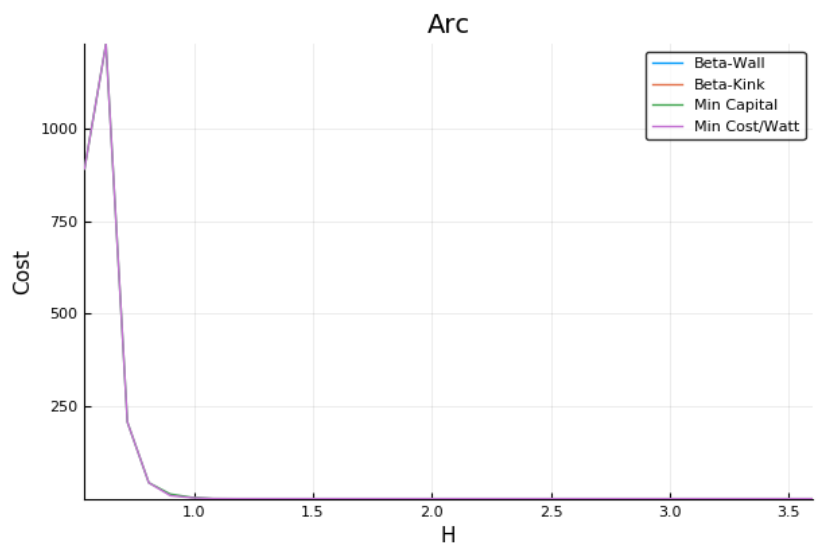


Figure B-3: An Unscaled Plot

A simple 2-D plot with Bad Limits.

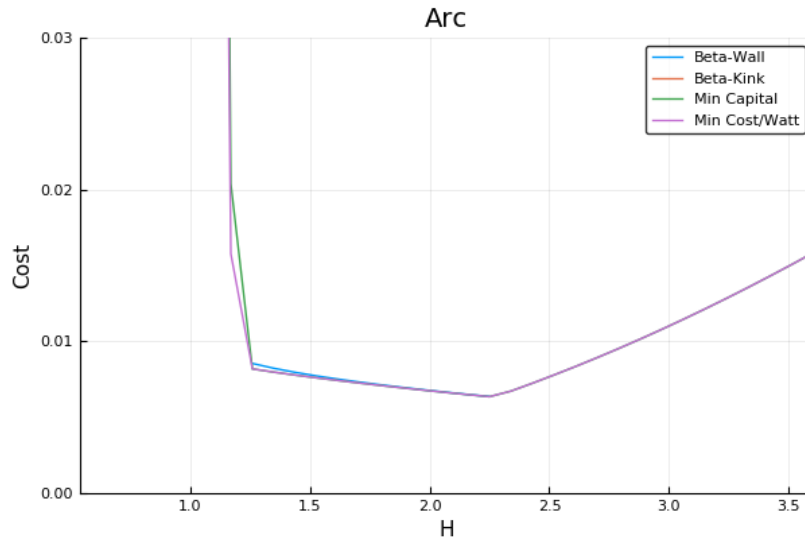


Figure B-4: A Scaled Plot

An example plot showing cost as a function of the H factor.

The final step is adding proper limits to make what is going on obvious to the reader:

```
ylims!(0, 0.03)
```

The addition of this can be seen in Fig. B-4.

This completes the example. At this point, you should now be able to use every feature of Fussy.jl. Good luck!



# Appendix C

## Discussing Fusion Power

In a tokamak reactor, the main source of output power is fusion. Therefore, this chapter goes over a quick background of fusion power and describes a method for how to calculate the reactivity term that appears inside it. The particular method used for this reactivity approximation was done by Bosch and Hale in 1992.<sup>46</sup>

### C.1 Theoretical Background

The natural place to start when introducing fusion energy is the binding energy per nucleon curve shown in Fig. C-1. As can be seen, this function reaches a maximum value around the element Iron ( $A=56$ ). What this means at a basic level is: elements lighter than iron can *fuse* into a heavier one (i.e. hydrogens into helium), whereas heavier elements can *fission* into lighter ones (e.g. uranium into krypton and barium). This is what differentiates fission (uranium-fueled) reactors from fusion (hydrogen-fueled) ones. For fusion reactors, the most common reaction in a first-generation tokamak will be:

$${}^2\text{H} + {}^3\text{H} \rightarrow {}^4\text{He} + {}^1\text{n} + E_F \tag{C.1}$$

$$E_F = 17.6 \text{ MeV} \tag{C.2}$$

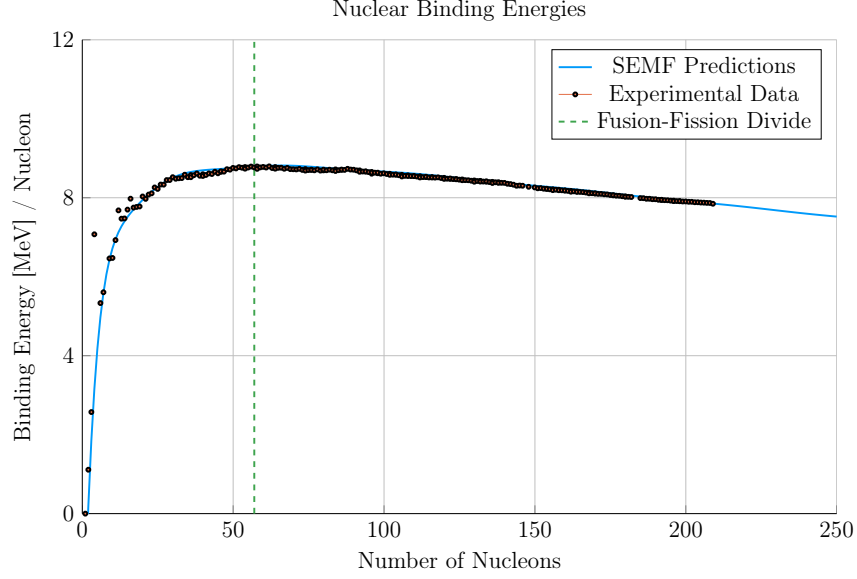


Figure C-1: Comparing Nuclear Fusion and Fission

The binding energy per nucleon is what differentiates nuclear fusion from fission. Nuclei heavier than Iron fission (e.g. Uranium), while light ones – such as Hydrogen – fuse.

What this reaction (shown in Fig. C-2) describes is two isotopes of hydrogen – i.e. deuterium and tritium – fusing into a heavier element, helium, while simultaneously ejecting a neutron. The entire energy of the fusion reaction ( $E_F$ ) is then divvied up 80-20 between the neutron and helium, respectively. Quantitatively, the helium (often referred to as an alpha particle) receives 3.5 MeV.

$$P_n = 0.8 \cdot P_F \quad (\text{C.3})$$

$$P_\alpha = 0.2 \cdot P_F \quad (\text{C.4})$$

The final point to make is the main difference between the two fusion products: helium (i.e. the alpha particle) and the neutron. First, neutrons lack a charge – they are neutral. This means they cannot be confined with magnetic fields. As such, they simply move in straight lines until they collide with other particles. As the structure

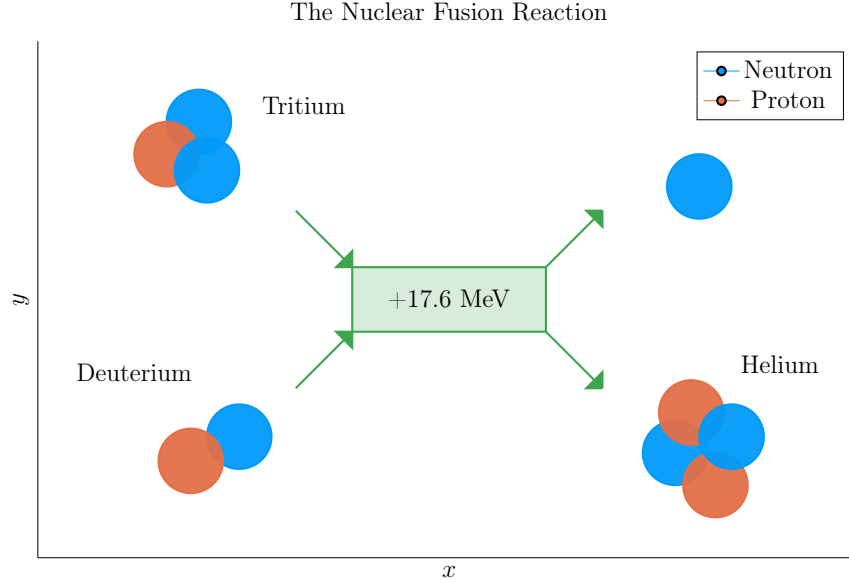


Figure C-2: The D-T Fusion Reaction

In a first generation tokamak reactor, the main source of energy will come from two hydrogen isotopes fusing into a helium particle – and ejecting a 14.1 MeV neutron.

of a tokamak is mainly metal, the neutron is much more likely to collide there than the gaseous plasma, which is orders of magnitude less dense. Conversely, alpha particles are charged – when stripped of their electrons – and can therefore be kept within the plasma using magnets. What this means practically is that of the 17.6 MeV that comes from every fusion reaction, only 3.5 MeV remains inside the plasma (within the helium particle species).

## C.2 Bosch-Hale Reactivity

The formula for fusion power used in this model makes use of a reactivity term –  $(\sigma v)$ :<sup>5</sup>

$$P_F = \int E_F n_D n_T \langle \sigma v \rangle d\mathbf{r} \quad (\text{C.5})$$

Summarizing the work of Section 2.2.3, this fusion power volume integral can be reduced to a 0-D form – assuming the geometry prescribed by this model:

$$P_F = K_F \cdot (\bar{n}^2 R_0^3) \cdot (\sigma v) \quad [MW] \quad (C.6)$$

$$(\sigma v) = 10^{21} (1 + \nu_n)^2 \int_0^1 (1 - \rho^2)^{2\nu_n} \langle \sigma v \rangle \rho d\rho \quad (C.7)$$

$$K_F = 278.3 (f_D^2 \varepsilon^2 \kappa g) \quad (C.8)$$

This reactivity term (or volumetric fusion reaction rate) can then be approximated by the Bosch-Hale parameterization, with coefficients given in Table C.1.<sup>46,47</sup>

$$\langle \sigma v \rangle = C_1 \cdot \theta \cdot \exp(-3\xi) \cdot \sqrt{\frac{\xi}{m_\mu c^2 T^3}} \quad [\text{m}^3/\text{s}] \quad (C.9)$$

$$\theta = T \cdot \left( 1 - \frac{T(C_2 + T(C_4 + TC_6))}{1 + T(C_3 + T(C_5 + TC_7))} \right)^{-1} \quad (C.10)$$

$$\xi = \left( \frac{B_G^2}{4\theta} \right)^{1/3} \quad (C.11)$$

For D-T (Deuterium-Tritium) fuel within a standard fusion temperature regime (i.e.  $T \in [10, 20]$  keV), this can be simplified to:<sup>47</sup>

$$\langle \sigma v \rangle_{\text{DT}} = 1.1 \times 10^{-24} \cdot T^2 \quad [\text{m}^3/\text{s}] \quad (C.12)$$

In our model, each appearance of T is set to the radial profile defined earlier – as it appears inside an integral.

Example tabulations for this reactivity are given in Table C.2.<sup>46–48</sup>



Table C.1: Bosch-Hale Parametrization Coefficients

	${}^2\text{H}(\text{d,n}){}^3\text{He}$	${}^2\text{H}(\text{d,p}){}^3\text{H}$	${}^3\text{H}(\text{d,n}){}^4\text{He}$	${}^3\text{He}(\text{d,p}){}^4\text{He}$
$B_G$ [keV $^{1/2}$ ]	31.3970	31.3970	34.3827	68.7508
$m_\mu c^2$ [keV]	937 814	937 814	1 124 656	1 124 572
$C_1$	$5.43360 \times 10^{-12}$	$5.65718 \times 10^{-12}$	$1.17302 \times 10^{-9}$	$5.51036 \times 10^{-10}$
$C_2$	$5.85778 \times 10^{-3}$	$3.41267 \times 10^{-3}$	$1.51361 \times 10^{-2}$	$6.41918 \times 10^{-3}$
$C_3$	$7.68222 \times 10^{-3}$	$1.99167 \times 10^{-3}$	$7.51886 \times 10^{-2}$	$-2.02896 \times 10^{-3}$
$C_4$	0.0	0.0	$4.60643 \times 10^{-3}$	$-1.91080 \times 10^{-5}$
$C_5$	$-2.96400 \times 10^{-6}$	$1.05060 \times 10^{-5}$	$1.35000 \times 10^{-2}$	$1.35776 \times 10^{-4}$
$C_6$	0.0	0.0	$-1.06750 \times 10^{-4}$	0.0
$C_7$	0.0	0.0	$1.36600 \times 10^{-5}$	0.0
Valid range (keV)	$0.2 < T_i < 100$	$0.2 < T_i < 100$	$0.2 < T_i < 100$	$0.5 < T_i < 190$

Table C.2: Tabulated Bosch-Hale Reactivities

T (keV)	${}^2\text{H}(\text{d,n}){}^3\text{He}$	${}^2\text{H}(\text{d,p}){}^3\text{H}$	${}^3\text{H}(\text{d,n}){}^4\text{He}$	${}^3\text{He}(\text{d,p}){}^4\text{He}$
1.0	$9.933 \times 10^{-29}$	$1.017 \times 10^{-28}$	$6.857 \times 10^{-27}$	$3.057 \times 10^{-32}$
1.5	$8.284 \times 10^{-28}$	$8.431 \times 10^{-28}$	$6.923 \times 10^{-26}$	$1.317 \times 10^{-30}$
2.0	$3.110 \times 10^{-27}$	$3.150 \times 10^{-27}$	$2.977 \times 10^{-25}$	$1.399 \times 10^{-29}$
3.0	$1.602 \times 10^{-26}$	$1.608 \times 10^{-26}$	$1.867 \times 10^{-24}$	$2.676 \times 10^{-28}$
4.0	$4.447 \times 10^{-26}$	$4.428 \times 10^{-26}$	$5.974 \times 10^{-24}$	$1.710 \times 10^{-27}$
5.0	$9.128 \times 10^{-26}$	$9.024 \times 10^{-26}$	$1.366 \times 10^{-23}$	$6.377 \times 10^{-27}$
8.0	$3.457 \times 10^{-25}$	$3.354 \times 10^{-25}$	$6.222 \times 10^{-23}$	$7.504 \times 10^{-26}$
10.0	$6.023 \times 10^{-25}$	$5.781 \times 10^{-25}$	$1.136 \times 10^{-22}$	$2.126 \times 10^{-25}$
12.0	$9.175 \times 10^{-25}$	$8.723 \times 10^{-25}$	$1.747 \times 10^{-22}$	$4.715 \times 10^{-25}$
15.0	$1.481 \times 10^{-24}$	$1.390 \times 10^{-24}$	$2.740 \times 10^{-22}$	$1.175 \times 10^{-24}$
20.0	$2.603 \times 10^{-24}$	$2.399 \times 10^{-24}$	$4.330 \times 10^{-22}$	$3.482 \times 10^{-24}$



# Appendix D

## Selecting Plasma Profiles

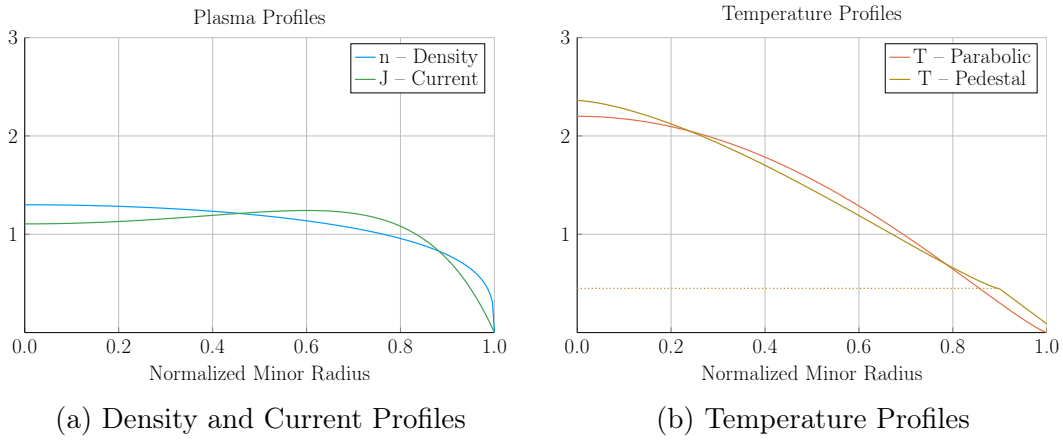


Figure D-1: Radial Plasma Profiles

The three most fundamental properties of a fusion plasma are its temperature, density, and current. These profiles allow the model to reduce from three dimensions to half of one.

### D.1 Density — $n$

The Density is important to us. We use it in the Greenwald density limit, so it should be clean in both line-averaged and volume-averaged forms. Because of its flat profile,

a parabola is a good approximation for H-mode pulses:

$$n(\rho) = \bar{n} \cdot (1 + \nu_n) \cdot (1 - \rho^2)^{\nu_n} \quad (\text{D.1})$$

The line average density is related to  $\bar{n}$  through:

$$\hat{n} = \bar{n} \cdot \left( \frac{\pi^{1/2}}{2} \right) \cdot \frac{\Gamma(\nu_n + 2)}{\Gamma(\nu_n + 3/2)} \quad (\text{D.2})$$

The convenience of this function comes from how the volumetric average comes out.

To relate this to the volume integral, we use:

$$\bar{x} = \frac{1}{V} \int x(\rho) dV \quad (\text{D.3})$$

For a normalized radial profile that does not depend on angle,

$$V = \int_0^1 \rho d\rho = 1/2 \quad (\text{D.4})$$

Then, when  $x = n$ ,

$$\bar{n} = 2 \int_0^1 n(\rho) \rho d\rho = \bar{n} \quad (\text{D.5})$$

Additionally, the Greenwald Density limit that we will use throughout,

$$\hat{n} = N_G \cdot \left( \frac{I_M}{\pi a^2} \right) \quad (\text{D.6})$$

can now be written in the following form:

$$\bar{n} = K_n \cdot \left( \frac{I_M}{R_0^2} \right) \quad (\text{D.7})$$

$$K_n = \frac{2 N_G}{\varepsilon^2 \pi^{3/2}} \cdot \left( \frac{\Gamma(\nu_n + 3/2)}{\Gamma(\nu_n + 2)} \right) \quad (\text{D.8})$$

## D.2 Temperature – $T$

The Temperature is the swept variable in our model framework. Therefore, it's the one we can allow people to be the most cavalier with. Additionally, as temperature profiles are highly peaked, their pedestal region is sometimes wrongfully neglected with a parabola.

$$T(\rho) = \bar{T} \cdot (1 + \nu_T) \cdot (1 - \rho^2)^{\nu_T} \quad (\text{D.9})$$

Therefore, our model sometimes treats the system as if it had a pedestal region. This is mainly for the bootstrap current and fusion power, which were previously known to misalign and overshoot, respectively.

$$T(\rho) = \begin{cases} T_{para} , & x \in [0, \rho_{ped}] \\ T_{line} , & x \in (\rho_{ped}, 1] \end{cases} \quad (\text{D.10})$$

Where the piecewise functions are given by,

$$T_{para} = T_{ped} + (T_0 - T_{ped}) \cdot \left( 1 - \left( \frac{\rho}{\rho_{ped}} \right)^{\lambda_T} \right)^{\nu_T} \quad (\text{D.11})$$

$$T_{line} = T_{sep} + (T_{ped} - T_{sep}) \cdot \left( \frac{1 - \rho}{1 - \rho_{ped}} \right) \quad (\text{D.12})$$

This temperature profile is related to the volume-averaged temperature through,

$$\bar{T} \cdot V = \int_0^{\rho_{ped}} T_{para}(\rho) \rho d\rho + \int_{\rho_{ped}}^1 T_{line}(\rho) \rho d\rho \quad (\text{D.13})$$

Starting with the second integral,

$$\int_{\rho_{ped}}^1 T_{line}(\rho) \rho d\rho = \frac{1}{3} \cdot (1 - \rho_{ped}) \cdot ((T_{sep} + T_{ped}/2) + \rho_{ped} \cdot (T_{ped} + T_{sep}/2)) \quad (\text{D.14})$$

The first integral can be handled by breaking it into to,

$$\int_0^{\rho_{ped}} T_{para}(\rho) \rho d\rho = T_{ped} \cdot \int_0^{\rho_{ped}} \rho d\rho + (T_0 - T_{ped}) \cdot \int_0^{\rho_{ped}} \left(1 - \left(\frac{\rho}{\rho_{ped}}\right)^{\lambda_T}\right)^{\nu_T} \cdot \rho d\rho \quad (D.15)$$

The first sub-integral is then,

$$T_{ped} \cdot \int_0^{\rho_{ped}} \rho d\rho = \frac{T_{ped} \rho_{ped}^2}{2} \quad (D.16)$$

Utilizing the following transformation,

$$u = \frac{\rho}{\rho_{ped}} \quad (D.17)$$

$$d\rho = \rho_{ped} du \quad (D.18)$$

$$u(\rho = \rho_{ped}) = 1 \quad (D.19)$$

The second sub-integral becomes (assuming independence from  $T_0$  and  $T_{ped}$ ),

$$(T_0 - T_{ped}) \cdot \rho_{ped}^2 \cdot \int_0^1 (1 - u^{\lambda_T})^{\nu_T} \cdot u du \quad (D.20)$$

Where:

$$\int_0^1 (1 - u^{\lambda_T})^{\nu_T} \cdot u du = \frac{\Gamma(1 + \nu_T) \Gamma\left(\frac{2}{\lambda_T}\right)}{\lambda_T \cdot \Gamma\left(1 + \nu_T + \frac{2}{\lambda_T}\right)} \quad (D.21)$$

We are now in a position to solve for  $T_0$  in terms of  $\bar{T}$ :

$$T_0 = T_{ped} + \frac{\bar{T} - K_{TU}}{K_{TD}} \quad (D.22)$$

$$K_{TU} = T_{ped} \rho_{ped}^2 + \frac{(1 - \rho_{ped})}{3} \cdot ((2T_{sep} + T_{ped}) + \rho_{ped} \cdot (2T_{ped} + T_{sep})) \quad (D.23)$$

$$K_{TD} = \rho_{ped}^2 \cdot \left( \frac{2}{\lambda_T} \right) \cdot \frac{\Gamma(1 + \nu_T) \Gamma\left(\frac{2}{\lambda_T}\right)}{\Gamma\left(1 + \nu_T + \frac{2}{\lambda_T}\right)} \quad (D.24)$$

Which although not pretty, can be plugged into the original equation.

### D.3 Pressure – $p$

The first point to make is that we are not using the same temperature profile for the pressure as for the temperature. This is because it would lead to hypergeometric functions that are not worth the headache.

As most of the pressure is at the center, we use simple parabolic profile. This leads to:

$$\bar{p} = 0.1581 (1 + f_D) \frac{(1 + \nu_n)(1 + \nu_T)}{1 + \nu_n + \nu_T} \bar{n} \bar{T} \quad [atm] \quad (D.25)$$

### D.4 Bootstrap Current – $f_{BS}$

We start with,

$$f_{BS} = \frac{I_{BS}}{I_P} = \frac{2\pi a^2 \kappa}{I_P} \int_0^1 J_B \rho d\rho \quad (D.26)$$

Expanding the previous equation using the following relations,

$$J_B = -4.85 \cdot R_0 \varepsilon^{1/2} \cdot \left( \frac{\rho^{1/2} n T}{d\psi/d\rho} \right) \cdot \left( \frac{dn/d\rho}{n} + 0.54 \cdot \frac{dT/d\rho}{T} \right) \quad (D.27)$$

$$\frac{d\psi}{d\rho} = \frac{\mu_0 R_0 I_P}{\pi} \cdot \left( \frac{\kappa}{1 + \kappa^2} \right) \cdot b_p(\rho) \quad (D.28)$$

Yields:

$$f_{BS} = -K_{BS} \int_0^1 (1 - \rho^2)^{\nu_n} \cdot \left( \frac{\rho^{3/2}}{b_p(\rho)} \right) \cdot \left( \frac{T}{n} \cdot \frac{dn}{d\rho} + 0.54 \cdot \frac{dT}{d\rho} \right) d\rho \quad (D.29)$$

$$K_{BS} = K_n \cdot \left( \frac{2\pi^2 \cdot 4.85 \cdot \varepsilon^{5/2}}{\mu_0} \right) \cdot (1 + \nu_n) \cdot (1 + \kappa^2) \quad (\text{D.30})$$

Here,  $b_p$  comes from:

$$b_p(\rho) = \frac{-e^{\gamma\rho^2}(\gamma\rho^2 - 1 - \gamma) - 1 - \gamma}{\rho(e^\gamma - 1 - \gamma)} \quad (\text{D.31})$$

And the value of  $\gamma$  comes from the the normalized internal inductance:

$$l_i = \frac{4\kappa}{1 + \kappa^2} \int_0^1 b_p^2 \rho d\rho \quad (\text{D.32})$$

With our profiles,

$$-\left(\frac{T}{n} \cdot \frac{dn}{d\rho}\right) = 2\nu_n \cdot \left(\frac{T \cdot \rho}{1 - \rho^2}\right) \quad (\text{D.33})$$

While treating temperature differently results in,

$$-\left(\frac{dT}{d\rho}\right)_{para} = \left(\frac{T_0 - T_{ped}}{\rho_{ped}^{\lambda_T}}\right) \cdot (\nu_T \lambda_T) \cdot \rho^{\lambda_T-1} \cdot \left(1 - \left(\frac{\rho}{\rho_{ped}}\right)^{\lambda_T}\right)^{\nu_T-1} \quad (\text{D.34})$$

$$-\left(\frac{dT}{d\rho}\right)_{line} = \left(\frac{T_{ped} - T_{sep}}{1 - \rho_{ped}}\right) \quad (\text{D.35})$$

Where we will be using the new symbol definition,

$$\partial T = -\left(\frac{dT}{d\rho}\right) \quad (\text{D.36})$$

Which ultimately allows us to write,

$$f_{BS} = K_{BS} \int_0^1 H_{BS} d\rho \quad (\text{D.37})$$

$$H_{BS} = (1 - \rho^2)^{\nu_n-1} \cdot \left(\frac{\rho^{3/2}}{b_p(\rho)}\right) \cdot \left(2\nu_n \cdot \rho \cdot T + 0.54 \cdot (1 - \rho^2) \cdot \partial T\right) \quad (\text{D.38})$$



Where the values of  $T$  are determined through,

$$T_{para} = T_{ped} + (T_0 - T_{ped}) \cdot \left( 1 - \left( \frac{\rho}{\rho_{ped}} \right)^{\lambda_T} \right)^{\nu_T} \quad (D.39)$$

$$T_{line} = T_{sep} + (T_{ped} - T_{sep}) \cdot \left( \frac{1 - \rho}{1 - \rho_{ped}} \right) \quad (D.40)$$

And the values of  $\partial T$  are:

$$\partial T_{para} = \left( \frac{T_0 - T_{ped}}{\rho_{ped}^{\lambda_T}} \right) \cdot (\nu_T \lambda_T) \cdot \rho^{\lambda_T - 1} \cdot \left( 1 - \left( \frac{\rho}{\rho_{ped}} \right)^{\lambda_T} \right)^{\nu_T - 1} \quad (D.41)$$

$$\partial T_{line} = \left( \frac{T_{ped} - T_{sep}}{1 - \rho_{ped}} \right) \quad (D.42)$$

## D.5 Volume Averaged Powers

The first thing to consider in a fusion reactor is power balance. It is what separates a net power producing reactor from a power-consuming research device.

$$P_\alpha + P_H = P_\kappa + P_B \quad (D.43)$$

$$P_\alpha = \frac{P_F}{5} \quad (D.44)$$

$$P_H = \frac{P_F}{Q} \quad (D.45)$$

$$P_\kappa = \frac{3}{2 \tau_E} \int p \, d\mathbf{r} \quad [3D] \quad (D.46)$$

$$P_B = 5.35e3 \, Z_{eff} \int n_{\bar{n}}^2 \sqrt{T} \, d\mathbf{r} \quad [3D] \quad (D.47)$$

As mentioned before,  $P_F$  is handled by  $(\sigma v)$  and therefore the lefthand-side uses the pedestal temperature profiles. However, for the same reasons as discussed earlier, the righthand-side ( $P_\kappa$  and  $P_B$ ) need to use the parabolic temperature profiles.

Using the parabolic profiles (for  $n$  and  $T$ ) gives for the Bremsstrahlung radiation,

$$P_B = K_B \cdot \left( R_0^3 \bar{n}^2 \sqrt{\bar{T}} \right) \quad [MW] \quad (D.48)$$

$$K_B = 0.1056 \cdot Z_{eff} \cdot (\varepsilon^2 \kappa g) \cdot \frac{(1 + \nu_n)^2 (1 + \nu_T)^{1/2}}{1 + 2\nu_n + 0.5\nu_T} \quad (D.49)$$

And a similar exercise for the thermal conduction losses results in:

$$P_\kappa = K_\kappa \cdot \left( \frac{R_0^3 \bar{n} \bar{T}}{\tau_E} \right) \quad [MW] \quad (D.50)$$

$$K_\kappa = 0.4744 \cdot (1 + f_D) \cdot (\varepsilon^2 \kappa g) \cdot \frac{(1 + \nu_n)(1 + \nu_T)}{1 + \nu_n + \nu_T} \quad (D.51)$$

This concludes an exploration into a slightly more accurate profile construction. It should be noted that these pedestals are still not self-consistent. A true description of profiles would result in a much slower model.

# Appendix E

## Determining Plasma Flux Surfaces

This chapter goes over the flux surface coordinates that define the tokamak geometry. These are then used to approximate the surface area and volume, as well as create surface and volume integrals.

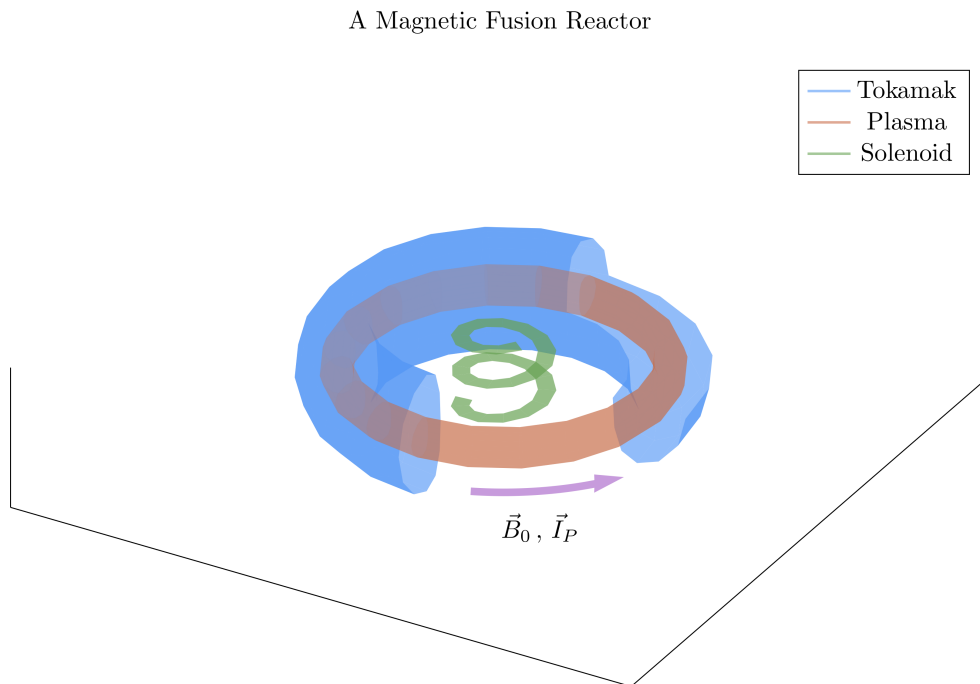


Figure E-1: Cut-Away of Tokamak Reactor

The three main components of a magnetic fusion reactor are: the tokamak structure, the plasma fuel, and the spring-like solenoid at the center.

## E.1 Flux Surface Coordinates

We begin with the shape of the outer plasma surface (i.e. the 95% flux surface) written in terms of normalized coordinates  $x$  and  $y$  as follows – with  $\alpha$  being an angle-like coordinate:

$$R = R_0 + ax(\alpha) \tag{E.1}$$

$$Z = ay(\alpha) \tag{E.2}$$

$$0 \leq \alpha \leq 2\pi \tag{E.3}$$

The surface representation can now be written as:

$$x(\alpha) = c_0 + c_1 \cos(\alpha) + c_2 \cos(2\alpha) + c_3 \cos(3\alpha) \tag{E.4}$$

$$y(\alpha) = \kappa \sin(\alpha) \tag{E.5}$$

The constraints determining  $c_j$  – for  $j = 1, 2, 3$  – are chosen as:

$$x(0) = 1 \tag{E.6}$$

$$x(\pi) = -1 \tag{E.7}$$

$$x\left(\frac{\pi}{2}\right) = -\delta \tag{E.8}$$

$$x_{\alpha\alpha}(\pi) = 0.3 \cdot (1 - \delta^2) \tag{E.9}$$

The last constraint, which is related to the surface curvature at  $\alpha = \pi$ , is chosen to make sure that the surface is always convex. A trial and error empirical fit resulted in the choice  $x_{\alpha\alpha}(\pi) = 0.3 \cdot (1 - \delta^2)$ . The constraint relations are easily evaluated and

then solved, leading to values for the  $c_j$ ,

$$c_0 = -\frac{\delta}{2} \quad (\text{E.10})$$

$$c_1 = g \quad (\text{E.11})$$

$$c_2 = \frac{\delta}{2} \quad (\text{E.12})$$

$$c_3 = 1 - g \quad (\text{E.13})$$

Here,  $g$  is a shaping parameter approximately equal to one:

$$g = \frac{9 - 2\delta - 0.3 \cdot (1 - \delta^2)}{8} \quad (\text{E.14})$$

## E.2 Cross-sectional Area and Volume

The plasma cross-sectional area and volume can be evaluated by straightforward calculations,

$$\begin{aligned} A &= \iint dRdZ = a^2 \iint dx dy = a^2 \int_0^{2\pi} x \frac{dy}{d\alpha} d\alpha \\ &= \pi a^2 \kappa g \end{aligned} \quad (\text{E.15})$$

$$\begin{aligned} V &= \iiint R dR dZ d\Phi = 2\pi a^2 \iint R dx dy \\ &= 2\pi a^2 R_0 \int_0^{2\pi} \left( x + \varepsilon \frac{x^2}{2} \right) \frac{dy}{d\alpha} d\alpha \approx 2\pi a^2 R_0 \int_0^{2\pi} x \frac{dy}{d\alpha} d\alpha \\ &= 2\pi^2 R_0 a^2 \kappa g \end{aligned} \quad (\text{E.16})$$

The second form of the volume integral makes use of the small inverse aspect ratio expansion,  $\varepsilon \ll 1$ , which is a good approximation and used throughout the analysis.

### E.3 Surface and Volume Integrals

Eqs. (E.4) and (E.5) are simple formulas describing the shape of the outer plasma surface. We next modify the model so that it gives a plausible description of the interior flux surfaces as well. The idea is to introduce a normalized flux label, which is radial-like in behavior. This label is denoted by  $\rho$  and  $\rho \in [0, 1]$  with  $\rho = 1$  being the outer plasma surface (i.e. the 95% surface) and  $\rho = 0$  being the magnetic axis. Additional trial and error results in the following representation for the flux surfaces,

$$x(\rho, \alpha) = \sigma(1 - \rho^2) + c_0\rho^4 + c_1\rho \cos(\alpha) + c_2\rho^2 \cos(2\alpha) + c_3\rho^3 \cos(3\alpha) \quad (\text{E.17})$$

$$y(\rho, \alpha) = \kappa\rho \sin(\alpha) \quad (\text{E.18})$$

with  $\sigma$  being the shift of the magnetic axis. Usually,  $\sigma \sim 0.1$  for a high field tokamak.

Lastly, we note that in the course of the work it will be necessary to integrate functions of  $\rho$  over the volume and cross-sectional area of the plasma. Specifically we will need to evaluate:

$$Q_V = \iiint Q(\rho) R dR dZ d\Phi \approx 2\pi R_0 a^2 \iint Q(\rho) dx dy \quad (\text{E.19})$$

$$Q_A = \iint Q(\rho) dR dZ = a^2 \iint Q(\rho) dx dy \quad (\text{E.20})$$

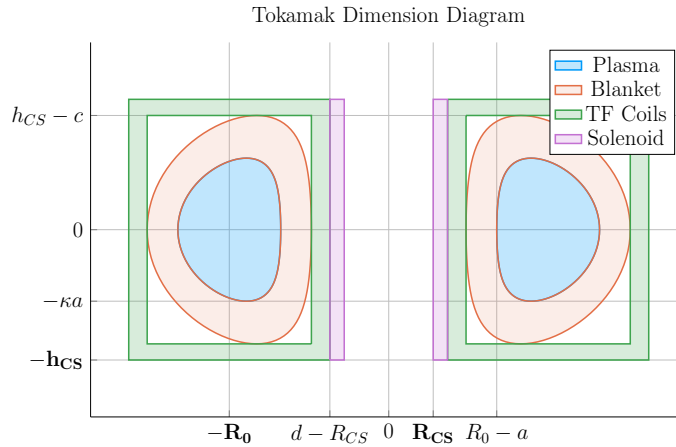


Figure E-2: Dimensions of Tokamak Cross-Section

Here,  $Q(\rho)$  is an arbitrary function of  $\rho$  such as pressure or temperature. In the large aspect ratio limit, both integrals require the evaluation of the same quantity:

$$K = \iint Q(\rho) dx dy \quad (\text{E.21})$$

To evaluate this integral, we need to convert from  $x, y$  coordinates to  $\rho, \alpha$  coordinates. Using the Jacobian of the transformation leads to

$$K = \iint Q(\rho) (x_\rho y_\alpha - x_\alpha y_\rho) d\rho d\alpha \quad (\text{E.22})$$

Here,

$$\begin{aligned} x_\rho y_\alpha - x_\alpha y_\rho &= \kappa \sin(\alpha) \cdot (c_1 \rho \sin(\alpha) + 2c_2 \rho^2 \sin(2\alpha) + 3c_3 \rho^3 \sin(3\alpha)) \\ &+ \kappa \rho \cos(\alpha) \cdot \left[ \right. \\ &\quad \left. - 2\rho\sigma + 4\rho^3 c_0 + c_1 \cos(\alpha) + 2c_2 \rho \cos(2\alpha) + 3c_3 \rho^2 \cos(3\alpha) \right] \end{aligned} \quad (\text{E.23})$$

Since  $Q$  is only a function of  $\rho$ , the  $\alpha$  integral can be carried out analytically. The only term that survives the averaging are the ones containing  $c_1$ . A simple integration over  $\alpha$  then yields the desired results:

$$Q_V = 4\pi^2 R_0 a^2 \kappa g \int_0^1 Q(\rho) \rho d\rho \quad (\text{E.24})$$

$$Q_S = 2\pi a^2 \kappa g \int_0^1 Q(\rho) \rho d\rho \quad (\text{E.25})$$





# Appendix F

## Expanding on the Bootstrap Current

The bootstrap current fraction –  $f_{BS}$  – is an important parameter that enters in the design of tokamak reactors. It must be calculated with reasonable accuracy to determine how much external current drive is required. The value of  $f_{BS}$  thus has a strong impact on the overall fusion energy gain. Obtaining reasonable accuracy requires a moderate amount of analysis, which is presented in a following section. The results are summarized below.

### F.1 Summarized Results

The analysis is based on an expression for the bootstrap current valid for arbitrary cross section assuming (1) equal temperature electrons and ions  $T_e = T_i = T$ , (2) large aspect ratio  $\varepsilon \ll 1$ , and (3) negligible collisionality  $\nu_* \rightarrow 0$ . Under these assumptions the bootstrap current  $\mathbf{J}_{BS} \approx J_{BS} \mathbf{e}_\phi$  has the form

$$J_{BS} = -3.32 f_T \cdot (R_0 n T) \cdot \left( \frac{1}{n} \frac{dn}{d\psi} + 0.054 \frac{1}{T} \frac{dT}{d\psi} \right) \quad (\text{F.1})$$

Here,  $f_T \approx 1.46 (r/R_0)^{1/2}$  is an approximate expression for the trapped particle fraction and  $\psi$  is the poloidal flux.

The analysis next section shows that Eq. (F.1) leads to an expression for the bootstrap fraction, assuming for simplicity elliptical flux surfaces, that can be written as:

$$f_{BS} = \frac{I_{BS}}{I} = \frac{2\pi a^2 \kappa}{I} \int_0^1 J_{BS} \rho d\rho = \frac{K_{BS}}{K_n} \frac{\bar{n} \bar{T} R_0^2}{I_P^2} \quad (\text{F.2})$$

$$K_{BS} = 4.879 \cdot K_n \cdot \left( \frac{1 + \kappa^2}{2} \right) \cdot \varepsilon^{5/2} \cdot H_{BS} \quad (\text{F.3})$$

$$H_{BS} = (1 + \nu_n)(1 + \nu_T)(\nu_n + 0.054\nu_T) \int_0^1 \frac{\rho^{5/2} (1 - \rho^2)^{\nu_n + \nu_T - 1}}{b_p} d\rho \quad (\text{F.4})$$

$$b_p(\rho) = \frac{-e^{\gamma \rho^2} (\gamma \rho^2 - 1 - \gamma) - 1 - \gamma}{\rho (e^\gamma - 1 - \gamma)} \quad (\text{F.5})$$

$$\bar{J}_\phi(\rho) = -\frac{I}{\pi a^2 \kappa} \left[ \frac{\gamma^2 (1 - \rho^2) e^{\gamma \rho^2}}{e^\gamma - 1 - \gamma} \right] \quad (\text{F.6})$$

In this expression  $b_p$  is a normalized form of the poloidal magnetic field derived from a prescribed model for the *total* flux surface averaged current density profile  $\bar{J}_\phi(\rho)$ . The  $\bar{J}_\phi(\rho)$  profile, in analogy with the density and temperature profiles, is not self-consistent but is chosen to have a plausible experimental shape characterized by the parameter  $\gamma$ . The profile can have either an on-axis ( $\gamma < 1$ ) or off-axis peak ( $\gamma > 1$ ). The normalized internal inductance  $l_i$  and radial location of the current peak  $\rho_m$  are related to the value of  $\gamma$  by:

$$l_i = \frac{4\kappa}{1 + \kappa^2} \int_0^1 b_p^2 \rho d\rho \quad (\text{F.7})$$

$$\rho_m = \begin{cases} \left( \frac{\gamma}{\gamma - 1} \right)^{1/2}, & \gamma > 1 \\ 0, & \gamma < 1 \end{cases} \quad (\text{F.8})$$

## F.2 Detailed Analysis

The starting point for the analysis is the general expression for the bootstrap current in a tokamak with arbitrary cross section.<sup>49</sup> This expression can be simplified by assuming (1) equal temperature electrons and ions  $T_e = T_i = T$ , (2) large aspect ratio  $\varepsilon \ll 1$ , and (3) negligible collisionality  $\nu_* \rightarrow 0$ . The bootstrap current  $\mathbf{J}_{BS} \approx J_{BS} \mathbf{e}_\phi$  reduces to

$$J_{BS} = -3.32 f_T \cdot (R_0 n T) \cdot \left( \frac{1}{n} \frac{dn}{d\psi} + 0.054 \frac{1}{T} \frac{dT}{d\psi} \right) \quad (\text{F.9})$$

Several values of the trapped particle fraction  $f_T$  have been given in the literature.<sup>50</sup> For simplicity we use a form valid for large aspect ratio. This is a slightly optimistic value but saves a large amount of detailed calculation. It can be written as,

$$f_T \approx 1.46 \sqrt{\frac{r}{R_0}} = 1.46 \sqrt{\varepsilon \rho} \quad (\text{F.10})$$

Here, as in the main text,  $\rho$  is a radial-like flux surface label that varies between  $0 \leq \rho \leq 1$ . In other words  $\psi = \psi(\rho)$ . Under these assumptions the bootstrap current reduces to:

$$J_{BS} = -4.85 R_0 \varepsilon^{1/2} \left( \frac{\rho^{1/2} n T}{d\psi/d\rho} \right) \left( \frac{1}{n} \frac{dn}{d\rho} + 0.054 \frac{1}{T} \frac{dT}{d\rho} \right) \quad (\text{F.11})$$

Since we have specified profiles for  $n(\rho)$  and  $T(\rho)$  all that remains in order to be able to evaluate  $J_{BS}(\rho)$  is to determine  $\psi' = d\psi/d\rho$ . Keep in mind that at this point, in spite of the approximations that have been made, the expression for  $J_{BS}(\rho)$  is still valid for arbitrary cross section.

The analysis that follows shows how to calculate  $\psi'$  for an arbitrary cross section including finite aspect ratio. As an example an explicit expression for large aspect ratio, finite elongation ellipse is obtained. Consider the Grad-Shafranov equation for the flux:  $\Delta^* \psi = -\mu_0 R J_\phi$ . We integrate this equation over the volume of an arbitrary

flux surface making use of Gauss' theorem, which leads to:

$$\int_S \frac{\mathbf{n} \cdot \nabla \psi}{R^2} dS = -\mu_0 \int_V \frac{J_\phi}{R} d\mathbf{r} \quad (\text{F.12})$$

Next, assume that the coordinates of the flux surface can be expressed in terms of  $\rho$  and an angular-like parameter  $\alpha$  with  $0 \leq \alpha \leq 2\pi$ . In other words, the flux surface coordinates can be written as  $R = R(\rho, \alpha) = R_0 + ax(\rho, \alpha)$  and  $Z = Z(\rho, \alpha) = ay(\rho, \alpha)$ . The functions  $R(\rho, \alpha)$  and  $Z(\rho, \alpha)$  are assumed to be known. The term on the left hand side can be evaluated by noting that

$$d\mathbf{l} = dl \mathbf{t} \quad (\text{F.13})$$

$$dl = (R_\alpha^2 + Z_\alpha^2)^{1/2} d\alpha \quad (\text{F.14})$$

$$\mathbf{t} = \frac{R_\alpha \mathbf{e}_R + Z_\alpha \mathbf{e}_Z}{(R_\alpha^2 + Z_\alpha^2)^{1/2}} \quad (\text{F.15})$$

$$\mathbf{n} = \mathbf{e}_\phi \times \mathbf{t} = \frac{Z_\alpha \mathbf{e}_R - R_\alpha \mathbf{e}_Z}{(R_\alpha^2 + Z_\alpha^2)^{1/2}} \quad (\text{F.16})$$

$$dS = R d\phi dl = 2\pi R (R_\alpha^2 + Z_\alpha^2)^{1/2} d\alpha \quad (\text{F.17})$$

It then follows that

$$\mathbf{n} \cdot \nabla \psi = \frac{1}{(R_\alpha^2 + Z_\alpha^2)^{1/2}} \left( Z_\alpha \frac{\partial \psi}{\partial R} - R_\alpha \frac{\partial \psi}{\partial Z} \right) = \frac{1}{(R_\alpha^2 + Z_\alpha^2)^{1/2}} \frac{d\psi}{d\rho} Z_\alpha \rho_R - R_\alpha \rho_Z \quad (\text{F.18})$$

We can rewrite the last term by noting that

$$\begin{aligned} dR = R_\rho d\rho + R_\alpha d\alpha &\rightarrow d\rho = (Z_\alpha dR - R_\alpha dZ) / (R_\rho Z_\alpha - R_\alpha Z_\rho) \\ dZ = Z_\rho d\rho + Z_\alpha d\alpha &\rightarrow d\alpha = (-Z_\rho dR + R_\rho dZ) / (R_\rho Z_\alpha - R_\alpha Z_\rho) \end{aligned} \quad (\text{F.19})$$

from which follows

$$\begin{aligned} \rho_R &= \frac{Z_\alpha}{(R_\rho Z_\alpha - R_\alpha Z_\rho)} \\ \rho_Z &= -\frac{R_\alpha}{(R_\rho Z_\alpha - R_\alpha Z_\rho)} \end{aligned} \quad (\text{F.20})$$

the normal gradient reduces to

$$\mathbf{n} \cdot \nabla \psi = \frac{\sqrt{R_\alpha^2 + Z_\alpha^2}}{(R_\rho Z_\alpha - R_\alpha Z_\rho)} \frac{d\psi}{d\rho} \quad (\text{F.21})$$

Using this relation we see that the left hand side of Eq. (F.12) can now be written as:

$$\int_S \frac{\mathbf{n} \cdot \nabla \psi}{R^2} dS = 2\pi \frac{d\psi}{d\rho} \int_0^{2\pi} \frac{R_\alpha^2 + Z_\alpha^2}{(R_\rho Z_\alpha - R_\alpha Z_\rho)} \frac{d\alpha}{R} \quad (\text{F.22})$$

Consider now the right hand side of Eq. (F.12). The critical assumption is that the current density is approximated by its flux surface averaged value,  $J_\phi(\rho, \alpha) \approx \bar{J}_\phi(\rho)$ . This is obviously not self-consistent with the Grad-Shafranov equation. Even so, it should suffice for present purposes where we only need to evaluate global volume integrals. Also, in the same spirit as prescribing  $n(\rho)$  and  $T(\rho)$  we assume that  $\bar{J}_\phi(\rho)$  is also prescribed. Under these assumptions the right hand side of Eq. (F.12) simplifies to:

$$\begin{aligned} -\mu_0 \int_V \frac{J_\phi}{R} d\mathbf{r} &= -2\pi\mu_0 \int_A J_\phi dA \\ &= -2\pi\mu_0 \int_0^\rho d\rho \int_0^{2\pi} J_\phi (R_\rho Z_\alpha - R_\alpha Z_\rho) d\alpha \\ &\approx -2\pi\mu_0 \int_0^\rho d\rho \left[ \bar{J}_\phi \int_0^{2\pi} (R_\rho Z_\alpha - R_\alpha Z_\rho) d\alpha \right] \end{aligned} \quad (\text{F.23})$$

Combining the results in Eqs. (F.22) and (F.23) leads to the required general expression for  $d\psi/d\rho$ ,

$$\frac{d\psi}{d\rho} \int_0^{2\pi} \frac{R_\alpha^2 + Z_\alpha^2}{(R_\rho Z_\alpha - R_\alpha Z_\rho)} \frac{d\alpha}{R} = -\mu_0 \int_0^\rho d\rho \left[ \bar{J}_\phi \int_0^{2\pi} (R_\rho Z_\alpha - R_\alpha Z_\rho) d\alpha \right] \quad (\text{F.24})$$

Next, to help specify a plausible choice for  $\bar{J}_\phi$  it is useful to define the kink safety factor and the actual local safety factor. The kink safety factor is defined by

$$q_* = \frac{2\pi a^2 B_0}{\mu_0 R_0 I} \left( \frac{1 + \kappa^2}{2} \right) \quad (\text{F.25})$$

where

$$I = \int J_\phi dA = \int_0^1 d\rho \left[ \bar{J}_\phi \int_0^{2\pi} (R_\rho Z_\alpha - R_\alpha Z_\rho) d\alpha \right] \quad (\text{F.26})$$

This leads to

$$\frac{1}{q_*} = \frac{\mu_0 R_0}{2\pi a^2 B_0} \left( \frac{2}{1 + \kappa^2} \right) \int_0^1 d\rho \left[ \bar{J}_\phi \int_0^{2\pi} (R_\rho Z_\alpha - R_\alpha Z_\rho) d\alpha \right] \quad (\text{F.27})$$

Similarly, the local safety factor can be expressed as

$$q(\rho) = \frac{F(\rho)}{2\pi} \int \frac{dl}{RB_p} \quad (\text{F.28})$$

Here,  $F(\rho) = RB_\phi$ . Substituting  $RB_p = \mathbf{n} \cdot \nabla \psi$  then yields

$$q(\rho) = \frac{F(\rho)}{2\pi\psi'} \int_0^{2\pi} \frac{1}{R} (R_\rho Z_\alpha - R_\alpha Z_\rho) d\alpha \quad (\text{F.29})$$

with  $\psi' = d\psi/d\rho$ .

For present purposes we can obtain relatively simple analytic expressions for all the quantities of interest by assuming the flux surfaces are concentric ellipses, characterized by  $R = R_0 + a\rho \cos \alpha$  and  $Z = \kappa a\rho \sin \alpha$ . We also assume low  $\beta$  so that  $F(\rho) \approx R_0 B_0$ . This model accounts for elongation but neglects the effects of triangularity and finite aspect ratio. The derivatives in Eqs. (F.24), (F.27) and (F.29) can now be easily evaluated. Also, after some trial and error we chose  $\bar{J}_\phi(\rho)$  to be a plausible profile which is peaked off-axis at  $\rho = \rho_m$ .

$$\bar{J}_\phi(\rho) = -\frac{I}{\pi a^2 \kappa} \left[ \frac{\gamma^2 (1 - \rho^2) e^{\gamma \rho^2}}{e^\gamma - 1 - \gamma} \right] \quad (\text{F.30})$$

Here,  $\gamma = 1/(1 - \rho_m^2)$ .

These profiles are substituted into Eq. (F.24) after which each of the integrals can be evaluated analytically. A straightforward calculation yields:

$$\begin{aligned}\rho \frac{d\psi}{d\rho} &= -2\mu_0 R_0 a^2 \left( \frac{\kappa^2}{1 + \kappa^2} \right) \int_0^\rho \bar{J}_\phi \rho d\rho \\ &= \frac{\mu_0 R_0 I}{\pi} \left( \frac{\kappa}{1 + \kappa^2} \right) \frac{(1 + \gamma - \gamma \rho^2) e^{\gamma \rho^2} - 1 - \gamma}{e^\gamma - 1 - \gamma}\end{aligned}\tag{F.31}$$

The safety factors are given by

$$\begin{aligned}\frac{1}{q_*} &= \frac{\psi'(1)}{\kappa a^2 B_0} \\ \frac{q(\rho)}{q_*} &= \frac{\rho \psi'(1)}{\psi'(\rho)}\end{aligned}\tag{F.32}$$

Eq. (F.31) is now substituted into the expression for the bootstrap current given by Eq. (F.11). The resulting expression can then be integrated over the plasma cross section to yield the bootstrap fraction. A straightforward calculation leads to:

$$f_{BS} = \frac{I_{BS}}{I} = \frac{2\pi a^2 \kappa}{I} \int_0^1 J_{BS} \rho d\rho = \frac{K_{BS}}{K_n} \frac{\bar{n} \bar{T} R_0^2}{I_P^2}\tag{F.33}$$

$$K_{BS} = 4.879 \cdot K_n \cdot \left( \frac{1 + \kappa^2}{2} \right) \cdot \varepsilon^{5/2} \cdot H_{BS}\tag{F.34}$$

$$H_{BS} = (1 + \nu_n)(1 + \nu_T)(\nu_n + 0.054\nu_T) \int_0^1 \frac{\rho^{5/2} (1 - \rho^2)^{\nu_n + \nu_T - 1}}{b_p} d\rho\tag{F.35}$$

$$b_p(\rho) = \frac{-e^{\gamma \rho^2} (\gamma \rho^2 - 1 - \gamma) - 1 - \gamma}{\rho (e^\gamma - 1 - \gamma)}\tag{F.36}$$

This is the desired result.





# Appendix G

## Elaborating on the Current Drive

The driven current fraction –  $f_{CD}$  – is an important parameter that enters in the design of steady-state tokamak reactors. It must be calculated with reasonable accuracy to determine how much bootstrap current is required. The value of  $f_{CD}$  thus has a strong impact on the overall fusion energy gain. Obtaining reasonable accuracy requires a moderate amount of analysis, which is presented in a following section. The results are summarized below.

### G.1 Summarized Results

We assume that current drive is provided by lower hybrid waves because of the corresponding relatively high efficiency and naturally occurring off-axis peaking which aligns with the bootstrap current. The externally driven lower hybrid current ( $I_{CD}$ ) is given in terms of the current drive efficiency,  $\eta_{CD}$ , defined as follows:<sup>26</sup>

$$I_{CD} = \eta_{CD} \frac{P_H}{\bar{n}_{20} R_0} = \frac{\eta_{CD}}{Q} \frac{P_F}{\bar{n}_{20} R_0} \quad (\text{G.1})$$

Here, for simplicity and slightly optimistically, we assume that 100% of the klystron RF power,  $P_H$ , is absorbed in the plasma.

The current drive fraction  $f_{CD} = I_{CD}/I_P$  can then be written as,

$$f_{CD} = K_{CD} \frac{\eta_{CD} \bar{n}_{20} R_0^2 (\hat{\sigma} v)}{I_P} \quad (\text{G.2})$$

$$K_{CD} = 278 \frac{f_D^2 \varepsilon^2 \kappa}{Q} \quad (\text{G.3})$$

Typical values for  $\eta_{CD}$  are around 0.3.<sup>26</sup> However, this current drive efficiency is actually a function of:  $\bar{n}$ ,  $\bar{T}$ , and  $B_0$ . This dependence must be included in the design to obtain reliable results. A self consistent calculation of  $\eta_{CD} = \eta_{CD}(\bar{n}, \bar{T}, B_0)$  requires considerable analysis, the details of which are presented next section.

## G.2 Detailed Analysis

To design a steady state fusion reactor, it is necessary to calculate  $\eta_{CD}$  for lower hybrid current drive (LHCD). Recall that the driven lower hybrid current  $I_{CD}$  is related to the lower hybrid RF klystron power absorbed by the plasma  $P_H$  by the relation:

$$I_{CD} = \eta_{CD} \frac{P_H}{n_{20} R} \quad (\text{G.4})$$

Here,  $P_H = \eta_{RF} P_{RF}$ , with  $P_{RF}$  equal to the total wall power used for current drive (plus heating) and  $\eta_{RF} \approx 0.5$  is the conversion efficiency from wall power to RF absorbed power. Also,  $n_{20} = n_{20}(\rho_J)$  and  $R = R(\rho_J, \theta)$  are the density and major radius evaluated at the minor radius  $\rho = \rho_J$  and launch angle  $\theta$  with  $\rho_J$  corresponding to the location of the peak driven current density:  $J_{\max} = J_{CD}(\rho_J, \theta)$ . The angle  $\theta$  is a known quantity set by the experimental configuration while  $\rho_J$  is yet to be determined.

The value of  $\eta_{CD}$  is related to a normalized quantity  $\tilde{\eta}$ , the efficiency usually calculated in the literature, by a series of connecting formulas. The inter-relations start with

$$\eta_I = \frac{\int_A J_{CD} dA}{\int_V S_H dV} \approx \frac{1}{2\pi} \left[ \frac{J_{CD}}{R S_H} \right]_{\rho_J, \theta} = \frac{\eta_{LH}}{2\pi R} \left[ \frac{J_{CD}}{R S_{LH}} \right]_{\rho_J, \theta} \quad (\text{G.5})$$

where  $\eta_I = I_{CD}/P_H$  A/W is the overall current drive efficiency measuring how many delivered watts of klystron RF power are required to drive one ampere of current. For simplicity and slightly optimistically all delivered power is assumed to be absorbed by the plasma. Also,  $S_H(\rho, \theta)$  is the klystron power density delivered to the plasma, whose absorption is localized around  $\rho = \rho_J$ .

Due to various losses, only a fraction of the absorbed klystron power,  $\eta_{LH} \approx 0.75$ , actually drives current. These losses have to do with the fact that the power spectrum arising from a realistic waveguide array has both positive and negative lobes – it is not an ideal positive delta function. The combination of finite spectral width plus oppositely driven current from the negative lobe implies that only a portion of the total absorbed power actually drives a net positive current. The result of this discussion is that the power density,  $S_{LH}$ , driving lower hybrid current is related to the delivered klystron power density by  $S_{LH} = \eta_{LH} S_H$ .

Now, the efficiency,  $\tilde{\eta}$  usually calculated in the literature is defined by:

$$\tilde{\eta}(\rho_J, \theta) = \left[ \frac{J_{CD}/en v_{Te}}{S_{LH}/m_e n \nu_0 v_{Te}^2} \right]_{\rho_J, \theta} \quad (\text{G.6})$$

$$v_{Te}(\rho_J) = \left[ \frac{2T_e}{m_e} \right]_{\rho_J}^{1/2} \quad (\text{G.7})$$

$$\nu_0(\rho_J) = \left[ \frac{\omega_{pe}^4 \ln \Lambda}{2\pi n_e v_{Te}^3} \right]_{\rho_J} \quad (\text{G.8})$$

It then follows that

$$\eta_I = \frac{\eta_{LH}}{2\pi} \left[ \frac{e}{R m_e \nu_0 v_{Te}} \right]_{\rho_J, \theta} \tilde{\eta}(\rho_J, \theta) \quad (\text{G.9})$$

From Eq. (G.4), we see that  $\eta_{CD} = \eta_I [n_{20} R]_{\rho_J, \theta}$ , which leads to the desired conversion relation:

$$\eta_{CD} = \frac{\eta_{LH}}{2\pi} \left[ \frac{e n_{20}}{m_e \nu_0 v_{Te}} \right]_{\rho_J} \tilde{\eta}(\rho_J, \theta) = 0.06108 \frac{\eta_{LH}}{\ln \Lambda} T_k \tilde{\eta} \quad (\text{G.10})$$

### An expression for $\tilde{\eta}$

Needed for the design code is an expression for  $\tilde{\eta}(\rho_J, \theta)$ . Such an expression, valid for arbitrary  $\rho$ , has been determined by Ehst and Karney<sup>27</sup> – based on a sophisticated theoretical analysis combined with extensive numerical results. Once  $\rho_J$  is determined we set  $\rho = \rho_J$  in the expression for  $\tilde{\eta}(\rho, \theta)$ . Ehst and Karney find that a good fit for  $\tilde{\eta}(\rho, \theta)$  can be written as:

$$\tilde{\eta} = CMR\eta_0 \quad (\text{G.11})$$

For LHCD, the parameters appearing in Eq. (G.11) have the form:

$$M = 1 \quad (\text{G.12})$$

$$R(\rho, \theta) = 1 - \frac{\varepsilon^n \rho^n (x_r^2 + w^2)^{1/2}}{\varepsilon^n \rho^n x_r + w} \quad n = 0.77 \quad x_r = 2.47 \quad (\text{G.13})$$

$$C(\rho, \theta) = 1 - \exp(-c^m x_t^{2m}) \quad m = 1.38 \quad c = 0.778 \quad (\text{G.14})$$

$$\eta_0(\rho, \theta) = \frac{K}{w} + D + \frac{8w^2}{5 + Z_{eff}} \quad K = \frac{2.12}{Z_{eff}} \quad D = \frac{3.83}{Z_{eff}^{0.707}} \quad (\text{G.15})$$

All quantities have been defined except for  $x_t^2(\rho, \theta)$  and  $w(\rho, \theta)$ . The quantity  $w$  is a normalized form of the resonant particle velocity which absorbs energy and momentum from the lower hybrid wave,

$$w(\rho, \theta) = \frac{\omega}{k_{\parallel} v_{Te}} = \frac{c}{v_{Te} n_{\parallel}} \quad (\text{G.16})$$

with  $n_{\parallel}$  the parallel index of refraction. The value of  $n_{\parallel}(\rho, \theta)$  will be discussed shortly.

The quantity  $x_t^2$  is a toroidal correction associated with the fact that trapped particles cannot contribute to toroidal current flow. It can be expressed in terms of the local mirror ratio by

$$x_t^2(\rho, \theta) = w^2 \left( \frac{B}{B_M - B} \right) \quad (\text{G.17})$$

where from simple guiding center theory assuming that  $B \approx B_\phi$ ,

$$B_M = \frac{B_0}{1 - \varepsilon \rho} \quad (\text{G.18})$$

$$B = \frac{B_0}{1 + \varepsilon \rho \cos \theta} \quad (\text{G.19})$$

### Calculation of $n_\parallel^2(\rho, \theta)$

The next step in the evaluation of  $\eta_{CD}$  is the calculation of  $n_\parallel^2(\rho, \theta)$ . Its value is determined by the requirements for accessibility from the plasma edge into the absorption layer. The relevant physics follows from an analysis of the cold plasma dispersion relation given by

$$n_\perp^2(\rho, \theta) = -\frac{K_\parallel}{2K_\perp} \left\{ n_\parallel^2 - K_\perp + \frac{K_A^2}{K_\parallel} \pm \left[ \left( n_\parallel^2 - K_\perp + \frac{K_A^2}{K_\parallel} \right)^2 + \frac{4K_\perp K_A^2}{K_\parallel} \right]^{1/2} \right\} \quad (\text{G.20})$$

The plus sign corresponds to the desired root and is often referred to as the slow wave.

In the lower hybrid regime the relevant ordering of parameters is

$$\begin{aligned} \omega_{pe}/\Omega_e &\sim \omega_{pi}/\omega \sim n_\parallel \sim 1 \\ \omega_{pi}/\Omega_i &\sim \omega/\Omega_i \sim \Omega_e/\omega \sim n_\perp \sim \sqrt{m_i/m_e} \gg 1 \end{aligned} \quad (\text{G.21})$$

leading to the following simple forms for the elements of the dielectric tensor

$$\begin{aligned} K_\perp(\rho, \theta) &= 1 + \frac{\omega_{pe}^2}{\Omega_e^2} - \frac{\omega_{pi}^2}{\omega^2} \sim 1 \\ K_A(\rho, \theta) &= \frac{\omega_{pe}^2}{\omega \Omega_e} \sim \sqrt{m_i/m_e} \\ K_\parallel(\rho) &= -\frac{\omega_{pe}^2}{\omega^2} \sim m_i/m_e \end{aligned} \quad (\text{G.22})$$

The first requirement for accessibility is that the function under the square root be positive. When this function passes through zero there is a double root for  $n_\perp^2$  causing a mode conversion from the slow wave to the fast wave. The fast wave does

not propagate into the plasma. It is reflected back out through the plasma surface, obviously an undesirable result. Avoiding mode conversion requires a sufficiently large value of  $n_{\parallel}^2$  to keep the function under the square root positive. This value must satisfy

$$n_{\parallel}^2(\rho, \theta) \geq \left[ K_{\perp}^{1/2} + \left( -\frac{K_A^2}{K_{\parallel}} \right)^{1/2} \right]^2 \quad (\text{G.23})$$

Since  $\eta_{CD} \propto 1/n_{\parallel}^2$  we see that current drive efficiency is maximized when  $n_{\parallel}^2(\rho, \theta)$  is minimized – the inequality in Eq. (G.23) must be set to equality.

At this point there is an important subtlety that must be taken into account. The issue is that the wavelength spectrum of the applied klystron source is not a delta function – it has a finite half width,  $\Delta n_{\parallel} \approx 0.2$ , and a negative lobe. For simplicity, we have modeled the spectrum as rectangular and ignore the negative lobe. The negative lobe is accounted for through the value of  $\eta_{LH}$ , since this power obviously does not drive current in the desired direction. Now, Eq. (G.23) is an inequality and we want to minimize  $n_{\parallel}^2(\rho, \theta)$  over all  $\rho$  for the given  $\theta$  where the power is absorbed. Therefore, we must use the equality sign in Eq. (G.23) for the strictest case – that  $n_{\parallel}(\hat{\rho}_J, \theta) = (n_{\parallel}(\rho_J, \theta) - \Delta n_{\parallel})$  – where  $\hat{\rho}_J$  and  $\rho_J$  (both as yet undetermined) are the corresponding strictest and average radii where power is absorbed.

With this in mind, after substituting the simplified expressions for the elements of the dielectric tensor we obtain

$$n_{\parallel}^2(\hat{\rho}_J, \theta) = \left[ \left( 1 - \frac{1 - \hat{\omega}^2}{\hat{\omega}^2} X \right)^{1/2} + X^{1/2} \right]^2 \quad (\text{G.24})$$

$$X(\hat{\rho}_J, \theta) = \frac{\omega_{pe}^2(\hat{\rho}_J)}{\Omega_e^2(\hat{\rho}_J, \theta)} \quad (\text{G.25})$$

$$\hat{\omega}^2(\hat{\rho}_J, \theta) = \frac{\omega^2}{\Omega_e(\hat{\rho}_J, \theta) \Omega_i(\hat{\rho}_J, \theta)} \quad (\text{G.26})$$

The question now is how do we choose the frequency:  $\hat{\omega}$ ? There are actually three constraints on the frequency and we must choose the strictest one to determine  $\hat{\omega}^2$ .

The constraints are as follows:

$$\begin{aligned}
\omega^2 &> \omega_{LH}^2(\hat{\rho}_J, \theta) && \text{Avoid mode conversion before reaching } \hat{\rho}_J, \theta \\
\omega^2 &> 4\omega_{LH}^2(\hat{\rho}_J, \theta) && \text{Avoid the PDI before reaching } \hat{\rho}_J, \theta \\
\omega^2 &> k_\perp^2(\hat{\rho}_J, \theta) v_\alpha^2 && \text{Avoid coupling to } \alpha \text{ particles before reaching } \hat{\rho}_J, \theta
\end{aligned} \tag{G.27}$$

Here,  $\omega_{LH}^2(\hat{\rho}_J, \theta) = \omega_{pi}^2 / (1 + \omega_{pe}^2 / \Omega_e^2)$  is the square of the lower hybrid frequency and  $v_\alpha = (2E_\alpha / m_\alpha)^{1/2}$  is the alpha particle speed. Also, PDI denotes parametric decay instability. The second and third constraints are approximate values, used here for simplicity.

Each of these constraints is substituted into the expression for  $n_\parallel^2$ . We find that in the regime of interest the  $\alpha$  particle coupling requirement is the strictest. We thus choose the frequency to satisfy  $\omega / k_\perp = v_\alpha$ , or in normalized units:

$$n_\perp^2(\hat{\rho}_J, \theta) = \frac{c^2}{v_\alpha^2} \tag{G.28}$$

This expression is simplified by evaluating  $n_\perp^2$  using Eq. (G.20) coupled with  $n_\parallel^2$  given by Eq. (G.23)

$$n_\perp^2(\hat{\rho}_J, \theta) = -\frac{K_\parallel}{K_\perp^{1/2}} \left( -\frac{K_A^2}{K_\parallel} \right)^{1/2} = \frac{m_i}{m_e} \frac{X^{3/2}}{\hat{\omega} [\hat{\omega}^2(1+X) - X]^{1/2}} \tag{G.29}$$

Eq. (G.29) is a quadratic equation for  $\hat{\omega}^2$ , which can be easily solved, yielding:

$$\hat{\omega}^2(\hat{\rho}_J, \theta) = \frac{1}{2} \frac{X}{1+X} + \frac{1}{2} \left[ \frac{X^2}{(1+X)^2} + 4\gamma^2 \frac{X^3}{1+X} \right]^{1/2} \tag{G.30}$$

$$\gamma = \frac{m_i}{m_e} \frac{1}{n_\perp^2} = \frac{2m_i E_\alpha}{m_e m_\alpha c^2} = 8.562 \tag{G.31}$$

This value of  $\hat{\omega}^2$  is substituted into Eq. (G.24) to obtain the desired expression for  $n_\parallel^2 = n_\parallel^2(X)$ .

### Calculation of $\hat{\rho}_J$

The calculation of  $\hat{\rho}_J$  requires a very lengthy analysis of Landau damping. We can bypass this complication by making use of a simple rule of thumb that is reasonably accurate. This rule states that lower hybrid power is absorbed and driven current produced in a somewhat narrow layer of the plasma profile whose location is determined by the requirement that the parallel phase velocity be approximately equal to three times the electron thermal speed,

$$\frac{\omega}{k_{\parallel}} \approx 3v_T \quad (\text{G.32})$$

The equation can be rewritten in terms of  $\hat{n}_{\parallel}$  leading to a transcendental algebraic equation for  $\hat{\rho}_J$ ,

$$(1 + \nu_T) (1 - \hat{\rho}_J^2)^{\nu_T} n_{\parallel}^2(\hat{\rho}_J, \theta) = \frac{m_e c^2}{18\overline{T}} = \frac{28.39}{\overline{T}_k} \quad (\text{G.33})$$

This is a simple equation to solve numerically.

### Calculation of $\rho_J$

The last step in the analysis is to map the results at the strictest absorption location –  $(\rho, \theta)$  – to the center of the absorption layer –  $(\rho_J, \theta)$  – where the current drive efficiency is defined. This is easily done by noting that power is always absorbed in at the local radius where  $\omega/k_{\parallel} = 3v_{Te}$ . Consequently, the relations at  $\rho_J$  are related to those at  $\hat{\rho}_J$  by:

$$(1 + \nu_T) (1 - \hat{\rho}_J^2)^{\nu_T} n_{\parallel}^2(\hat{\rho}_J, \theta) = \frac{28.39}{\overline{T}_k} \quad (\text{G.34})$$

$$(1 + \nu_T) (1 - \rho_J^2)^{\nu_T} n_{\parallel}^2(\rho_J, \theta) = \frac{28.39}{\overline{T}_k} \quad (\text{G.35})$$



Since  $n_{\parallel}(\hat{\rho}_J, \theta) = n_{\parallel}(\rho_J, \theta) - \Delta n_{\parallel}$ , it follows that  $\hat{\rho}_J$  and  $\rho_J$  are related by:

$$\frac{(1 - \rho_J^2)^{\nu_T}}{(1 - \hat{\rho}_J^2)^{\nu_T}} = \left[ 1 - \frac{\Delta n_{\parallel}}{n_{\parallel}(\rho_J, \theta)} \right]^2 \rightarrow \rho_J^2 = 1 - (1 - \hat{\rho}_J^2) \left[ 1 - \frac{\Delta n_{\parallel}}{n_{\parallel}(\rho_J, \theta)} \right]^{\frac{2}{\nu_T}} \quad (\text{G.36})$$

Note that in general:  $\rho_J > \hat{\rho}_J$ . The strictest location determining  $n_{\parallel}(\hat{\rho}_J, \theta)$  is the innermost radial point on the temperature profile where power is absorbed.

### Abridged Algorithm

Assume the following quantities are given as inputs:  $B_0, \theta, \bar{n}_{20}, \bar{T}_k, \varepsilon, \Delta n_{\parallel}, \eta_{LH}$ . Carry out the following steps:

1. Solve the equations below simultaneously to determine  $n_{\parallel}^2(\hat{\rho}_J, \theta), \hat{\omega}^2(\hat{\rho}_J, \theta)$ , and  $\hat{\rho}_J$

$$\begin{aligned} n_{\parallel}^2(\hat{\rho}_J, \theta) &= \left[ \left( 1 - \frac{1 - \hat{\omega}^2}{\hat{\omega}^2} X \right)^{1/2} + X^{1/2} \right]^2 \\ \hat{\omega}^2(\hat{\rho}_J, \theta) &= \frac{1}{2} \frac{X}{1+X} + \frac{1}{2} \left[ \frac{X^2}{(1+X)^2} + 4\gamma^2 \frac{X^3}{1+X} \right]^{1/2} \\ (1 + \nu_T) (1 - \hat{\rho}_J^2)^{\nu_T} n_{\parallel}^2(\hat{\rho}_J, \theta) &= \frac{m_e c^2}{2T} = \frac{28.39}{T_k} \end{aligned} \quad (\text{G.37})$$

2. Solve for  $\tilde{\eta}(\hat{\rho}_J, \theta)$

$$\tilde{\eta}(\hat{\rho}_J, \theta) = C M R \eta_0 \quad (\text{G.38})$$

3. Solve for  $n_{\parallel}(\rho_J, \theta)$

$$n_{\parallel}(\rho_J, \theta) = n_{\parallel}(\hat{\rho}_J, \theta) + \Delta n_{\parallel} \quad (\text{G.39})$$

4. Solve for  $\rho_J$

$$\rho_J^2 = 1 - (1 - \hat{\rho}_J^2) \left[ 1 - \frac{\Delta n_{\parallel}}{n_{\parallel}(\rho_J, \theta)} \right]^{2/\nu_T} \quad (\text{G.40})$$

5. Re-evaluate  $\tilde{\eta}(\rho_J, \theta)$  by substituting the values of  $\rho_J, n_{\parallel}(\rho_J, \theta)$  into Eq. (G.38)

6. Solve for  $\eta_{CD}$

$$\eta_{CD} = \frac{1}{2\pi} \left( \frac{e n_{20}}{m_e \nu_0 v_{Te}} \right) \tilde{\eta} = 0.06108 \frac{\eta_{LH}}{\ln \Lambda} (1 + \nu_T) \bar{T}_k (1 - \rho_J^2)^{\nu_r} \tilde{\eta}(\rho_J, \theta) \quad (\text{G.41})$$

In the end there will have to be some iteration with the rest of the analysis to make sure the values of  $\bar{n}_{20}$  and  $\bar{T}_k$  are self-consistent.



# Appendix H

## Compending Code Plots

This chapter gives a brief overview of the plots that come about from using this model on several reactor prototypes: Charybdis, Proteus, ARC, DEMO Pulsed, and the two ARIES ACT designs. The two types of results this information come in are: magnet strength scans and cost sensitivity studies.

In the former, all static variables are kept constant and only the magnet strength is allowed to change. Whereas, the latter focuses on changing one static variable at a time and finding several magnet strengths that satisfy certain constraints – e.g. the minimum capital cost or when the beta and kink limits are both just marginally satisfied.

You can recreate all the plots shown here at the following website. Note that this interactive plotting tool also allows you to view the Monte Carlo samplings, which produced the scatter plots used in this document.

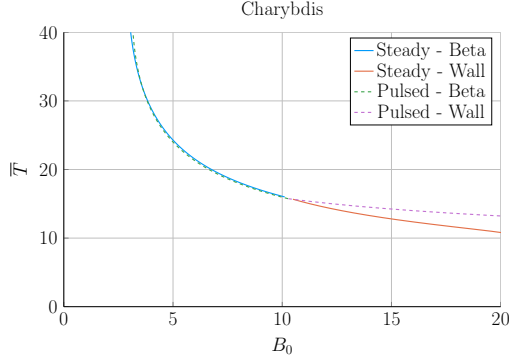
[www.fusion.codes](http://www.fusion.codes)

## H.1 Magnet Strength Scans

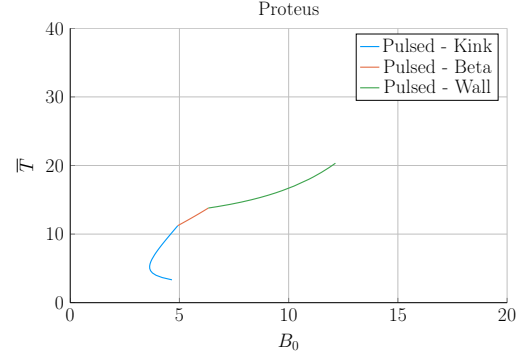
This section includes the following magnet strength scans:

1. Plasma Temperature –  $\overline{T}$
2. Plasma Density –  $\overline{n}$
3. Plasma Current –  $I_P$
4. Major Radius –  $R_0$
5. Plasma Pressure –  $\overline{p}$
6. Confinement Time –  $\tau_E$
7. Current Drive Efficiency –  $\eta_{CD}$
8. Bootstrap Fraction –  $f_{BS}$
9. Magnetic Energy –  $W_M$
10. Cost-per-Watt –  $C_W$
11. Divertor Head Load –  $q_{DV}$
12. Normalized Beta Normal –  $(\beta_N)_{norm}$
13. Normalized Kink Safety Factor –  $(q_{95})_{norm}$
14. Normalized Wall Loading –  $(P_W)_{norm}$
15. Fusion Power –  $P_F$
16. Blanket Thickness –  $b$
17. TF Coil Thickness –  $c$
18. Central Solenoid Thickness –  $d$
19. Central Solenoid Height –  $h_{CS}$
20. Central Solenoid Inner Radius –  $R_{CS}$

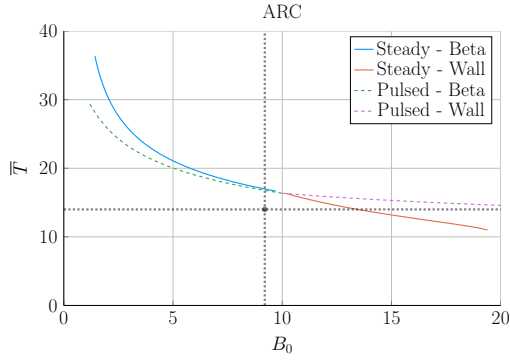
### H.1.1 Plasma Temperature – $\overline{T}$



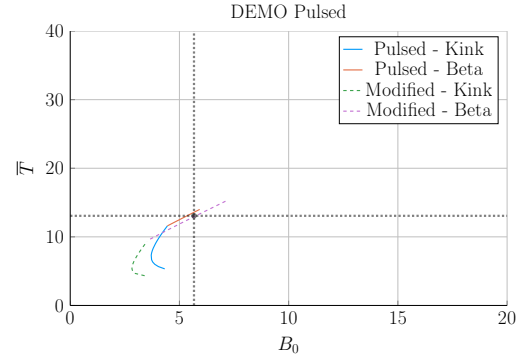
(a) Charybdis



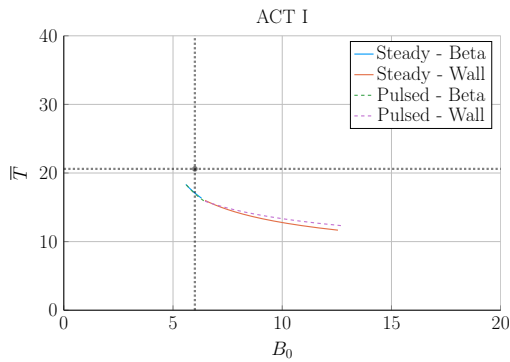
(b) Proteus



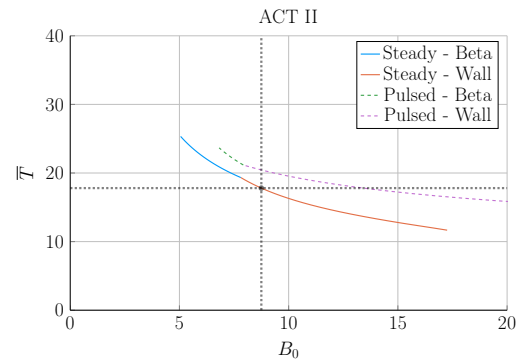
(c) ARC



(d) DEMO Pulsed



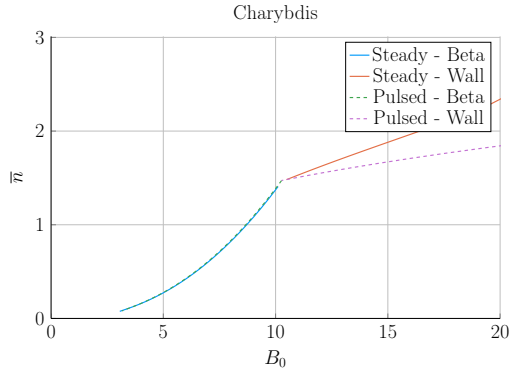
(e) ACT I



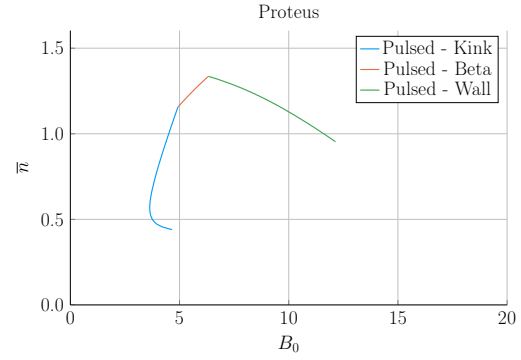
(f) ACT II

Figure H-1: Magnet Scan:  $\overline{T}$  vs.  $B_0$

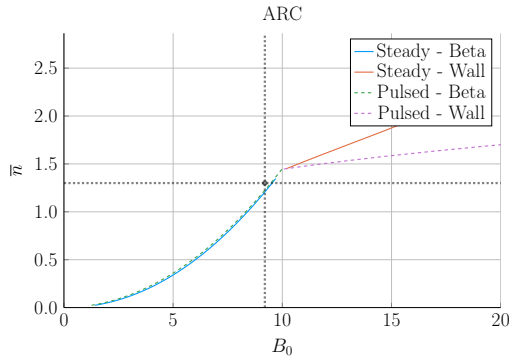
## H.1.2 Plasma Density – $\bar{n}$



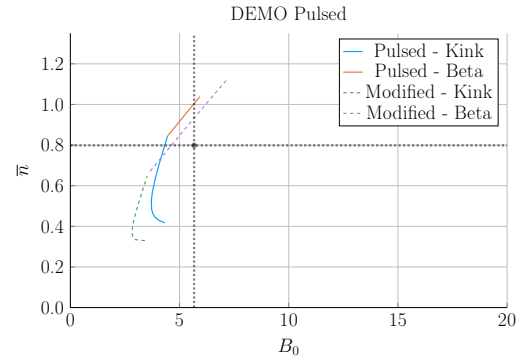
(a) Charybdis



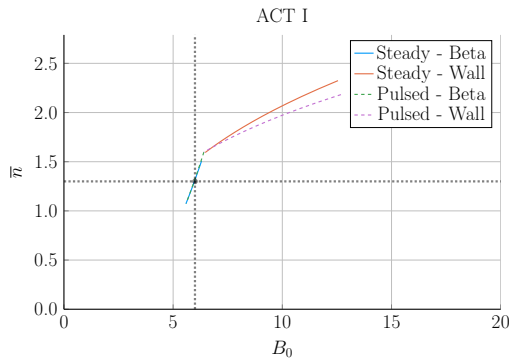
(b) Proteus



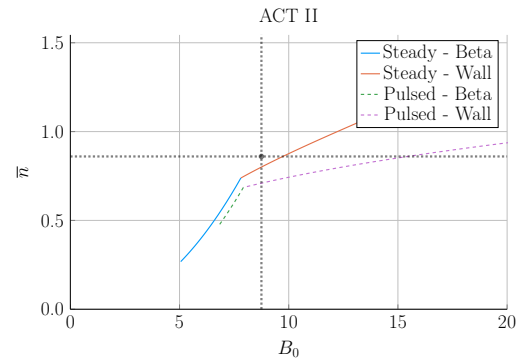
(c) ARC



(d) DEMO Pulsed



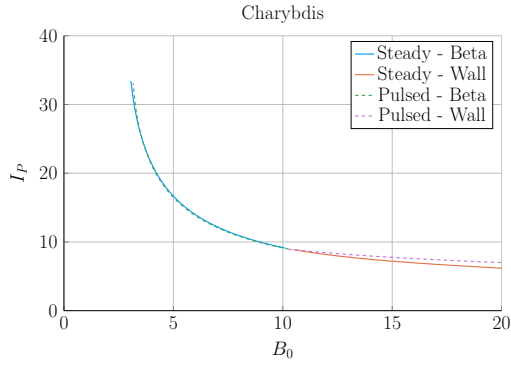
(e) ACT I



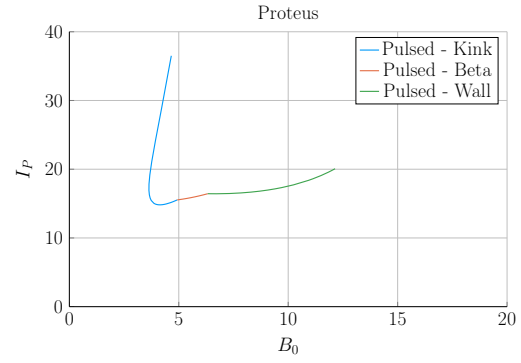
(f) ACT II

Figure H-2: Magnet Scan:  $\bar{n}$  vs.  $B_0$

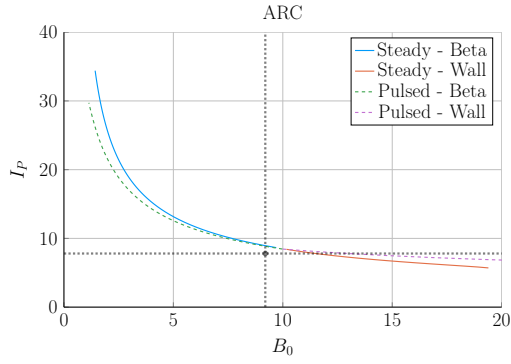
### H.1.3 Plasma Current – $I_P$



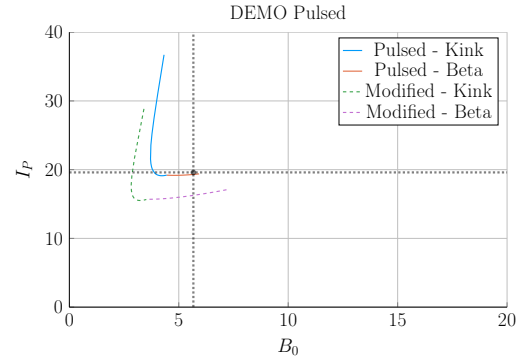
(a) Charybdis



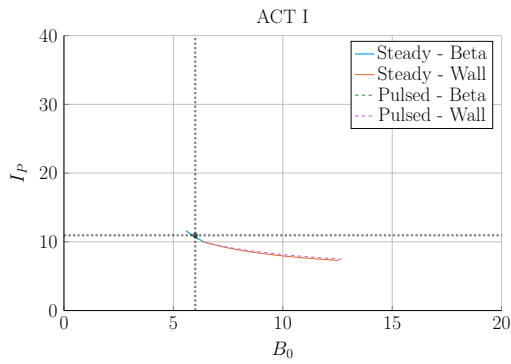
(b) Proteus



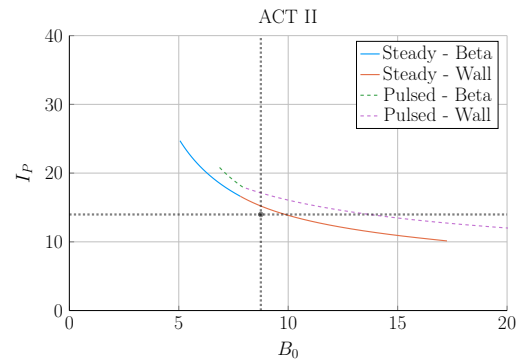
(c) ARC



(d) DEMO Pulsed



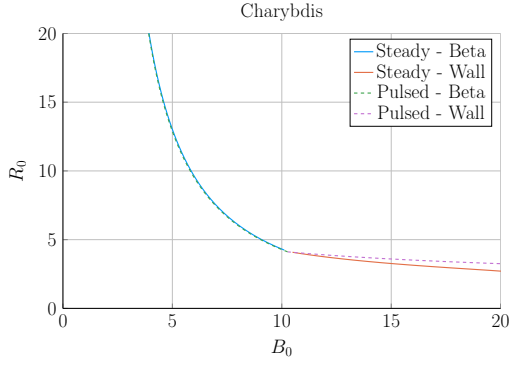
(e) ACT I



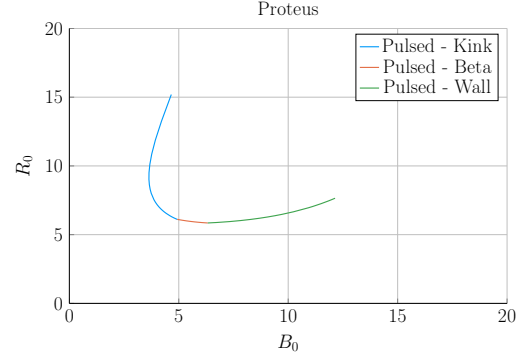
(f) ACT II

Figure H-3: Magnet Scan:  $I_P$  vs.  $B_0$

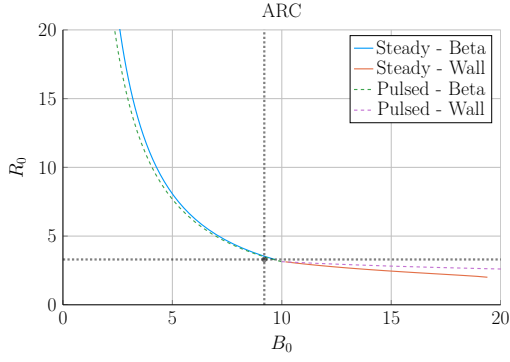
### H.1.4 Major Radius – $R_0$



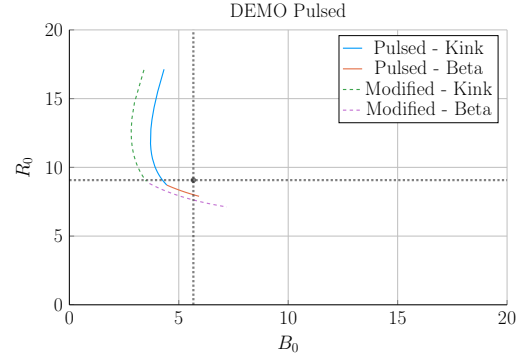
(a) Charybdis



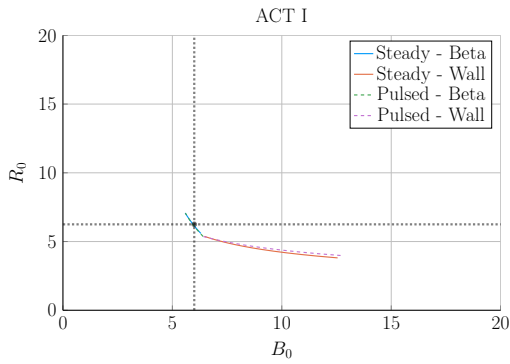
(b) Proteus



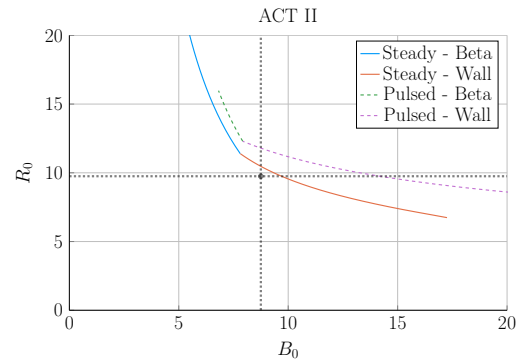
(c) ARC



(d) DEMO Pulsed



(e) ACT I

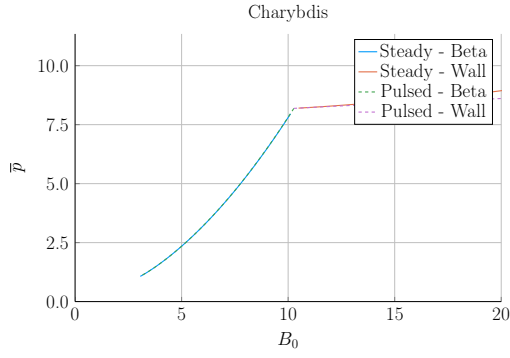


(f) ACT II

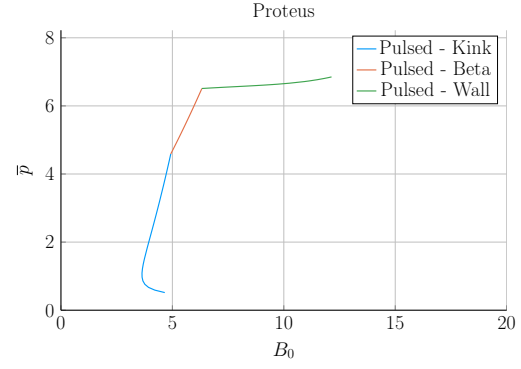
Figure H-4: Magnet Scan:  $R_0$  vs.  $B_0$



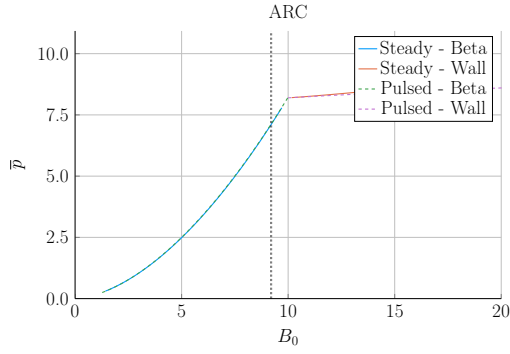
## H.1.5 Plasma Pressure – $\bar{p}$



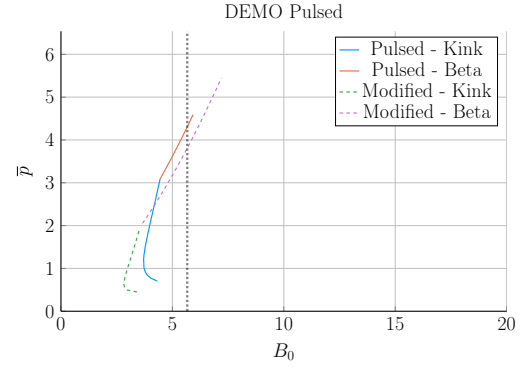
(a) Charybdis



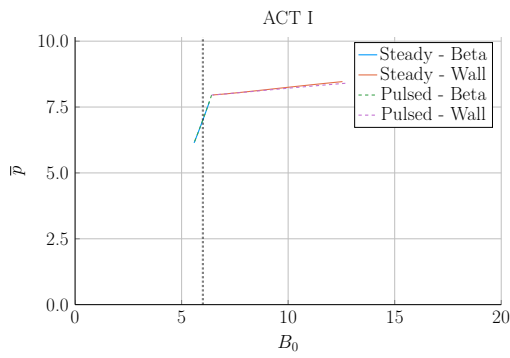
(b) Proteus



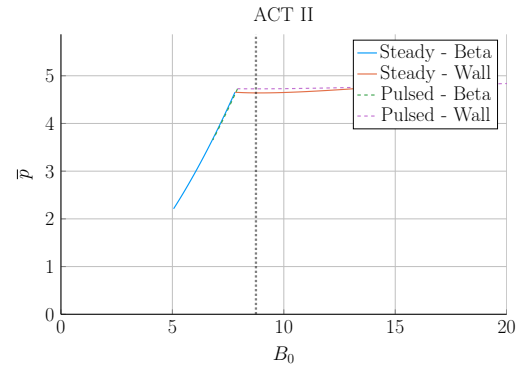
(c) ARC



(d) DEMO Pulsed



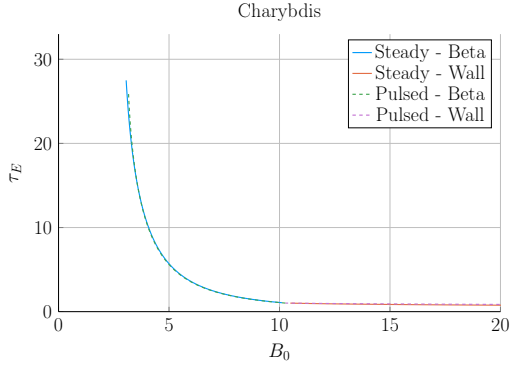
(e) ACT I



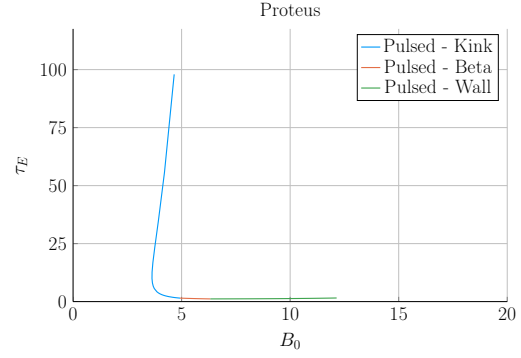
(f) ACT II

Figure H-5: Magnet Scan:  $\bar{p}$  vs.  $B_0$

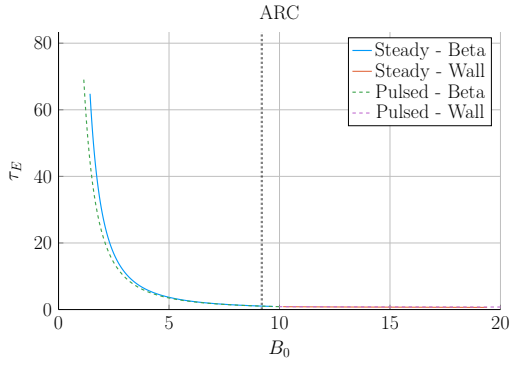
## H.1.6 Confinement Time – $\tau_E$



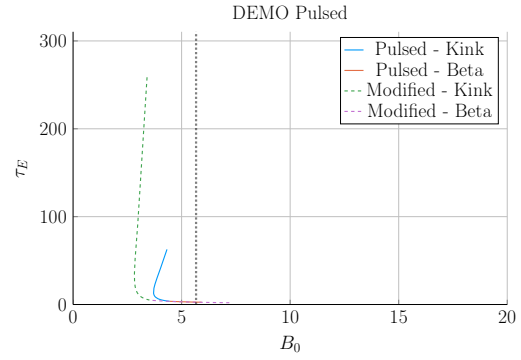
(a) Charybdis



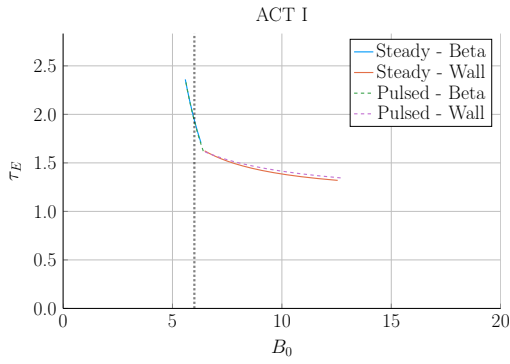
(b) Proteus



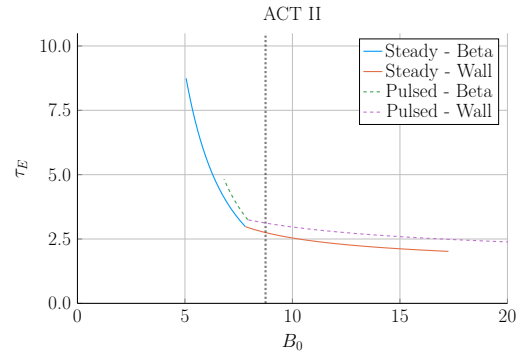
(c) ARC



(d) DEMO Pulsed



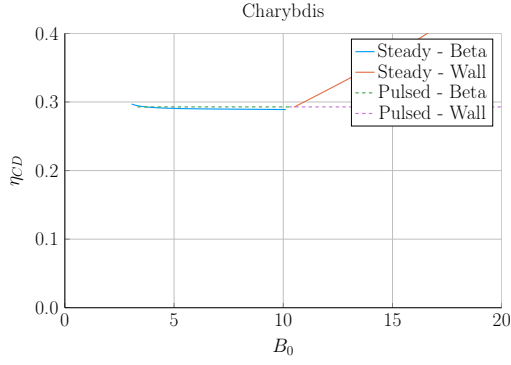
(e) ACT I



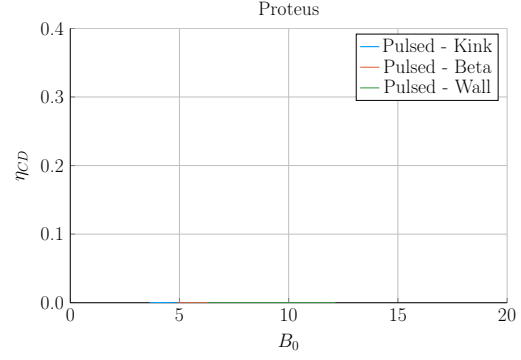
(f) ACT II

Figure H-6: Magnet Scan:  $\tau_E$  vs.  $B_0$

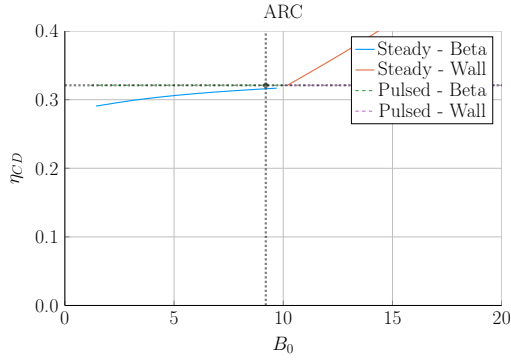
### H.1.7 Current Drive Efficiency – $\eta_{CD}$



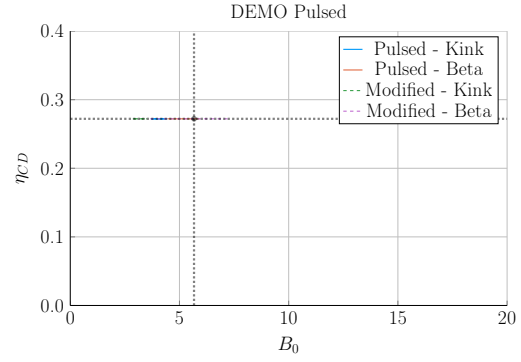
(a) Charybdis



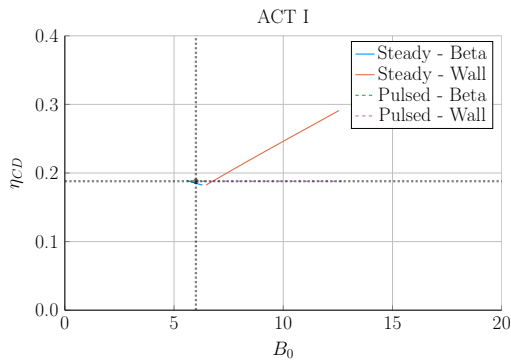
(b) Proteus



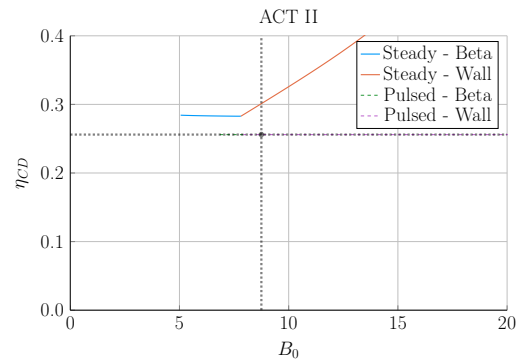
(c) ARC



(d) DEMO Pulsed



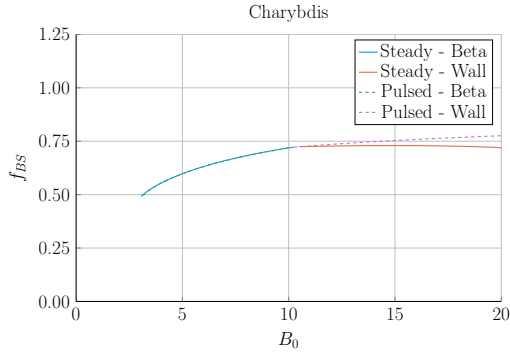
(e) ACT I



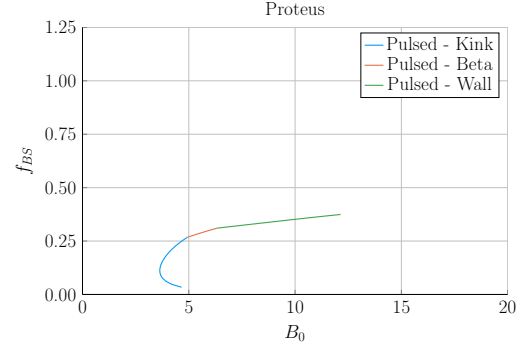
(f) ACT II

Figure H-7: Magnet Scan:  $\eta_{CD}$  vs.  $B_0$

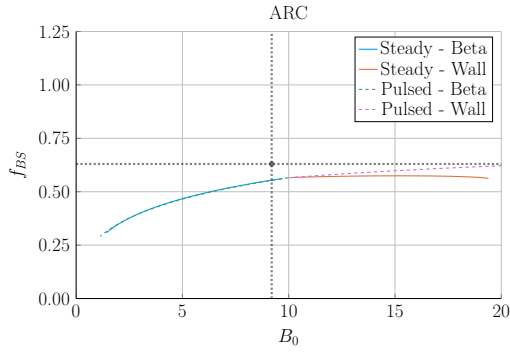
## H.1.8 Bootstrap Fraction – $f_{BS}$



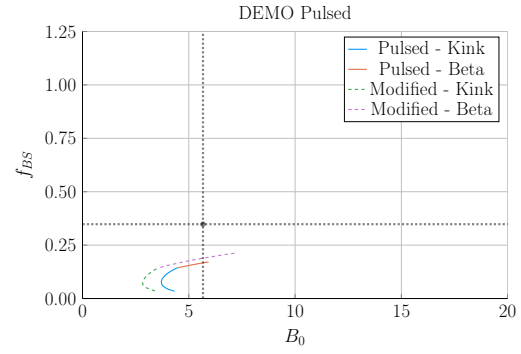
(a) Charybdis



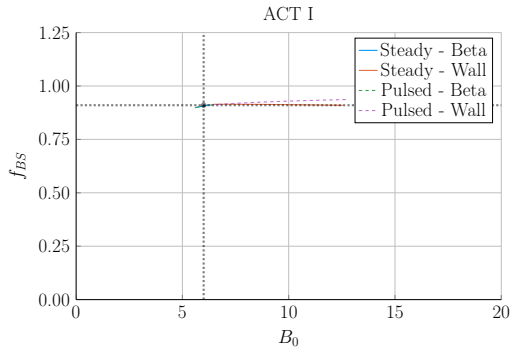
(b) Proteus



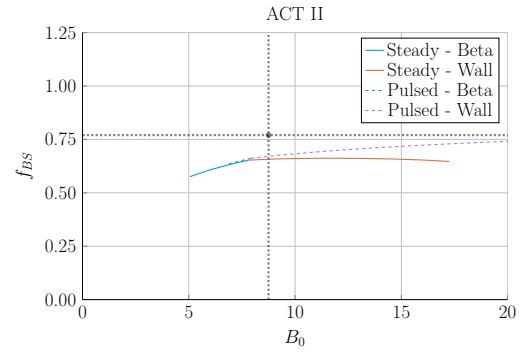
(c) ARC



(d) DEMO Pulsed



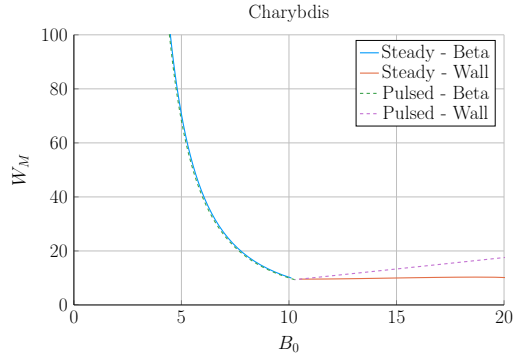
(e) ACT I



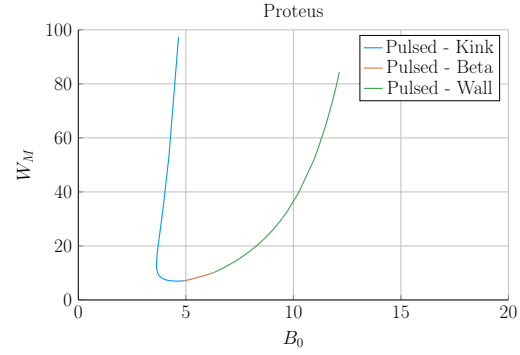
(f) ACT II

Figure H-8: Magnet Scan:  $f_{BS}$  vs.  $B_0$

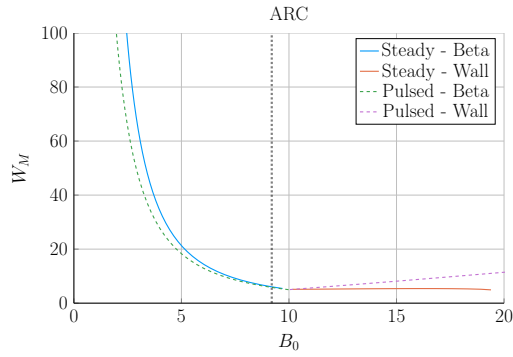
## H.1.9 Magnetic Energy – $W_M$



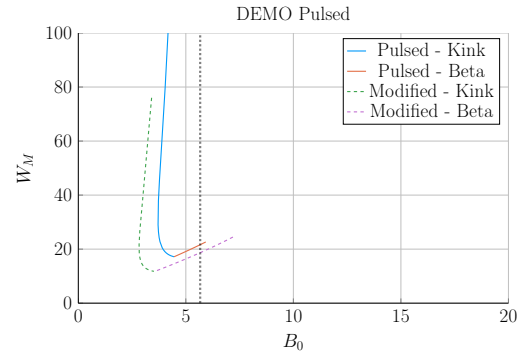
(a) Charybdis



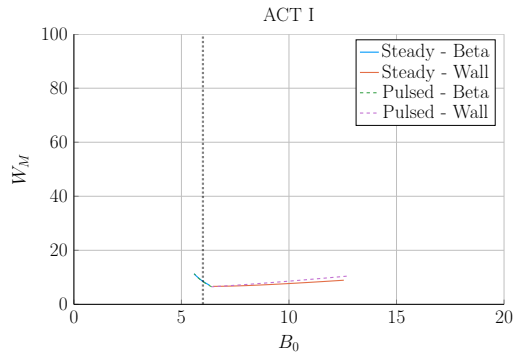
(b) Proteus



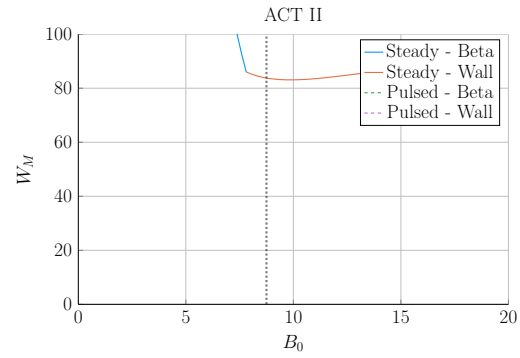
(c) ARC



(d) DEMO Pulsed



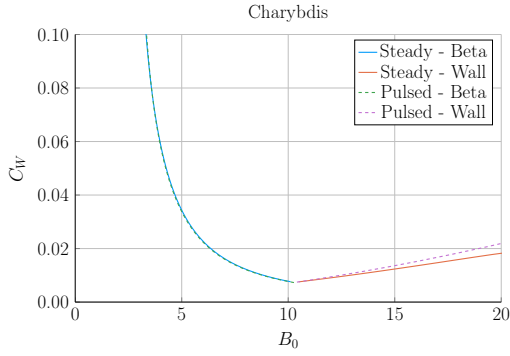
(e) ACT I



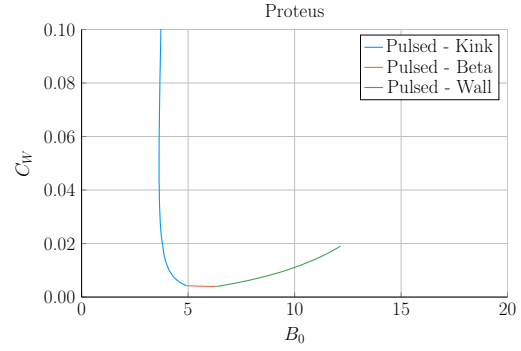
(f) ACT II

Figure H-9: Magnet Scan:  $W_M$  vs.  $B_0$

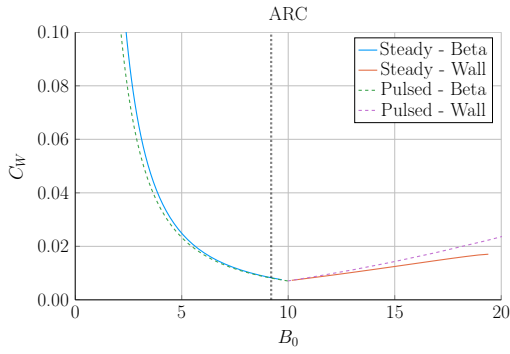
## H.1.10 Cost-per-Watt – $C_W$



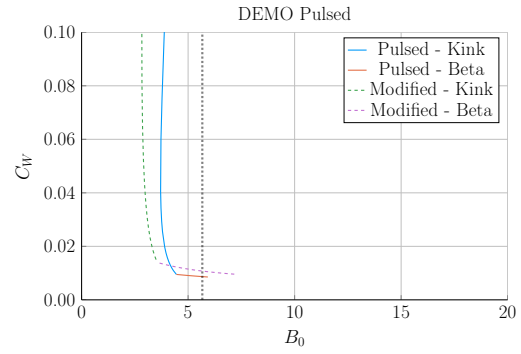
(a) Charybdis



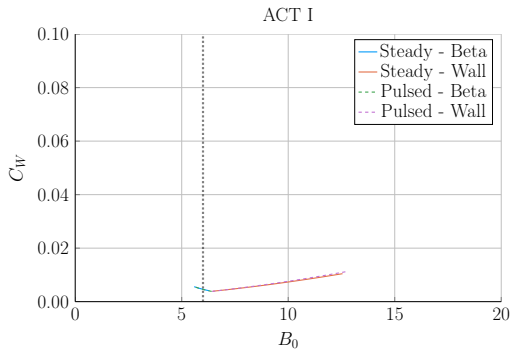
(b) Proteus



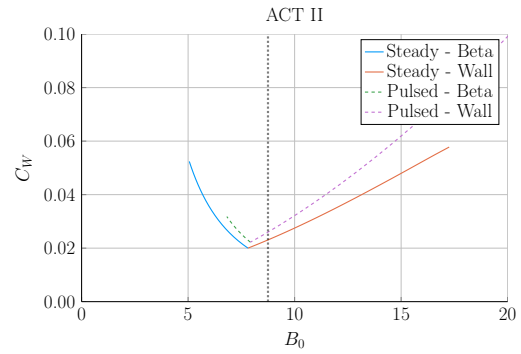
(c) ARC



(d) DEMO Pulsed



(e) ACT I



(f) ACT II

Figure H-10: Magnet Scan:  $C_W$  vs.  $B_0$

### H.1.11 Divertor Head Load – $q_{DV}$

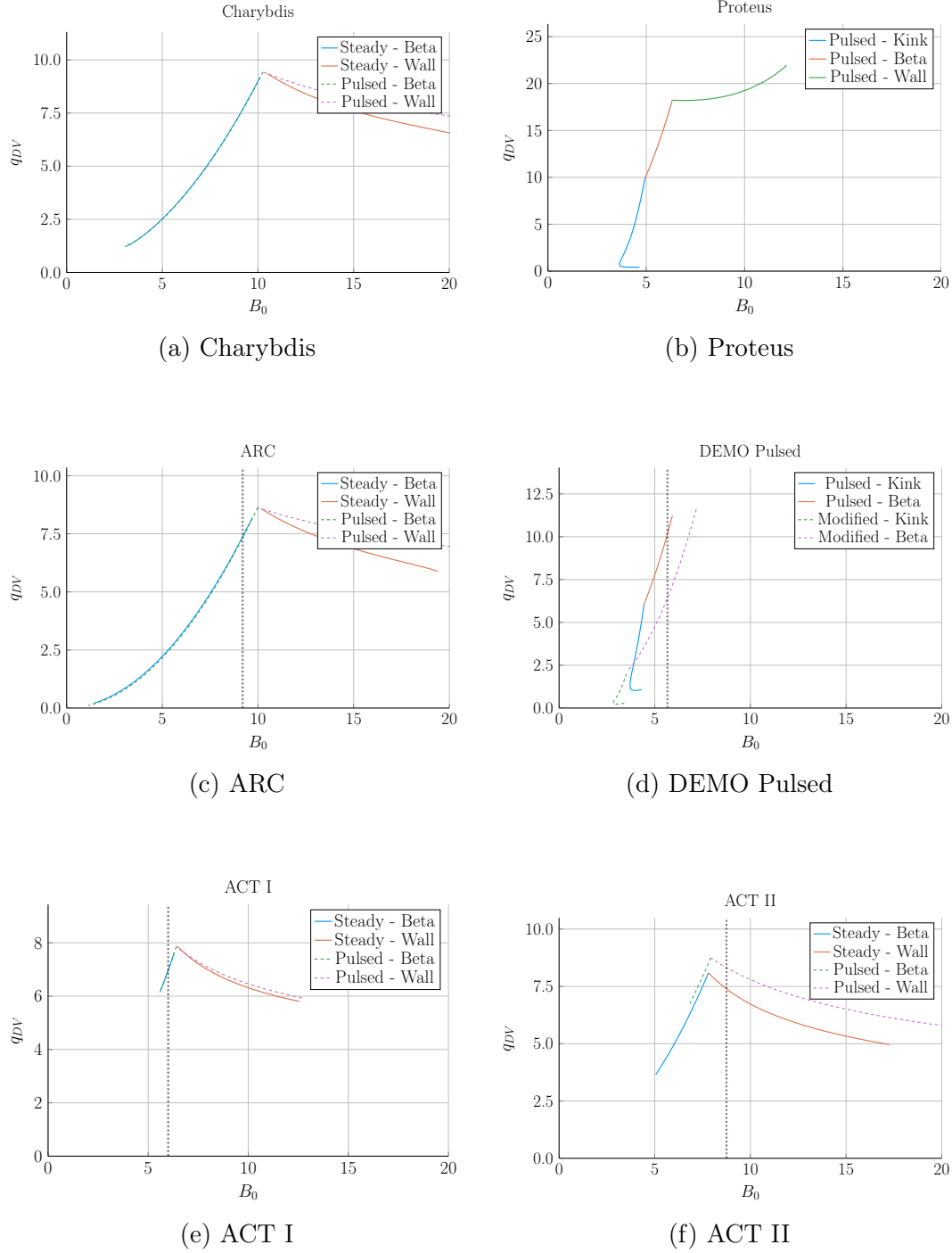
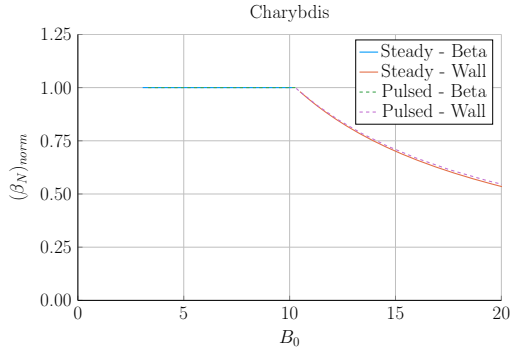
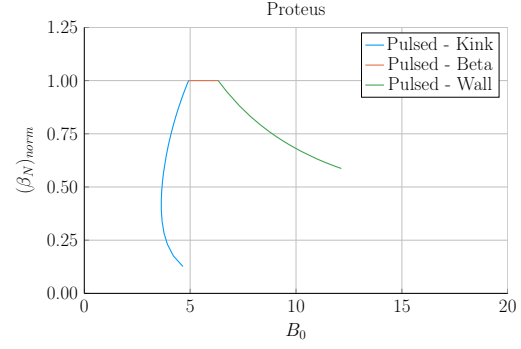


Figure H-11: Magnet Scan:  $q_{DV}$  vs.  $B_0$

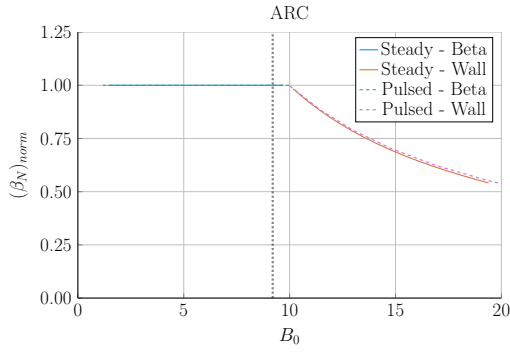
## H.1.12 Normalized Beta Normal – $(\beta_N)_{norm}$



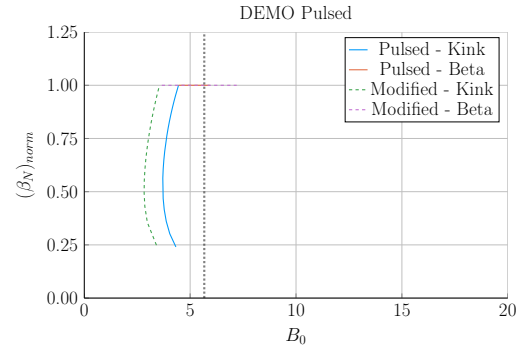
(a) Charybdis



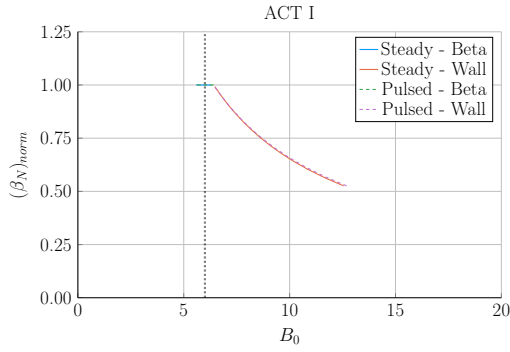
(b) Proteus



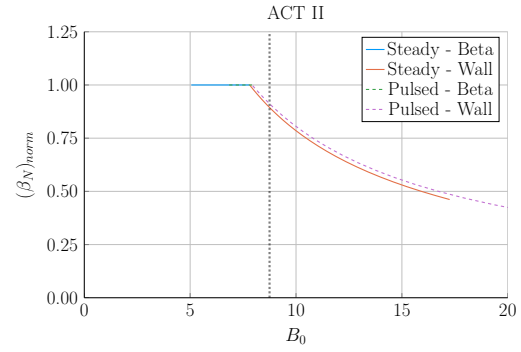
(c) ARC



(d) DEMO Pulsed



(e) ACT I

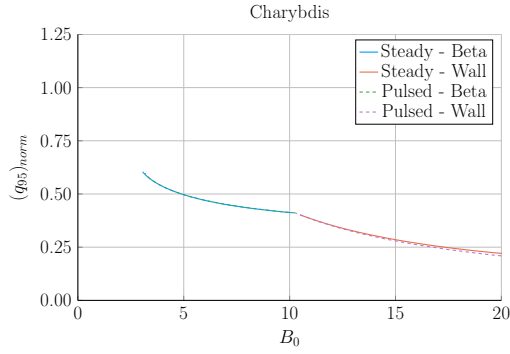


(f) ACT II

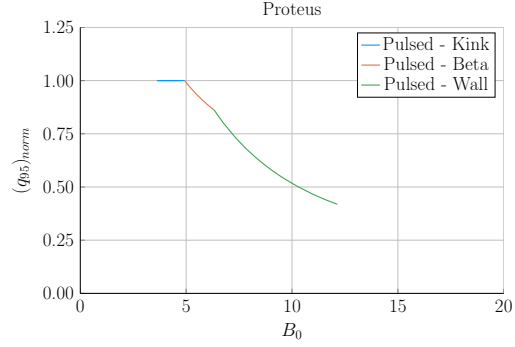
Figure H-12: Magnet Scan:  $(\beta_N)_{norm}$  vs.  $B_0$



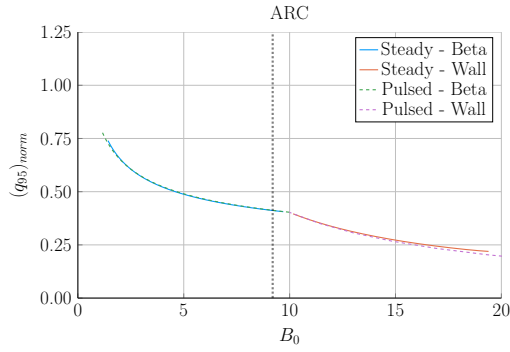
### H.1.13 Normalized Kink Safety Factor – $(q_{95})_{norm}$



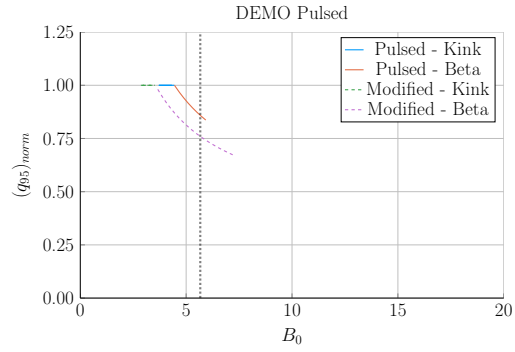
(a) Charybdis



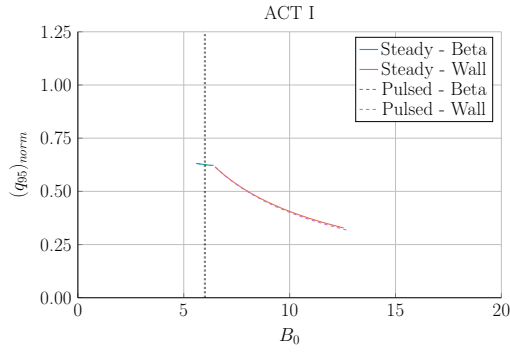
(b) Proteus



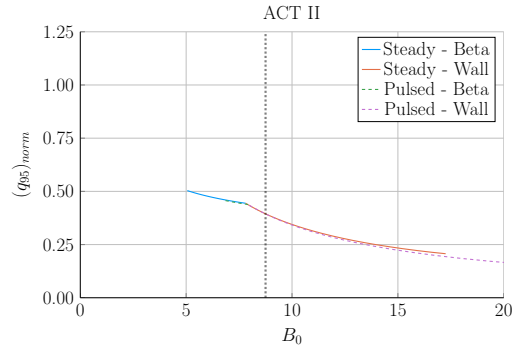
(c) ARC



(d) DEMO Pulsed



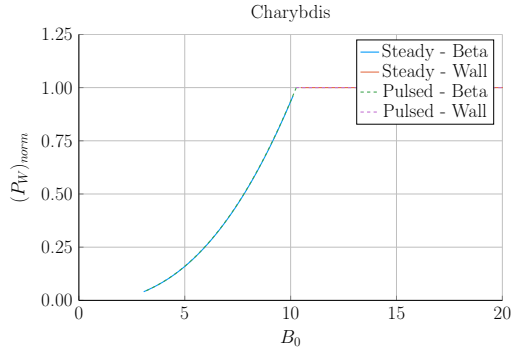
(e) ACT I



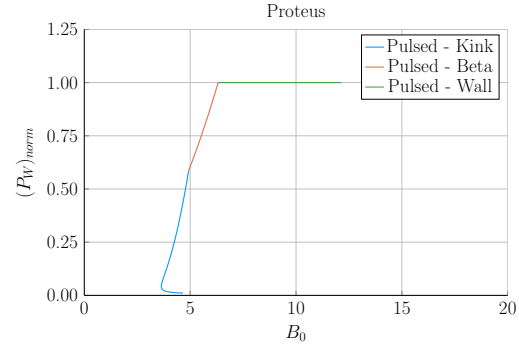
(f) ACT II

Figure H-13: Magnet Scan:  $(q_{95})_{norm}$  vs.  $B_0$

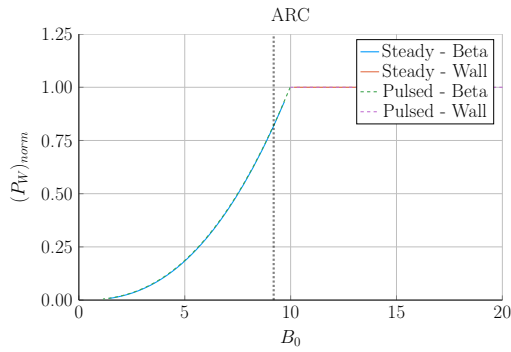
### H.1.14 Normalized Wall Loading – $(P_W)_{norm}$



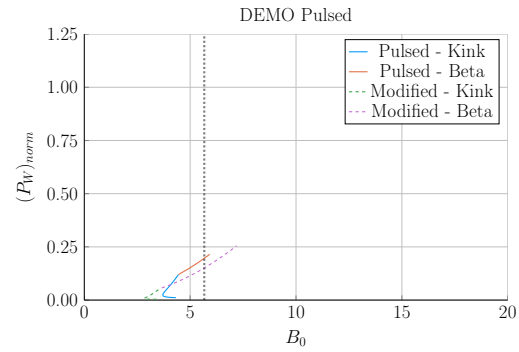
(a) Charybdis



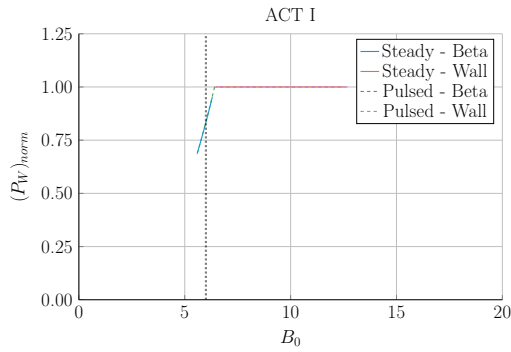
(b) Proteus



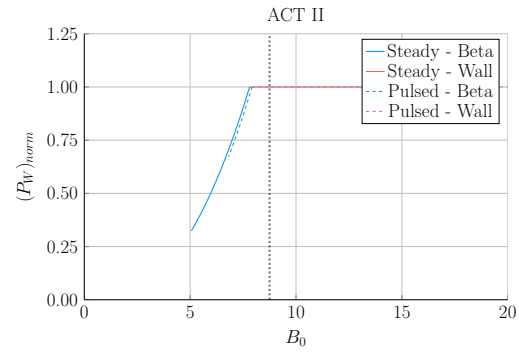
(c) ARC



(d) DEMO Pulsed



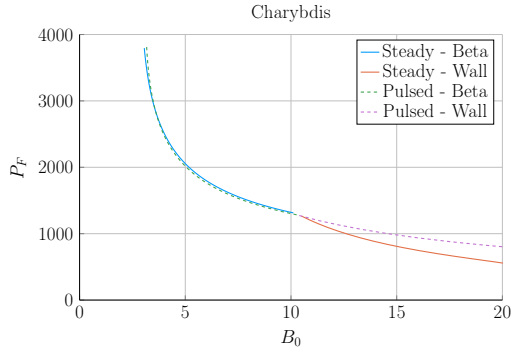
(e) ACT I



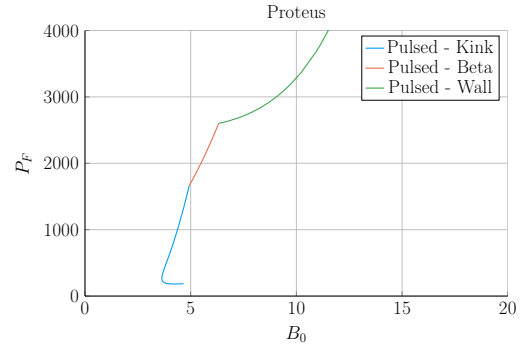
(f) ACT II

Figure H-14: Magnet Scan:  $(P_W)_{norm}$  vs.  $B_0$

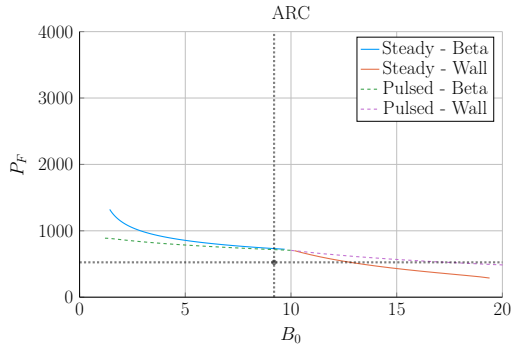
## H.1.15 Fusion Power – $P_F$



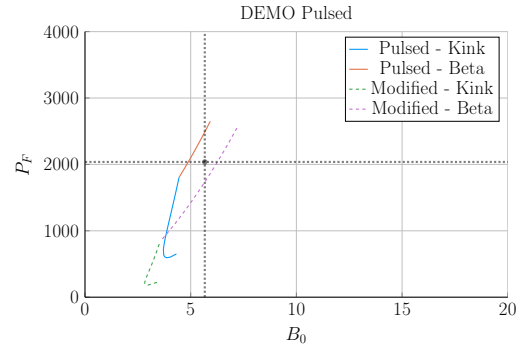
(a) Charybdis



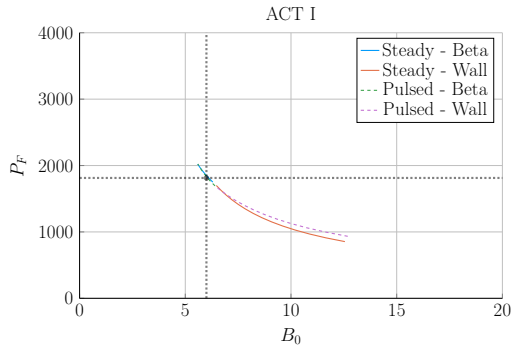
(b) Proteus



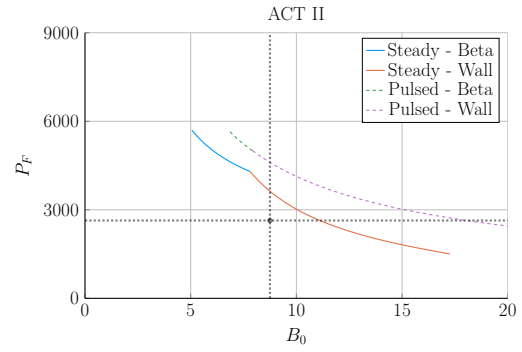
(c) ARC



(d) DEMO Pulsed



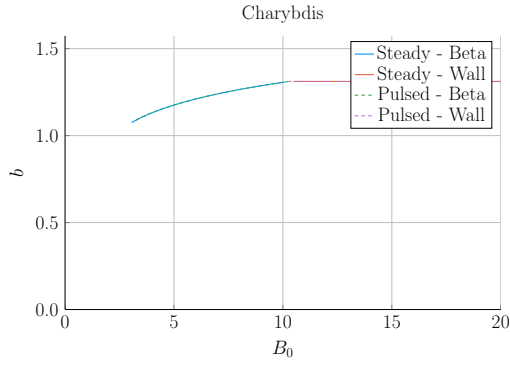
(e) ACT I



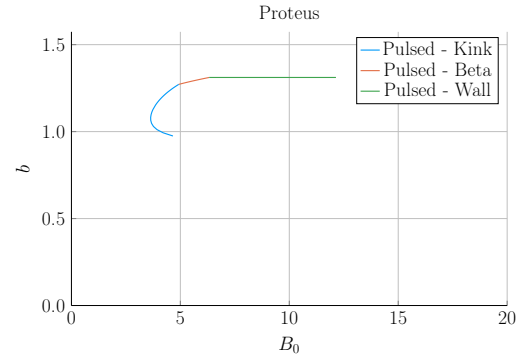
(f) ACT II

Figure H-15: Magnet Scan:  $P_F$  vs.  $B_0$

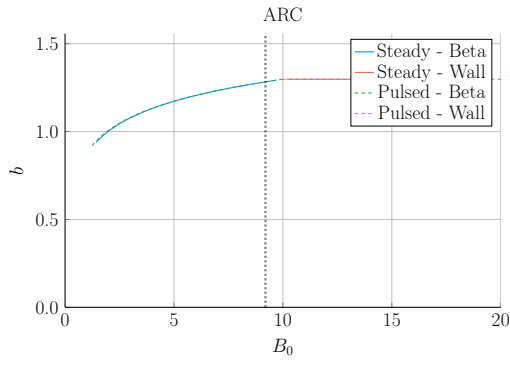
## H.1.16 Blanket Thickness – $b$



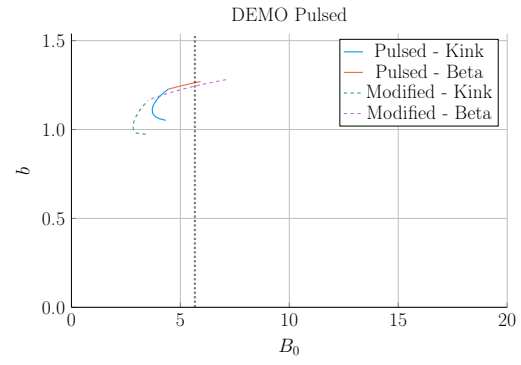
(a) Charybdis



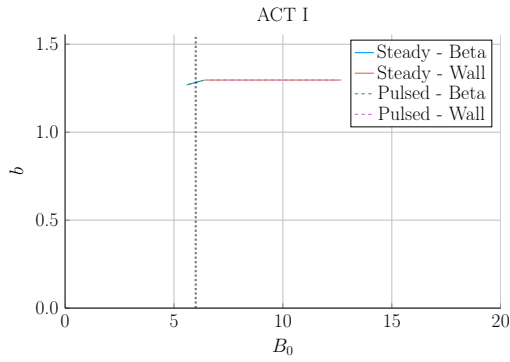
(b) Proteus



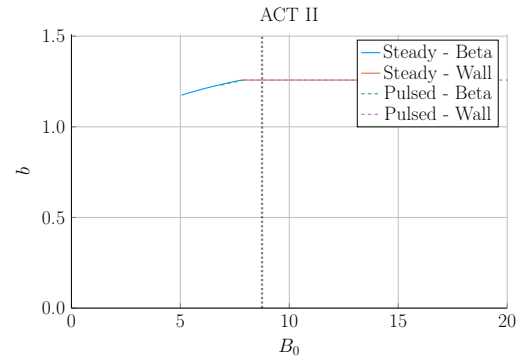
(c) ARC



(d) DEMO Pulsed



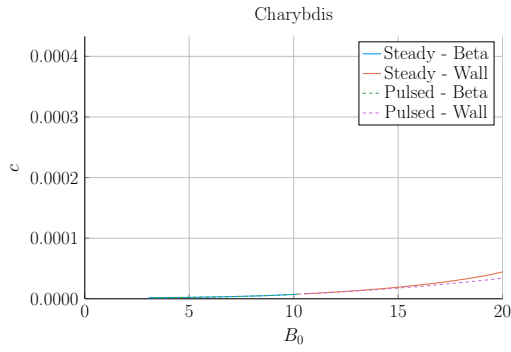
(e) ACT I



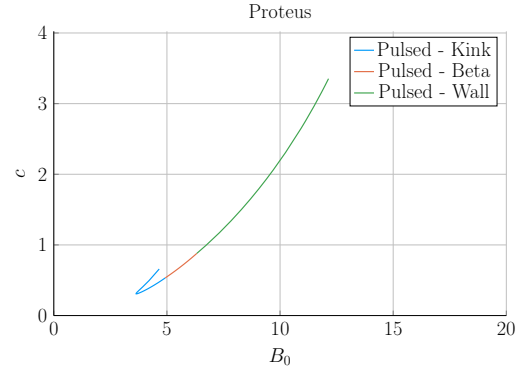
(f) ACT II

Figure H-16: Magnet Scan:  $b$  vs.  $B_0$

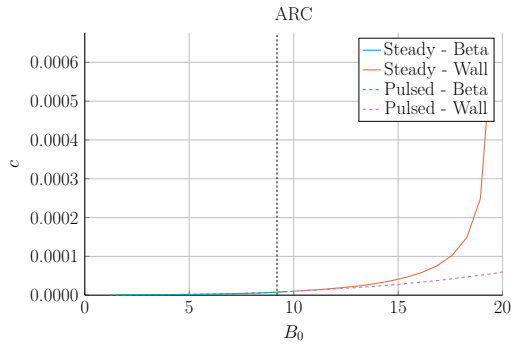
### H.1.17 TF Coil Thickness – $c$



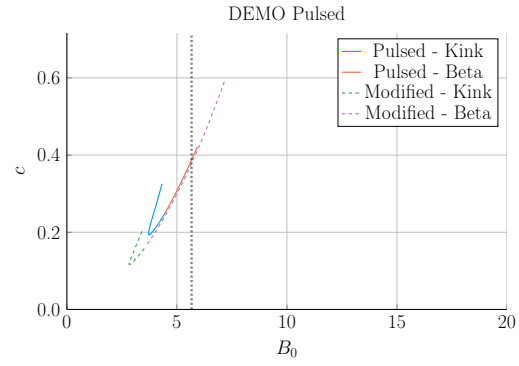
(a) Charybdis



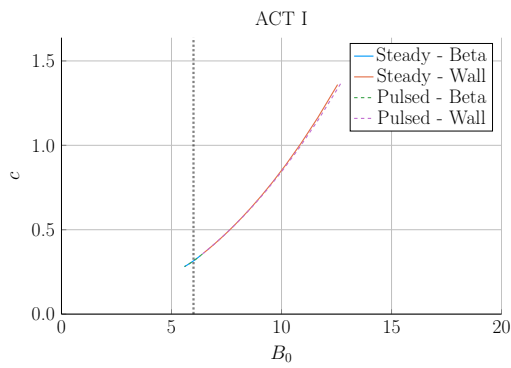
(b) Proteus



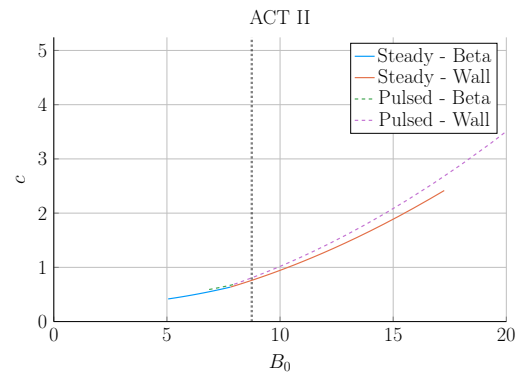
(c) ARC



(d) DEMO Pulsed



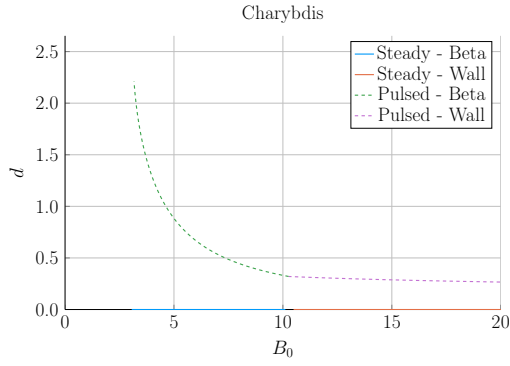
(e) ACT I



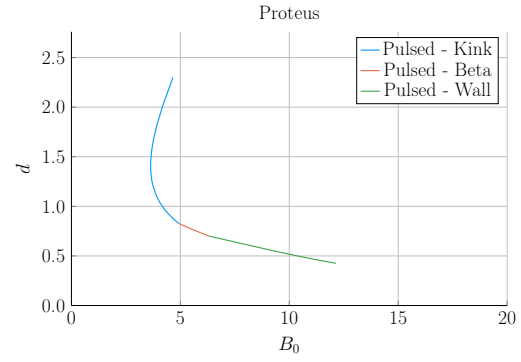
(f) ACT II

Figure H-17: Magnet Scan:  $c$  vs.  $B_0$

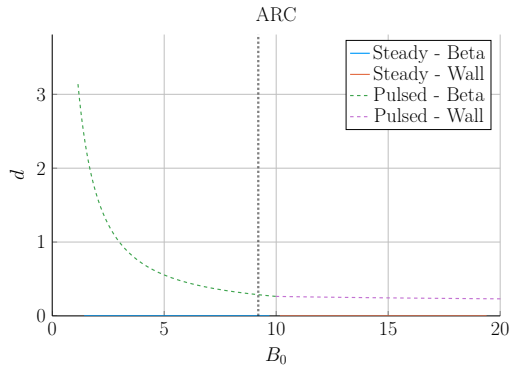
## H.1.18 Central Solenoid Thickness – $d$



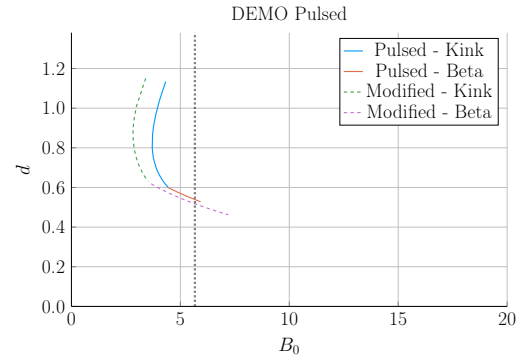
(a) Charybdis



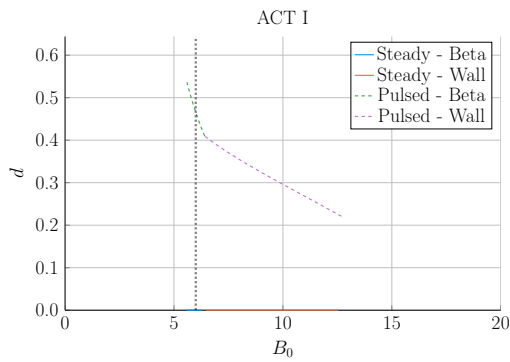
(b) Proteus



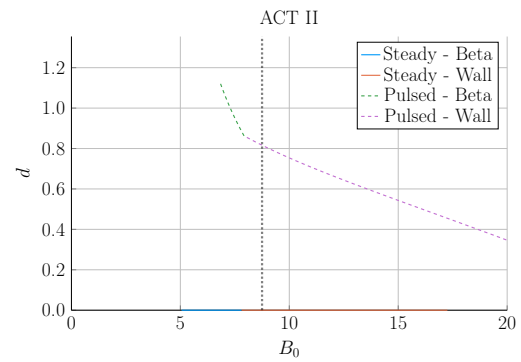
(c) ARC



(d) DEMO Pulsed



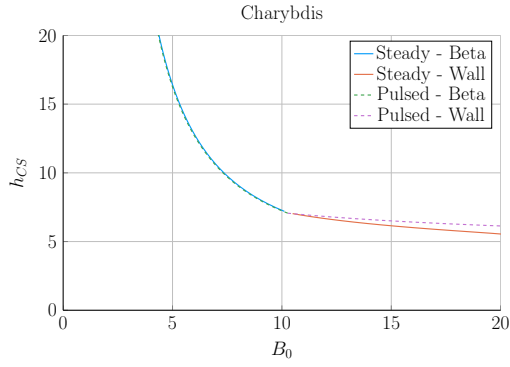
(e) ACT I



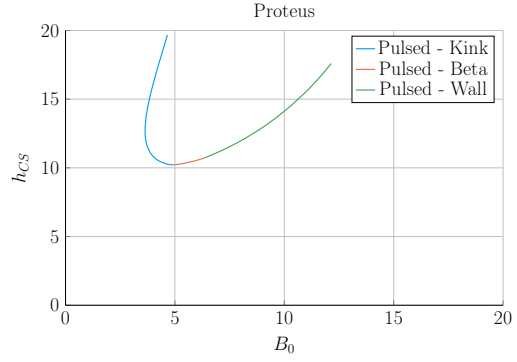
(f) ACT II

Figure H-18: Magnet Scan:  $d$  vs.  $B_0$

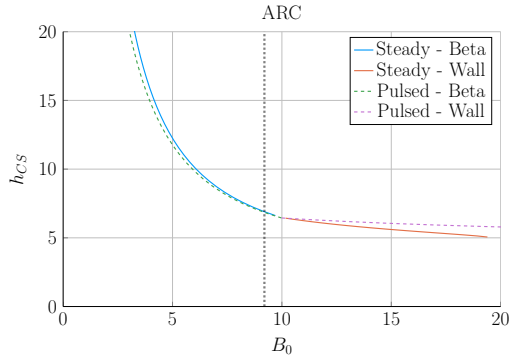
## H.1.19 Central Solenoid Height – $h_{CS}$



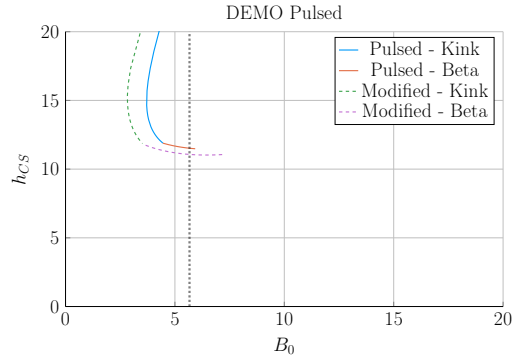
(a) Charybdis



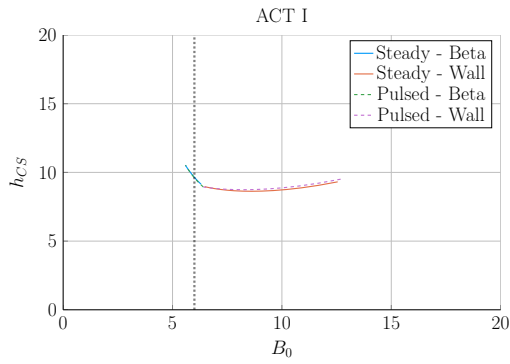
(b) Proteus



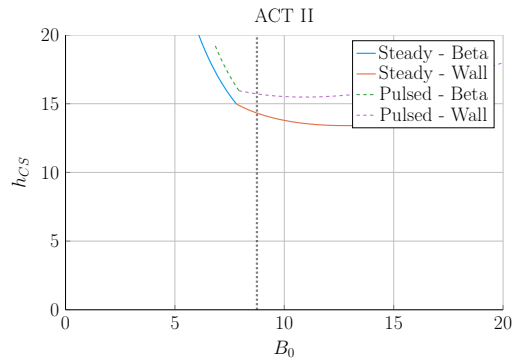
(c) ARC



(d) DEMO Pulsed



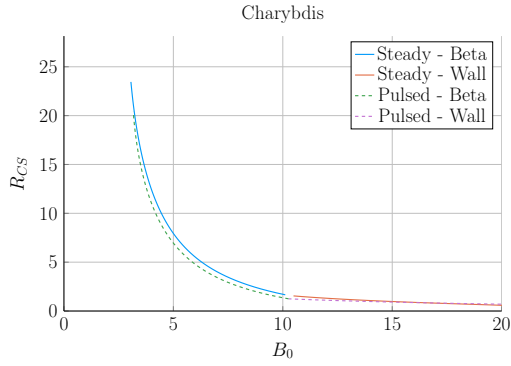
(e) ACT I



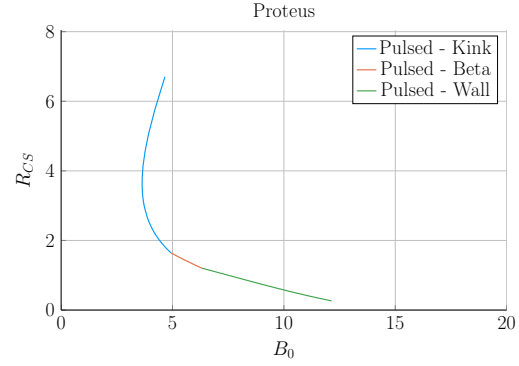
(f) ACT II

Figure H-19: Magnet Scan:  $h_{CS}$  vs.  $B_0$

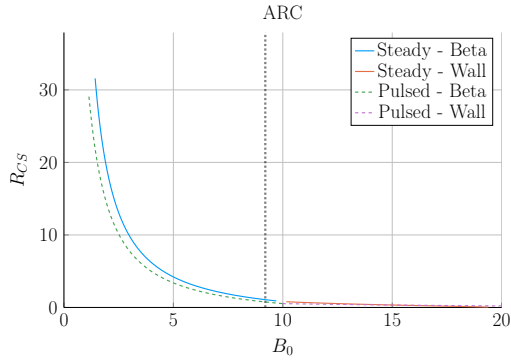
## H.1.20 Central Solenoid Inner Radius – $R_{CS}$



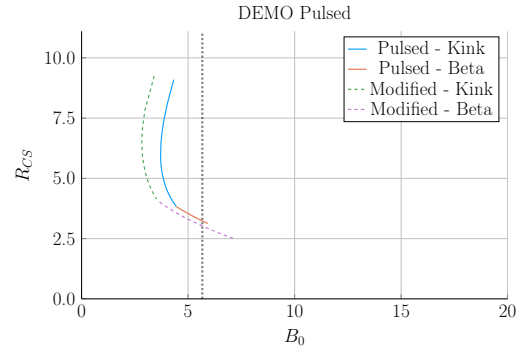
(a) Charybdis



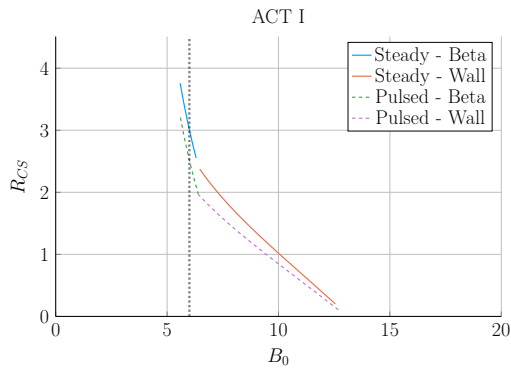
(b) Proteus



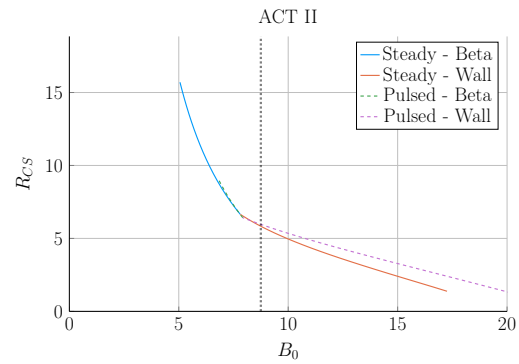
(c) ARC



(d) DEMO Pulsed



(e) ACT I



(f) ACT II

Figure H-20: Magnet Scan:  $R_{CS}$  vs.  $B_0$

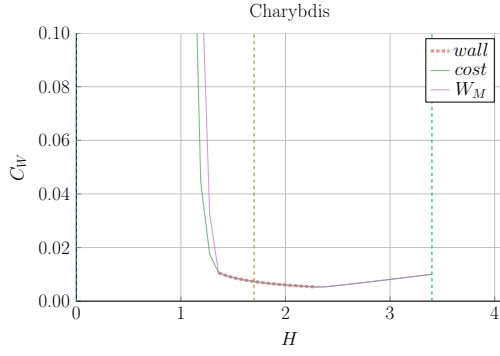


## H.2 Cost Sensitivity Studies

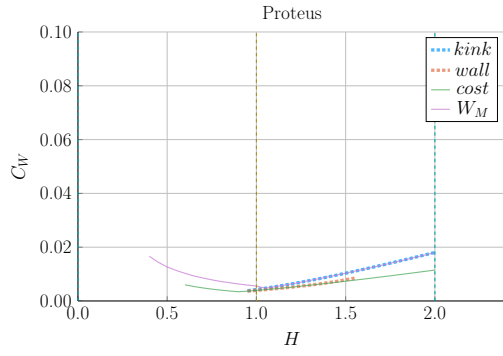
This section includes the following cost sensitivity studies:

1. Enhancement Factor –  $H$
2. Physics Gain –  $Q$
3. Flattop Duration –  $\tau_{FT}$
4. Greenwald Fraction –  $N_G$
5. Dilution Factor –  $f_D$
6. Effective Charge –  $Z_{eff}$
7. Inverse Aspect Ratio –  $\varepsilon$
8. Elongation –  $\kappa_{95}$
9. Triangularity –  $\delta_{95}$
10. Density Peaking Factor –  $\nu_n$
11. Temperature Peaking Factor –  $\nu_T$
12. Internal Inductance –  $l_i$
13. Max Beta Normal –  $(\beta_N)_{max}$
14. Max Kink Safety Factor –  $(q_{95})_{max}$
15. Max Wall Loading –  $(P_W)_{max}$

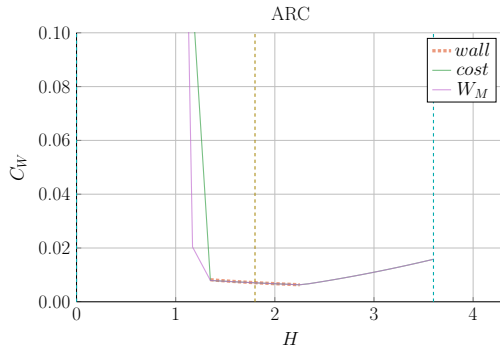
## H.2.1 Enhancement Factor – $H$



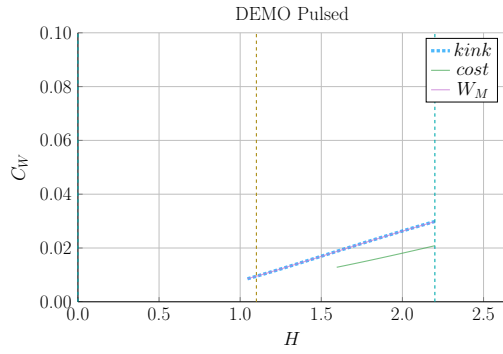
(a) Charybdis



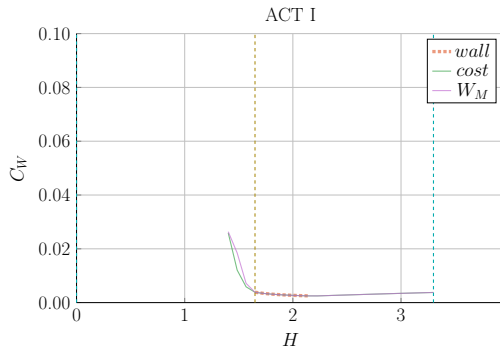
(b) Proteus



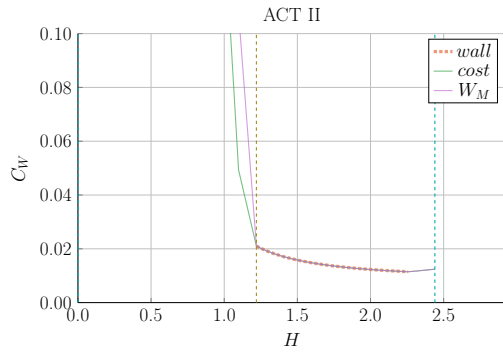
(c) ARC



(d) DEMO Pulsed



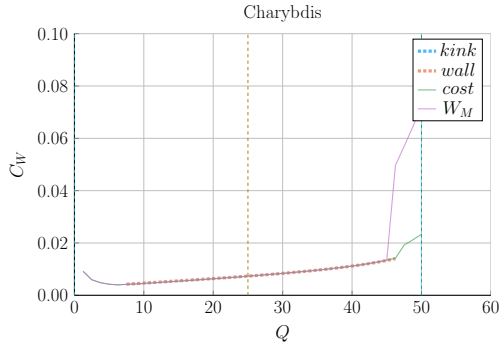
(e) ACT I



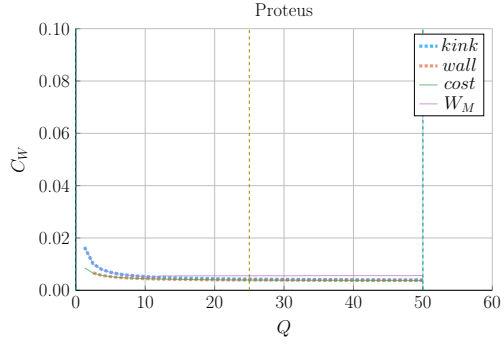
(f) ACT II

Figure H-21: Cost Sensitivity:  $H$  vs.  $B_0$

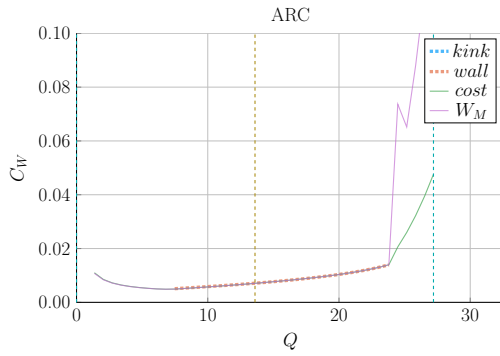
## H.2.2 Physics Gain – $Q$



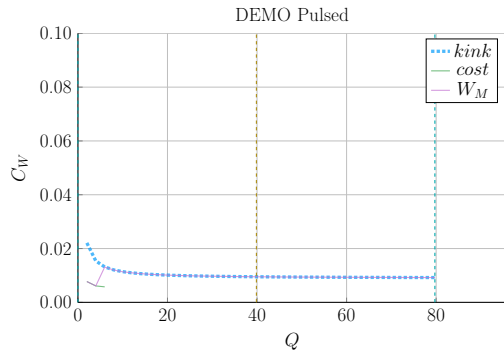
(a) Charybdis



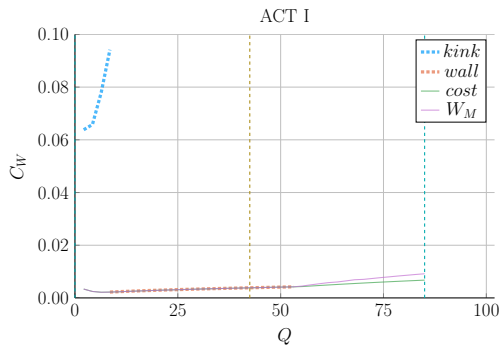
(b) Proteus



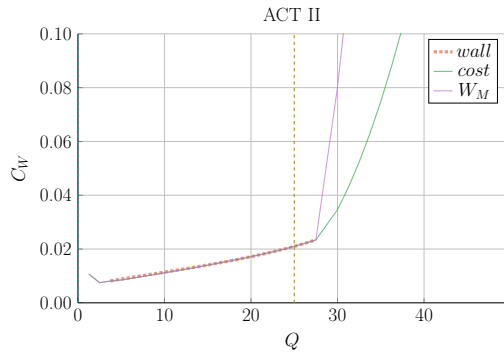
(c) ARC



(d) DEMO Pulsed



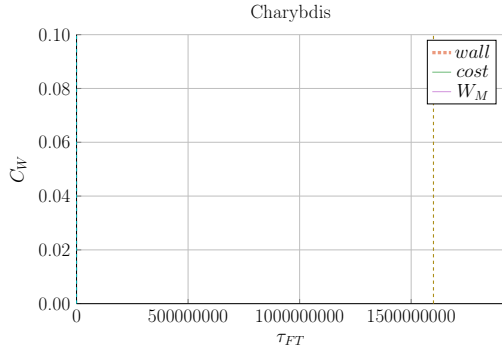
(e) ACT I



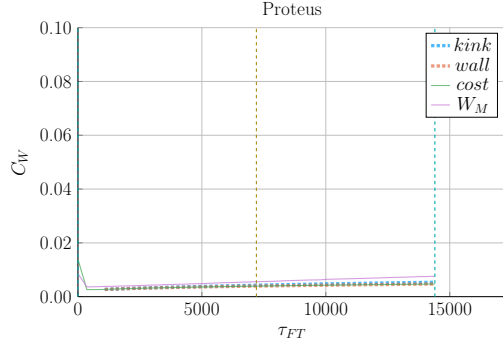
(f) ACT II

Figure H-22: Cost Sensitivity:  $Q$  vs.  $B_0$

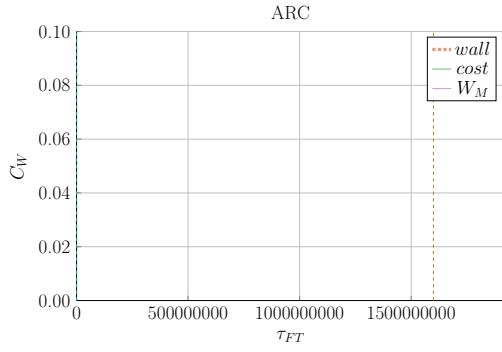
### H.2.3 Flattop Duration – $\tau_{FT}$



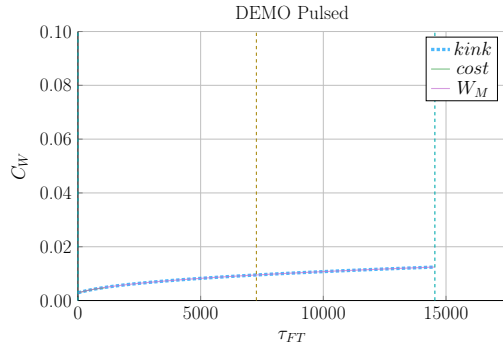
(a) Charybdis



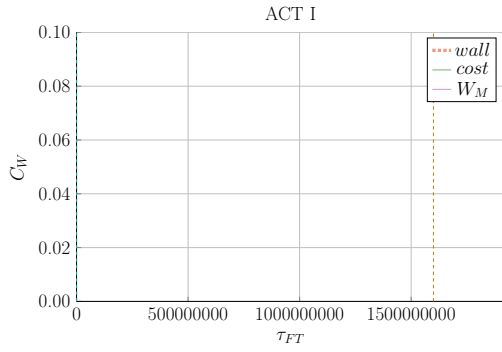
(b) Proteus



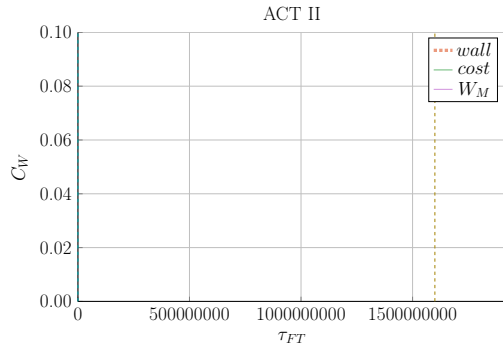
(c) ARC



(d) DEMO Pulsed



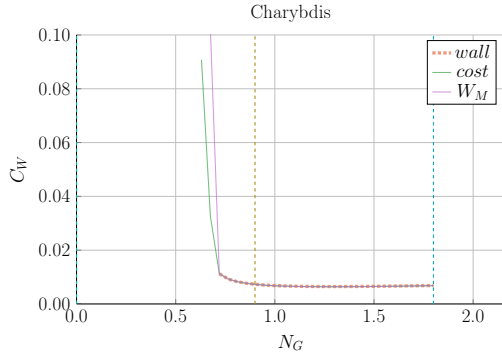
(e) ACT I



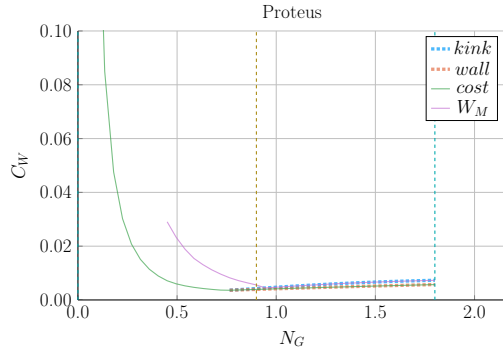
(f) ACT II

Figure H-23: Cost Sensitivity:  $\tau_{FT}$  vs.  $B_0$

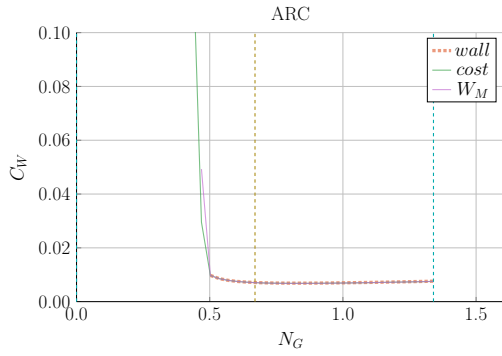
## H.2.4 Greenwald Fraction – $N_G$



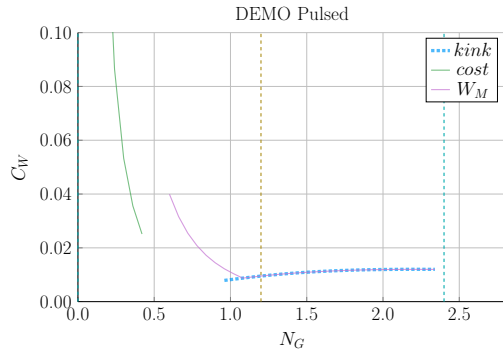
(a) Charybdis



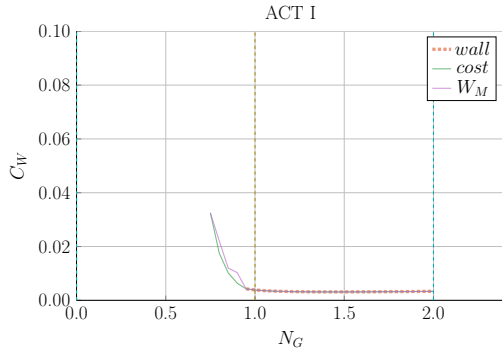
(b) Proteus



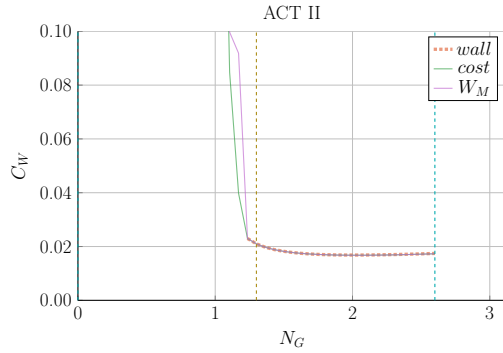
(c) ARC



(d) DEMO Pulsed



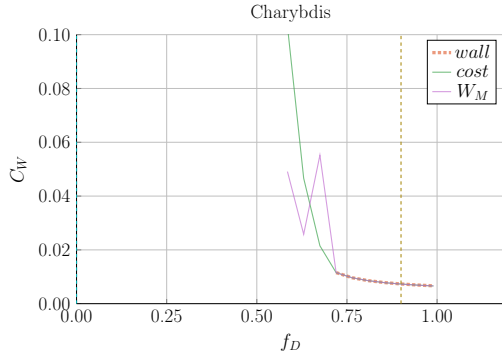
(e) ACT I



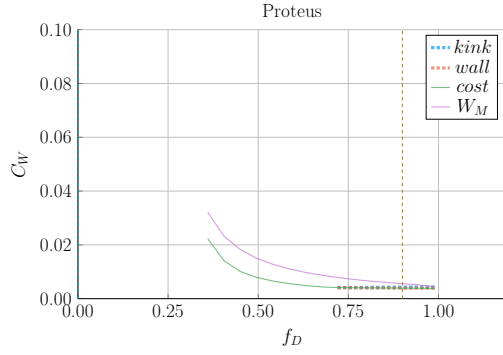
(f) ACT II

Figure H-24: Cost Sensitivity:  $N_G$  vs.  $B_0$

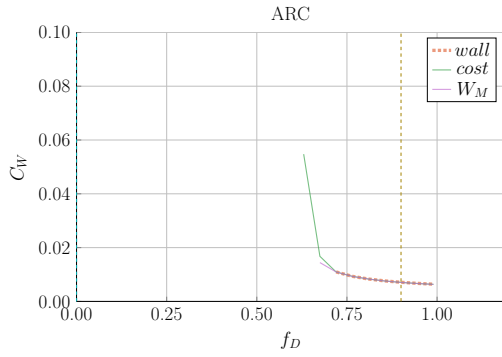
## H.2.5 Dilution Factor – $f_D$



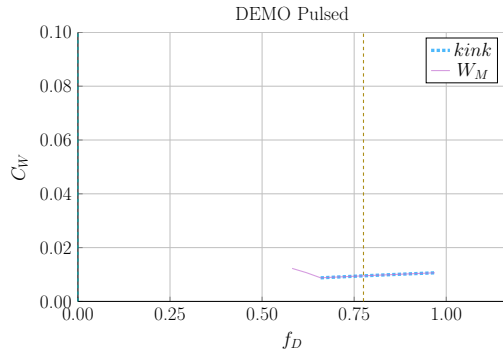
(a) Charybdis



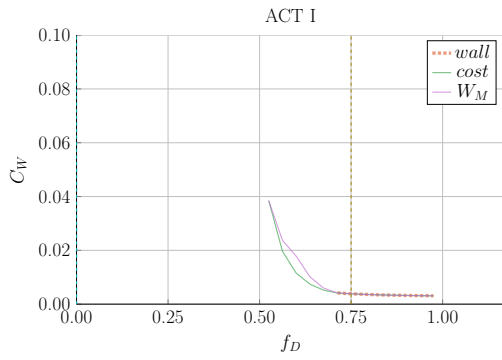
(b) Proteus



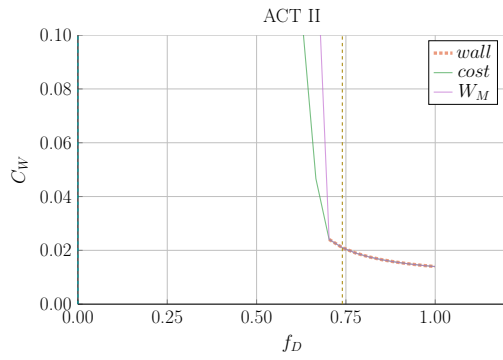
(c) ARC



(d) DEMO Pulsed



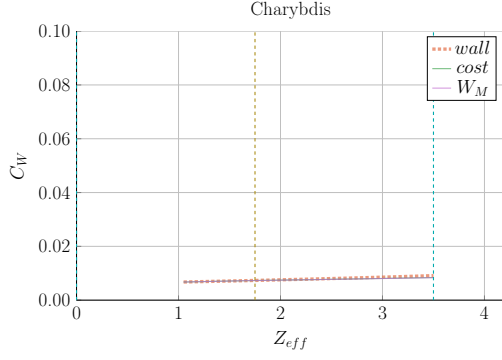
(e) ACT I



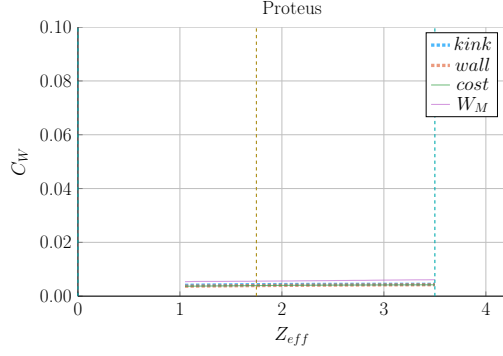
(f) ACT II

Figure H-25: Cost Sensitivity:  $f_D$  vs.  $B_0$

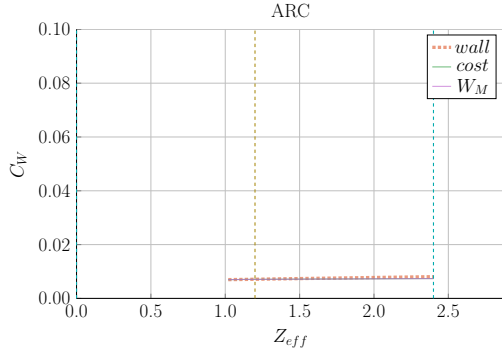
## H.2.6 Effective Charge – $Z_{eff}$



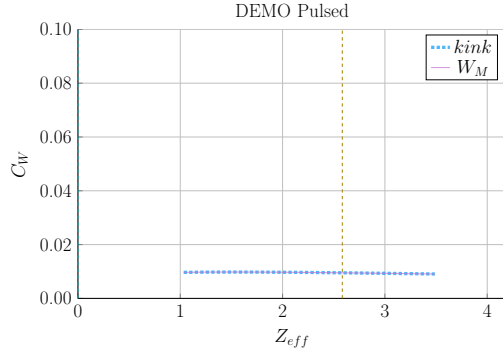
(a) Charybdis



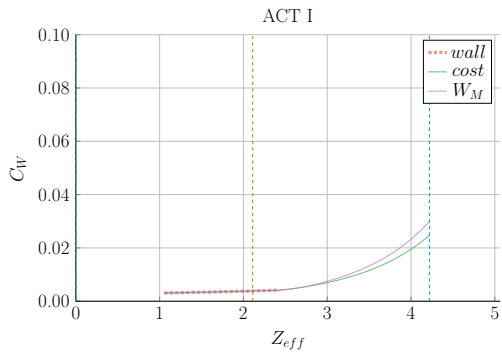
(b) Proteus



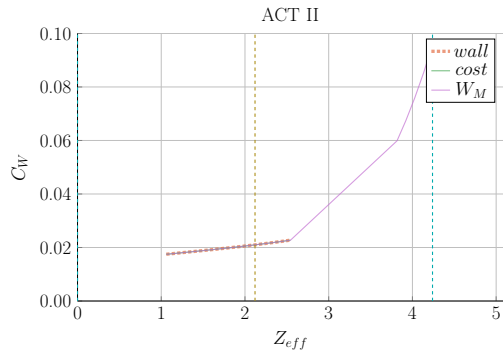
(c) ARC



(d) DEMO Pulsed



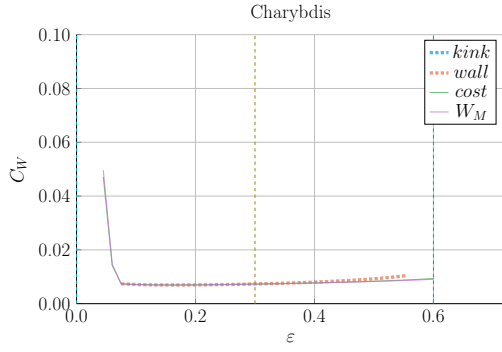
(e) ACT I



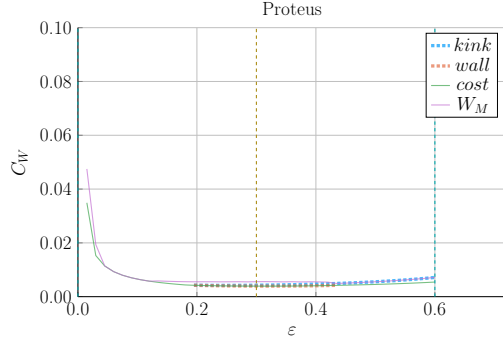
(f) ACT II

Figure H-26: Cost Sensitivity:  $Z_{eff}$  vs.  $B_0$

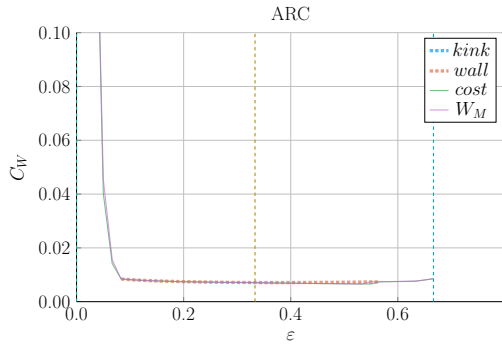
## H.2.7 Inverse Aspect Ratio – $\varepsilon$



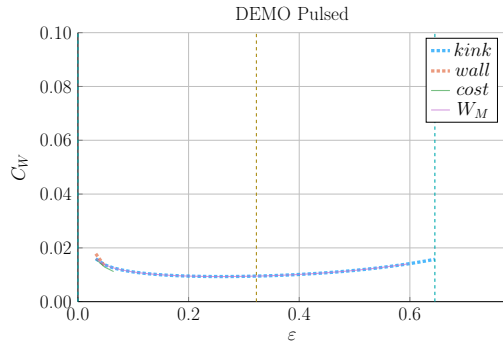
(a) Charybdis



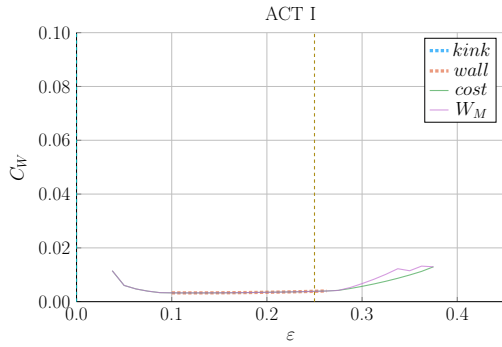
(b) Proteus



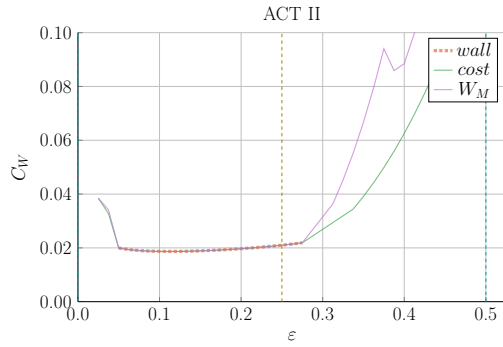
(c) ARC



(d) DEMO Pulsed



(e) ACT I

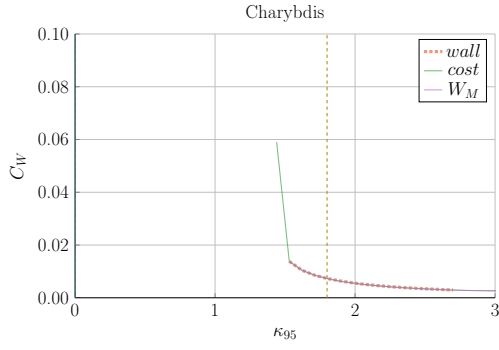


(f) ACT II

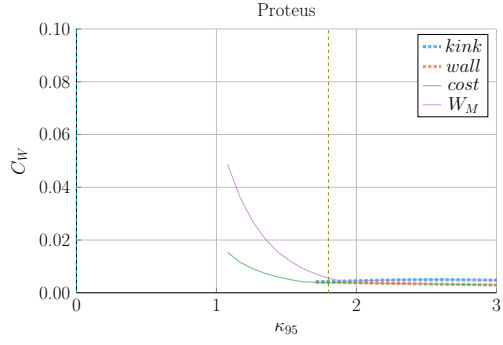
Figure H-27: Cost Sensitivity:  $\varepsilon$  vs.  $B_0$



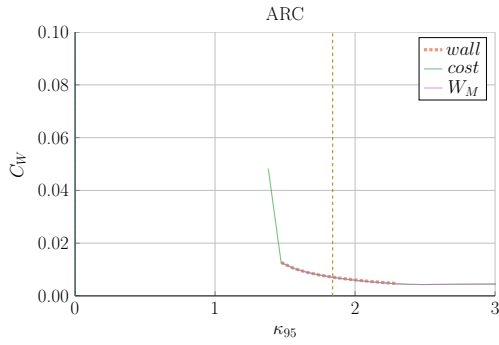
## H.2.8 Elongation – $\kappa_{95}$



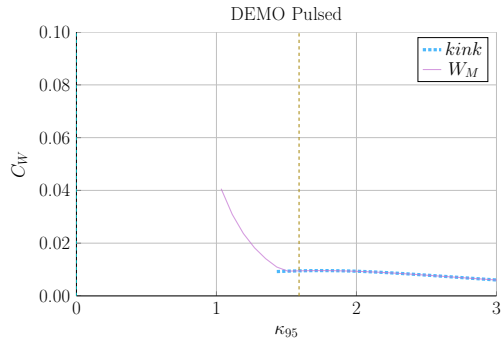
(a) Charybdis



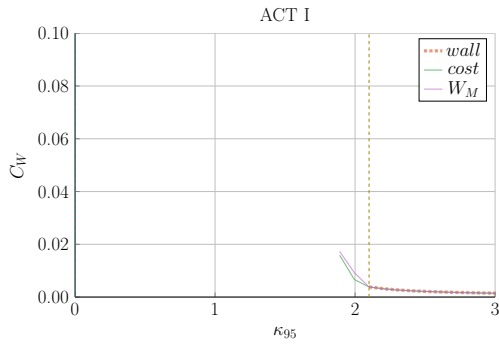
(b) Proteus



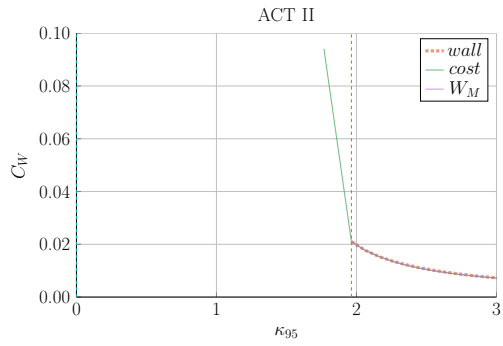
(c) ARC



(d) DEMO Pulsed



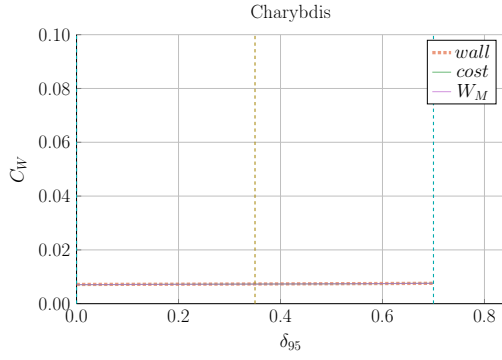
(e) ACT I



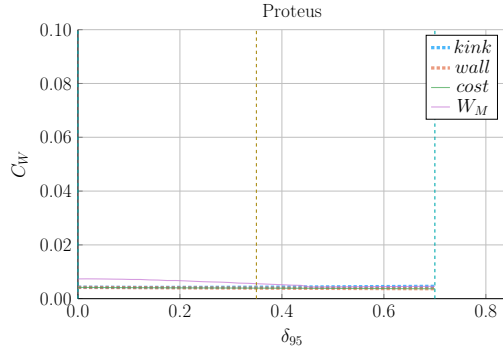
(f) ACT II

Figure H-28: Cost Sensitivity:  $\kappa_{95}$  vs.  $B_0$

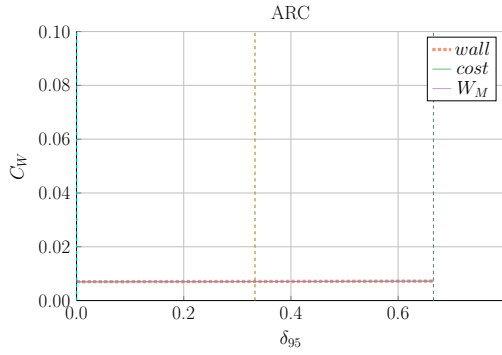
## H.2.9 Triangularity – $\delta_{95}$



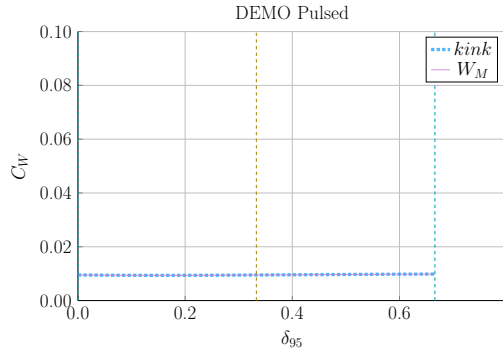
(a) Charybdis



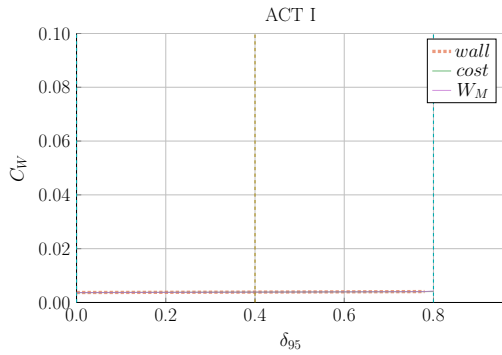
(b) Proteus



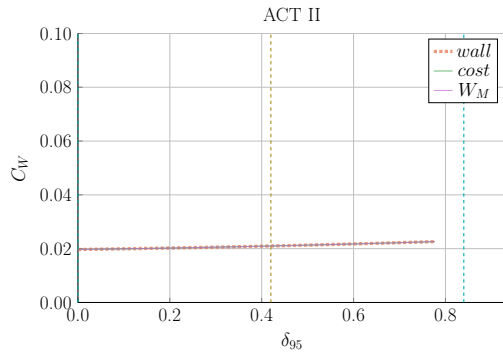
(c) ARC



(d) DEMO Pulsed



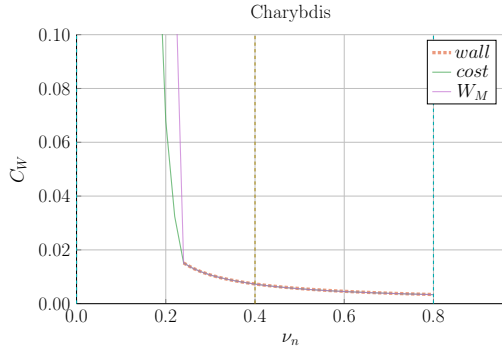
(e) ACT I



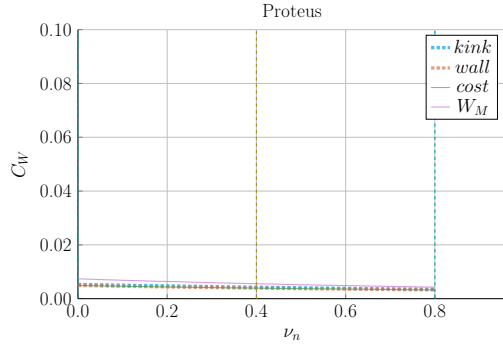
(f) ACT II

Figure H-29: Cost Sensitivity:  $\delta_{95}$  vs.  $B_0$

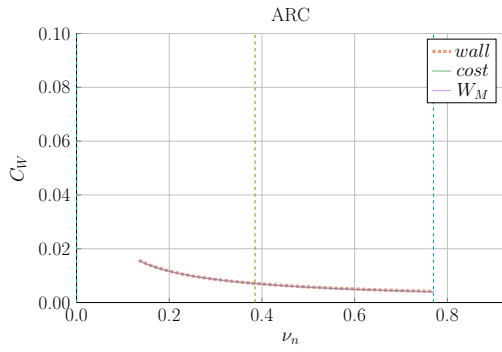
## H.2.10 Density Peaking Factor – $\nu_n$



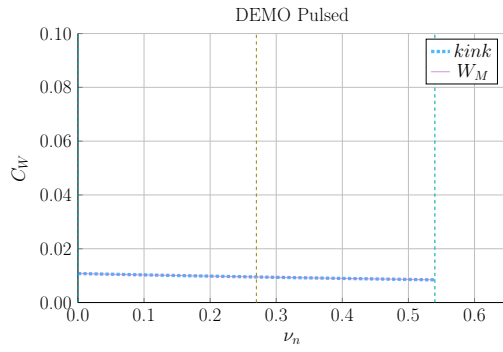
(a) Charybdis



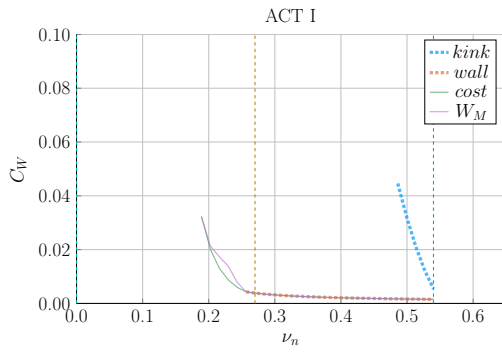
(b) Proteus



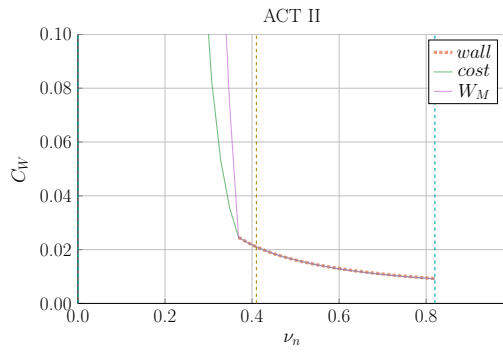
(c) ARC



(d) DEMO Pulsed



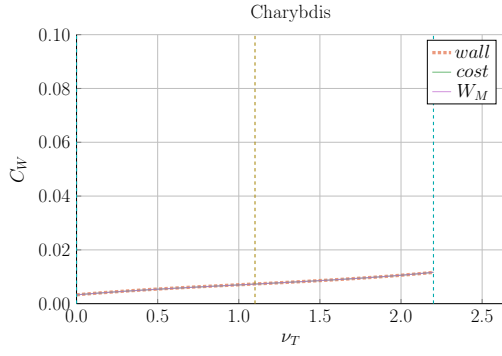
(e) ACT I



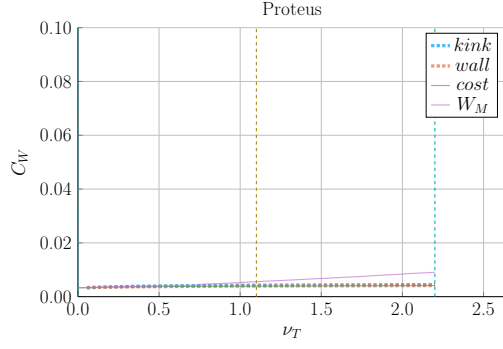
(f) ACT II

Figure H-30: Cost Sensitivity:  $\nu_n$  vs.  $B_0$

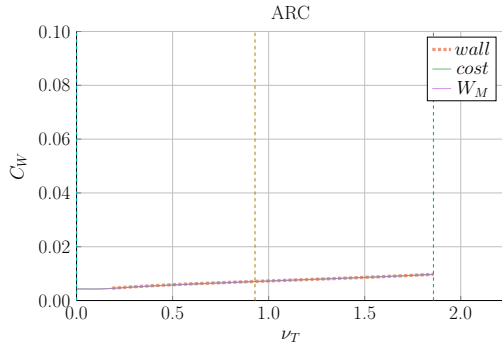
## H.2.11 Temperature Peaking Factor – $\nu_T$



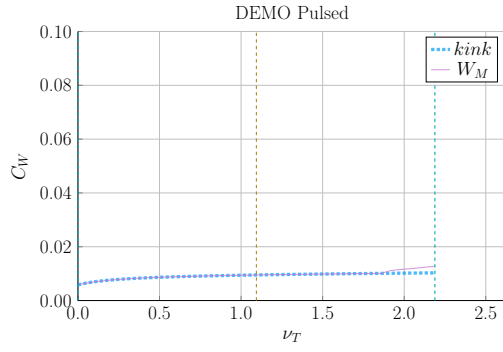
(a) Charybdis



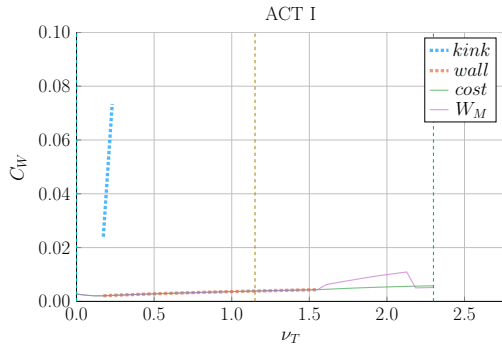
(b) Proteus



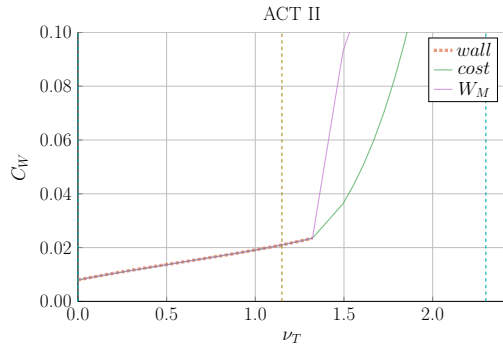
(c) ARC



(d) DEMO Pulsed



(e) ACT I



(f) ACT II

Figure H-31: Cost Sensitivity:  $\nu_T$  vs.  $B_0$

## H.2.12 Internal Inductance – $l_i$

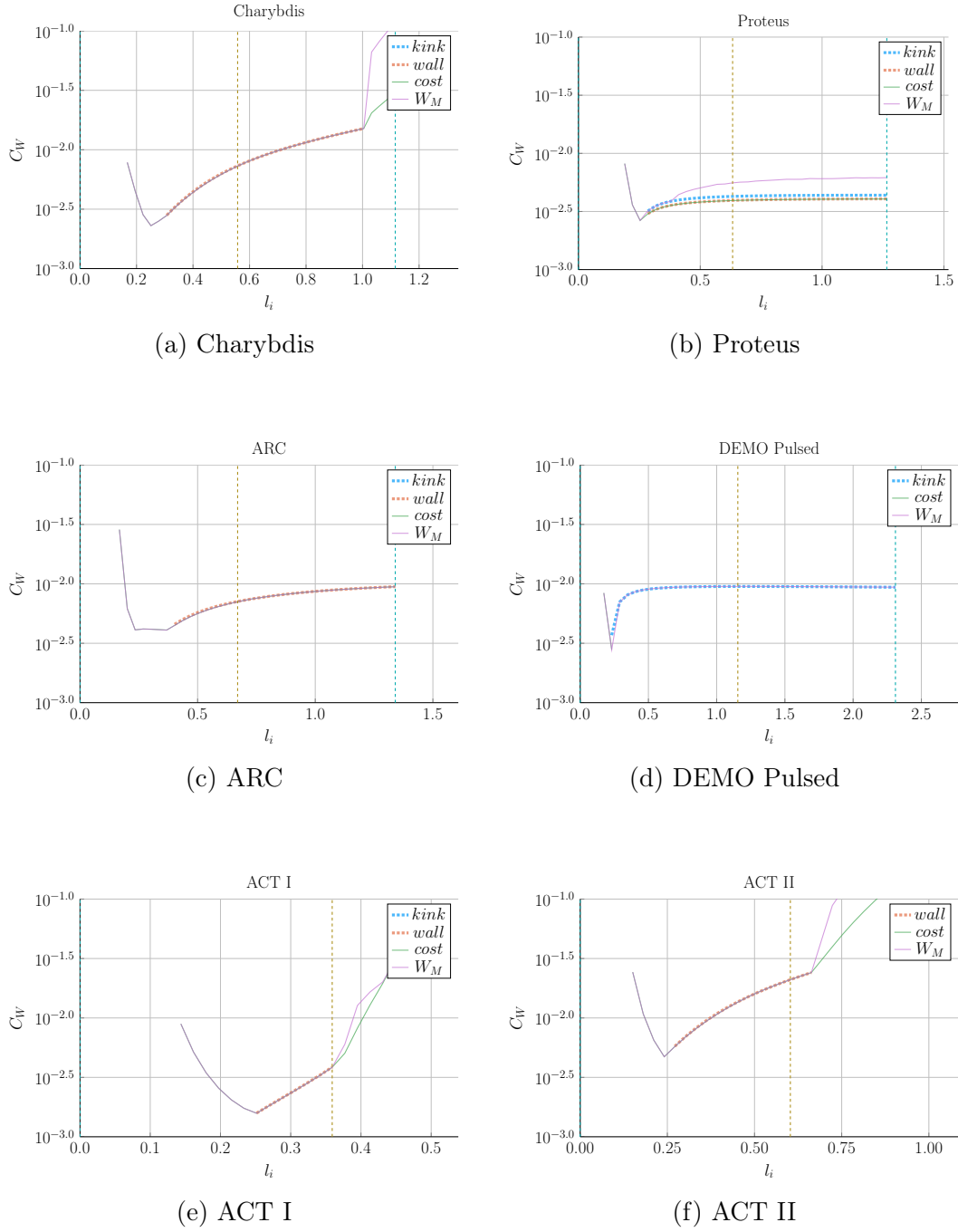
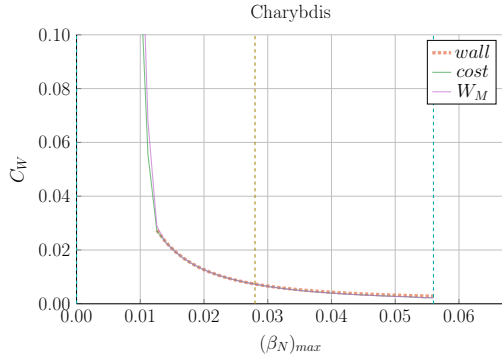
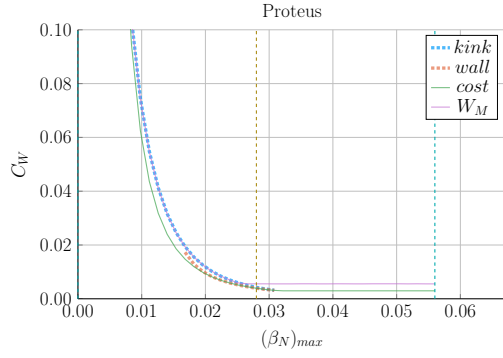


Figure H-32: Cost Sensitivity:  $l_i$  vs.  $B_0$

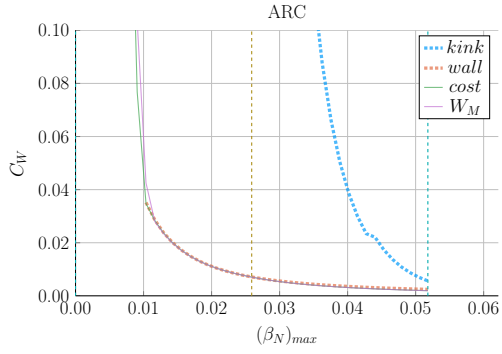
### H.2.13 Max Beta Normal – $(\beta_N)_{max}$



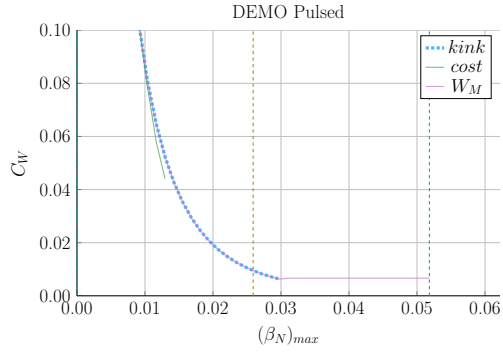
(a) Charybdis



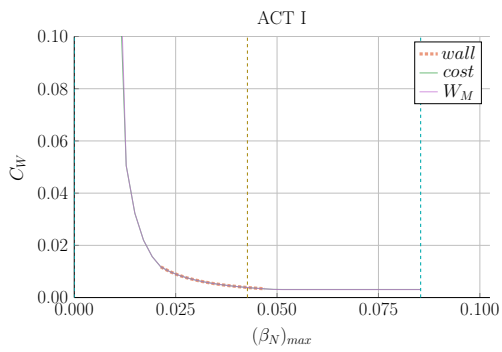
(b) Proteus



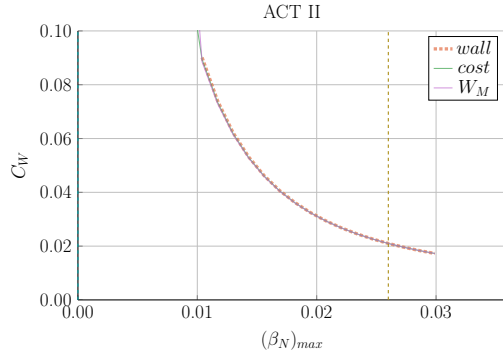
(c) ARC



(d) DEMO Pulsed



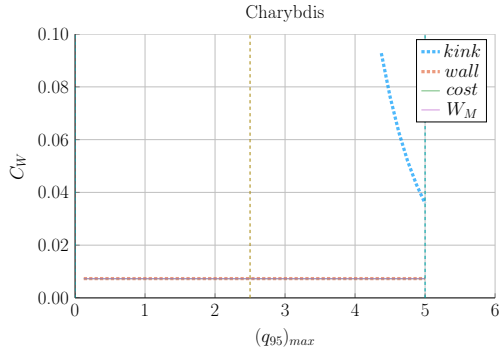
(e) ACT I



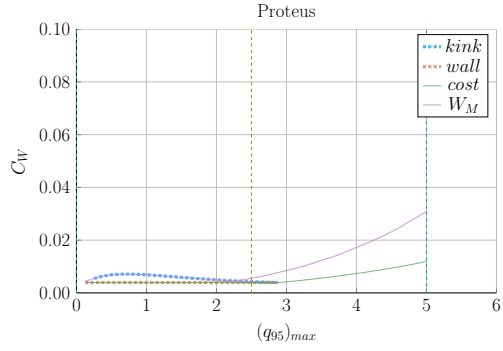
(f) ACT II

Figure H-33: Cost Sensitivity:  $(\beta_N)_{max}$  vs.  $B_0$

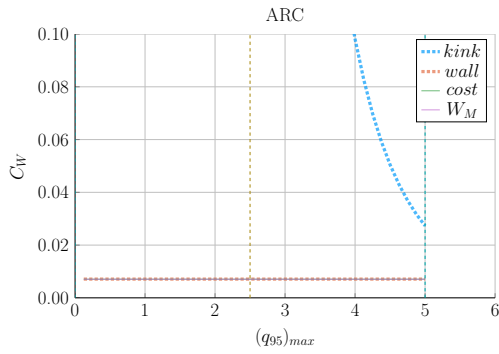
## H.2.14 Max Kink Safety Factor – $(q_{95})_{max}$



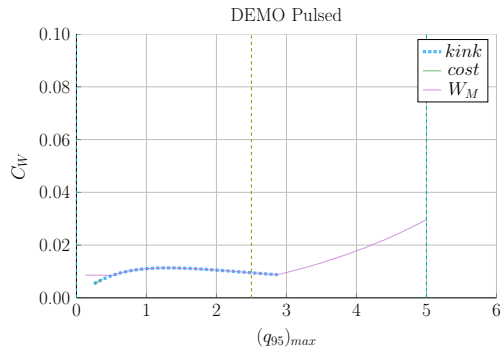
(a) Charybdis



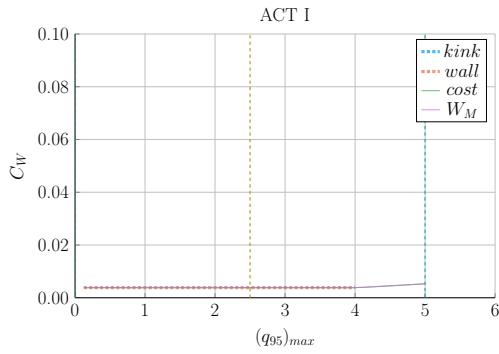
(b) Proteus



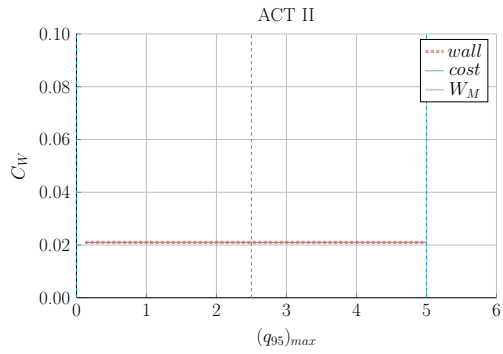
(c) ARC



(d) DEMO Pulsed



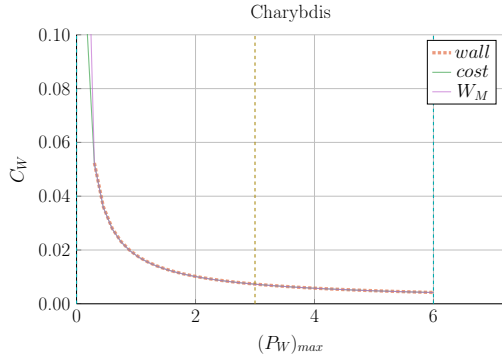
(e) ACT I



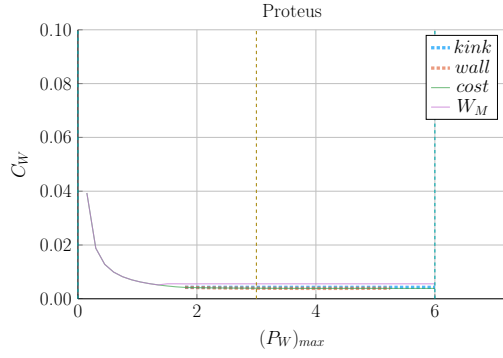
(f) ACT II

Figure H-34: Cost Sensitivity:  $(q_{95})_{max}$  vs.  $B_0$

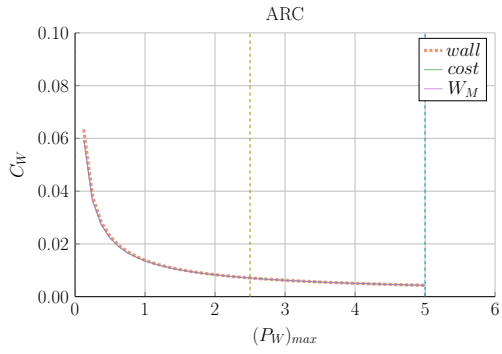
## H.2.15 Max Wall Loading – $(P_W)_{max}$



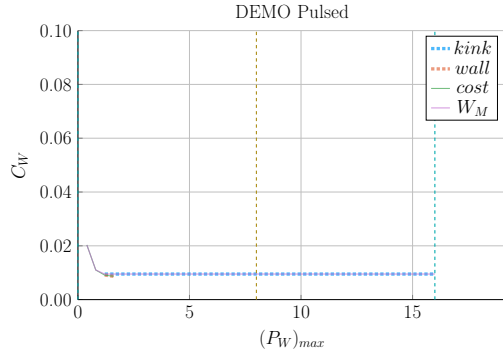
(a) Charybdis



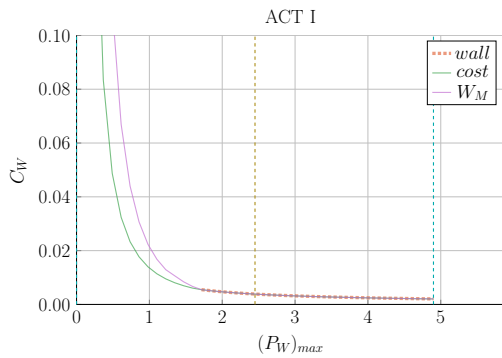
(b) Proteus



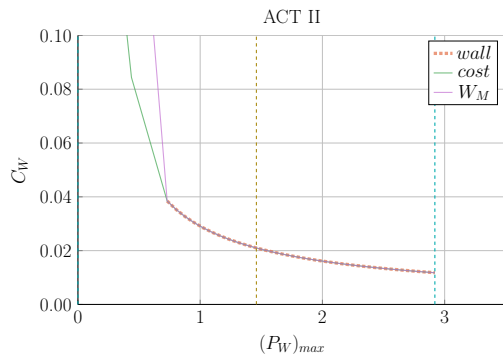
(c) ARC



(d) DEMO Pulsed



(e) ACT I



(f) ACT II

Figure H-35: Cost Sensitivity:  $(P_W)_{max}$  vs.  $B_0$



This page intentionally left blank.



# References

- [1] W. Biel, M. Beckers, R. Kemp, R. Wenninger, and H. Zohm, “Systems code studies on the optimization of design parameters for a pulsed DEMO tokamak reactor,” *Fusion Engineering and Design*, vol. 123, pp. 206–211, 2017.
- [2] G. Federici, C. Bachmann, W. Biel, L. Boccaccini, F. Cismondi, S. Ciattaglia, M. Coleman, C. Day, E. Diegele, T. Franke, *et al.*, “Overview of the design approach and prioritization of R&D activities towards an EU DEMO,” *Fusion Engineering and Design*, vol. 109, pp. 1464–1474, 2016.
- [3] C. Kessel, M. Tillack, F. Najmabadi, F. Poli, K. Ghantous, N. Gorelenkov, X. Wang, D. Navaei, H. Toudeshki, C. Koehly, *et al.*, “The ARIES advanced and conservative tokamak power plant study,” *Fusion Science and Technology*, vol. 67, no. 1, pp. 1–21, 2015.
- [4] G. Lee, J. Kim, S. Hwang, C.-S. Chang, H.-Y. Chang, M. Cho, B. Choi, K. Kim, K. Cho, *et al.*, “The KSTAR project: An advanced steady state superconducting tokamak experiment,” *Nuclear Fusion*, vol. 40, no. 3Y, p. 575, 2000.
- [5] J. P. Freidberg, *Plasma physics and fusion energy*. Cambridge university press, 2008.
- [6] B. Sorbom, J. Ball, T. Palmer, F. Mangiarotti, J. Sierchio, P. Bonoli, C. Kasten, D. Sutherland, H. Barnard, C. Haakonsen, *et al.*, “ARC: A compact, high-field, fusion nuclear science facility and demonstration power plant with demountable magnets,” *Fusion Engineering and Design*, vol. 100, pp. 378–405, 2015.
- [7] M. Kovari, R. Kemp, H. Lux, P. Knight, J. Morris, and D. Ward, “"PROCESS": A systems code for fusion power plants—Part 1: Physics,” *Fusion Engineering and Design*, vol. 89, no. 12, pp. 3054–3069, 2014.
- [8] B. Meszaros *et al.*, “DEMO Input File.” [http://ccfe.ac.uk/assets/Documents/Other/DEM01\\_Reference\\_Design\\_-\\_2015\\_April\\_\(EU\\_2MDKFH\\_v1\\_0.txt\)](http://ccfe.ac.uk/assets/Documents/Other/DEM01_Reference_Design_-_2015_April_(EU_2MDKFH_v1_0.txt)).
- [9] H. Fountain, “A Dream of Clean Energy at a Very High Price.” <https://www.nytimes.com/2017/03/27/science/fusion-power-plant-iter-france.html>, 2017. Accessed: 2018-12-6.

- [10] J. Tirone, “World’s Biggest Science Experiment Seeks More Time and Money.” <https://www.bloomberg.com/news/articles/2016-06-15/world-s-biggest-science-experiment-seeks-more-time-and-money>, 2016. Accessed: 2018-12-6.
- [11] D. J. Griffiths, “Introduction to electrodynamics,” 2005.
- [12] T. Hartmann, “Development of a modular systems code to analyse the implications of physics assumptions on the design of a demonstration fusion power plant,” 2013.
- [13] J. Freidberg, F. Mangiarotti, and J. Minervini, “Designing a tokamak fusion reactor—How does plasma physics fit in?,” *Physics of Plasmas*, vol. 22, no. 7, p. 070901, 2015.
- [14] J. Jean, “HELIOS: a zero-dimensional tool for next step and reactor studies,” *Fusion Science and Technology*, vol. 59, no. 2, pp. 308–349, 2011.
- [15] C. Reux, L. Di Gallo, *et al.*, “DEMO reactor design using the new modular system code SYCOMORE,” *Nuclear Fusion*, vol. 55, no. 7, p. 073011, 2015.
- [16] C. Bustreo, G. Casini, G. Zollino, T. Bolzonella, and R. Piovan, “FRESCO, a simplified code for cost analysis of fusion power plants,” *Fusion Engineering and Design*, vol. 88, no. 12, pp. 3141–3151, 2013.
- [17] Z. Dragojlovic, A. R. Raffray, F. Najmabadi, C. Kessel, L. Waganer, *et al.*, “An advanced computational algorithm for systems analysis of tokamak power plants,” *Fusion Engineering and Design*, vol. 85, no. 2, pp. 243–265, 2010.
- [18] E. Fable, C. Angioni, M. Siccino, and H. Zohm, “Plasma physics for fusion reactor system codes: Framework and model code,” *Fusion Engineering and Design*, vol. 130, pp. 131–136, 2018.
- [19] P. Knight, “A user’s guide to the PROCESS systems code,” *UKAEA Fusion*, vol. 2, no. 0, 1996.
- [20] C. Angioni, H. Weisen, O. Kardaun, M. Maslov, A. Zabolotsky, C. Fuchs, *et al.*, “Scaling of density peaking in H-mode plasmas based on a combined database of AUG and JET observations,” *Nuclear Fusion*, vol. 47, no. 9, p. 1326, 2007.
- [21] T. Onjun, G. Bateman, A. Kritz, and G. Hammett, “Models for the pedestal temperature at the edge of H-mode tokamak plasmas,” *Physics of Plasmas*, vol. 9, no. 12, pp. 5018–5030, 2002.
- [22] A. E. Hubbard, “Physics and scaling of the H-mode pedestal,” *Plasma Physics and Controlled Fusion*, vol. 42, no. 5A, p. A15, 2000.
- [23] M. Greenwald, “Density limits in toroidal plasmas,” *Plasma Physics and Controlled Fusion*, vol. 44, no. 8, p. R27, 2002.

- [24] C. Roach, M. Walters, R. Budny, F. Imbeaux, T. Fredian, M. Greenwald, *et al.*, “The 2008 public release of the international multi-tokamak confinement profile database,” *Nuclear Fusion*, vol. 48, no. 12, p. 125001, 2008.
- [25] J. D. Lawson, “Some criteria for a power producing thermonuclear reactor,” *Proceedings of the Physical Society. Section B*, vol. 70, no. 1, p. 6, 1957.
- [26] J. Jacquinot, S. Putvinski, G. Bosia, A. Fukuyama, R. Hemsworth, S. Konovalov, W. Nevins, F. Perkins, K. Rasumova, F. Romanelli, *et al.*, “Plasma auxiliary heating and current drive,” *Nuclear Fusion*, vol. 39, no. 12, pp. 2495–2539, 1999.
- [27] D. Ehst and C. Karney, “Approximate formula for radiofrequency current drive efficiency with magnetic trapping,” *Nuclear fusion*, vol. 31, no. 10, p. 1933, 1991.
- [28] I. H. Hutchinson, “Principles of plasma diagnostics,” *Plasma Physics and Controlled Fusion*, vol. 44, no. 12, p. 2603, 2002.
- [29] J. Cordey, K. Thomsen, A. Chudnovskiy, O. Kardaun, T. Takizuka, J. Snipes, M. Greenwald, L. Sugiyama, F. Ryter, A. Kus, *et al.*, “Scaling of the energy confinement time with  $\beta$  and collisionality approaching ITER conditions,” *Nuclear fusion*, vol. 45, no. 9, p. 1078, 2005.
- [30] E. Doyle, W. Houlberg, Y. Kamada, V. Mukhovatov, T. Osborne, A. Polevoi, G. Bateman, J. Connor, J. Cordey, T. Fujita, *et al.*, “Plasma confinement and transport,” *Nuclear Fusion*, vol. 47, no. 6, p. S18, 2007.
- [31] N. Uckan, “ITER physics design guidelines at high aspect ratio,” tech. rep., Oak Ridge National Lab., 1991.
- [32] B. LaBombard, E. Marmor, J. Irby, J. Terry, R. Vieira, G. Wallace, D. Whyte, S. Wolfe, *et al.*, “ADX: a high field, high power density, advanced divertor and RF tokamak,” *Nuclear Fusion*, vol. 55, no. 5, p. 053020, 2015.
- [33] O. Mitarai, S. W. Wolfe, A. Hirose, and H. M. Skarsgard, “Alternating current tokamak reactor with long pulses,” *Fusion technology*, vol. 15, no. 2P1, pp. 204–213, 1989.
- [34] S. Hirshman and G. Neilson, “External inductance of an axisymmetric plasma,” *The Physics of fluids*, vol. 29, no. 3, pp. 790–793, 1986.
- [35] P. Libeyre, N. Mitchell, D. Bessette, Y. Gribov, C. Jong, and C. Lyraud, “Detailed design of the ITER central solenoid,” *Fusion Engineering and Design*, vol. 84, no. 7-11, pp. 1188–1191, 2009.
- [36] J. P. Freidberg, A. Cerfon, and J. Lee, “Tokamak elongation—how much is too much? Part 1. Theory,” *Journal of Plasma Physics*, vol. 81, no. 6, 2015.
- [37] L. Giancarli, V. Chuyanov, M. Abdou, M. Akiba, B. Hong, *et al.*, “Breeding blanket modules testing in ITER: an international program on the way to DEMO,” *Fusion Engineering and Design*, vol. 81, no. 1-7, pp. 393–405, 2006.

- [38] H. Lux, R. Kemp, E. Fable, and R. Wenninger, “Radiation and confinement in 0D fusion systems codes,” *Plasma Physics and Controlled Fusion*, vol. 58, no. 7, p. 075001, 2016.
- [39] G. Giruzzi, J. Artaud, M. Baruzzo, T. Bolzonella, E. Fable, L. Garzotti, I. Ivanova-Stanik, R. Kemp, D. King, M. Schneider, *et al.*, “Modelling of pulsed and steady-state DEMO scenarios,” *Nuclear Fusion*, vol. 55, no. 7, p. 073002, 2015.
- [40] R. Maingi, A. Lumsdaine, S. Barish, A. White, L. Chacon, S. Gourlay, *et al.*, “Fusion Energy Sciences Advisory Committee Report: Transformative Enabling Capabilities for Efficient Advance Toward Fusion Energy,” tech. rep., 2018.
- [41] M. Mauel, M. Shochet, C. A. Back, R. Betti, I. Chapman, C. Forest, T. K. Fowler, J. Freidberg, R. Gilgenbach, W. Heidbrink, M. Herrmann, F. Jenko, *et al.*, *Final Report of the Committee on a Strategic Plan for U.S. Burning Plasma Research*. Washington, DC: The National Academies Press, 2018.
- [42] J. Menard, S. Gerhardt, M. Bell, J. Bialek, A. Brooks, J. Canik, J. Chrzanowski, M. Denault, L. Dudek, D. Gates, *et al.*, “Overview of the physics and engineering design of NSTX upgrade,” *Nuclear Fusion*, vol. 52, no. 8, p. 083015, 2012.
- [43] U. Stroth, M. Murakami, R. Dory, H. Yamada, S. Okamura, F. Sano, and T. Obiki, “Energy confinement scaling from the international stellarator database,” *Nuclear Fusion*, vol. 36, no. 8, p. 1063, 1996.
- [44] L. Giannone, J. Baldzuhn, R. Burhenn, P. Grigull, U. Stroth, F. Wagner, R. Brakel, C. Fuchs, H. Hartfuss, K. McCormick, *et al.*, “Physics of the density limit in the W7-AS stellarator,” *Plasma physics and controlled fusion*, vol. 42, no. 6, p. 603, 2000.
- [45] D. Whyte, A. Hubbard, J. Hughes, B. Lipschultz, J. Rice, E. Marmor, M. Greenwald, I. Cziegler, A. Dominguez, T. Golfinopoulos, *et al.*, “I-mode: an H-mode energy confinement regime with L-mode particle transport in Alcator C-Mod,” *Nuclear Fusion*, vol. 50, no. 10, p. 105005, 2010.
- [46] H. Bosch and G. Hale, “Improved formulas for fusion cross-sections and thermal reactivities,” *Nuclear fusion*, vol. 32, no. 4, p. 611, 1992.
- [47] Z. Hartwig and Y. Podpaly, “The magnetic fusion energy formulary,” 2012.
- [48] J. D. Huba, “NRL plasma formulary,” tech. rep., Naval Research Lab Washington DC Plasma Physics Div, 2006.
- [49] J. Wesson and D. J. Campbell, *Tokamaks*, vol. 149. Oxford University Press, 2011.
- [50] C. Kessel, “Bootstrap current in a tokamak,” *Nuclear Fusion*, vol. 34, no. 9, p. 1221, 1994.